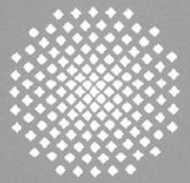
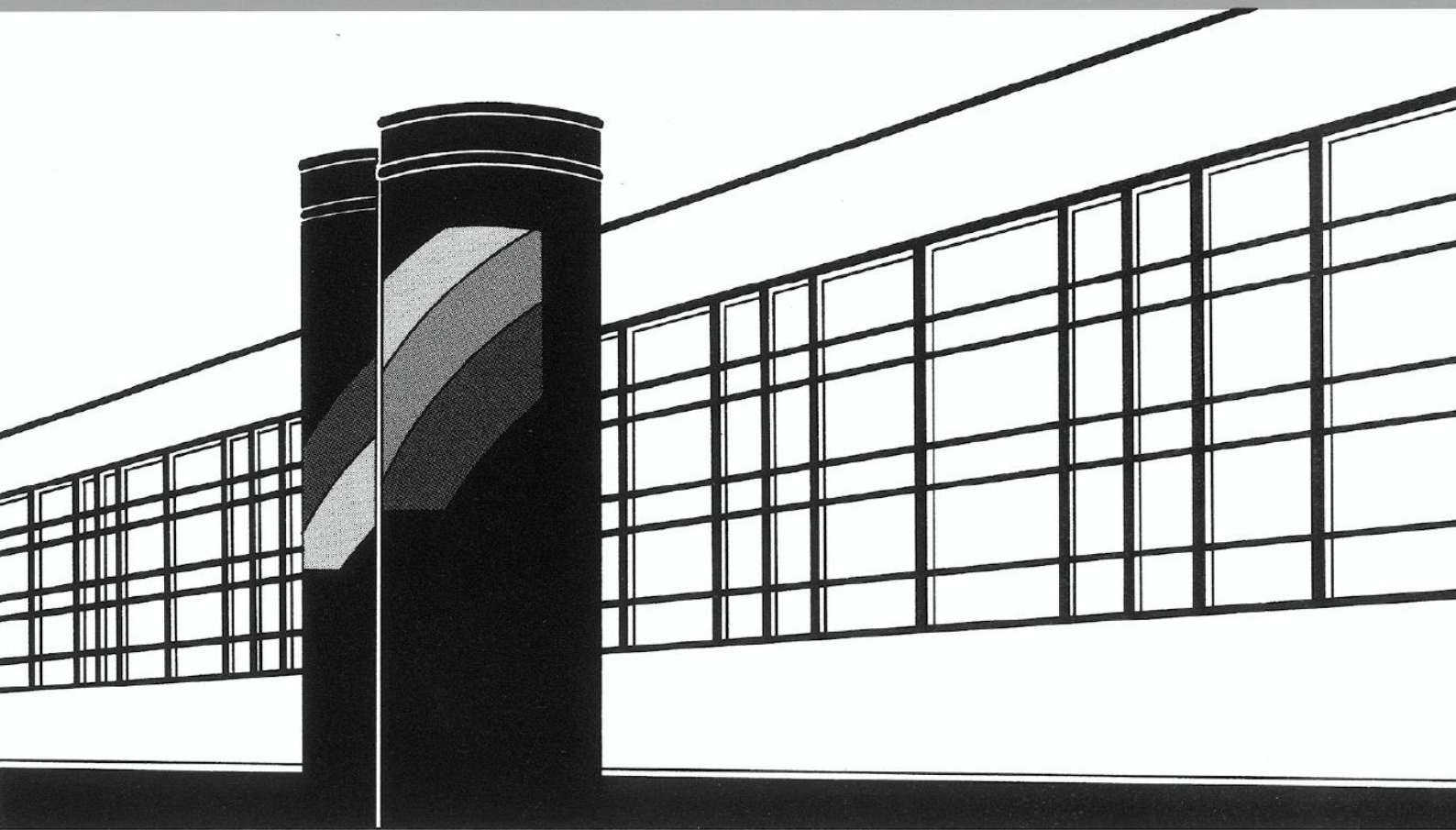


Universität Stuttgart



Institut für Wasser- und Umweltsystemmodellierung

Mitteilungen



Heft 222 Markus Wolff

Multi-Scale Modeling of
Two-Phase Flow in Porous Media
Including Capillary Pressure Effects

Multi-Scale Modeling of Two-Phase Flow in Porous Media Including Capillary Pressure Effects

Von der Fakultät Bau- und Umweltingenieurwissenschaften und dem
Stuttgart Research Centre for Simulation Technology
der Universität Stuttgart zur Erlangung der Würde eines
Doktor-Ingenieurs (Dr.-Ing.) genehmigte Abhandlung

Vorgelegt von
Markus Wolff
aus Stuttgart

Hauptberichter:	Prof. Dr.-Ing. Rainer Helmig
Mitberichter:	Prof. Hamdi Tchelepi, Ph.D.
Mitberichter:	Prof. Dr. rer. nat. Peter Bastian

Tag der mündlichen Prüfung: 24. Juli 2013

Institut für Wasser- und Umweltsystemmodellierung
der Universität Stuttgart
2013

Heft 222 Multi-Scale Modeling
of Two-Phase Flow in
Porous Media Including
Capillary Pressure Effects

von
Dr.-Ing.
Markus Wolff

Eigenverlag des Instituts für Wasser- und Umweltsystemmodellierung
der Universität Stuttgart

D93 Multi-Scale Modeling of Two-Phase Flow in Porous Media Including Capillary Pressure Effects

Bibliografische Information der Deutschen Nationalbibliothek

Die Deutsche Nationalbibliothek verzeichnet diese Publikation in der Deutschen Nationalbibliografie; detaillierte bibliografische Daten sind im Internet über <http://www.d-nb.de> abrufbar

Wolff, Markus:

Multi-Scale Modeling of Two-Phase Flow in Porous Media Including Capillary Pressure Effects von Markus Wolff. Institut für Wasser- und Umweltsystemmodellierung, Universität Stuttgart. - Stuttgart: Institut für Wasser- und Umweltsystemmodellierung, 2013

(Mitteilungen Institut für Wasser- und Umweltsystemmodellierung, Universität Stuttgart: H. 222)

Zugl.: Stuttgart, Univ., Diss., 2013

ISBN 978-3-942036-26-9

NE: Institut für Wasser- und Umweltsystemmodellierung <Stuttgart>: Mitteilungen

Gegen Vervielfältigung und Übersetzung bestehen keine Einwände, es wird lediglich um Quellenangabe gebeten.

Herausgegeben 2013 vom Eigenverlag des Instituts für Wasser- und Umweltsystemmodellierung

Druck: Document Center S. Kästl, Ostfildern

Danksagung

Diese Arbeit entstand während meiner Zeit am Lehrstuhl für Hydromechanik und Hydrosystemmodellierung der Universität Stuttgart im Rahmen des Forschungsprojekts „Multi-Scale Multi-Physics Numerical Models for Flow and Transport in Porous Media“. Ich danke der Deutschen Forschungsgemeinschaft (DFG) für die Förderung dieses Projekts im Rahmen des Exzellenzclusters Simulation Technology (EXC 310/1) an der Universität Stuttgart.

Mein besonderer Dank gilt Rainer Helmig für die Anregung zu dieser Forschungsarbeit und die Unterstützung während der letzten Jahre. Die außergewöhnliche Atmosphäre an seinem Lehrstuhl, die geprägt ist von Kollegialität, gegenseitiger Unterstützung, aber auch kritischer Diskussion, hat entscheidend zum erfolgreichen Abschluss dieser Arbeit beigetragen. Des Weiteren danke ich Peter Bastian und Hamdi Tchelepi für die Übernahme des Mitberichts und für fruchtbare Gespräche. Insbesondere möchte ich mich bei Hamdi Tchelepi für die Einladung als Gastwissenschaftler in der SUPRI-B Gruppe des Department of Energy Resources Engineering an der Stanford University bedanken. Die Eindrücke, Erfahrungen und Anregungen, die ich bei diesem Aufenthalt sammeln konnte, haben meine Arbeit entscheidend geprägt.

Ich danke allen Kolleginnen und Kollegen am Lehrstuhl für Hydromechanik und Hydrosystemmodellierung für die gute Zusammenarbeit. Insbesondere möchte ich mich bei Bernd Flemisch für die Ratschläge und Hilfestellungen und bei Yufei Cao bedanken. Des Weiteren danke ich allen Entwicklern der Open-Source-Softwareprojekte DuMu^x und DUNE.

Abschließend möchte ich meiner Familie danken, die mir besonders nach Rückschlägen, die vermutlich Teil jeder Promotion und jedes Forschungsprojekts sind, immer wieder Rückhalt gegeben hat.

Contents

List of Figures	III
Nomenclature	XIII
Abstract	i
Zusammenfassung	v
1 Introduction	1
2 Theoretical Background and Mathematical Models	5
2.1 Basic Concepts for Modeling Porous Media	5
2.1.1 Phases and Wettability	6
2.1.2 Representative Elementary Volume	6
2.1.3 Darcy's Law	10
2.1.4 Fluid Properties	13
2.2 Fine Scale Model Equations	14
2.2.1 Immiscible Two-Phase Flow Equations	14
2.2.2 Fractional Flow Formulation	15
2.3 Coarse Scale Model Equations	21
2.3.1 Immiscible Two-phase Flow Equations	21
2.3.2 Fractional Flow Formulation	22
3 Numerical Methods	27
3.1 Finite Volume Discretization with MPFA	28
3.1.1 The O-Method	34
3.1.2 The L-Method	37
3.1.3 The L-Method in Three Dimensions	40
3.1.4 A New Criterion for Choosing the L-Stencil	44

3.1.5	Boundary Handling	48
3.1.6	Extension to Two-Phase Flow	50
3.1.7	Tests	53
3.2	Non-Conforming Adaptive Grids	67
3.2.1	Boundary Handling	68
3.2.2	Tests	72
3.3	The Treatment of Tensorial Solution Dependent Coefficients	79
3.3.1	Advective Flux	80
3.3.2	Capillary Flux	81
3.3.3	Wetting Phase Flux	83
3.3.4	Some Remarks on Upwinding	85
3.3.5	Tests	86
4	Upscaling and Multi-Scale Modeling	93
4.1	Upscaling	93
4.1.1	Effective Porosity	94
4.1.2	Effective Capillary Pressure	95
4.1.3	Effective Absolute Permeability	99
4.1.4	Effective Relative Permeability	100
4.1.5	Limitations of Upscaling	110
4.1.6	Tests	113
4.2	Multi-Scale Modeling	125
4.2.1	Grid adaptation – Switching Scales	126
4.2.2	Criteria	127
4.2.3	Tests	130
5	Application	143
5.1	Two-Dimensional Drainage Scenarios	144
5.2	Two-Dimensional Imbibition Scenarios	152
5.3	Application to the Three-Dimensional SPE10 Benchmark	158
6	Final Remarks	167
6.1	Summary	167
6.2	Discussion and Future Work	169
	Bibliography	173

List of Figures

1.1	Schematic of the different interacting layers of a multi-scale model.	4
2.1	Contact angle between a wetting and a non-wetting fluid.	6
2.2	Illustration of the term representative elementary volume (REV) for the porosity.	7
3.1	Grid cell (thick lines) divided into four sub-control-volumes in 2-d (a), and into eight sub-control-volumes in 3-d (b)	31
3.2	Triangle (a) (2-d) and tetrahedron (b) (3-d) described by the continuity points for the pressure approximation of one sub-control-volume.	32
3.3	Sub-fluxes at a cell-cell interface according to the sub-control-volumes. (a): Two sub-fluxes (2-d); (b): Four sub-fluxes (3-d)	34
3.4	Sub-control-volumes (dashed and solid black lines) and interaction volume (bold line) for the flux approximation for the corresponding half faces between cells i , j , k and l	35
3.5	Sub-control-volumes (dashed and solid black lines) and interaction volumes (bold line) for the approximation of the flux across the interface 12 (half face between i and j)	37
3.6	Four L-stencils for the flux calculation through sub-interface $\bar{x}_1\bar{x}_4\bar{x}_0\bar{x}_5$	41
3.7	Visualization of the anisotropic permeability tensor (ellipsoid) inside the test domain.	46
3.8	Cell stencils for differently skewed parallelepiped grids using the s_1 -criterion (upper row) and the \bar{t}_1 -criterion (lower row). The skewness of the grid is increased from left to right by decreasing the angle β (Figure 3.7): (a) 90° , (b) 45° , (c) 22.5° , (d) 11.25°	47
3.9	Top view on the cell stencils of the s_1 -criterion (a) and the \bar{t}_1 -criterion (b) for $\beta = 11.25^\circ$	47

3.10 Flux calculation at boundary faces in two space dimensions: (a) flux across a boundary face; (b) flux across faces intersecting with a boundary face.	48
3.11 Flux calculation at boundary faces in three space dimensions: (a) flux across a boundary face; (b) flux across faces intersecting with one boundary face; (c) flux across faces intersecting with two boundary faces. . .	49
3.12 Setup of the Buckley-Leverett problem. The arrows mark the wetting fluid inflow and the non-wetting fluid outflow.	54
3.13 Simulation grid of level 1 in the two-dimensional case (a) (64 cells) and in the three-dimensional case (b) (256 cells) of the Buckley-Leverett problem.	54
3.14 Wetting phase saturation at $t = 2 \times 10^5$ s. The results are shown for the grid levels 1-4 (top to bottom) using the MPFA O-method (a) and the MPFA L-method (b).	55
3.15 Wetting phase saturation at $t = 2 \times 10^5$ s. The results are shown for the grid levels 1-4 (top to bottom) using an analytic solution (a) and a simple TPFA model (b).	55
3.16 Wetting phase saturation error at $t = 2 \times 10^5$ s. From top to bottom the results are shown for TPFA, O-method, and L-method, for grid level 1 (a) and 4 (b).	56
3.17 Global error of the transport solution of the Buckley-Leverett problem at $t = 2 \times 10^5$ s over the number of cells.	56
3.18 Wetting phase saturation at $t = 2 \times 10^5$ s using the 3-d MPFA L-method.	57
3.19 Comparison of the 2-d solution (a) and a 2-d slice of the 3-d solution (b) of the L-method with the analytic solution (c).	57
3.20 Setup of the McWhorter problem. The arrows mark the wetting fluid inflow and the non-wetting fluid outflow.	58
3.21 Wetting phase saturation at $t = 2 \times 10^5$ s. The results are shown for the grid levels 1-5 (top to bottom) using the MPFA O-method (a) and the MPFA L-method (b).	59
3.22 Wetting phase saturation at $t = 2 \times 10^5$ s. The results are shown for the grid levels 1-5 (top to bottom) using an analytic solution (a) and a simple TPFA model (b).	59
3.23 Wetting phase saturation error at $t = 2 \times 10^5$ s. From top to bottom the results are shown for TPFA, O-method, and L-method, for grid level 1 (a) and 5 (b).	60

3.24	Global error of the transport solution of the McWhorter problem at $t = 2 \times 10^5$ s over the number of cells.	61
3.25	Wetting phase saturation at $t = 2 \times 10^5$ s using the 3-d MPFA L-method.	61
3.26	Comparison of the 2-d solution (a) and a 2-d slice of the 3-d solution (b) of the L-method with the analytic solution (c).	61
3.27	Setup of the capillary pressure heterogeneity problem. The arrows mark the non-wetting fluid inflow and the wetting fluid outflow. In the vertical column a fine material is surrounded by coarse material.	62
3.28	Function plots of the p_c - S_w -functions illustrating the interface saturation S_w^* , where $p_c^c(S_w^*) = p_d^f$	63
3.29	Non-wetting phase saturation at $t = 1.5 \times 10^3$ s using the O-method: (a) (structured grid), (b) (unstructured grid), and the L-method, (c) (structured grid), (d) (unstructured grid).	65
3.30	Non-wetting phase saturation plot along the y -axis at $x = 0.05$ m at the end of the simulation (a) and at the time of the breakthrough into the fine material (b) (structured grid).	66
3.31	Non-wetting phase saturation plot along the y -axis at $x = 0.05$ m at the end of the simulation (a) and at the time of the breakthrough into the fine material (b) (unstructured grid).	66
3.32	Flux stencil around a hanging node (2-d).	67
3.33	Interaction-volume-types around hanging nodes allowing only one hanging node (HN) per cell face. (Type 1): one face HN; (Type 2): one edge HN, one coarser cell; (Type 3): one edge HN, two coarser cells; (Type 4): one edge HN, two coarser cells, diagonal configuration; (Type 5): one edge HN, three coarser cells; (Type 6): three edge HNs, special case of (Type 2); (Type 7): three edge HNs, special case of (Type 5).	69
3.34	Flux faces of the different interaction-volume-types shown in Figure 3.33. The numbering of the faces relates to the general case without hanging nodes (12 faces per interaction-volume). (Type 1): 8 flux faces; (Type 2): 11 flux faces; (Type 3): 10 flux faces; (Type 4): 10 flux faces; (Type 5): 5 flux faces; (Type 6): see (Type 2); (Type 7): see (Type 5).	70
3.35	Example for boundary treatment with hanging nodes (2-d). The dashed line marks the boundary faces. (a) MPFA flux area (gray) and sub-fluxes (arrows) - Fluxes are not calculated by the MPFA for the whole cell face! (b) MPFA flux area (gray) only for the boundary cells.	70

3.36	Example for boundary treatment with hanging nodes (3-d). The hatched area marks the boundary faces. (a) MPFA flux area (gray) and sub-fluxes (arrows) - Fluxes are not calculated by the MPFA for the whole cell face! (b) MPFA flux area (gray) only for the boundary cells.	71
3.37	Problem setup of the DNAPL infiltration example in 2-d (a) and 3-d (b). The arrow indicates where the DNAPL is released. The gray boxes are lenses of lower permeability and higher entry pressure.	73
3.38	Saturation distributions of the lense scenario at $t = 6 \times 10^4$ s using a TPFA method (a), the O-method (b), the L-method (c), and the adaptive L-method (d).	74
3.39	Saturation distributions of the three-dimensional lense scenario for 1.8×10^5 s simulated time: The upper row shows the results of the TPFA method, the lower row the results of the adaptive MPFA L-method. . .	75
3.40	Locally adapted grids of the adaptive MPFA model for the lense scenario.	75
3.41	Saturation distributions of the anisotropic scenario at $t = 3.4 \times 10^4$ s using a TPFA method (a), the O-method (b), the L-method (c), and the adaptive L-method (d).	76
3.42	Saturation distributions of the three-dimensional anisotropic scenario for 2×10^5 s simulated time: The upper row shows the results of the TPFA method, the lower row the results of the adaptive MPFA L-method. . . .	77
3.43	Saturation distributions of the three-dimensional anisotropic scenario for 2×10^5 s simulated time: Comparison of the results using a locally refined grid (c) - (d), a coarse structured grid (a) - (b), and a fine structured grid (e) - (f).	78
3.44	Locally adapted grids of the MPFA model for the anisotropic scenario.	79
3.45	Setup of the infiltration experiment.	87
3.46	Model domain with the discrete lenses showing the different entry pressures.	87
3.47	Coarse scale constitutive relations (<i>Eichel et al.</i> , 2005).	88
3.48	Saturation distributions calculated with the fine-scale parameter distribution resolving the lenses.	88
3.49	The types of unstructured grids used to test the mpfa methods.	89
3.50	Saturation distributions obtained using the O-method (upper row) and the L-method (lower row), on a structured grid (a), an unstructured grid of type UG 1 (b), and an unstructured grid of type UG 2 (c).	89

3.51	Saturation distributions obtained using the O-method (upper row) and the L-method (lower row), on a structured grid (a), an unstructured grid of type UG 1 (b), and an unstructured grid of type UG 2 (c).	90
3.52	Saturation distributions obtained using the adaptive L-method for the case of the diagonal relative permeability tensor (upper row) and full relative permeability tensor (lower row), on a structured grid (a), and an unstructured grid of type UG 1 (b).	91
4.1	Sketch of a multi-scale grid.	94
4.2	Schematic of percolation for capillary pressure upscaling.	96
4.3	Workflow of the capillary pressure upscaling.	96
4.4	Workflow of the relative permeability upscaling.	101
4.5	Sketch of a multi-scale grid. The dashed square marks a potential local sub-domain for the numerical permeability upscaling.	102
4.6	Schematic of percolation for a relative permeability upscaling.	103
4.7	Sketch of the percolation pattern after one percolation step.	103
4.8	Transfer of average face fluxes from a coarse grid cell (a) to a reference element (b).	108
4.9	Local fine-scale problem for relative permeability upscaling in x-direction.	109
4.10	Problem setup 1 (a) (two-well setup) and 2 (b) (one-well setup) for testing the upscaling method. The dashed lines mark the positions for the evaluation of breakthrough curves.	114
4.11	Permeability distributions for setup 1 (a) and setup 2 (b).	115
4.12	Saturation distribution of the fine-scale reference simulations of setup 1: (a) drainage ($t = 2.4 \times 10^6$ s); (b) imbibition ($t = 5 \times 10^6$ s).	116
4.13	Saturation distributions of setup 1 for the case of drainage at $t = 2.4 \times 10^6$ s: (a) fine-scale reference solution (averaged to the coarse grid resolution); (b) upscaling using average operator 1 (av1);(c) upscaling using average operator 2 (av2);(d) upscaling using average operator 3 (av3).	117
4.14	Saturation distributions of setup 1 for the case of imbibition at $t = 5 \times 10^6$ s: (a) fine-scale reference solution (averaged to the coarse grid resolution); (b) upscaling using average operator 1 (av1);(c) upscaling using average operator 2 (av2);(d) upscaling using average operator 3 (av3).	117
4.15	Saturation breakthrough curves for setup 1 (Figure 4.10a) at $x = 0.5x_{\max}$ along the y-axis: (a) drainage, (b) imbibition.	118

4.16	Saturation distribution of the fine-scale reference simulations of setup 2: (a) drainage ($t = 1 \times 10^6$ s); (b) imbibition ($t = 1 \times 10^6$ s).	119
4.17	Saturation distributions of setup 2 for the case of drainage at $t = 1 \times 10^6$ s: (a) fine-scale reference solution (averaged to the coarse grid resolution); (b) upscaling using average operator 1 (av1);(c) upscaling using average operator 2 (av2);(d) upscaling using average operator 3 (av3).	119
4.18	Saturation distributions of setup 2 for the case of imbibition at $t = 1 \times 10^6$ s: (a) fine-scale reference solution (averaged to the coarse grid resolution); (b) upscaling using average operator 1 (av1);(c) upscaling using average operator 2 (av2);(d) upscaling using average operator 3 (av3).	120
4.19	Saturation breakthrough curves for setup 2 (Figure 4.10b) along the x-axis (lower two rows) and y-axis (upper two rows): (a) drainage; (b) imbibition.	121
4.20	Comparison of two coarse-scale capillary-pressure-saturation functions: (a) drainage, (b) imbibition.	122
4.21	Comparison of two coarse-scale relative-permeability-saturation functions for the case of imbibition: \mathbf{K}_r is the tensorial coarse-scale function, $\lambda(\mathbf{K}_r)$ are the averaged eigenvalues of \mathbf{K}_r , and k_r is the fine-scale function (Equations (4.33) and (4.34)).	123
4.22	Comparison of four coarse-scale relative-permeability-saturation functions for the case of drainage: \mathbf{K}_r is the tensorial coarse-scale function, $\lambda(\mathbf{K}_r)$ are the averaged eigenvalues of \mathbf{K}_r , and k_r is the fine-scale function (Equations (4.33) and (4.34)).	124
4.23	Sketch of the multi-scale adaptation procedure. The coarse grid (level 0) is refined up to the fine scale (level l_{\max}) depending on the adaptation indicators.	127
4.24	Illustration of the minimum saturation $\hat{S}_{w,\min}$ of the linear approximation (solid line) of the lower part of a capillary-pressure-saturation function (dashed line).	130
4.25	Problem setup for the indicator tests.	131
4.26	Porosity (a), permeability (b), and entry pressure (c) distribution accord- ing to layer 15 of the SPE 10 benchmark model 2 (top formation).	131
4.27	Saturation breakthrough curves along the x -axis at $y = \frac{1}{3}y_{\max}$ (solid lines) and at $y = \frac{2}{3}y_{\max}$ (dashed lines)	132

4.28	Total velocity distribution of the fine-scale simulation (a), the multi-scale simulation with v_t -indicator (b), with S -indicator (c), and using both indicators (d) at $t = 1.5 \times 10^8$ s.	133
4.29	Saturation distribution of the fine-scale simulation (a) averaged to the coarse grid resolution, and the coarse-scale simulation using the upscaled parameters (b) at $t = 1.5 \times 10^8$ s.	133
4.30	Saturation distribution of the fine-scale simulation (a), , the multi-scale simulation with v_t -indicator (b), with S -indicator (c), and using both indicators (d) at $t = 1.5 \times 10^8$ s.	134
4.31	Locally adapted grid of the multi-scale solution shown in Figure 4.30d.	135
4.32	Saturation distributions (top row), total velocity distribution (middle row) and refined grids (bottom row) of the capillary-dominated case at $t = 6 \times 10^9$ s applying: (a) $p_c^c = p_c(0.8) \approx p_d^*$, $\varepsilon_{Ca,r} = 2$, $\varepsilon_{Ca,c} = 1$; (b) $p_c^c = p_c(0.8) \approx p_d^*$, $\varepsilon_{Ca,r} = 1$, $\varepsilon_{Ca,c} = 10$; (c) $p_c^c = p_c^*(0.2)$, $\varepsilon_{Ca,r} = 1.1$, $\varepsilon_{Ca,c} = 0.9$; (d) $p_c^c = p_c^*(0.2)$, $\varepsilon_{Ca,r} = 2$, $\varepsilon_{Ca,c} = 1$	137
4.33	Saturation breakthrough curves along the x-axis for the capillary-dominated case: (a) and (b) $p_c^c = p_c(0.8) \approx p_d^*$; (c) and (d) $p_c^c = p_c^*(0.2)$	138
4.34	Saturation distributions (top row), total velocity distribution (middle row) and refined grids (bottom row) of the viscous-dominated case at $t = 4 \times 10^8$ s applying: (a) $p_c^c = p_c(0.8) \approx p_d^*$, $\varepsilon_{Ca,r} = 2$, $\varepsilon_{Ca,c} = 1$; (b) $p_c^c = p_c(0.8) \approx p_d^*$, $\varepsilon_{Ca,r} = 1$, $\varepsilon_{Ca,c} = 10$; (c) $p_c^c = p_c^*(0.2)$, $\varepsilon_{Ca,r} = 1.1$, $\varepsilon_{Ca,c} = 0.9$; (d) $p_c^c = p_c^*(0.2)$, $\varepsilon_{Ca,r} = 2$, $\varepsilon_{Ca,c} = 1$	140
4.35	Saturation breakthrough curves along the x-axis for the viscous-dominated case: (a) and (b) $p_c^c = p_c(0.8) \approx p_d^*$; (c) and (d) $p_c^c = p_c^*(0.2)$	141
5.1	Problem setup of drainage scenario.	144
5.2	Permeability distributions of used for the drainage scenario.	144
5.3	Saturation distribution of the fine-scale simulation (a) and the multi-scale simulation (b) at $t = 3 \times 10^5$ s and saturation breakthrough curves along the y-axis (c); permeability field (1) (Figure 5.2), $p_c = 0$	146
5.4	Saturation distributions of the fine-scale simulations (upper row) and the multi-scale simulations (lower row) at $t = 3 \times 10^5$ s using the permeability fields (1): (a), (2): (b), (3): (c), and (4): (d) ($p_c \neq 0$, viscous-dominated flow conditions).	146

5.5	Saturation distribution of the fine-scale simulation (a) and the multi-scale simulation (b) at $t = 3 \times 10^5$ s averaged to the coarse grid resolution; permeability field (1) (Figure 5.2), $p_c = 0$	147
5.6	Saturation breakthrough curves along the y-axis using permeability fields (1): (a), (2): (b), (3): (c), and (4): (d) ($p_c \neq 0$, viscous-dominated flow conditions).	148
5.7	Saturation distributions of the fine-scale simulations (upper row) and the multi-scale simulations (lower row) at $t = 5 \times 10^6$ s using the permeability fields (1): (a), (2): (b), (3): (c), and (4): (d) ($p_c \neq 0$, capillary-dominated flow conditions).	149
5.8	Saturation breakthrough curves along the y-axis using permeability fields (1): (a), (2): (b), (3): (c), and (4): (d) ($p_c \neq 0$, capillary-dominated flow conditions).	150
5.9	Grids of the multi-scale solutions shown in: (a) Figure 5.3b ($p_c = 0$), (b) Figure 5.4a ($p_c \neq 0$, viscous dominated), and (c) Figure 5.7a ($p_c \neq 0$, capillary dominated)	150
5.10	Ratio of multi-scale and fine-scale numbers of degrees of freedom (n_{DOF}) over dimensionless simulation time τ . Solid lines show the viscous-dominated cases, dashed lines the capillary dominated cases.	151
5.11	Porosity (a), permeability (b), and entry pressure (c) distribution according to layer 15 of the SPE 10 benchmark model 2 (top formation).	152
5.12	Porosity (a), permeability (b), and entry pressure (c) distribution according to layer 50 of the SPE 10 benchmark model 2 (bottom formation).	153
5.13	Problem setup of the imbibition scenario.	153
5.14	Saturation distribution of the fine-scale simulations: (a) viscous-dominated flow conditions, $t = 2.6 \times 10^8$ s; (c) capillary-dominated flow conditions, $t = 4.2 \times 10^9$ s, and the multi-scale simulations: (b) viscous-dominated flow conditions, $t = 2.6 \times 10^8$ s; (d) capillary-dominated flow conditions, $t = 4.2 \times 10^9$ s (layer 15, $p_c \neq 0$).	154
5.15	Saturation breakthrough curves along the x-axis: (a) viscous-dominated flow conditions; (b) capillary-dominated flow conditions (layer 15, $p_c \neq 0$).	155
5.16	Saturation distribution of the fine-scale simulations: (a) viscous-dominated flow conditions, $t = 2 \times 10^8$ s; (c) capillary-dominated flow conditions, $t = 2 \times 10^9$ s, and the multi-scale simulations: (b) viscous-dominated flow conditions, $t = 2 \times 10^8$ s; (d) capillary-dominated flow conditions, $t = 2 \times 10^9$ s (layer 50, $p_c \neq 0$).	156

5.17	Saturation breakthrough curves along the x-axis: (a) viscous-dominated flow conditions; (b) capillary-dominated flow conditions (layer 50, $p_c \neq 0$).	156
5.18	Ratio of multi-scale and fine-scale numbers of degrees of freedom (n_{DOF}) over dimensionless simulation time τ . Solid lines show the viscous-dominated cases, dashed lines the capillary dominated cases.	157
5.19	Porosity (a) and permeability (b)/(c) distribution according to model 2 of the SPE 10 benchmark. The left column shows a top view, the right column a bottom view (z-direction scaled by 5).	159
5.20	Problem setup: One vertical central injector (q_i) and one vertical producer in each corner of the domain (q_p); all wells are completed throughout the formation (z-direction scaled by 5).	160
5.21	Saturation of the injected water plume using a mixed flux approximation scheme (TPFA + MPFA) (a) - (d), and using only MPFA (e) - (h) (z-direction scaled by 5).	161
5.22	Saturation distribution in the injected water plume and the corresponding adapted grid using a mixed flux approximation scheme (TPFA + MPFA) (a) - (d), and using only MPFA (e) - (h) (z-direction scaled by 5). . . .	163
5.23	Ratio of multi-scale and fine-scale numbers of degrees of freedom (n_{DOF}) over dimensionless simulation time τ	164

Nomenclature

Greek Letters

ε_c	coarsening threshold, [-]
ε_r	refinement threshold, [-]
λ_α	phase mobility, [(m·s)/kg]
μ_α	phase viscosity, [kg/(m·s)]
Λ_α^*	coarse-scale phase mobility, [(m·s)/kg]
λ_t	total mobility, [(m·s)/kg]
Λ_t^*	coarse-scale total mobility, [(m·s)/kg]
ϕ	porosity, [-]
ϕ^*	coarse-scale porosity, [-]
Φ_α	phase potential, [Pa]
Φ_α^*	coarse-scale phase potential, [Pa]
Φ_c	capillary potential, [Pa]
Φ_c^*	coarse-scale capillary potential, [Pa]
ϱ_α	phase density, [kg/m ³]

Roman Letters

A	area, [m ²]
Ca	capillary number, [-]
f_α	phase fractional flow function, [-]
F_α^*	coarse-scale phase fractional flow function, [-]
f	numerical flux, [m ² /s]
g	gravity constant, [m/s ²]
I	identity matrix, [-]
K	absolute permeability, [m ²]
k	scalar absolute permeability, [m ²]
K_α^*	coarse-scale phase permeability, [m ²]
K^*	coarse-scale permeability, [m ²]
$k_{r\alpha}$	relative phase permeability, [-]
$K_{r\alpha}^*$	coarse-scale relative phase permeability, [m ²]
n	normal vector, [-]

p	global pressure, [Pa]	z	z-coordinate (in direction of gravity), [m]
p_α	phase pressure, [Pa]		
p_α^*	coarse-scale phase pressure, [Pa]		
p_c	capillary pressure, [Pa]		
p_c^*	coarse-scale capillary pressure, [Pa]		
p_d	capillary entry/displacement pressure, [Pa]		
q_α	phase source, [kg/(m ³ ·s)] / [1/s]		
S_α	phase saturation, [-]		
\mathbf{T}	transmissibility matrix		
$\mathbf{v}_{a\alpha}$	advective phase velocity, [m/s]		
$\mathbf{v}_{a\alpha}^*$	coarse-scale advective phase velocity, [m/s]		
\mathbf{v}_α	phase velocity, [m/s]		
\mathbf{v}_α^*	coarse-scale phase velocity, [m/s]		
\mathbf{v}_c	capillary velocity, [m/s]		
\mathbf{v}_c^*	coarse-scale capillary velocity, [m/s]		
V	volume, [m ³]		
\mathbf{v}_t	total velocity, [m/s]		
\mathbf{v}_t^*	total coarse-scale velocity, [m/s]		

Abstract

The simulation of an increasing number of important applications in porous media such as CO₂ storage or more general gas storage, geothermal energy production, or investigation of storage sites for nuclear waste, requires complex physical models and high spatial resolutions, but also the investigation of large-scale effects. Due to the limitations of computational resources, huge model domains often have to be simulated on relatively coarse grids. However, depending on the application, a high spatial resolution may be necessary to capture important effects, for example due to small scale heterogeneities. One solution strategy is multi-scale modeling. The idea is to decrease the number of global degrees of freedom while preserving important fine-scale features.

In this work, a novel approach for multi-scale modeling of two-phase flow in porous media is developed. The method can be applied in a wide range of physical regimes, in particular, in regimes in which capillary effects have a major impact on the flow processes. In this case, many existing upscaling or multi-scale techniques, originally developed and successfully used for advection-dominated systems, fail or are not able to yield sufficiently accurate results.

In the new approach, an adaptive grid method based on multi-point flux approximation is combined with various local upscaling techniques. In particular, the numerical method has to be able to treat complex effective parameters like anisotropic phase permeabilities. A crucial point is the development of suitable grid-adaptation strategies to account correctly for important effects. The method is tested and proven to work for various two- and three-dimensional examples including varying heterogeneous parameter fields and different flow regimes.

The model equations for the multi-scale method are phase-potential-saturation formulations. The equations are implemented using an IMPES algorithm (Implicit Pressure Explicit Saturation). By solving for the potentials, the gravity term is not completely moved to the right-hand side of the linear system of equations that has to be solved. This can improve the solution behavior of the sequential IMPES solver which decouples the solution for the velocity field and for the transport of the phases. Another advantage of the potential formulation is the minimal number of different terms. Additionally,

the different flux terms have a similar form. Thus, a minimal number of different transmissibilities has to be calculated for the multi-point flux approximation.

For discretizing the two-phase flow equations, in particular the coarse-scale equations, a finite volume scheme based on the multi-point flux approximation L-method is developed and validated on various test problems. The tests show that the method is able to approximate important two-phase flow features, to account for the effects of anisotropic coefficients, and to treat hanging nodes which appear in non-conforming adaptive grids.

The developed multi-scale method combines a local steady-state numerical upscaling method with an h-adaptive grid. In a first step, different numerical upscaling techniques are combined and extended to get a set of methods which enables the calculation of the effective parameters that appear in the coarse-scale equations. The numerical upscaling approach is tested and could be validated on several test scenarios. To overcome the limitations of the numerical upscaling, an adaptive grid method based on multi-point flux approximation is combined with the numerical upscaling. Using the adaptive grid provides a scale transfer mechanism and therefore enables a multi-scale solution. The key factor of this novel multi-scale approach is an appropriate adaptation strategy, which aims to refine and coarsen the grid such that the method is efficient and sufficiently accurate. Therefore, different adaptation indicators are suggested. Besides the so-called standard indicators, which try to minimize numerical errors in the solutions, the development of special multi-scale indicators has to be emphasized. The idea of such indicators is to take into account the validity of the upscaled parameters for the error estimation. One new multi-scale indicator based on the definition of a capillary number is introduced. Several numerical tests demonstrate that the multi-scale approach can significantly improve the quality of a solution in comparison to a pure upscaling method. Moreover, all suggested indicators can help to considerably improve the quality of the multi-scale approximation.

Finally, the multi-scale concept is tested and validated on various two- and three-dimensional scenarios relating to realistic applications. The two-dimensional applications show that the multi-scale method performs very well for a variety of challenging heterogeneous parameter fields and for various flow regimes, ranging from the purely viscous dominated case to the capillary dominated case. The results show that the characteristic of saturation transport can dramatically change depending on the capillary pressure influence. Thus, it is extremely important to have efficient multi-scale models which allow us to model large-scale problems and still account for this effect correctly. The application to the full three-dimensional model 2 of the SPE 10 benchmark clearly demonstrates the

capabilities of the multi-scale approach with respect to three-dimensional applications. This is essential for the employment on realistic scenarios. In most of the test problems, the two-dimensional as well as three-dimensional, the computational costs can be significantly reduced, usually below 50% of those of the fine-scale simulations. Considering realistic large-scale applications, important transport processes often appear in relatively small and isolated areas. As can be concluded from the application examples, in such cases the multi-scale method may be even more efficient (20-35% of the fine-scale costs).

The focus of this thesis is on the development of a multi-scale approach which, in particular, can be used for modeling regimes which are capillary dominated or in which capillary pressure at least influences the flow and transport behavior considerably. Therefore, the influence of gravity is not explicitly considered in the context of the multi-scale method, although the method is derived and implemented for the general case including gravity.

The introduced multi-scale method has to be developed further, improved, and tested in the future. The long-term goal is a flexible and robust method which can be used for modeling real world applications. The large-scale simulation of current and important applications such as those mentioned at the beginning, which may become even more important in the future, is essential for the investigation of potentials and risks.

Zusammenfassung

Für wichtige Anwendungsbereiche wie CO₂- oder allgemeiner Gasspeicherung, die Nutzung von Geothermie zur Energiegewinnung oder die Beurteilungen potentieller Standorte für nukleare Endlager, gewinnt die Simulation von Strömungs- und Transportvorgängen in porösen Medien zunehmend an Bedeutung. Dies erfordert sowohl die Anwendung komplexer physikalischer Modelle und eine hohe räumliche Auflösung, als auch die Untersuchung großskaliger Auswirkungen. Aufgrund von limitierten Hardwareresourcen können große Modellgebiete oft nur auf relativ groben Gittern simuliert werden. Abhängig von der jeweiligen Anwendung kann jedoch eine hohe Auflösung erforderlich sein um alle wichtigen Prozesse, die zum Beispiel durch kleinskalige Heterogenitäten maßgeblich beeinflusst werden können, abzubilden. Ein möglicher Lösungsansatz ist die Mehrskalenmodellierung. Die Grundidee von Mehrskalenmethoden ist die Verringerung der Anzahl globaler Freiheitsgrade bei gleichzeitiger Erhaltung wichtiger feinskaliger Strömungs- und Transporteffekte und Eigenschaften.

In dieser Arbeit wird ein neuartiger Ansatz für die Modellierung von Zweiphasenströmungen in porösen Medien entwickelt. Die Methode kann für ein breites Spektrum physikalischer Regime eingesetzt werden, im Besonderen aber für Systeme, in denen Kapillarkräfte einen entscheidenden Einfluss auf die Strömungsprozesse nehmen. Solche Systeme können von vielen bestehenden Ansätzen, die oft für den Fall advektionsdominierter Verhältnisse entwickelt wurden und dort auch erfolgreich eingesetzt werden, nicht ausreichend genau oder überhaupt nicht beschrieben werden.

Für den neu entwickelten Ansatz wird eine Mehrpunktflussapproximationsmethode für adaptive Gitter mit verschiedenen „Local-Upscaling“-Techniken kombiniert. Dabei muss die numerische Methode insbesondere in der Lage sein komplexe effektive Parameter wie anisotrope Phasenpermeabilitäten zu berücksichtigen. Um wichtige Effekte richtig abzubilden ist außerdem die Entwicklung einer geeigneten Gitteradaptionsstrategie ein entscheidender Faktor. Abschließend wird die Mehrskalenmethode an verschiedenen zwei- und dreidimensionalen Beispielen, die sowohl die heterogenen Parameterfelder als auch die physikalischen Regime variieren, erfolgreich getestet.

Als mathematisches Modell für die Mehrskalermethode werden Phasenpotential-Sättigungs-Formulierungen eingesetzt. Die Gleichungen sind mit Hilfe eines IMPES Algorithmus (IMplicit Pressure EXplicit Saturation) implementiert. Durch die Wahl von Potentialen als Primärvariablen geht der Gravitationsterm der Druckgleichung nicht nur als „Rechte Seite“ in das lineare Gleichungssystem ein, sondern ist auch teilweise in der Primärvariablen enthalten. Dadurch kann das Lösungsverhalten des IMPES-Lösers verbessert werden, in dem das Geschwindigkeitsfeld und der Phasentransport entkoppelt berechnet werden. Ein weiterer Vorteil der Potentialformulierung ist die minimale Anzahl verschiedener Terme in den Gleichungen. Zusätzlich sind die Terme von ähnlicher Form. Dadurch kann die Anzahl an Transmissibilitäten, die für die Mehrpunktflussapproximation berechnet werden müssen, minimiert werden.

Für die Diskretisierung der Gleichungen für Zweiphasenströmungen, insbesondere für die Gleichungen der groben Skala, wird eine Finite-Volumen Diskretisierung basierend auf der L-Mehrpunktflussapproximationsmethode entwickelt und an verschiedenen Testproblemen validiert. Diese Tests zeigen deutlich, dass die Diskretisierungsmethode dazu in der Lage ist wichtige Eigenschaften von Zweiphasenströmungen, sowie Effekte anisotroper Koeffizienten, richtig abzubilden. Des Weiteren kann die Methode mit hängende Knoten, die in nichtkonformen adaptiven Gittern auftreten, umgehen.

Die entwickelte Mehrskalermethode ist eine Kombination lokaler numerischer Upscaling-Methoden, die auf stationären Bedingungen basieren, mit einem h-adaptiven Gitter. Zunächst werden verschiedene Upscaling-Techniken ausgewählt, kombiniert und so erweitert, dass alle effektiven Parameter, die in den Gleichungen der groben Skala enthalten sind, berechnet werden können. Dieser Upscaling-Ansatz wird an verschiedenen Szenarien getestet und erfolgreich validiert. Um die Grenzen des Upscaling-Ansatzes aufzuheben, wird anschließend das numerische Upscaling mit einem adaptiven Gitter kombiniert, das einen Skalentransfer und damit eine Mehrskalenerlösung erlaubt. Mit Hilfe der zuvor entwickelten Mehrpunktflussapproximationsmethode ist auch auf nichtkonformen adaptiven Gitter mit hängenden Knoten eine korrekte Flussapproximation möglich. Der entscheidende Punkt der neuartigen Mehrskalermethode ist die richtige Adaptionsstrategie. Diese sollte das Gitter so verfeinern und vergrößern, dass die Methode ausreichend genau und maximal effizient ist. Um dieses zu erreichen, werden verschiedene Adaptionsindikatoren vorgestellt. Dabei muss neben so genannten Standardindikatoren, die das Ziel haben Fehler in der approximativen Lösung zu minimieren, die Entwicklung spezieller Mehrskalenerindikatoren hervorgehoben werden. Die Idee dieser Indikatoren

ist, dass auch die Gültigkeit der mit der Upscaling-Methode berechneten effektiven Parameter überprüft und für die Fehlerabschätzung berücksichtigt wird. Dafür wird ein neuer Mehrskalenindikator basierend auf einer Kapillarzahl eingeführt. An verschiedenen numerischen Tests kann klar gezeigt werden, dass der Mehrskalenansatz die Qualität der Lösungen im Vergleich zum reinen numerischen Upscaling deutlich verbessern kann. Außerdem konnten sich alle vorgeschlagenen Indikatoren bewähren und zeigen, dass ihre Anwendung die Qualität der Mehrskalenlösung deutlich verbessern kann.

Abschließend wird die Mehrskalenmethode mit Hilfe verschiedener realitätsnaher zwei- und dreidimensionaler Testszenarien validiert. Für eine Reihe schwieriger heterogener Parameterverteilungen und für variierende Strömungsverhältnisse, die von rein viskos dominierten bis zu kapillar dominierten Verhältnissen reichen, liefert die Mehrskalenmethode in der zwei-dimensionalen Anwendung sehr gute Ergebnisse. Es zeigt sich, dass sich der Charakter des Sättigungstransports abhängig vom Einfluss des Kapillardrucks signifikant ändern kann. Um dieses auch bei großskaligen Problemstellungen berücksichtigen zu können, ist es von enormer Bedeutung ein effizientes Mehrskalenmodell zur Verfügung zu haben. Das Potential des Mehrskalenansatzes für die Anwendung auf dreidimensionale Problemstellungen wird anhand von Modell 2 des SPE 10 Benchmarks demonstriert. Dieses Potential ist entscheidend für den Einsatz für reale Problemstellungen. In den meisten Tests und im zweidimensionalen sowie im dreidimensionalen Fall konnte der Rechenaufwand deutlich reduziert werden. In den meisten Fällen konnte eine Reduktion um mehr als 50% des Aufwands, der für entsprechende feinskalige Rechnungen benötigt wird, erreicht werden. Betrachtet man reale großskalige Anwendungsbereiche finden wichtige Prozesse oft nur in sehr räumlich begrenzten Gebieten statt. Die Analyse der Testbeispiele erlaubt den Schluss, dass die Mehrskalenmethode in solchen Fällen noch effizienter ist (20-30% des Rechenaufwands für feinskalige Simulation).

Der Schwerpunkt dieser Arbeit ist die Entwicklung eines Mehrskalenansatzes, der insbesondere für die Modellierung kapillardruckbeeinflusster oder kapillardruckdominierter Systeme eingesetzt werden kann. Der Einfluss der Gravitation wird deshalb bei den Tests und Validierungen der Mehrskalenmethode nicht explizit untersucht. Die Methode ist allerdings auch für den Fall, in dem die Gravitation nicht vernachlässigt wird, hergeleitet und implementiert.

Die vorgestellte Mehrskalenmethode muss in der Zukunft weiterentwickelt, verbessert und getestet werden. Das Fernziel ist eine flexible und robuste Methode, die auch für die Simulation realer Problemstellungen eingesetzt werden kann. Die großskalige

Simulation aktueller und wichtiger Anwendungsbereiche wie die zu Beginn erwähnten, ist ein Grundbaustein für die Untersuchung von Alternativen, Möglichkeiten und Risiken.

1 Introduction

During recent years, the large-scale modeling of complex porous media systems has become more and more important. Especially applications in the subsurface, such as CO₂ storage or more general gas storage, geothermal energy production, or investigation of storage sites for nuclear waste, require complex models and high spatial resolutions, but also the investigation of large-scale effects. This can lead to very fine grids and to huge numbers of degrees of freedom, and hence to enormous computational costs. The basic idea of multi-scale models is to decrease the number of global degrees of freedom while preserving important fine-scale features. As the name implies, a multi-scale method should provide transfer mechanisms for information in both directions: from finer scales to coarser scales (upscaling) and from coarser scales to finer scales (downscaling). In contrast, classical upscaling approaches transfer information only from a fine scale to a coarser scale (e.g. *Durlofsky, 1991; Pickup and Sorbie, 1996; Artus and Noetinger, 2004; Lohne et al., 2006*). Existing multi-scale methods with a special focus on two-phase flow in porous media have been developed mainly for solving an elliptic pressure equation appearing in the so-called fractional flow formulation. Common assumptions are that capillary pressure, gravity and often also compressibility are neglected. Once the pressure equation is solved, the saturation transport is usually solved explicitly and directly on the fine scale (e.g. *Jenny et al., 2003; Aarnes et al., 2006; Lipnikov et al., 2008; Nordbotten, 2009*).

In the following, two existing types of multi-scale approach are introduced and distinguished which have proven capable of modeling such simplified two-phase flow systems very efficiently and accurately. The common idea of these multi-scale methods for modeling flow in porous media is that solutions of numerical fine-scale problems are used to extract information for a scale transfer.

The first type of model introduced here uses local fine-scale solutions to modify coarse-scale basis functions. The so-called multi-scale finite element method was presented

in *Hou and Wu* (1997). For the simulation of multi-phase systems and the correct approximation of phase transport, it is important that numerical methods are locally conservative. Thus, in recent years, the method has been transferred from the standard finite element framework to the framework of mixed finite element methods (e.g. *Chen and Hou*, 2003; *Aarnes et al.*, 2006; *Arbogast et al.*, 2007; *Efendiev and Hou*, 2007). In the so-called multi-scale finite volume method, introduced in *Jenny et al.* (2003), the idea is to construct coarse-scale transmissibilities using the coarse-scale basis functions. The basis functions are constructed on a dual mesh leading to a multi-point flux approximation for the finite volume scheme. The method has been progressively extended to two-phase flow (e.g. *Jenny et al.*, 2004, 2006; *Hajibeygi et al.*, 2008), where conservative fine-scale fluxes for the solution of the saturation transport are reconstructed from the multi-scale solution of the elliptic pressure equation. It has also been extended to parabolic pressure equations (e.g. *Hajibeygi and Jenny*, 2009) and applied to a hyperbolic saturation transport equation (*Lee et al.*, 2009). As shown in *Nordbotten and Bjørstad* (2008), the multi-scale finite volume method can also be considered a special case of a non-overlapping domain decomposition preconditioner. A comparison of the multi-scale finite element and the multi-scale finite volume method for elliptic equations can be found in *Kippe et al.* (2008).

The second type of method is an extension of classical numerical upscaling methods. These methods provide a tool for calculating effective coarse-scale functions or parameters, like permeabilities, transmissibilities, or pseudo functions, from solutions of representative fine-scale (flow or transport) problems. So-called local methods define and solve the reference fine-scale problems on the scale of a coarse grid block (e.g. *Durlofsky*, 1991; *Wen et al.*, 2003; *Pickup and Sorbie*, 1996; *Wallstrom et al.*, 2002a,b). So-called global methods need reference fine-scale solutions on the global scale (e.g. *Kyte and Berry*, 1975; *Stone*, 1991). Local methods can be extended to local-global methods, which add a downscaling step in which local fine-scale boundary conditions are approximated from the global coarse-scale solution (*Chen et al.*, 2003; *Chen and Durlofsky*, 2006; *Chen and Li*, 2009). Combining numerical upscaling and downscaling, adaptive local-global methods can also be viewed as multi-scale methods. A detailed review and classification of multi-scale methods can also be found in *Helmig et al.* (2012).

The extension of the methods introduced previously for modeling both pressure and transport, and for cases in which capillary effects are significant are, to the authors knowledge, still part of ongoing research. This motivates the development of an alternative

approach, which is flexible with regard to expendability, which is applicable to real world problems, and which, in particular, can be applied for capillary-dominated as well as for viscous-dominated flow regimes.

In this work, a novel multi-scale method is developed which combines a local numerical steady-state upscaling method with an h-adaptive grid. The improvement of upscaling by flow-based gridding has been addressed by several authors (e.g. *He and Durlofsky, 2006; Hauge et al., 2011*). The idea of combining upscaling and grid-adaptation interactively was introduced for single phase flow problems in *Gerritsen and Lambers (2008)*. However, in the case of time-dependent multi-phase flow simulations, it is challenging to get an efficient and sufficiently accurate method. In the worst case, the gridding and upscaling procedures have to be repeated every time step. To increase efficiency, the multi-scale approach developed in this work decouples the adaptive grid from the numerical upscaling which is done separately in a preprocessing step. This is possible since local steady-state methods are used, which are independent of the actual global flow simulation. Steady-state upscaling techniques are described and discussed for example in *Ekrann and Aasen (2000); Pickup and Stephen (2000); Virnovsky et al. (2004); Jonoud and Jackson (2008)*. The steady state upscaling approach introduced in this work is slightly different although the basic ideas are similar.

In the following, the term multi-scale mainly includes two scales, which are called the fine scale and the coarse scale (Figure 1.1). Both scales are much larger than the length scale of a single pore. The fine scale is the length scale of the finest heterogeneous structures for which information is available, for example, the length-scale of the cells of a high resolution geological model. The coarse scale is the length scale of a cell of a simulation grid on which a large scale simulation would be efficient or at least feasible. Usually, the coarse scale is considerably larger than the fine scale. The global length scale of a coarse-scale grid is equal to the global model scale. The sub-model scale for local fine-scale simulations is on the length scale of a coarse grid-block.

In Chapter 2 the theoretical concepts and equations for modeling flow in porous media are introduced. In particular, the conservation equations used for modeling two-phase flow and transport on the different length scales are derived and a physical interpretation of the parameters appearing in these equations is given. A key issue for developing the multi-scale method is the development of suitable numerical methods. In Chapter 3, a cell-centered-finite-volume discretization for the two-phase flow equations based on multi-point flux approximation (MPFA) is derived. Two particular challenges are the numerical

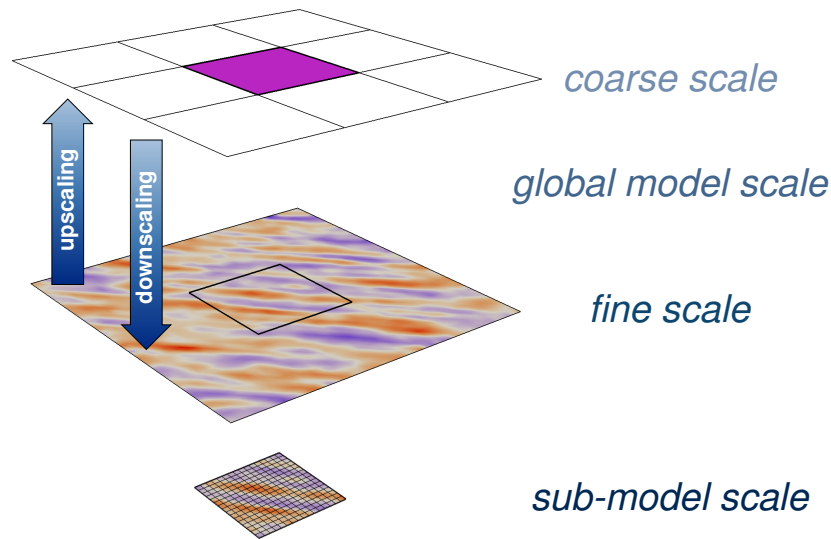


Figure 1.1: Schematic of the different interacting layers of a multi-scale model.

treatment of the coarse-scale equations and the support of the h-adaptivity. In Chapter 4, the numerical upscaling methods are described and discussed in detail. Afterwards, they are embedded in the multi-scale approach. Besides the development of the multi-scale method a special focus of this chapter is on the identification and discussion of potential sources of error and the development of multi-scale strategies to avoid them. Finally, in Chapter 5 the multi-scale method is applied to several scenarios. The applications range from two-dimensional remediation scenarios with varying parameter distributions and regimes to the three-dimensional model 2 of the SPE 10 benchmark (*Christie and Blunt*, 2001). The methods presented in the following chapters were, as part of this work, implemented in the simulator DuMu^x (*Flemisch et al.*, 2011). All simulation results presented in this thesis were calculated using DuMu^x.

2 Theoretical Background and Mathematical Models

In this chapter, the basic concepts and equations for modeling flow, in particular two-phase flow, in porous media on a so-called REV or Darcy scale are introduced. On this length scale, the pore space is not explicitly resolved but described by averaged quantities.

In the first part of the chapter, the averaged quantities and the underlying concepts, which are important for describing immiscible isothermal two-phase flow, are introduced and explained (Section 2.1). In the second part of the chapter, the conservation equations for modeling two-phase flow on different length scales, which are implemented subsequently in the multi-scale approach, are introduced (Sections 2.2 and 2.3). The basic concepts for describing porous media and flow through porous media presented in this chapter are derived in, for example, *Bear* (1972), *Scheidegger* (1974), or *Helmig* (1997), where they are explained and discussed in much more detail.

2.1 Basic Concepts for Modeling Porous Media

This section gives brief introductions and physical interpretations of the basic concepts and quantities for modeling two-phase flow in porous media. The multi-scale approach is developed for the simplified case of immiscible incompressible fluids under isothermal conditions. Thus, only the quantities which are relevant in this simplified case are described in the following sections.

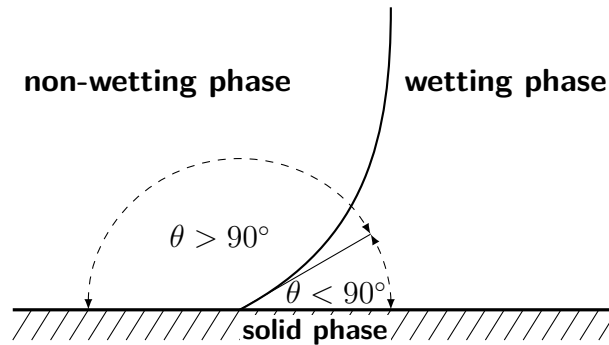


Figure 2.1: Contact angle between a wetting and a non-wetting fluid.

2.1.1 Phases and Wettability

If two or more fluids fill a volume (e.g. the pore space), are immiscible and separated by a sharp interface, each fluid is called a phase of a multi-phase system. The solid matrix of a porous medium can be counted as an additional phase. However, if it is assumed to be rigid with constant mass, it is often not explicitly considered. If the fluids are immiscible, but the solubility of one fluid in another fluid is not negligible a fluid system has to be considered as multi-phase-multi-component system.

In a multi-phase system, fluid phases can be divided into wetting and non-wetting phases. Here, the important property is the contact angle θ between fluid-fluid interface and the solid surface. A fluid developing an acute contact angle is called wetting fluid, a fluid developing an obtuse contact angle is called non-wetting fluid (Figure 2.1). Instead of showing a clear separation into wetting and non-wetting phases a fluid system can also be mixed wet. In this case the wettability can change depending on the fluid configuration (e.g. depending on the amount of phases present). Mixed wet behavior has been investigated for example in *Kovscek et al.* (1993) or *Doerr et al.* (2000).

In this work the porous media are always assumed to be water-wet.

2.1.2 Representative Elementary Volume

Modeling of flow in porous media is very challenging. One reason is the variety of important length scales and the fact that most porous media are heterogeneous on every length scale, from the pore scale to geological scales. The fundamental concept which allows to model porous media on larger scales (scales much larger than a single pore)

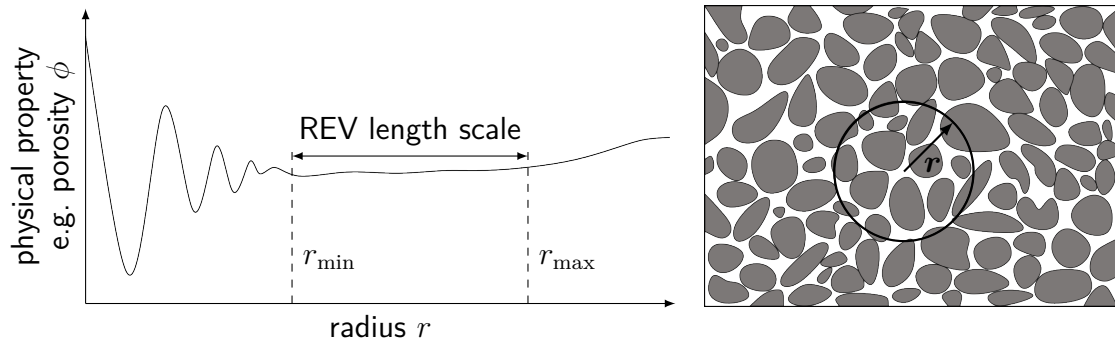


Figure 2.2: Illustration of the term representative elementary volume (REV) for the porosity.

is the continuum approach. As in continuum mechanics, where particles of continuous mass (consisting of a large number of molecules) are considered rather than the single molecules, a continuum consisting of a large number of pores is considered instead of the single pores. The continuum has to be a representative elementary volume (REV) in order to describe the porous medium by meaningful physical quantities. The concept of the REV is exemplarily illustrated in Figure 2.2 for the porosity of a porous medium. The porosity is calculated (Equation (2.1)) and plotted beginning with a small averaging volume with a radius r in the order of a single pore size. If the radius of the volume increases, more and more pores and grains are included changing the geometry of the pore space in the averaging volume. As the ratio of void space and solid volume depends on the pore geometry, porosity changes with the radius until the volume is large enough to reach a state of statistical homogeneity ($r > r_{\min}$). If the physical quantity does no longer change with increasing radius, the volume is called representative elementary volume (REV). Above an upper limit ($r > r_{\max}$) porosity might start fluctuating again due to larger scale heterogeneous structures such as lenses or channels of different material. Different physical quantities (porosity, permeability, entry pressure, etc.) may require different REV's. In the following, the term REV always refers to an REV of a porous medium, meaning a continuum of a large number of pores. The length scale of the REV is also called Darcy scale as it is the length scale on which Darcy's law is valid. The Darcy scale can vary from millimeter scale over meter scale to kilometer scale depending on the application. In the next sections, important REV or Darcy-scale parameters are introduced and explained.

Porosity

A porous medium consists of a solid matrix and the pores. The ratio of pore space in the REV and the volume of the REV is defined as porosity:

$$\phi = \frac{\text{volume of pore space in the REV}}{\text{volume of the REV}}. \quad (2.1)$$

The porosity is not necessarily constant. It can change due to deformation of the solid matrix, solution or precipitation, or adsorption and desorption processes. However, porous media are often assumed to be rigid with constant mass. In this case the porosity is also constant and independent of temperature, pressure or other variables.

Saturation

The pore space is always filled by fluid. If more than one fluid phase is present, the pore space is divided into different volumes. In the REV approach the volume fraction of a fluid phase in the pore space is described by the phase saturation:

$$S_\alpha = \frac{\text{volume of phase } \alpha \text{ in the REV}}{\text{volume of the pore space in the REV}}. \quad (2.2)$$

Thus, the actual volume of phase α can be expressed as

$$V_\alpha = S_\alpha \phi V \quad (2.3)$$

where V is the volume of the REV. As the pore space is always completely filled with fluid, the sum of the phase saturations must add up to one:

$$\sum_{\alpha} S_\alpha = 1. \quad (2.4)$$

A saturation can change due to phase transition or due to displacement. In the latter case, two processes can be distinguished: imbibition where a non-wetting phase is displaced by a wetting phase, or drainage where a wetting phase is displaced by a non-wetting phase. The character of these processes differs fundamentally. This leads to hysteresis effects if a porous medium is imbibed and drained alternately. Important sources of hysteresis on the pore scale are, for example, boundary angle hysteresis or the ink bottle effect. One effect of hysteresis on the Darcy scale are so-called residual

saturations. A residual saturation is the volume fraction of immobile phase which can not be further removed by displacement. Wetting phase can become immobile if it gets trapped in the finer pore channels during a drainage process. Non-wetting phase bubbles can get trapped in the pore centers by a surrounding wetting phase during an imbibition process. Therefore, a residual saturation may depend on the pore geometry, the heterogeneity and the displacement process, but also on the number of drainage and imbibition cycles. The concept of residual saturations can be easily included in a model by defining effective saturations. The mathematical definition of an effective saturation varies depending on the law which is applied to parameterize the constitutive relations (capillary-pressure-saturation function, relative-permeability-saturation function, etc.).

Capillary Pressure

Liquid fluids aim to minimize free surfaces. Similarly, two immiscible fluids tend to minimize common surfaces or interfaces. This process is driven by interactions of the fluids on the molecular scale and results in a curvature of the interface. On the continuum scale the force or tension which stabilizes the interface is called interfacial tension. At the equilibrium state interfacial tension leads to a pressure discontinuity at the interface, which is called capillary pressure p_c :

$$p_c^p = p_n^p - p_w^p \quad (2.5)$$

where p_n^p is the non-wetting phase and p_w^p the wetting phase pressure on the pore scale. In a porous medium capillary pressure depends on the pore geometry and on the material properties of the fluids and the solid matrix. On the pore scale it can be determined by the Young-Laplace equation:

$$p_c = \sigma \left(\frac{1}{r_x} + \frac{1}{r_y} \right) \quad (2.6)$$

where σ is the interfacial tension and r_x and r_y the main curvature radii. Considering an REV on the Darcy-scale, a capillary pressure has to be viewed as an integral quantity for the entire pore space in the REV. However, the basic definition remains the same:

$$p_c = p_n - p_w \quad (2.7)$$

where p_n and p_w are wetting and non-wetting phase pressure averages of the Darcy-scale REV. Equation (2.6) shows that the capillary pressure increases with a decreasing pore

radius. This implies that a non-wetting phase favors to drain the larger pores of a porous medium filled with a wetting phase. The wetting phase retreats to smaller pores and the capillary pressure in the REV increases. On the other hand, the wetting phase displaces the porous medium from smaller pores to larger pores during an imbibition process leading to a decreasing capillary pressure in the REV. Thus, the Darcy-scale capillary pressure is usually defined depending on the saturation:

$$p_c = p_c(S_w), \quad (2.8)$$

with $p_c(1.0) < p_c(0.0)$ (for water wet porous media). Various capillary-pressure-saturation models have been developed, which are usually based on averages of idealized porous media. One approach is the approximation of the porous medium by a bundle of capillary tubes. For each tube the capillary pressure is defined by the simplified Young-Laplace equation:

$$p_c = \frac{4\sigma \cos \theta}{d} \quad (2.9)$$

where θ is the contact angle and d the pore diameter. An averaging over the bundle of tubes gives a relation for $p_c(S_w)$. Popular examples for capillary-pressure-saturation functions are the Brooks-Corey model or the van Genuchten model (*Brooks and Corey, 1964; van Genuchten, 1980*).

2.1.3 Darcy's Law

The macroscopic (average) velocity of a fluid in an REV of a porous medium can be calculated using Darcy's law. Originally, it was obtained experimentally for single phase flow (*Darcy, 1856*). In a general form, it states that the average velocity of a fluid through a porous medium is proportional to the potential gradient:

$$\mathbf{v} = -\frac{1}{\mu} \mathbf{K} \nabla \Phi \quad (2.10)$$

where the proportionality factor \mathbf{K} is called the absolute permeability of the porous medium, Φ the potential, and μ the dynamic fluid viscosity. For two-phase systems an extended Darcy's law can be formulated for each phase:

$$\mathbf{v}_\alpha = -\frac{1}{\mu_\alpha} \mathbf{K}_\alpha \nabla \Phi_\alpha, \quad \alpha = w, n. \quad (2.11)$$

In this case, an absolute permeability \mathbf{K}_α is required for each fluid phase α . Commonly, instead of using phase permeabilities, an additional phase dependent factor, the relative permeability $k_{r\alpha}$ of a phase, is introduced as a scaling factor for the the single-phase absolute permeability:

$$\mathbf{v}_\alpha = -\frac{k_{r\alpha}}{\mu_\alpha} \mathbf{K} \nabla \Phi_\alpha. \quad (2.12)$$

The phase potentials Φ_α are defined as

$$\Phi_\alpha = p_\alpha + \rho_\alpha g z \quad (2.13)$$

where p_α is the phase pressure, ρ_α the fluid density, and g the gravity constant acting in z -direction.

Absolute Permeability

The absolute permeability is the proportionality factor appearing in Darcy's law for single phase flow (Equation (2.10)). Physically, it can be interpreted as the ability of a fluid to flow in a porous medium, or in other words, the inverse resistance for fluid flow through a porous medium. It depends only on properties of the solid matrix and in general, it is a tensor ($[\mathbf{K}] = \text{m}^2$). Equation (2.10) has the form of a diffusion equation with the permeability being the diffusion coefficient for the potential. From this analogy it becomes obvious that, in the general anisotropic case, \mathbf{K} should be a symmetric tensor (real eigenvalues which are the permeabilities acting in the direction of the associated eigenvectors) and it should be positive semi-definite (which means that the eigenvalues are non-negative) so that flow always takes place in the direction of decreasing potential. In case of an isotropic porous medium, \mathbf{K} reduces to $\mathbf{K} = k\mathbf{I}$, where k is a scalar permeability and \mathbf{I} the identity matrix.

Relative Permeability

Flow in porous media is strongly influenced by the interaction between the fluid and the solid phase. This effect is taken into account by the absolute permeability. If more than one fluid phase fill the pore space, both fluid-solid and fluid-fluid interaction affect the flow behavior. Simply speaking, the presence of one fluid phase disturbs the flow behavior of another phase additionally. In this case, the proportionality factor in Darcy's law

has to be different for different phases, but it also has to vary depending on the actual fluid-fluid-solid configuration. In the REV approach where only averaged quantities are known, the saturation gives the simplest measure for the fluid-fluid configuration. Thus, it is commonly assumed that the phase permeabilities depend on a fluid saturation:

$$\mathbf{K}_\alpha := \mathbf{K}_\alpha(S). \quad (2.14)$$

As the absolute permeability, phase permeabilities generally have to be symmetric positive semi-definite tensors. Moreover, in the fully saturated case where only one phase is present, the phase permeability should be the absolute permeability:

$$\mathbf{K}_\alpha(1) \stackrel{!}{=} \mathbf{K}. \quad (2.15)$$

In the unsaturated case, where a phase is not present, the medium has to be effectively impermeable for the corresponding phase:

$$\mathbf{K}_\alpha(0) \stackrel{!}{=} \mathbf{O}. \quad (2.16)$$

As written in Equation (2.12), the phase permeability is usually split up into the relative permeability of a phase and the absolute permeability of the porous medium:

$$\mathbf{K}_\alpha(S) = k_{r\alpha}(S)\mathbf{K}. \quad (2.17)$$

The absolute or intrinsic permeability depends on the geometric structure of the porous medium and, in general, appears as a full tensor in the Darcy equation. Usually, anisotropies are described solely by the absolute permeability tensor. This includes the assumption that an anisotropic flow behavior is independent of the actual flow process and influenced only by the geometry of the porous medium. Hence, the relative permeability, which includes fluid-fluid as well as fluid-fluid-solid interactions, is usually a scalar coefficient. A more general expression for the relative permeability is given by:

$$\mathbf{K}_\alpha(S) = \mathbf{K}_{r\alpha}(S)\mathbf{K} \quad (2.18)$$

where both absolute and relative permeabilities are tensors. This allows us to additionally include anisotropic flow behavior due to multi-phase processes. Anisotropic relative permeabilities arising from upscaling can be observed at various scales (e.g. *Saad et al.*, 1995; *Pickup and Sorbie*, 1996; *Braun et al.*, 2005; *Eichel et al.*, 2005). In this work they

become important in the context of numerical large scale upscaling methods.

There exist various parameterizations for scalar relative-permeability-saturation functions. Widely used examples for two-phase flow are the *Brooks-Corey* or the *van Genuchten* model (*Brooks and Corey*, 1964; *van Genuchten*, 1980).

2.1.4 Fluid Properties

In the following chapters the fluids are assumed to be immiscible and incompressible. Moreover, isothermal conditions are assumed. In this case, only two fluid properties are relevant which take on a constant value.

Viscosity

Viscosity is the fluid property which measures the resistance to deformation induced by shear stress. This resistance is caused by internal friction. For Newtonian fluids the shear stress τ_{yx} acting in x-direction (along the fluid surface) can be expressed proportional to the local gradient of velocity in y-direction (direction of the outer normal of the fluid surface), where the dynamic viscosity μ ($[\mu] = \text{kg}/(\text{m} \cdot \text{s})$) is the proportionality factor:

$$\tau_{yx} = \mu \frac{\partial u}{\partial y}. \quad (2.19)$$

In general, the viscosity depends on the temperature and the pressure, given a certain phase composition. However, for most fluids the variation with pressure is negligibly small compared to the variation with temperature. Thus, it can be reasonable to chose a constant density if an isothermal system can be assumed. Compared to Newtonian fluids, Non-Newtonian fluids show non-linear $\tau - \frac{\partial u}{\partial y}$ relations.

Density

The density ϱ ($[\varrho] = \text{kg}/\text{m}^3$) relates the mass m of a fluid to its volume V :

$$\varrho = \frac{m}{V}. \quad (2.20)$$

In general, the density depends on the temperature and the pressure, given a certain phase composition. For liquid phases, the variation with pressure is often small compared to variation with temperature. Thus, it can be reasonable to chose a constant density if an isothermal system can be assumed. The density of gases is highly dependent on both, temperature and pressure.

2.2 Fine Scale Model Equations

The models for two-phase flow in porous media, which are described in this chapter, are derived assuming immiscible incompressible fluids under isothermal conditions. Fine-scale and coarse-scale models are distinguished. On both scales an REV concept for modeling the porous medium including a *Darcy* approach for describing the velocities is applied. The fine scale in this context is the length scale of the finest heterogeneous structures for which information in form of material parameters and constitutive relations described in Section 2.1 is available. As an example, the fine scale can be defined as the length scale of the cells of a high resolution geological reservoir model.

2.2.1 Immiscible Two-Phase Flow Equations

A system consisting of two fluid phases and one solid phase can be described by the following mass balances equations:

$$\frac{\partial(\phi \varrho_w S_w)}{\partial t} + \nabla \cdot (\varrho_w \mathbf{v}_w) = \varrho_w q_w \quad (2.21)$$

$$\frac{\partial(\phi \varrho_n S_n)}{\partial t} + \nabla \cdot (\varrho_n \mathbf{v}_n) = \varrho_n q_n. \quad (2.22)$$

The wetting phase fluid is indicated by subscript w and the non-wetting phase fluid by subscript n, S is the saturation and ϱ the density of a phase, ϕ is the porosity of the porous medium and q a source term. In the following, isothermal conditions, incompressible, immiscible fluids, and a rigid solid phase of constant mass is assumed.

In this case, the system is sufficiently described by the simplified balance equations:

$$\phi \frac{\partial S_w}{\partial t} + \nabla \cdot \mathbf{v}_w = q_w \quad (2.23)$$

$$\phi \frac{\partial S_n}{\partial t} + \nabla \cdot \mathbf{v}_n = q_n. \quad (2.24)$$

To close the system of two equations and four unknowns (S_w , S_n , \mathbf{v}_w , \mathbf{v}_n) additional relations are necessary. The phase velocities can be calculated directly by the multiphase *Darcy's* law (Section 2.1.3). By inserting Equation (2.12) the velocity unknowns are replaced by potential or pressure unknowns. The two-phase system can now be closed by the constitutive relation

$$S_w + S_n = 1, \quad (2.25)$$

which states that the pore space is entirely filled with the two fluid phases, and

$$p_c = p_n - p_w, \quad (2.26)$$

which relates the phase pressures to each other by the capillary pressure. The capillary pressure as well as the relative phase permeabilities are commonly assumed to be functions of the saturation ($p_c := p_c(S_w)$, $k_{rw} := k_{rw}(S_w)$, $k_{rn} := k_{rn}(S_w)$). Combining Equation (2.13) formulated for a wetting and a non-wetting phase with Equation (2.26) yields a closer relation for the phase potentials:

$$\Phi_c := \Phi_n - \Phi_w = p_c + (\rho_n - \rho_w)gz. \quad (2.27)$$

Analogously to the capillary pressure definition, the difference in the phase potentials is called capillary potential Φ_c .

2.2.2 Fractional Flow Formulation

The two-phase flow equations (Equation (2.21) and (2.22)) can be reformulated into one equation for the pressure and one equation for the saturation transport. This type of approach was originally developed for the application in the field of petroleum engineering (see e.g. *Aziz and Settari, 1979; Chen et al., 2006*). It is often called fractional flow formulation, because it introduces the idea of considering the flow of a phase as a flow fraction or fractional flow of the flow of a total phase (of the total flow). A fractional flow formulation of a saturation equation for a one-dimensional immiscible displacement

process was already derived and analytically solved in *Buckley and Leverett* (1942). A further development of the formulation that has to be mentioned was derived primarily in *Chavent* (1976), who called it “*A New Formulation*” for two-phase flow in porous media. This formulation extends the idea of considering the total flow by introducing a new total pressure variable, the global pressure. Depending on the non-linearity of the system and the constitutive relations, the equations of a fractional flow formulation are quasi decoupled or weakly coupled. Thus, the system of equations can be solved sequentially, for example, applying an IMPES algorithm (e.g. *Aziz and Settari*, 1979). For simplified systems, for example, neglecting capillary pressure and gravity, the sequential solution strategy can be very efficient. Only the pressure equation has to be solved implicitly applying a linear numerical solver while the saturation can be calculated explicitly. A classical example for systems in which dominant pressure gradients allow to neglect capillary and gravitational forces is the simulation of oil production. In this field, fractional flow formulations have been successfully applied for many years. However, with increasing complexity of the modeled processes, the non-linear coupling of the equations increases. This can considerably decrease the efficiency of an IMPES algorithm because internal iterations (between pressure solution and saturation solution) or smaller time-steps may become necessary.

Another advantage of a set of equations which can be solved decoupled is that individual and specialized numerical methods can be applied to solve the single equations. There exist various discretization methods which are either developed for elliptical equations such as the pressure equation, or for parabolic or hyperbolic equations such as the saturation equation. The strategy for solving the coarse-scale equations, which is developed in *Wolff et al.* (2012) and explained in the next chapter, also exploits the fact that the equations of a fractional flow formulation can be solved decoupled.

Pressure Equation

The pressure equation is obtained by summing up Equation (2.21) and Equation (2.22) to one total mass balance equation:

$$\begin{aligned} (S_w + S_n) \frac{\partial \phi}{\partial t} + \frac{1}{\rho_w} \left(\phi S_w \frac{\partial \rho_w}{\partial t} + \rho_w \phi \frac{\partial S_w}{\partial t} + \nabla \cdot (\rho_w \mathbf{v}_w) \right) \\ + \frac{1}{\rho_n} \left(\phi S_n \frac{\partial \rho_n}{\partial t} + \rho_n \phi \frac{\partial S_n}{\partial t} + \nabla \cdot (\rho_n \mathbf{v}_n) \right) = q_w + q_n. \end{aligned} \quad (2.28)$$

Inserting Equation (2.25) into Equation (2.28) and rewriting the terms $\nabla(\varrho_w \mathbf{v}_w)$ and $\nabla(\varrho_n \mathbf{v}_n)$ yields the general pressure equation for immiscible two-phase flow:

$$\begin{aligned} \frac{\partial \phi}{\partial t} + \nabla \cdot \mathbf{v}_w + \nabla \cdot \mathbf{v}_n + \frac{1}{\varrho_w} \left(\phi S_w \frac{\partial \varrho_w}{\partial t} + \mathbf{v}_w \nabla \varrho_w \right) \\ + \frac{1}{\varrho_n} \left(\phi S_n \frac{\partial \varrho_n}{\partial t} + \mathbf{v}_n \nabla \varrho_n \right) = q_w + q_n. \end{aligned} \quad (2.29)$$

Introducing the total velocity

$$\mathbf{v}_t = \mathbf{v}_w + \mathbf{v}_n, \quad (2.30)$$

the second and third term in Equation (2.29) can be combined to:

$$\nabla \cdot \mathbf{v}_w + \nabla \cdot \mathbf{v}_n = \nabla \cdot (\mathbf{v}_w + \mathbf{v}_n) = \nabla \cdot \mathbf{v}_t. \quad (2.31)$$

For the case of incompressible flow under isothermal conditions, Equation (2.29) reduces to:

$$\nabla \cdot \mathbf{v}_t = q_w + q_n. \quad (2.32)$$

Expressing the total velocity in terms of the multi-phase *Darcy's* law, Equation (2.32) can be reformulated to:

$$\nabla \cdot [-\lambda_t \mathbf{K} (f_w \nabla \Phi_w + f_n \nabla \Phi_n)] = q_w + q_n. \quad (2.33)$$

The pressure equation balances total flux instead of phase fluxes. Thus, new quantities related to the total flux appear, which are the total mobility $\lambda_t = \lambda_w + \lambda_n$, with the phase mobilities $\lambda_\alpha = \frac{k_{r\alpha}}{\mu_\alpha}$, and the phase fractional flow functions $f_\alpha = \frac{\lambda_\alpha}{\lambda_t}$.

In the following, three different types of pressure equation are distinguished: Phase pressure formulations, phase potential formulations and a global pressure formulation. The latter is especially helpful for mathematical considerations because it is an always well defined and smooth function (*Chavent and Jaffré, 1986*). However, a quantitative physical interpretation of the global pressure and thus application to real problems is difficult.

The phase pressure formulation is obtained by inserting Equation (2.13) in Equation (2.33):

$$\nabla \cdot [-\lambda_t \mathbf{K} (f_w \nabla p_w + f_n \nabla p_n + (f_w \varrho_w + f_n \varrho_n) g \nabla z)] = q_w + q_n. \quad (2.34)$$

Inserting Equation (2.26), Equation 2.34 can be formulated in terms of the wetting phase pressure:

$$\nabla \cdot [-\lambda_t \mathbf{K} (\nabla p_w + f_n \nabla p_c + (f_w \varrho_w + f_n \varrho_n) g \nabla z)] = q_w + q_n \quad (2.35)$$

or in terms of the non-wetting phase pressure:

$$\nabla \cdot [-\lambda_t \mathbf{K} (\nabla p_n - f_w \nabla p_c + (f_w \varrho_w + f_n \varrho_n) g \nabla z)] = q_w + q_n. \quad (2.36)$$

For the solution of Equation (2.35) or (2.36) on a domain Ω with boundary $\Gamma = \Gamma_D \cup \Gamma_N$, where Γ_D denotes a Dirichlet and Γ_N a Neumann boundary, the boundary conditions are:

$$p_\alpha = p_D \quad \text{on} \quad \Gamma_D \quad (2.37)$$

$$\mathbf{v}_t \cdot \mathbf{n} = v_N \quad \text{on} \quad \Gamma_N. \quad (2.38)$$

Derivation and investigation of phase pressure fractional flow formulations can for example be found in *Chen et al. (2006)*.

The phase potential formulation is shown in Equation (2.33). By inserting Equation (2.27) it can be formulated for the wetting phase potential:

$$\nabla \cdot [-\lambda_t \mathbf{K} (\nabla \Phi_w + f_n \nabla \Phi_c)] = q_w + q_n, \quad (2.39)$$

or for the non-wetting phase potential:

$$\nabla \cdot [-\lambda_t \mathbf{K} (\nabla \Phi_n - f_w \nabla \Phi_c)] = q_w + q_n. \quad (2.40)$$

The wetting phase potential formulation has been used in *Hoteit and Firoozabadi (2008)* where the authors further suggest to reformulate the equation to:

$$\nabla \cdot \left[\underbrace{-\lambda_t \mathbf{K} \nabla \Phi_w}_{\mathbf{v}_{aw}} - \underbrace{\lambda_n \mathbf{K} \nabla \Phi_c}_{\mathbf{v}_c} \right] = q_w + q_n. \quad (2.41)$$

The velocity in Equation (2.41) is split into the advective velocity \mathbf{v}_{aw} and the capillary velocity \mathbf{v}_c . This reformulation can be advantageous depending on the discretization method (see Chapter 3). Boundary conditions for the solution of Equations (2.39) and (2.40) on

domain Ω are:

$$\Phi_\alpha = p_D + \varrho_\alpha g z \quad \text{on } \Gamma_D \quad (2.42)$$

$$\mathbf{v}_t \cdot \mathbf{n} = v_N \quad \text{on } \Gamma_N \quad (2.43)$$

where the boundary $\Gamma = \Gamma_D \cup \Gamma_N$ (D = Dirichlet, N = Neumann).

The global pressure formulation defines a global pressure p , such that

$$\nabla p = f_w \nabla p_w + f_n \nabla p_n. \quad (2.44)$$

Inserting this expression in Equation (2.34) yields

$$\nabla \cdot [-\lambda_t \mathbf{K} (\nabla p + (f_w \varrho_w + f_n \varrho_n) g \nabla z)]. \quad (2.45)$$

For a domain Ω with boundary $\Gamma = \Gamma_D \cup \Gamma_N$, where Γ_D denotes a *Dirichlet* and Γ_N a *Neumann* boundary, the boundary conditions are:

$$\begin{aligned} p &= p_D \quad \text{on } \Gamma_D \quad \text{and} \\ \mathbf{v}_t \cdot \mathbf{n} &= v_N \quad \text{on } \Gamma_N. \end{aligned} \quad (2.46)$$

The definition of meaningful Dirichlet boundary conditions for a global pressure (Equation (2.46)) is however not straightforward. The global pressure is no physically interpretable quantity and can not be measured directly, although it has superior properties from a mathematical point of view. Following *Chavent and Jaffré (1986)* the total pressure is defined as:

$$p = \frac{1}{2} (p_w + p_n) - \int_{S_c}^{S_w} \left(f_w(S_w) - \frac{1}{2} \right) \frac{dp_c}{dS_w}(S_w) dS_w \quad (2.47)$$

where S_c is the saturation which satisfies $p_c(S_c) = 0$. As shown, for example, in *Binning and Celia (1999)*, an iterative solution technique may be necessary for modelling realistic scenarios where boundary conditions are usually defined for phase pressures. If the capillary pressure between the phases is neglected $p = p_w = p_n$.

Saturation Equation

To model the saturation transport one of the phase mass balance equations (Equation (2.21) or (2.22)), or in the incompressible case one of the saturation balance equations (Equation (2.23) or (2.24)) has to be solved. Depending on the primary pressure variable the calculation of the corresponding phase velocity differs.

The phase pressure formulation allows the direct calculation of the phase velocities applying the extended Darcy's law (Equation (2.12) and (2.13)).

The phase potential formulation either allows the direct calculation of the phase velocities applying the extended Darcy's law (Equation (2.12)) or from the advective phase velocity as:

$$\mathbf{v}_\alpha = f_\alpha \mathbf{v}_{a\alpha}. \quad (2.48)$$

The global pressure formulation requires a more complex reconstruction of the phase velocities. Only the total velocity can be calculated directly from a known global pressure distribution. Thus, the phase velocities have to be formulated in terms of the total velocity. From Equation 2.30 an expression for the wetting phase velocity in terms of the total velocity is:

$$\mathbf{v}_w = \mathbf{v}_t - \mathbf{v}_n. \quad (2.49)$$

Inserting Equations (2.12), (2.13) and (2.26) yields

$$\mathbf{v}_w = \mathbf{v}_t + \lambda_n \mathbf{K} \nabla p_w + \lambda_n \mathbf{K} \nabla p_c + \lambda_n \mathbf{K} \varrho_n g \nabla z. \quad (2.50)$$

An expression for the wetting phase pressure gradient can be obtained by reformulating the wetting phase darcy velocity:

$$\nabla p_w = -\frac{1}{\lambda_w} \mathbf{K}^{-1} \mathbf{v}_w - \varrho_w g \nabla z. \quad (2.51)$$

With Equation (2.51), Equation (2.50) can be rewritten into

$$\mathbf{v}_w = f_w \mathbf{v}_t + f_w \lambda_n \mathbf{K} \nabla p_c + f_w \lambda_n \mathbf{K} (\varrho_n - \varrho_w) g \nabla z. \quad (2.52)$$

A similar expression can be derived for the non-wetting phase velocity:

$$\mathbf{v}_n = f_n \mathbf{v}_t - f_n \lambda_w \mathbf{K} \nabla p_c + f_n \lambda_w \mathbf{K} (\rho_w - \rho_n) g \nabla z. \quad (2.53)$$

2.3 Coarse Scale Model Equations

In general, coarse scale equations can be derived by upscaling of the fine-scale equations. Large scale equations for two-phase flow have been derived for example by *Quintard and Whitaker* (1988) or *Sáez et al.* (1989). However, such approaches lead to complex equations including many new and unknown coarse-scale parameters. On the one hand, these complicated equations can allow to account sophisticatedly for different kinds of small scale effects on the large scale. On the other hand, the equations have to be solved numerically and higher number of different terms and parameters will increase the complexity of the numerical scheme and decrease the stability. Further, meaningful coarse-scale quantities have to be determined. This is a crucial point of many upscaling strategies and the quality of the parameters determines the quality of the model. Considering realistic applications, it can decrease possible sources of errors if only few coarse-scale model parameters have to be determined. Thus, an approach is chosen which allows to stick with the comparatively simple equations of the fine-scale model with exchanged model parameters. This allows the direct transfer of numerical methods and expertise, which are available for the treatment of the fine-scale system, to the coarse-scale system. However, as the complexity of the equations themselves is not increased and there are only few model parameters, the complexity of these coarse-scale parameters or pseudo functions has to increase to account for important small scale effects. Additionally, a more elaborated numerical upscaling or multi-scale strategy may be necessary.

2.3.1 Immiscible Two-phase Flow Equations

Following the definition of the fine-scale equations, we can write the coarse-scale conservation equations for a wetting (w) and a non-wetting (n) saturation of immiscible

incompressible fluids under isothermal conditions directly as:

$$\phi^* \frac{\partial S_w}{\partial t} + \nabla \cdot \mathbf{v}_w^* = q_w \quad (2.54)$$

$$\phi^* \frac{\partial S_n}{\partial t} + \nabla \cdot \mathbf{v}_n^* = q_n. \quad (2.55)$$

Superscript * indicates a new effective coarse-scale quantity and ϕ^* is the effective porosity. As already done for the fine scale, a *Darcy*-like law is used as constitutive relationship for the coarse-scale phase velocities:

$$\mathbf{v}_\alpha^* = -\frac{1}{\mu_\alpha} \mathbf{K}_\alpha^* (\nabla p_\alpha^* + \varrho_\alpha g \nabla z), \quad \alpha = w, n. \quad (2.56)$$

In Equation (2.56) p_α^* is the coarse-scale phase pressure and $\mathbf{K}_\alpha^* = \mathbf{K}_\alpha^*(S)$ is the phase permeability which is usually split up into relative permeability of a phase multiplied with the absolute permeability of the porous medium (see Section 2.1.3):

$$\mathbf{K}_\alpha^* = \mathbf{K}_{r\alpha}^* \mathbf{K}^*. \quad (2.57)$$

On the coarse scale, the relative permeability $\mathbf{K}_{r\alpha}^* = \mathbf{K}_{r\alpha}^*(S)$ is assumed to be a full second order tensor. The issue of needing full tensor relative permeabilities has been touched, for example, in *Saad et al. (1995)*; *Pickup and Sorbie (1996)*; *Braun et al. (2005)*; *Eichel et al. (2005)*; *Wolff et al. (2012)* and is discussed in detail in the later chapters. effective capillary pressure

$$p_c^* = p_n^* - p_w^*, \quad (2.58)$$

which is, as well as the effective phase permeabilities, modeled as functions of the saturation $p_c^* = p_c^*(S_w)$.

2.3.2 Fractional Flow Formulation

The tensorial coefficients, especially the tensorial relative permeabilities, lead to new challenges for numerical methods. These will be discussed in detail in Chapter 3, which deals with the discretization of the mathematical models. However, meeting these challenges also influences the choice of the mathematical formulation and thus some points are already mentioned here: If the direction of flow is saturation dependent via

saturation dependent tensorial coefficients, the upwind direction can not necessarily be estimated directly from the solution of the old time step. Thus, Equations (2.54) and (2.55) are reformulated into a system of equations which can be solved sequentially. It is a common assumption that the resulting pressure equation (Equation (2.59), (2.64), or (2.65)) can be treated without upwinding, because it balances the total flow instead of a phase flow. Further, a formulation is chosen which introduces phase potentials instead of phase pressures (*Hoteit and Firoozabadi, 2008*). By solving for the potentials, the gravity term is not completely moved to the right-hand side of the linear system of equations. We have observed that this can lead to a better solution behavior in the context of a sequential solution strategy where the solution for the velocity field and for the transport of the phases are decoupled. Finally, for reasons of efficiency, the formulation should ensure that the number of operators that have to be provided by the numerical scheme (e.g. transmissibilities in a MPFA method, Chapter 3) is as small as possible.

Pressure Equation

A coarse scale pressure equation similar to the fine-scale pressure equation can be derived by summation of Equations (2.54) and (2.55) to the total saturation balance:

$$\nabla \cdot (\mathbf{v}_w^* + \mathbf{v}_n^*) = \nabla \cdot \mathbf{v}_t^* = q_w^* + q_n^*. \quad (2.59)$$

With the definitions of the phase mobilities $\Lambda_\alpha^* = \frac{1}{\mu_\alpha} \mathbf{K}_{r_w}^*$, the total mobility $\Lambda_t^* = \Lambda_w^* + \Lambda_n^*$, and the potentials

$$\begin{aligned} \Phi_\alpha^* &= p_\alpha^* + \varrho_\alpha g z \\ \Phi_c^* &= \Phi_n^* - \Phi_w^* = p_c^* + (\varrho_n - \varrho_w) g z, \end{aligned} \quad (2.60)$$

the phase velocities can be added up to the total velocity as:

$$\mathbf{v}_t^* = -\Lambda_w^* \mathbf{K}^* \nabla \Phi_w^* - \Lambda_n^* \mathbf{K}^* \nabla \Phi_n^*. \quad (2.61)$$

The coarse scale pressure equation can now be formulated using the wetting or non-wetting phase potential or pressure as primary pressure variable. To get the wetting

phase pressure equation, Equation (2.61) is rewritten as follows:

$$\begin{aligned}
\mathbf{v}_t^* &= -\Lambda_w^* \mathbf{K}^* \nabla \Phi_w^* + \Lambda_n^* \mathbf{K}^* \nabla \Phi_w^* - \Lambda_n^* \mathbf{K}^* \nabla \Phi_w^* - \Lambda_n^* \mathbf{K}^* \nabla \Phi_n^* \\
&= -\Lambda_t^* \mathbf{K}^* \nabla \Phi_w^* - \Lambda_n^* \Lambda_t^{*-1} \Lambda_t^* \mathbf{K}^* \nabla (\Phi_n^* - \Phi_w^*) \\
&= \underbrace{-\Lambda_t^* \mathbf{K}^* \nabla \Phi_w^*}_{\mathbf{v}_{aw}^*} \underbrace{- \mathbf{F}_n^* \Lambda_t^* \mathbf{K}^* \nabla (\Phi_n^*)}_{\mathbf{v}_c^*}
\end{aligned} \tag{2.62}$$

where $\mathbf{v}_{a\alpha}^*$ is called advective velocity of the phase α , \mathbf{v}_c^* can be called capillary velocity, although it also includes gravity effects, and $\mathbf{F}_\alpha^* = \Lambda_\alpha^* \Lambda_t^{*-1}$ is a tensorial definition of the fractional flow function of the phase α . Analogously, the total velocity for a non-wetting phase pressure equation can be written as:

$$\mathbf{v}_t^* = \underbrace{-\Lambda_t^* \mathbf{K}^* \nabla \Phi_n^*}_{\mathbf{v}_{an}^*} + \underbrace{\mathbf{F}_w^* \Lambda_t^* \mathbf{K}^* \nabla (\Phi_c^*)}_{\mathbf{v}_c^*}. \tag{2.63}$$

With the definitions of the advective and capillary velocity, the pressure equation can alternatively be written as

$$\nabla \cdot \mathbf{v}_t^* = \nabla \cdot (\mathbf{v}_{aw}^* + \mathbf{v}_c^*) = q_w^* + q_n^* \tag{2.64}$$

for the wetting phase pressure or potential, or as

$$\nabla \cdot \mathbf{v}_t^* = \nabla \cdot (\mathbf{v}_{an}^* - \mathbf{v}_c^*) = q_w^* + q_n^* \tag{2.65}$$

for the non-wetting phase pressure or potential.

Saturation Equation

For the saturation transport, one of the saturation balance equations (Equation (2.54) or (2.55)) has to be solved. Therefore, phase velocities have to be calculated either directly as:

$$\mathbf{v}_\alpha^* = -\Lambda_\alpha^* \mathbf{K}^* \nabla \Phi_\alpha^* \tag{2.66}$$

or in terms of \mathbf{v}_a^* and \mathbf{v}_c^* as

$$\mathbf{v}_\alpha^* = \mathbf{F}_\alpha^* \mathbf{v}_{a\alpha}^* \tag{2.67}$$

where $\mathbf{v}_{an}^* = \mathbf{v}_{aw}^* + \mathbf{v}_c^*$.

Summary In this chapter the concepts and mathematical equations for modeling two-phase flow of immiscible incompressible fluids under isothermal conditions were introduced. A focus was on the derivation of different types of fractional flow formulations, which were derived for a fine Darcy scale (fine scale) and a coarse Darcy scale (coarse scale). Fractional flow formulations for immiscible incompressible two-phase flow are composed of an elliptic pressure equation and a saturation transport equation. Pressure or potential equations were derived for the global pressure, the phase pressures and for phase potentials.

For the multi-scale approach which will be developed in the following chapters phase-potential-saturation formulations based on Equations (2.39), (2.40), (2.23), (2.24) and (2.64),(2.65), (2.54),(2.55) are chosen. They are implemented using an IMPES algorithm (for example *Aziz and Settari, 1979*). In contrast to the global pressure, a potential is a physically motivated quantity. In addition, phase velocities can be calculated directly from the phase potentials. This greatly simplifies the saturation transport equation. If a phase or global pressure formulation is discretized explicitly in time, the gravity term is completely moved to the right-hand side of the linear system of equations. In contrast, the gravity term is partly included in the unknown if a phase potential formulation is used. This can improve the solution behavior of the sequential IMPES solver where the solution for the velocity field and for the transport of the phases are decoupled. Another advantage of the potential formulation is the minimal number of different terms. Additionally, the different flux terms have a similar form. Thus, a minimal number of different transmissibilities has to be calculated for the multi-point flux approximation.

3 Numerical Methods

In the previous chapter, the equations for modeling two-phase flow on different length scales are derived. In order to solve these equations in a multi-scale approach, suitable numerical methods are required. They have to approximate two-phase flow features such as saturation discontinuities due to shock fronts or material interfaces, or capillary diffusion correctly. Moreover, special strategies are necessary to account for parameters of increased complexity in the coarse scale equations, for example, tensorial relative permeabilities. Finally, a correct flux approximation on non-conforming adaptive grids is important. The employment of these type of grids is the key instrument for transferring information between length scales in the multi-scale approach (Chapter 4).

In the following sections a finite volume formulation based on multi-point flux approximation (MPFA) is developed. First, state of the art MPFA methods are extended to approximate the “full” two-phase flow equations including capillary pressure and gravity (Section 3.1). Second, the approximation of fluxes in the surrounding of hanging nodes is described (Section 3.2). Third, a strategy for treating tensorial solution dependent coefficients like the relative permeability tensor is developed (3.3). In addition to these main aspects, a simplified but very flexible concept for the approximation of boundary fluxes is introduced. The content of Sections 3.1.3 - 3.1.7 and 3.2 is to some extent also part of *Wolff et al.* (2013a), Section 3.3 is to some extent taken from *Wolff et al.* (2012). The numerical methods are tested and validated on various well-known two-phase flow problems such as the Buckley-Leverett problem or the McWhorter problem. The tests are selected and set up in such a way that the important two-phase flow and multi-scale features which are mentioned before are tested.

3.1 Finite Volume Discretization with MPFA

In integral (conservation) form, a p_w - S_w formulation of the two-phase flow equations derived in Chapter 2 can be written as:

$$\int_{\partial V} \mathbf{v}_t \cdot \mathbf{n} dA = \int_V q_t dV \quad (3.1)$$

$$\int_V \phi \frac{\partial S_w}{\partial t} dV + \int_{\partial V} \mathbf{v}_w \cdot \mathbf{n} dA = \int_V q_w dV \quad (3.2)$$

where \mathbf{n} is the normal vector pointing outward of volume V at the volume boundary ∂V . Applying a cell centered finite volume scheme (CCFV), Equations (3.1) and (3.2) can now be written in discrete form (discrete in space) for each finite volume (grid cell) as:

$$\sum_{i=1}^n \mathbf{f}_{ti} = q_t V \quad (3.3)$$

$$\phi \frac{\partial S_w}{\partial t} V + \sum_{i=1}^n \mathbf{f}_{wi} = q_w V \quad (3.4)$$

where \mathbf{f}_{ti} is the total flux and \mathbf{f}_{wi} the wetting phase flux at a cell face i and n is the number of faces ($n = 4$, for quadrilateral cells (2-d); $n = 6$, for quadrilaterally faced hexahedra (3-d)). According to the definitions of the advective and the capillary velocity given before (Equation (2.64)), the total flux can be further split into its two components:

$$\sum_{i=1}^n \mathbf{f}_{ti} = \sum_{i=1}^n (\mathbf{f}_{awi} + \mathbf{f}_{ci}) = q_t V. \quad (3.5)$$

The main challenge using the CCFV scheme is the calculation of the numerical flux. The method most commonly used in finite-volume codes for ground water or reservoir simulation is the two-point flux approximation method (TPFA), which is physically intuitive, simple, and can be implemented very efficiently. It assumes a first order approximation of the pressure between two neighboring cell centers (two points). At face i this leads to the gradient approximation

$$\nabla p_i \approx \frac{p_2 - p_1}{|\mathbf{x}_2 - \mathbf{x}_1|} \quad (3.6)$$

and thus, to the flux approximation

$$\mathbf{f}_i \approx T_i(p_2 - p_1) \quad (3.7)$$

where p_1 and p_2 are the cell pressures and \mathbf{x}_1 and \mathbf{x}_2 the position vectors of the cell centers of two neighboring cells. The face transmissibility T_i includes the necessary geometrical information and, in dependence on the complexity, physical properties such as permeability or mobility. It is important to mention that TPFA corresponds to a one-dimensional approximation of the flux. Thus, the grid has to be K-orthogonal in order to get a consistent flux approximation (see *Aavatsmark et al.*, 1996; *Aavatsmark*, 2002). If the grid is not K-orthogonal, TPFA leads to an $\mathcal{O}(1)$ error in the solution, which cannot be reduced by grid refinement as long as it does not improve the K-orthogonality of the grid (*Aavatsmark*, 2007; *Wu and Parashkevov*, 2009). To extend CCFV methods to work with general grids and general anisotropic coefficients (like permeabilities), multi-point flux approximation methods have been developed, originally in the research groups of *Aavatsmark et al.* (1994), and of *Edwards and Rogers* (1994). During the last decade various variants of MPFA methods have been introduced, such as the O(η)-method *Aavatsmark et al.* (1996); *Edwards and Rogers* (1998); *Pal et al.* (2006), the L-method *Aavatsmark et al.* (2008); *Cao et al.* (2009), the U-method *Aavatsmark et al.* (1996, 1998a,b); *Aavatsmark and Eigestad* (2006), the Z-method *Nordbotten and Eigestad* (2005), the enriched MPFA method *Chen et al.* (2008), or the nine point scheme of *Sheng and Yuan* (2008).

MPFA methods were originally designed for elliptic flow laws like Darcy's law (Equation (2.10)). The main aspect of MPFA is increasing the accuracy compared to TPFA, in particular, in the case of general non-orthogonal grids or anisotropic coefficients, by increasing the flux stencil. The various methods differ in the size of the flux stencil due to differently shaped control volumes for the flux approximation. This leads to a different convergence behavior and monotonicity of the methods, although, so far, no method seems to be superior for all types of grids or applications.

The fundamental concept of a MPFA is simple: Instead of the one-dimensional approximation used by the TPFA, a multi-dimensional approximation is applied:

$$\mathbf{f}_i \approx \sum_{j \in J} t_{ij}(p_j) \quad (3.8)$$

where the set J includes all cells j which influence the flux \mathbf{f}_i , and t_{ij} are called

transmissibility coefficients. The size of J depends on the individual method. If J includes only the two neighboring cells sharing an interface i , the MPFA simplifies to a TPFA. The same applies if the grid is K-orthogonal. The core of MPFA is the determination of the transmissibility coefficients including the approximation of gradients. In the following, two different MPFA methods are introduced.

The first method, which is the most frequently applied MPFA method, is the MPFA-O(0) method, which is usually simply called MPFA-O method. It has been applied to various types of meshes, for example of quadrilaterals (*Aavatsmark, 2002*), of hexahedra of quadrilaterals (*Aavatsmark et al., 1998c; Lee et al., 2002*), or for general polyhedra (*Gunasekera et al., 1998*). The convergence of the O-method has been extensively studied and analyzed for example in *Aavatsmark and Eigestad (2006); Aavatsmark et al. (2007); Eigestad and Klausen (2005); Pal et al. (2006); Klausen and Winther (2006); Agelas and Masson (2008)* either by numerical convergence studies or by theoretical proofs. The issue of the M-matrix monotonicity, which is an important property to avoid unphysical oscillations in the pressure solution, is discussed for example in *Nordbotten and Aavatsmark (2005); Nordbotten et al. (2007a); Edwards and Zheng (2008)*.

The second method is the MPFA L-method, which has some advantages compared to the O-method. The flux stencils are smaller, the domain of convergence as well as the domain of monotonicity is larger and the treatment of hanging nodes and thus the capability for straightforward local adaptivity is naturally included. The first introduction of the L-method is given in *Aavatsmark et al. (2008)* for quadrilateral grids in two dimensions. In *Aavatsmark et al. (2010)* it is extended to three dimensions. An alternative but closely related scheme with anisotropy-favoring triangulation is presented in *Pal and Edwards (2011); Edwards et al. (2011)*. The L-method has been tested on different heterogeneous, highly anisotropic, elliptic problems from the FVCA5 benchmark on triangular and quadrilateral two-dimensional grids in *Mundal et al. (2008)*, and from the FVCA6 benchmark on three-dimensional hexahedral grids in *Wolff et al. (2012)*. In *Cao et al. (2009)* the boundary influence on the convergence rate is studied. Further, the authors give a geometrical interpretation of the transmissibility-based criterion to choose a proper L-stencil in the case of homogeneous media. Theoretical convergence proofs for the L-method are given in *Cao et al. (2011)* and *Stephansen (2012)*. The monotonicity in case of two-dimensional MPFA methods is discussed in *Aavatsmark et al. (2008)* and *Nordbotten et al. (2007a)*.

The crucial point for both methods is the approximation of the pressure or potential

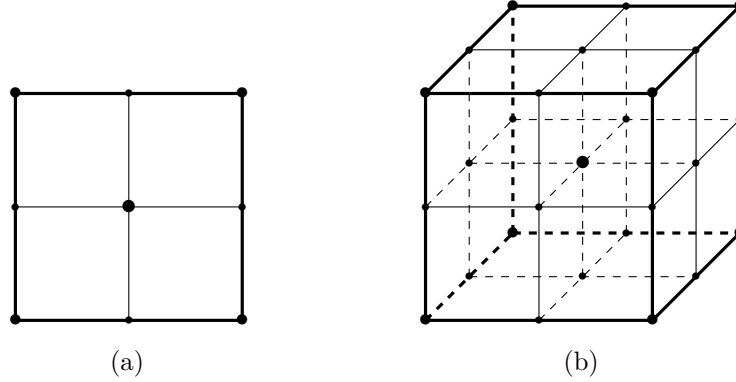


Figure 3.1: Grid cell (thick lines) divided into four sub-control-volumes in 2-d (a), and into eight sub-control-volumes in 3-d (b)

and thus of the gradient. Therefore, each cell is subdivided into sub-control-volumes, one related to each corner of a cell. The corners of each sub-control-volume are: The current corner of the cell, the cell center, the midpoints of the cell faces which surround the current cell corner, and, in the three-dimensional case, additionally the midpoints of the cell edges in the surrounding of the current cell corner (Figure 3.1).

In each of the sub-control-volumes the pressure (or potential) is approximated linearly between the continuity points which are located at the corners of the sub-control-volume in case of the MPFA O- and L-method. In the two-dimensional case, three continuity points describing a triangle, in the three-dimensional case, four continuity points describing a tetrahedron are necessary (Figure 3.2). The approximation between the continuity points is defined as:

$$p(\mathbf{x}) = \nabla p \cdot (\mathbf{x} - \mathbf{x}_0) + p_0. \quad (3.9)$$

Equation (3.9) can be reformulated into the system of equations

$$\mathbf{X} \nabla p = \mathbf{P}. \quad (3.10)$$

In the two-dimensional case

$$\mathbf{X} = \begin{pmatrix} (\bar{\mathbf{x}}_1 - \mathbf{x}_0)^T \\ (\bar{\mathbf{x}}_2 - \mathbf{x}_0)^T \end{pmatrix} \quad (3.11)$$

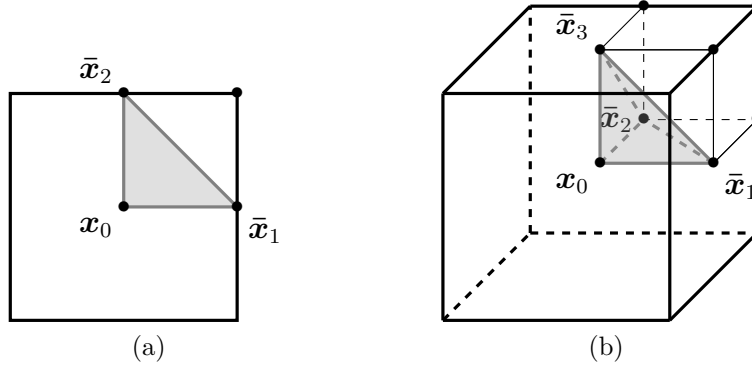


Figure 3.2: Triangle (a) (2-d) and tetrahedron (b) (3-d) described by the continuity points for the pressure approximation of one sub-control-volume.

and

$$\mathbf{P} = \begin{pmatrix} \bar{p}_1 - p_0 \\ \bar{p}_2 - p_0 \end{pmatrix}. \quad (3.12)$$

To get an explicit expression for the gradient from Equation (3.10), the inverse of \mathbf{X} can be derived as:

$$\mathbf{X}^{-1} = \frac{1}{T}(\boldsymbol{\nu}_1, \boldsymbol{\nu}_2), \quad (3.13)$$

with

$$T = (\bar{\mathbf{x}}_1 - \mathbf{x}_0)^T \mathbf{R} (\bar{\mathbf{x}}_2 - \mathbf{x}_0) \quad \mathbf{R} = \begin{pmatrix} 0 & 1 \\ -1 & 0 \end{pmatrix} \quad (3.14)$$

and

$$\boldsymbol{\nu}_1 = \mathbf{R}(\bar{\mathbf{x}}_2 - \mathbf{x}_0), \quad \boldsymbol{\nu}_2 = -\mathbf{R}(\bar{\mathbf{x}}_1 - \mathbf{x}_0). \quad (3.15)$$

The vector $\boldsymbol{\nu}$ is the inward normal vector of the face of the triangle opposite to the corresponding position $\bar{\mathbf{x}}$ (e.g. $\boldsymbol{\nu}_1$ the normal of $\mathbf{x}_0\bar{\mathbf{x}}_2$ opposite to $\bar{\mathbf{x}}_1$). The length of $\boldsymbol{\nu}$ is equal to the length of the face to which it is normal. The coefficient T is equal to twice the area of the triangle.

In the three-dimensional case,

$$\mathbf{X} = \begin{pmatrix} (\bar{\mathbf{x}}_1 - \mathbf{x}_0)^T \\ (\bar{\mathbf{x}}_2 - \mathbf{x}_0)^T \\ (\bar{\mathbf{x}}_3 - \mathbf{x}_0)^T \end{pmatrix} \quad (3.16)$$

and

$$\mathbf{P} = \begin{pmatrix} \bar{p}_1 - p_0 \\ \bar{p}_2 - p_0 \\ \bar{p}_3 - p_0 \end{pmatrix}, \quad (3.17)$$

and analogous to the two-dimensional case the inverse of \mathbf{X} is derived as:

$$\mathbf{X}^{-1} = \frac{1}{T}(\boldsymbol{\nu}_1, \boldsymbol{\nu}_2, \boldsymbol{\nu}_3). \quad (3.18)$$

The vectors $\boldsymbol{\nu}$ again are the inward normal vectors of the faces of the tetrahedron opposite to the corresponding position $\bar{\mathbf{x}}$ (e.g. $\boldsymbol{\nu}_1$ the normal of $\mathbf{x}_0\bar{\mathbf{x}}_2\bar{\mathbf{x}}_3$ opposite to $\bar{\mathbf{x}}_1$). They have the length of twice the area of the face they are normal to. The face area can be expressed by the cross product of the two vectors that span the tetrahedron face. Referring to Figure 3.2b the vectors $\boldsymbol{\nu}$ can be defined as:

$$\begin{aligned} \boldsymbol{\nu}_1 &= (\bar{\mathbf{x}}_2 - \mathbf{x}_0) \times (\bar{\mathbf{x}}_3 - \mathbf{x}_0) \\ \boldsymbol{\nu}_2 &= (\bar{\mathbf{x}}_3 - \mathbf{x}_0) \times (\bar{\mathbf{x}}_1 - \mathbf{x}_0) \\ \boldsymbol{\nu}_3 &= (\bar{\mathbf{x}}_1 - \mathbf{x}_0) \times (\bar{\mathbf{x}}_2 - \mathbf{x}_0). \end{aligned} \quad (3.19)$$

The coefficient T is given by the triple product of the three vectors that span the tetrahedron and is equal to 6 times the volume of the tetrahedron:

$$T = ((\bar{\mathbf{x}}_1 - \mathbf{x}_0)(\bar{\mathbf{x}}_2 - \mathbf{x}_0)(\bar{\mathbf{x}}_3 - \mathbf{x}_0)). \quad (3.20)$$

The gradient approximation for both cases can finally be defined as:

$$\nabla p = \frac{1}{T} \sum_i^{n_{\text{dim}}} \boldsymbol{\nu}_i (\bar{p}_i - p_0), \quad n_{\text{dim}} = 2, 3. \quad (3.21)$$

For more details on the derivation of the gradient approximation see for example *Aavatsmark* (2002).

Given the pressure approximation for each sub-control-volume, MPFA methods usually approximate the fluxes across sub-interfaces. Thus, the flux over a cell face is the sum of the sub-interface fluxes (Figure 3.3)

$$\mathbf{f}_i = \sum_{j=1}^{n_s} \mathbf{f}_{ij} \quad (3.22)$$

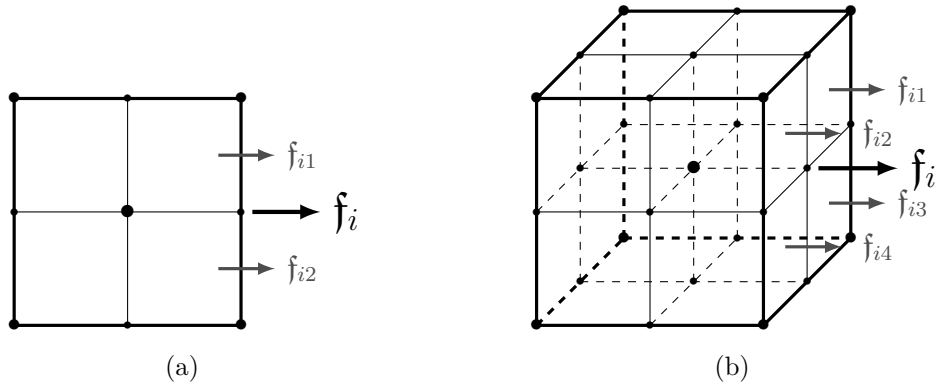


Figure 3.3: Sub-fluxes at a cell-cell interface according to the sub-control-volumes. (a): Two sub-fluxes (2-d); (b): Four sub-fluxes (3-d)

where n_s is the number of sub-interfaces j per cell-cell interface i ($n_s = 2$ (2-d), and $n_s = 4$, for quadrilaterally faced hexahedra (3-d)).

The MPFA O- and L-method apply the described multi-dimensional gradient approximation. However, they differ in the choice of the so-called interaction volume which is used for the flux approximation and thus in the flux stencil. The L-method is preferred for the application in the subsequently introduced multi-scale method for several reasons: it is advantageous regarding the convergence behavior and the monotonicity of the solution and, first of all, it can be applied for non-conforming h-adaptive grids straightforwardly. The O-method is mainly used for validation and test purposes and thus only briefly introduced for the two-dimensional case in the following. The L-method is introduced in more detail and for both, the two-dimensional and the three-dimensional case. Furthermore, the MPFA methods are extended to two-phase flow including capillary pressure and gravity effects. As pointed out before, so far, they have been mainly developed for elliptic flow laws such as Darcy's law for one phase flow.

3.1.1 The O-Method

One interaction volume of the O-method consists of all sub-control-volumes surrounding a grid vertex. In the two-dimensional case this results in an O-shaped interaction volume. Four cells of a finite-volume grid are sketched in Figure 3.4 (solid lines). The cells are subdivided into sub-control-volumes by the dashed lines. Let us consider the interaction volume I (bold line) around vertex I consisting of four sub-control-volumes 1, 2, 3,

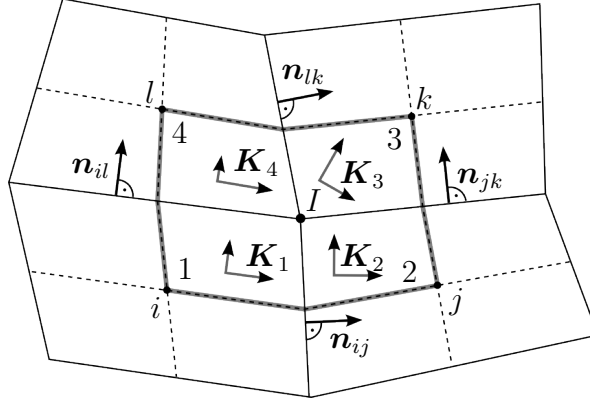


Figure 3.4: Sub-control-volumes (dashed and solid black lines) and interaction volume (bold line) for the flux approximation for the corresponding half faces between cells i , j , k and l

and 4 of the surrounding cells i , j , k , and l . Using the previously introduced linear approximation for the pressure in every sub-control-volume of the interaction volume, the fluxes through the corresponding half faces between cells i , j , k , and l can be formulated. As an example, the one-phase Darcy-flux between sub-control-volume 1 and 2 (over the half face between i and j) can be written as:

$$\mathbf{f}_{12} \approx \frac{-\Gamma_{ij} \mathbf{n}_{ij}^T \mathbf{K}_i}{T_1} [\boldsymbol{\nu}_{12} (\bar{p}_{12} - p_i) + \boldsymbol{\nu}_{14} (\bar{p}_{14} - p_i)] \quad (3.23)$$

where \bar{p}_{12} and \bar{p}_{14} are the pressures at the continuity points (\mathbf{x}_1 and \mathbf{x}_2 in Figure 3.2a) and Γ_{ij} is the area of the sub-interface between cell i and j . To preserve the local conservation of fluxes it is requested that the flux leaving one sub-control-volume is equal to that entering the next one, e.g. $\mathbf{f}_{12} \stackrel{!}{=} \mathbf{f}_{21}$:

$$\begin{aligned} & \frac{-\Gamma_{ij} \mathbf{n}_{ij}^T \mathbf{K}_i}{T_1} [\boldsymbol{\nu}_{12} (\bar{p}_{12} - p_i) + \boldsymbol{\nu}_{14} (\bar{p}_{14} - p_i)] \\ & \stackrel{!}{=} \frac{\Gamma_{ij} \mathbf{n}_{ij}^T \mathbf{K}_j}{T_2} [\boldsymbol{\nu}_{21} (\bar{p}_{21} - p_j) + \boldsymbol{\nu}_{23} (\bar{p}_{23} - p_j)]. \end{aligned} \quad (3.24)$$

Besides flux continuity, pressure continuity at the continuity points is required:

$$\begin{aligned} \bar{p}_{12} &= \bar{p}_{21} = \bar{p}_1 \\ \bar{p}_{23} &= \bar{p}_{32} = \bar{p}_2 \\ \bar{p}_{34} &= \bar{p}_{43} = \bar{p}_3 \\ \bar{p}_{41} &= \bar{p}_{14} = \bar{p}_4. \end{aligned} \quad (3.25)$$

Inserting the conditions of Equation (3.25), the system of equations arising from the flux continuity conditions

$$\begin{aligned} \mathbf{f}_{12} &= \mathbf{f}_{21} \\ \mathbf{f}_{23} &= \mathbf{f}_{32} \\ \mathbf{f}_{34} &= \mathbf{f}_{43} \\ \mathbf{f}_{41} &= \mathbf{f}_{14}. \end{aligned} \tag{3.26}$$

can be used to construct the transmissibility matrix \mathbf{T}_I where

$$\mathbf{f}_I = \mathbf{T}_I \mathbf{p}_I. \tag{3.27}$$

The vector \mathbf{f}_I includes the fluxes over the half edges inside the interaction volume and the vector $\mathbf{p}_I = (p_i, p_j, p_k, p_l)^T$ the cell pressures of the four adjacent finite volume cells at vertex I . Defining the vector of the pressures at the continuity points $\bar{\mathbf{p}}_I = (\bar{p}_1, \bar{p}_2, \bar{p}_3, \bar{p}_4)^T$, the left-hand side of system (3.26) can be written in the matrix form

$$\mathbf{f}_I = \mathbf{C}_I \bar{\mathbf{p}}_I - \mathbf{D}_I \mathbf{p}_I, \quad \mathbf{C} \in \mathcal{R}^{4 \times 4}, \quad \mathbf{D} \in \mathcal{R}^{4 \times 4}. \tag{3.28}$$

Further, the entire system (3.26) is reformulated in the matrix form

$$\mathbf{A}_I \bar{\mathbf{p}}_I = \mathbf{B}_I \mathbf{p}_I, \quad \mathbf{A} \in \mathcal{R}^{4 \times 4}, \quad \mathbf{B} \in \mathcal{R}^{4 \times 4}. \tag{3.29}$$

Inserting Equation (3.29) into Equation (3.1.1) yields:

$$\mathbf{f}_I = (\mathbf{C}_I \mathbf{A}_I^{-1} \mathbf{B}_I - \mathbf{D}_I) \mathbf{p}_I, \tag{3.30}$$

provided that \mathbf{A} is invertible (non-singular). In the case of one-phase flow this can be assumed as long as \mathbf{K} is no zero matrix. The comparison of Equations (3.1.1) and (3.27) gives an expression for the transmissibility matrix of interaction volume I as:

$$\mathbf{T}_I = \mathbf{C}_I \mathbf{A}_I^{-1} \mathbf{B}_I - \mathbf{D}_I. \tag{3.31}$$

For a detailed introduction and derivation of a MPFA-O method and the coefficient matrices \mathbf{A} , \mathbf{B} , \mathbf{C} and \mathbf{D} see, for example, *Aavatsmark* (2002); *Aavatsmark and Eigestad* (2006); *Eigestad and Klausen* (2005).

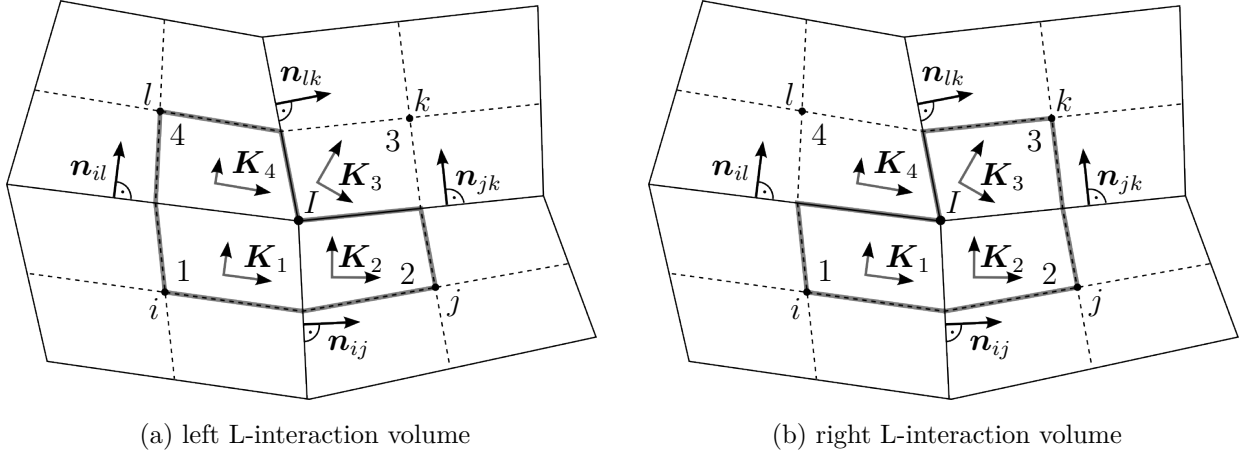


Figure 3.5: Sub-control-volumes (dashed and solid black lines) and interaction volumes (bold line) for the approximation of the flux across the interface 12 (half face between i and j)

3.1.2 The L-Method

In comparison with the O-method, in which only one interaction volume for all fluxes across the half faces adjacent to a vertex is constructed, the L-method applies a separate interaction volume to each flux face (half face). In two space dimensions this interaction volumes are L-shaped. For each flux interface there exist two possibilities to construct the interaction volume, either by a left L, or by a right (mirrored) L. For the flux interface 12 the possible L-stencils are shown in Figure 3.5. We consider the interaction volume for the flux through interface 12 (bold line) consisting of three of the sub-control-volumes 1, 2, 3, or 4 of the surrounding cells i , j , k , and l . As for the O-method the previously introduced linear pressure approximation in the sub-control-volumes of the interaction volume is applied. However, for the boarder cells (2 and 4 (left L) or 1 and 3 (right L)) one pressure continuity point is missing compared to the O-method (23 and 34 (left L) or 34 and 41 (right L)). Thus, a new continuity point is defined at the position of the central vertex I . In the following, only the flux approximation using the left L-interaction-volume is described, which can be directly transferred to right L (for more details, see *Aavatsmark et al.*, 2008). The one-phase Darcy-flux between the sub-control-volumes 1 and 2 (over the half face between i and j) can now be written as:

$$\mathbf{f}_{12} \approx \frac{-\Gamma_{ij} \mathbf{n}_{ij}^T \mathbf{K}_i}{T_1} [\boldsymbol{\nu}_{12} (\bar{p}_{12} - p_i) + \boldsymbol{\nu}_{14} (\bar{p}_{14} - p_i)] \quad (3.32)$$

where \bar{p}_{12} and \bar{p}_{14} are the pressures at the continuity points (\mathbf{x}_1 and \mathbf{x}_2 in Figure 3.2a) and Γ_{ij} is the area of the sub-interface between cell i and j . The conservation of fluxes requires that $\mathbf{f}_{12} \stackrel{!}{=} \mathbf{f}_{21}$:

$$\begin{aligned} & \frac{-\Gamma_{ij} \mathbf{n}_{ij}^T \mathbf{K}_i}{T_1} [\boldsymbol{\nu}_{12} (\bar{p}_{12} - p_i) + \boldsymbol{\nu}_{14} (\bar{p}_{14} - p_i)] \\ & \stackrel{!}{=} \frac{\Gamma_{ij} \mathbf{n}_{ij}^T \mathbf{K}_j}{T_2} [\boldsymbol{\nu}_{21} (\bar{p}_{21} - p_j) + \boldsymbol{\nu}_{2I} (\bar{p}_I - p_j)]. \end{aligned} \quad (3.33)$$

A similar expression can be written for the flux through interface 14 yielding the system of equations:

$$\begin{aligned} \mathbf{f}_{12} &= \mathbf{f}_{21} \\ \mathbf{f}_{41} &= \mathbf{f}_{14}. \end{aligned} \quad (3.34)$$

The condition of a pressure continuity at the continuity points allows to reduce the number of pressure unknowns by two:

$$\begin{aligned} \bar{p}_{12} &= \bar{p}_{21} = \bar{p}_1, \\ \bar{p}_{41} &= \bar{p}_{14} = \bar{p}_2. \end{aligned} \quad (3.35)$$

To eliminate the additional unknown p_I it can be substituted by the linear pressure variation of sub-control-volume 1:

$$\bar{p}_I = (\nabla p)_1 \cdot \mathbf{r} + p_i = r_1(\bar{p}_1 - p_i) + r_2(\bar{p}_2 - p_i) + p_i, \quad (3.36)$$

with $r_1 = (\boldsymbol{\nu}_{12}^T \cdot \mathbf{r})/T_1$, $r_2 = (\boldsymbol{\nu}_{14}^T \cdot \mathbf{r})/T_1$, and $\mathbf{r} = (\bar{\mathbf{x}}_I - \mathbf{x}_i)$. The additional continuity point at vertex I leads to two pressure continuity points per flux face. As the pressure approximation is linear this results in a pressure continuity for the complete flux face, in contrast to the O-method, which only forces continuity at the midpoints of the cell faces. Inserting Equations (3.35) and (3.36) into Equation (3.34), a transmissibility matrix \mathbf{T}_I can be constructed similar to the O-method. First, the left-hand side of system (3.34) is reformulated in the matrix form:

$$\mathbf{f}_I = \mathbf{C}_I \bar{\mathbf{p}}_I - \mathbf{D}_I \mathbf{p}_I, \quad \mathbf{C} \in \mathcal{R}^{2 \times 2}, \quad \mathbf{D} \in \mathcal{R}^{3 \times 2} \quad (3.37)$$

where \mathbf{f}_I includes the fluxes over the half edges inside the interaction volume, the vector $\mathbf{p}_I = (p_i, p_j, p_l)^T$ the cell pressures of the three finite volume cells and $\bar{\mathbf{p}}_I = (\bar{p}_1, \bar{p}_2)^T$

the pressures at the continuity points. Second, the whole system (3.34) is rewritten in matrix form:

$$\mathbf{A}_I \bar{\mathbf{p}}_I = \mathbf{B}_I \mathbf{p}_I, \quad \mathbf{A} \in \mathcal{R}^{2 \times 2}, \quad \mathbf{B} \in \mathcal{R}^{3 \times 2}. \quad (3.38)$$

Inserting Equation (3.38) into Equation (3.1.2) the pressure unknowns at the continuity points can be eliminated yielding the flux expression:

$$\mathbf{f}_I = (\mathbf{C}_I \mathbf{A}_I^{-1} \mathbf{B}_I - \mathbf{D}_I) \mathbf{p}_I. \quad (3.39)$$

This reformulation includes the assumption that \mathbf{A} is non-singular and invertible. In case of one-phase flow this is usually the case if \mathbf{K} is no zero matrix. If the transmissibility matrix is defined as:

$$\mathbf{T}_I = \mathbf{C}_I \mathbf{A}_I^{-1} \mathbf{B}_I - \mathbf{D}_I, \quad (3.40)$$

the fluxes through the two half faces of the interaction volume can be finally calculated as:

$$\mathbf{f}_I = \mathbf{T}_I \mathbf{p}_I. \quad (3.41)$$

For more details and the definitions of the coefficient matrices \mathbf{A} , \mathbf{B} , \mathbf{C} and \mathbf{D} see *Aavatsmark et al.* (2008). The O-method always results in a nine-cell-stencil in the two-dimensional case. The stencil of the L-method is more flexible. For each of the eight half faces of a cell of a quadrilateral grid one of the two L-shapes has to be chosen. Thus, a crucial point of the L-method is the selection of the L (left or right in 2-d) depending on effects such as anisotropy or unregular grid shapes. However, this implies that the choice between the two cases can be made a priori. *Aavatsmark et al.* (2008) suggest the following criterion for choosing the interaction volume used for the flux face 12 in Figure 3.5:

$$\mathbf{T}_{12} = \begin{cases} \mathbf{T}_{L12}, & \text{if } |t_{L12i}| < |t_{R12j}| \\ \mathbf{T}_{R12}, & \text{else} \end{cases} \quad (3.42)$$

In Equation (3.42) \mathbf{T}_{L12} is the transmissibility from the left L-interaction-volume, \mathbf{T}_{R12} from the right L-interaction-volume, and t_{L12i} and t_{R12j} are the corresponding transmissibility coefficients for the flux across face 12 resulting from pressure p_i and p_j . A similar criterion is proposed in *Aavatsmark et al.* (2010) as

$$\mathbf{T}_{12} = \begin{cases} \mathbf{T}_{L12}, & \text{if } s_{L12} < s_{R12} \\ \mathbf{T}_{R12}, & \text{else} \end{cases} \quad (3.43)$$

where $s_I = |t_i - t_j|$. Both criteria are based on the same idea: considering a certain flux face on a regular grid all transmissibility coefficients of cells located at one side of this flux face should have the same sign, leading to fluxes in the same direction. All transmissibility coefficients on the other side should have the opposite sign. The criteria in Equations (3.42) and (3.43) should lead to the L-shape with the highest probability of satisfying this sign property. A more detailed discussion and analysis of the criteria and the sign property can be found in *Aavatsmark et al. (2008)* and *Aavatsmark et al. (2010)*.

3.1.3 The L-Method in Three Dimensions

The basic idea of the MPFA L-method is introduced in Section 3.1.2 for the two-dimensional case. The extension to three dimensions is not straight forward as more than two L-like shapes are possible. The three-dimensional MPFA L-scheme has been introduced in *Aavatsmark et al. (2010)*. In *Wolff et al. (2013a)* it is explained and analyzed in more detail and extended to two-phase flow. As done before for the two-dimensional case, the basic scheme is explained for the second-order elliptic equation given by Darcy's law for one-phase flow.

In case of three space dimensions the L-stencils consist of four cells instead of three in the two-dimensional case. The shape is no longer a real L, but it is still called L-shape. In three space dimensions four possible L-stencils for calculating the numerical fluxes through each sub-interface inside the domain can be identified. Figure 3.6 shows the four possibilities corresponding to the sub-interface $\bar{\mathbf{x}}_1\bar{\mathbf{x}}_4\bar{\mathbf{x}}_0\bar{\mathbf{x}}_5$. The stencils (a) and (b) in the respective subfigures are centered L-stencils, which have a center cell interacting with the other three cells, and the stencils (c) and (d) are named non-centered L-stencils (see *Aavatsmark et al., 2010*).

In the following, the flux calculation through the sub-interface $\bar{\mathbf{x}}_1\bar{\mathbf{x}}_4\bar{\mathbf{x}}_0\bar{\mathbf{x}}_5$ is described. For each sub-volume, e.g. $\mathbf{x}_1\bar{\mathbf{x}}_1\bar{\mathbf{x}}_4\bar{\mathbf{x}}_2\bar{\mathbf{x}}_3\bar{\mathbf{x}}_5\bar{\mathbf{x}}_0\bar{\mathbf{x}}_6$ in the L-stencil (a), a linear pressure approximation with the continuity points describing a tetrahedron (Figure 3.2b) is applied. Referring to Figure 3.6a, the tetrahedra $\bar{\mathbf{x}}_1\bar{\mathbf{x}}_2\bar{\mathbf{x}}_3\mathbf{x}_1$, $\bar{\mathbf{x}}_1\bar{\mathbf{x}}_4\bar{\mathbf{x}}_5\mathbf{x}_2$, $\bar{\mathbf{x}}_2\bar{\mathbf{x}}_4\bar{\mathbf{x}}_6\mathbf{x}_3$ and $\bar{\mathbf{x}}_3\bar{\mathbf{x}}_5\bar{\mathbf{x}}_6\mathbf{x}_5$ are used for the pressure approximation.

The continuity of fluxes through the 3 sub-interfaces $\bar{\mathbf{x}}_1\bar{\mathbf{x}}_4\bar{\mathbf{x}}_0\bar{\mathbf{x}}_5$, $\bar{\mathbf{x}}_2\bar{\mathbf{x}}_4\bar{\mathbf{x}}_0\bar{\mathbf{x}}_6$ and $\bar{\mathbf{x}}_3\bar{\mathbf{x}}_5\bar{\mathbf{x}}_0\bar{\mathbf{x}}_6$

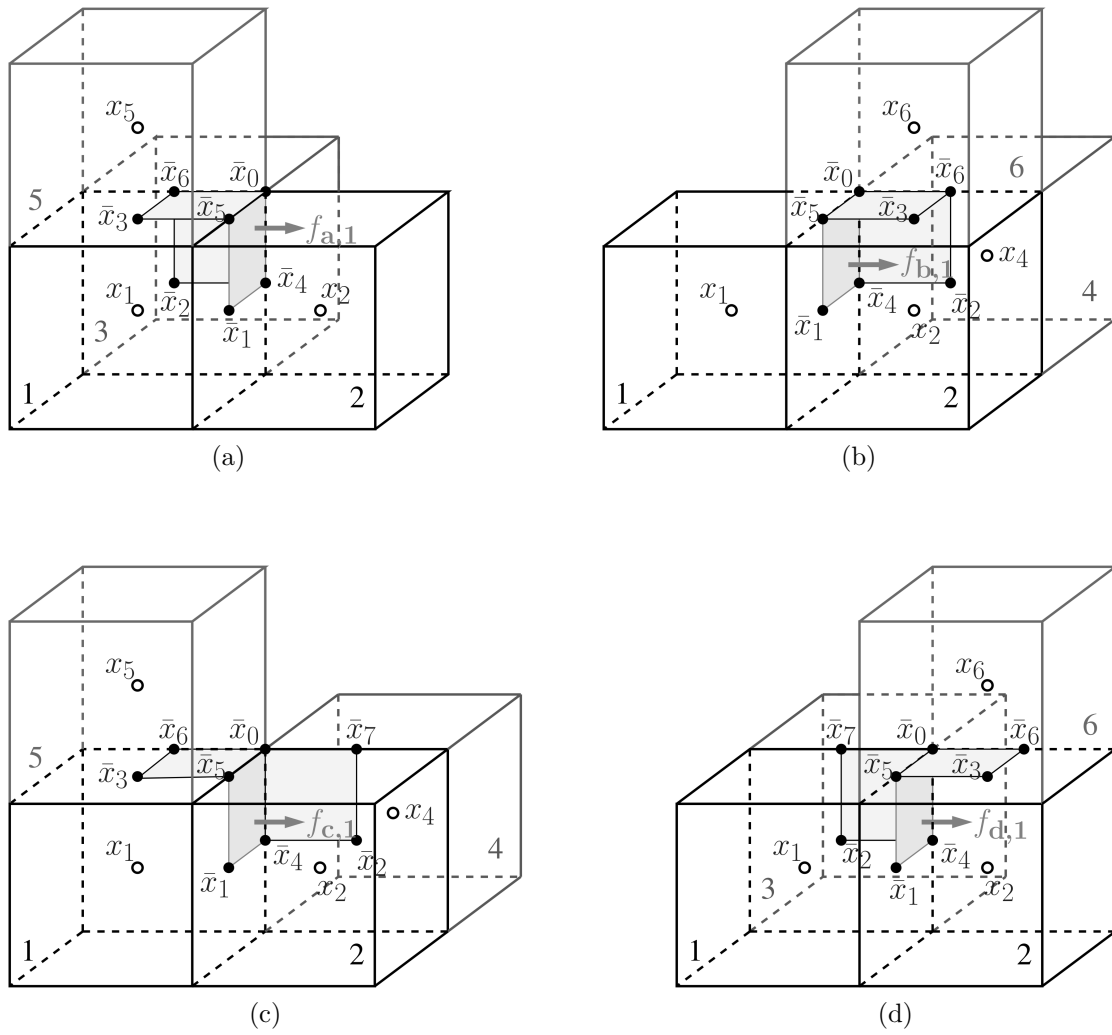


Figure 3.6: Four L-stencils for the flux calculation through sub-interface $\bar{x}_1\bar{x}_4\bar{x}_0\bar{x}_5$.

inside the L-stencil (a) gives the system of equations:

$$\begin{aligned}
-\Gamma_1 \mathbf{n}_1^T \mathbf{K}_1 \nabla p_1 &= -\Gamma_1 \mathbf{n}_1^T \mathbf{K}_2 \nabla p_2 \\
-\Gamma_2 \mathbf{n}_2^T \mathbf{K}_1 \nabla p_1 &= -\Gamma_2 \mathbf{n}_2^T \mathbf{K}_3 \nabla p_3 \\
-\Gamma_3 \mathbf{n}_3^T \mathbf{K}_1 \nabla p_1 &= -\Gamma_3 \mathbf{n}_3^T \mathbf{K}_5 \nabla p_5
\end{aligned} \tag{3.44}$$

where \mathbf{n}_i , $i = 1, 2, 3$, are the unit normal vectors of the three sub-interfaces, Γ is the sub-interface area, and \mathbf{K}_j , $j = 1, 2, 3, 5$, are the permeabilities of the four interacting cells. The pressure gradients in Equation (3.44) are defined by Equation (3.21). The three pressures at the continuity points of each sub-control-volume are written as \bar{p}_{ij} where i is the cell index and j the index in the sub-control-volume. For the particular case of L-stencil (a), the pressure continuity condition allows to define the pressures at the continuity points $\bar{\mathbf{x}}_1$ - $\bar{\mathbf{x}}_6$ as:

$$\begin{aligned}
\bar{p}_{11} &= \bar{p}_1, \quad \bar{p}_{12} = \bar{p}_2, \quad \bar{p}_{13} = \bar{p}_3 \\
\bar{p}_{21} &= \bar{p}_4, \quad \bar{p}_{22} = \bar{p}_1, \quad \bar{p}_{23} = \bar{p}_5 \\
\bar{p}_{31} &= \bar{p}_2, \quad \bar{p}_{32} = \bar{p}_4, \quad \bar{p}_{33} = \bar{p}_6 \\
\bar{p}_{51} &= \bar{p}_6, \quad \bar{p}_{52} = \bar{p}_5, \quad \bar{p}_{53} = \bar{p}_3.
\end{aligned} \tag{3.45}$$

Similar to the two-dimensional case the additional unknowns \bar{p}_4 , \bar{p}_5 , and \bar{p}_6 at the edge centers are eliminated by using the linear pressure variation of the interacting cell 1. From Equation (3.9) we get:

$$\bar{p}_4 = (\nabla p)_1 \cdot (\bar{\mathbf{x}}_4 - \mathbf{x}_1) + p_1 \tag{3.46}$$

$$\bar{p}_5 = (\nabla p)_1 \cdot (\bar{\mathbf{x}}_5 - \mathbf{x}_1) + p_1 \tag{3.47}$$

$$\bar{p}_6 = (\nabla p)_1 \cdot (\bar{\mathbf{x}}_6 - \mathbf{x}_1) + p_1. \tag{3.48}$$

Inserting Equation (3.21) yields:

$$\bar{p}_4 = r_{111}(\bar{p}_{11} - p_1) + r_{121}(\bar{p}_{12} - p_1) + r_{131}(\bar{p}_{13} - p_1) + p_1 \tag{3.49}$$

$$\bar{p}_5 = r_{112}(\bar{p}_{11} - p_1) + r_{122}(\bar{p}_{12} - p_1) + r_{132}(\bar{p}_{13} - p_1) + p_1 \tag{3.50}$$

$$\bar{p}_6 = r_{113}(\bar{p}_{11} - p_1) + r_{123}(\bar{p}_{12} - p_1) + r_{133}(\bar{p}_{13} - p_1) + p_1, \tag{3.51}$$

with $r_{1jk} = \boldsymbol{\nu}_{1j}^T \mathbf{r}_k / T_1$, $i, j = 1, 2, 3$ and $\mathbf{r}_k = \bar{\mathbf{x}}_{3+k} - \mathbf{x}_1$, $k = 1, 2, 3$, the normals $\boldsymbol{\nu}_{1j}$ defined in Equation (3.19) and the coefficient T_1 defined in Equation (3.20).

Inserting Equations (3.45) and (3.49) into the system of flux continuity (Equation (3.44)), the fluxes through the sub-interfaces of L-stencil (a) are only expressed using the pressures at the points $\bar{\mathbf{x}}_1$, $\bar{\mathbf{x}}_2$ and $\bar{\mathbf{x}}_3$, and at the cell centers \mathbf{x}_1 , \mathbf{x}_2 , \mathbf{x}_3 and \mathbf{x}_5 . Like in the two-dimensional case, the left-hand side of system (3.44) can be reformulated in the matrix form:

$$\mathbf{f}_a = \mathbf{C}_a \bar{\mathbf{p}}_a - \mathbf{D}_a \mathbf{p}_a, \quad \mathbf{C} \in \mathcal{R}^{3 \times 3}, \quad \mathbf{D} \in \mathcal{R}^{3 \times 4} \quad (3.52)$$

where \mathbf{f}_a includes the fluxes over the sub-interfaces inside the interaction volume, the vector $\mathbf{p}_a = (p_1, p_2, p_3, p_5)^T$ the cell pressures of the four finite volume cells and $\bar{\mathbf{p}}_a = (\bar{p}_1, \bar{p}_2, \bar{p}_3)^T$ the pressures at the continuity points. Moreover, the system (3.44) can be rewritten in matrix form as:

$$\mathbf{A}_a \bar{\mathbf{p}}_a = \mathbf{B}_a \mathbf{p}_a, \quad \mathbf{A} \in \mathcal{R}^{3 \times 3}, \quad \mathbf{B} \in \mathcal{R}^{3 \times 4}. \quad (3.53)$$

Inserting Equation (3.53) into Equation (3.1.3), the pressure unknowns at the continuity points can be eliminated yielding the flux expression:

$$\mathbf{f}_a = (\mathbf{C}_a \mathbf{A}_a^{-1} \mathbf{B}_a - \mathbf{D}_a) \mathbf{p}_a, \quad (3.54)$$

provided that the matrix \mathbf{A} is non-singular. In case of one-phase flow this is usually the case if \mathbf{K} is no zero matrix. Additionally, monotonicity of the method ensures that the matrix \mathbf{A} is regular. However, analysis of monotonicity for the three-dimensional case still is a topic of ongoing research. If the transmissibility matrix is defined as:

$$\mathbf{T}_a = \mathbf{C}_a \mathbf{A}_a^{-1} \mathbf{B}_a - \mathbf{D}_a, \quad (3.55)$$

the fluxes through the sub-interfaces of the interaction volume can be finally calculated as:

$$\mathbf{f}_a = \mathbf{T}_a \mathbf{p}_a. \quad (3.56)$$

Due to the similarity, the derivations of the transmissibility matrices \mathbf{T}_b , \mathbf{T}_c , \mathbf{T}_d are omitted. For more details and the definitions of the coefficient matrices \mathbf{A} , \mathbf{B} , \mathbf{C} and \mathbf{D} see *Wolff et al.* (2013a).

As already explained for the two-dimensional case, criteria are necessary to decide which L-stencil should be chosen. In principle, the criteria for the three-dimensional case do not differ from those introduced in Section 3.1.2. However, tests of the method on complex problem setups showed that the selection criteria proposed in *Aavatsmark et al.* (2008)

and *Aavatsmark et al.* (2010) can lead to unstable non-monotonous solutions in three dimensions (*Wolff et al.*, 2013a). Thus, a new criterion is proposed, which is introduced in the following section.

3.1.4 A New Criterion for Choosing the L-Stencil

The choice of a proper L-stencil for each sub-interface is crucial for the robustness of the L-method. In this context we define a method to be robust, if it provides physically meaningful solutions with an acceptable magnitude of error and for a wide spectrum of applications. As the selection of one of the four cases (see Figure 3.6) has to be made a priori, an appropriate criterion is needed. In *Aavatsmark et al.* (2008) and *Aavatsmark et al.* (2010) the sign property of the transmissibility coefficients of a L-stencil is identified to be an important criterion. Considering a certain flux face on a regular grid the idea is that all transmissibility coefficients of cells located at one side of this flux face should have the same sign, leading to fluxes in the same direction. All transmissibility coefficients on the other side should have the opposite sign. Therefore, *Aavatsmark et al.* (2010) propose to choose the L-stencil with the smallest s_I value, where

$$s_I = |\mathbf{T}_{I,11} - \mathbf{T}_{I,12}|. \quad (3.57)$$

The capital index $I = a, b, c, d$ denotes the type of the L-stencil, $\mathbf{T}_{I,1i}$ are the transmissibility coefficients of cell i for flux sub-interface 1 ($\bar{x}_1\bar{x}_4\bar{x}_0\bar{x}_5$). In *Aavatsmark et al.* (2010) the authors show that for parallelepiped grids the s_I -criterion always yields a robust L-stencil. However, for irregular grids, which are not close to \mathbf{K} -orthogonal grids, a good choice of the L-stencil is more difficult. For grids with large skewness, none of the transmissibilities of the four L-cases might fulfill the sign criterion. Especially in the three-dimensional case, it is not obvious if the smallest s_I value also leads to the most robust stencil.

In *Wolff et al.* (2013a) a convergence study is presented in which the MPFA L-method is tested on two test cases and different grids of the benchmark session of the FVCA6 conference (*Forřt et al.*, 2011). The FVCA6 examples solve the one-phase Darcy equation (Equation (2.10)) applying an anisotropic permeability. It is shown that, for grids of high skewness and anisotropic coefficients, it can occur that the s_I -criterion does not lead to proper L-stencils. This leads to non-monotonous over- and undershoots in the pressure solution. Thus, a new criterion is developed from the following ideas:

1. in the \mathbf{K} -orthogonal case the chosen transmissibility should satisfy the sign property;
2. it should include more than the two neighboring cells at the respective flux sub-interface to cover the three-dimensional behavior better;
3. it should lead to a unique flux stencil for the cases in which the sign property cannot give a unique choice.

We propose to choose the L-stencil with the largest \bar{t}_I value where

$$\begin{aligned}
 \bar{t}_a &= |\mathbf{T}_{a,11} + \mathbf{T}_{a,13} + \mathbf{T}_{a,15}| \\
 \bar{t}_b &= |\mathbf{T}_{b,12} + \mathbf{T}_{b,14} + \mathbf{T}_{b,16}| \\
 \bar{t}_c &= |\mathbf{T}_{c,11} + \mathbf{T}_{c,15}| \\
 \bar{t}_d &= |\mathbf{T}_{d,11} + \mathbf{T}_{d,13}|.
 \end{aligned} \tag{3.58}$$

On the one hand, the $\mathbf{T}_{I,li}$ in (3.58) tend to have the same sign if the absolute of their sum is larger. Thus, it is more likely that the chosen transmissibility shows the expected sign property. On the other hand, the transmissibility which has the largest impact on the flux through sub-interface $\bar{x}_1\bar{x}_4\bar{x}_0\bar{x}_5$ is always preferred. This is in line with one of the basic ideas of the L-method, namely, to choose the flux stencil according to the preferred direction of flow. If the contributing cells lead to higher fluxes through a sub-interface, the orientation of the L-shape most likely is in better agreement with the direction of the streamlines. This leads to a consistent choice of the L-stencils even in the case of irregular grids with large skewness and thus increases the robustness of the MPFA L-method (see *Wolff et al.*, 2013a).

In the following, a small study analyzing the flux stencils resulting from the different selection criteria is presented. The aim is to identify possible sources of errors with regard to grid skewness. Therefore, a domain discretized by a $3 \times 3 \times 3$ parallelepiped mesh is considered. Again Equation (2.10) is solved with the homogeneous anisotropic permeability tensor

$$\mathbf{K} = \begin{pmatrix} 1 & 0.5 & 0 \\ 0.5 & 1 & 0.5 \\ 0 & 0.5 & 1 \end{pmatrix}, \tag{3.59}$$

which is visualized as ellipsoid in Figure 3.7.

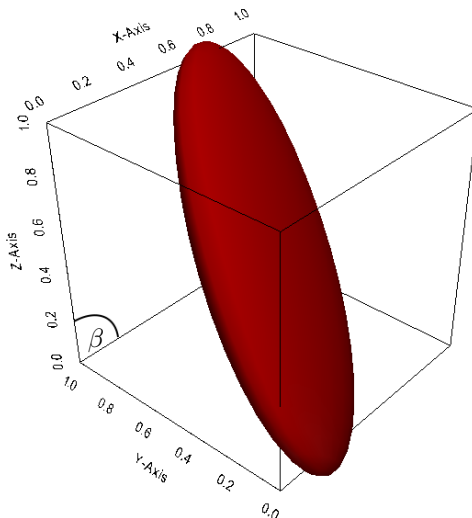


Figure 3.7: Visualization of the anisotropic permeability tensor (ellipsoid) inside the test domain.

Figure 3.8 shows the flux stencils of the center cell applying the two L-selection criteria for differently skewed grids. In case (a) with cubic cells the s_I -criterion chooses a flux stencil of minimal size that is perfectly aligned with the permeability tensor. The \bar{t}_I -criterion chooses a larger stencil which is actually the maximal L-stencil. From Figure 3.8a to 3.8d the angle β (Figure 3.7) is decreased. The stencil selected by the \bar{t}_I -criterion remains the same, whereas the stencil selected by the s_I -criterion changes. The preferred direction of the flux stencil, which results from the s_I -criterion, turns from case (a) to case (d) compared to the direction of the permeability tensor. This becomes even more obvious in a top view (Figure 3.9). For this very skewed grid with $\beta = 11.25^\circ$, the preferred direction of the chosen flux stencil is opposite to the main direction of the permeability tensor. Therefore, the stencil most likely does not lead to a meaningful flux approximation. In contrast, the flux stencil using the \bar{t}_I -criterion covers the main direction of the permeability tensor better, and thus, supports the skewed grids well. In case of the full permeability tensor applied in this test (Equation (3.59)), the \bar{t}_I -criterion always resulted in the maximal L-flux-stencil (19 cells). However, in other cases, which are not presented here, it can also lead to reduced stencils preferring certain directions.

To summarize, the s_I -criterion tends to minimize the flux stencil while the \bar{t}_I -criterion results in larger stencils. Comparing the shape of the stencils, the s_I -criterion is more selective with regard to certain directions. In the grid cells with large skewness it appears that the preferred direction of the flux stencil strongly differs from the direction of the streamlines. This also explains the large errors due to the non-monotonous solution

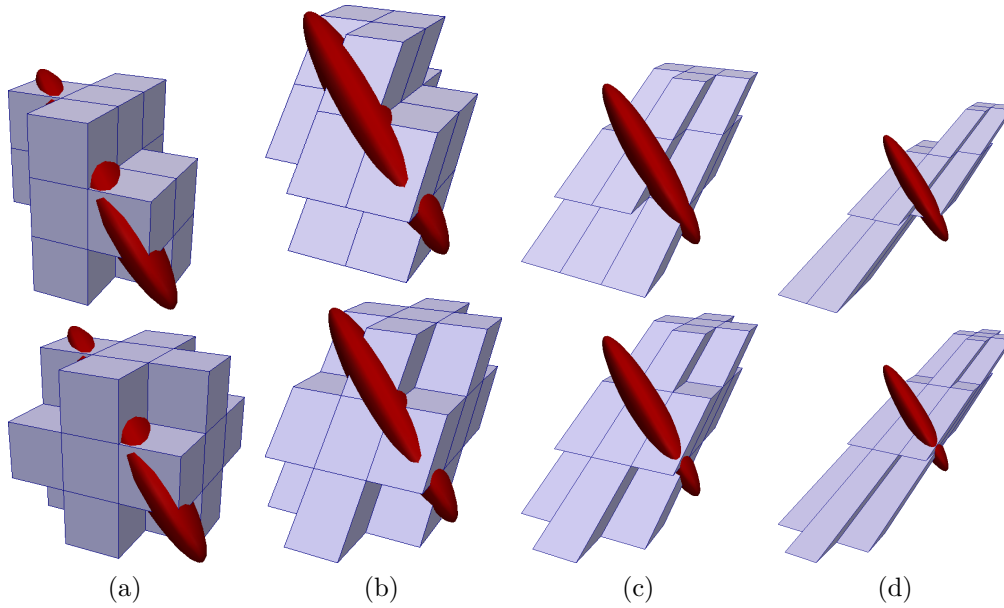


Figure 3.8: Cell stencils for differently skewed parallelepiped grids using the s_I -criterion (upper row) and the \bar{t}_I -criterion (lower row). The skewness of the grid is increased from left to right by decreasing the angle β (Figure 3.7): (a) 90° , (b) 45° , (c) 22.5° , (d) 11.25° .

shown in *Wolff et al. (2013a)*. In such cases, the cell stencil of the \bar{t}_I -criterion still leads to consistent fluxes. However, the robustness is increased at the cost of slightly larger stencils. Thus, the choice of the criterion finally has to be made depending on the problem that has to be solved.

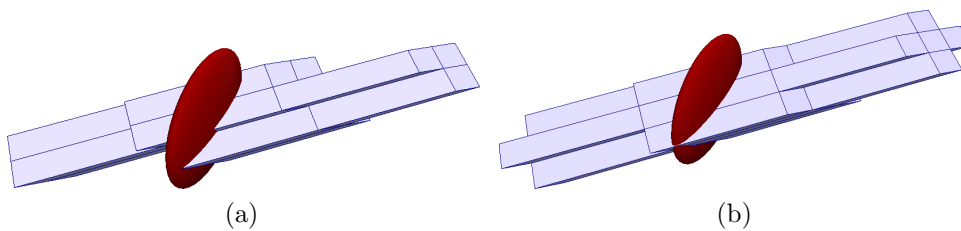


Figure 3.9: Top view on the cell stencils of the s_I -criterion (a) and the \bar{t}_I -criterion (b) for $\beta = 11.25^\circ$.

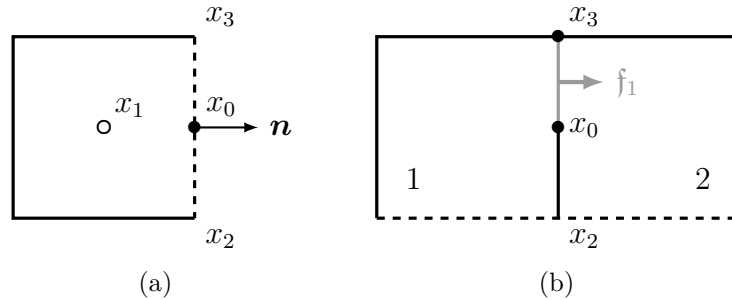


Figure 3.10: Flux calculation at boundary faces in two space dimensions: (a) flux across a boundary face; (b) flux across faces intersecting with a boundary face.

3.1.5 Boundary Handling

The implementation of boundaries is not trivial using a MPFA method. The interaction volumes around the boundary vertices can have various shapes, especially considering three space dimensions, and never consist of a full set of interaction volume cells. In previous works, the use of ghost cells is suggested for both O- and L-method (for example *Aavatsmark, 2002; Aavatsmark et al., 2008*) where often no-flow conditions are applied (*Aavatsmark et al., 1998a*). An alternative approach for the implementation of Dirichlet boundary conditions without ghost cells is introduced in *Eigestad and Klausen (2005)*. In case of the L-method, *Aavatsmark et al. (2008)* point out that for every second half edge at the boundary it is difficult to derive the fluxes in a consistent way. Therefore, the authors suggest to use the O-method at domain boundaries. In *Cao et al. (2009)* the combination of L-method and O-method at the boundaries is further investigated. A common disadvantage of all mentioned approaches is that the use of MPFA at the boundary requires many different modifications to cover all possible boundary shapes and configurations.

Instead of ghost cells or a modified MPFA, we combine TPFA at the boundaries with weighting factors to correct the fluxes along the boundary. Experience has shown that this method is still sufficiently accurate for many applications, although it is rather simple (*Wolff et al., 2013a*). Additionally, the method is very flexible and can be straightforwardly applied to complex boundary configurations and shapes and also to adaptively refined grids (see Section 3.2.1).

Figures 3.10 and 3.11 show the different types of faces at a boundary for which fluxes have to be approximated. In case (a) fluxes across the boundary faces (x_2x_3 (2-d),

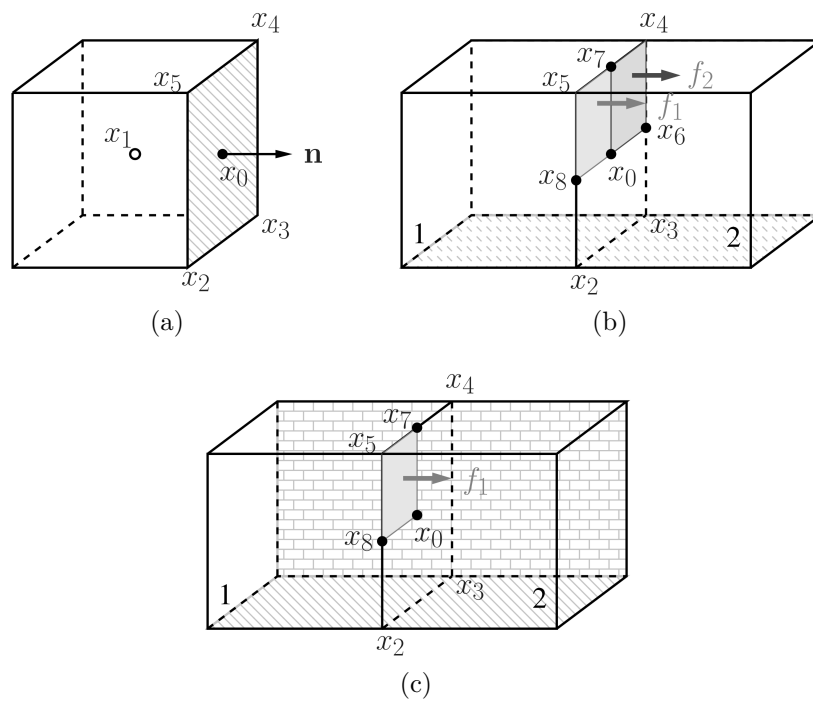


Figure 3.11: Flux calculation at boundary faces in three space dimensions: (a) flux across a boundary face; (b) flux across faces intersecting with one boundary face; (c) flux across faces intersecting with two boundary faces.

$x_2x_3x_4x_5$ (3-d)) have to be calculated. In case of Neumann boundaries the flux is directly given by the boundary condition. At Dirichlet boundaries, a two-point approximation

$$\mathbf{f}_{\text{TPFA}} = -\frac{|\mathbf{K}^T \mathbf{n}|}{|x_0 - x_1|} (p_0 - p_1) |s| \quad (3.60)$$

is used where \mathbf{n} is the unit outer normal vector of the cell face, $|\mathbf{K}^T \mathbf{n}|$ is the norm of the face permeability vector $\mathbf{K}^T \mathbf{n}$, p_0 and p_1 are the pressures at the face center x_0 and the cell center x_1 , $|x_0 - x_1|$ is the distance between the two centers, and $|s|$ is the area of the cell face. This discretization is exact for \mathbf{K} -orthogonal grids and its impact on the convergence of the whole domain is very small for non- \mathbf{K} -orthogonal grids (see *Wolff et al.*, 2013a).

Case (b) considers a cell face intersecting with one boundary face. The flux \mathbf{f}_1 through the sub-interface x_0x_3 (2-d) and $x_0x_7x_5x_8$ (3-d), and the flux \mathbf{f}_2 through the sub-interface $x_0x_6x_4x_7$ (3-d) can be calculated applying one of the MPFA schemes described before. These faces are included in full interaction volumes associated with an inner vertex (no boundary vertex). The flux through the whole cell face x_2x_3 (2-d) or $x_2x_3x_4x_5$ (3-d) is then obtained by scaling as:

$$\mathbf{f} = \begin{cases} \frac{|s|}{|s_h|} \mathbf{f}_1, & (2\text{-d}) \\ \frac{|s|}{|s_h|} (\mathbf{f}_1 + \mathbf{f}_2), & (3\text{-d}) \end{cases} \quad (3.61)$$

where the known inner fluxes are scaled with an area weighting factor, in which $|s_h|$ is the area of the half face x_0x_3 (2-d) or $x_6x_4x_5x_8$ (3-d).

In the three-dimensional case, the additional boundary face type (c) has to be considered, in which a cell face intersects two boundary faces. Similar to the previous case (b) the flux can then be approximated as

$$\mathbf{f} = \mathbf{f}_1 \frac{|s|}{|s_q|}, \quad (3.62)$$

where $|s_q|$ is the area of the face $x_0x_7x_5x_8$.

3.1.6 Extension to Two-Phase Flow

In the case of one-phase flow, the whole procedure of calculating the global transmissibility matrix can be accomplished in a single pre-processing step as the transmissibilities do

not change during the simulation. For K-orthogonal grids, the described MPFA method reduces to a TPFA with harmonic averages. However, the former can also be consistently applied to any full-tensor permeability fields on arbitrary grids. In case of two-phase flow, the approximation described for one-phase flow can be directly applied to the pressure equation of a fractional flow formulation if:

- gravity and capillary pressure are neglected (Equation (2.35));
- capillary pressure is neglected and a potential formulation is chosen (Equation (2.39));
- gravity is neglected and a global pressure formulation is chosen (Equation (2.45)).

Assuming scalar relative permeabilities, which are constant along the cell faces, such simplified two-phase pressure equations have a similar character than the one-phase pressure equation (*Aavatsmark et al.*, 1996; *Aavatsmark*, 2002). However, for more complex cases modifications are necessary. In the following, the MPFA method is extended for the full wetting phase potential equation (Equation (2.39)). This formulation has the advantage that gravity can be easily included and, compared to the global pressure, the potential is a physical quantity, which can be directly interpreted.

From Equations (2.41) and (2.23) the flux functions in Equations (3.5) and (3.4) are defined as:

$$\mathbf{f}_{\text{aw}} = (-\lambda_t \mathbf{K} \nabla \Phi_w) \cdot \mathbf{n} A \quad (3.63)$$

$$\mathbf{f}_c = (-f_n \lambda_t \mathbf{K} \nabla \Phi_c) \cdot \mathbf{n} A \quad (3.64)$$

$$\mathbf{f}_w = (-f_w \lambda_t \mathbf{K} \nabla \Phi_w) \cdot \mathbf{n} A \quad (3.65)$$

where A is the area of a flux face. Writing the flux terms as in Equations (3.63) to (3.65) shows that the term $-\lambda_t \mathbf{K} \nabla$ appears in all three terms. If a MPFA-operator \mathbf{T}_t is defined which approximates $-\lambda_t \mathbf{K} \nabla$ the flux functions for an interaction volume can be written as:

$$\mathbf{f}_{\text{aw}} = \mathbf{T}_t \Phi_w \quad (3.66)$$

$$\mathbf{f}_c = \mathbf{f}_n (\mathbf{T}_t \Phi_c) \quad (3.67)$$

$$\mathbf{f}_w = \mathbf{f}_w (\mathbf{T}_t \Phi_w) \quad (3.68)$$

where \mathbf{f}_{aw} , \mathbf{f}_c and \mathbf{f}_w are the vectors of the fluxes through the half faces in the interaction volume, \mathbf{f}_w and \mathbf{f}_n are the vectors of the fractional flow functions at the flux faces, and

Φ_w and Φ_c are the vectors of the wetting phase and capillary pressure potentials at the adjacent cell centers. Referring to Equation (3.24), the flux balance for face 12 in Figure 3.4 using the O-method is extended to:

$$\begin{aligned} & \frac{-\Gamma_{ij} \mathbf{n}_{ij}^T \lambda_{ti} \mathbf{K}_i}{T_1} [\boldsymbol{\nu}_{12} (\bar{\Phi}_{12} - \Phi_i) + \boldsymbol{\nu}_{14} (\bar{\Phi}_{14} - \Phi_i)] \\ &= \frac{\Gamma_{ij} \mathbf{n}_{ij}^T \lambda_{tj} \mathbf{K}_j}{T_2} [\boldsymbol{\nu}_{21} (\bar{\Phi}_{21} - \Phi_j) + \boldsymbol{\nu}_{23} (\bar{\Phi}_{23} - \Phi_j)]. \end{aligned} \quad (3.69)$$

For the L-method a similar extension of Equation (3.33) leads to the flux continuity

$$\begin{aligned} & \frac{-\Gamma_{ij} \mathbf{n}_{ij}^T \lambda_{ti} \mathbf{K}_i}{T_1} [\boldsymbol{\nu}_{12} (\bar{p}_{12} - p_i) + \boldsymbol{\nu}_{14} (\bar{p}_{14} - p_i)] \\ & \stackrel{!}{=} \frac{\Gamma_{ij} \mathbf{n}_{ij}^T \lambda_{tj} \mathbf{K}_j}{T_2} [\boldsymbol{\nu}_{21} (\bar{p}_{21} - p_j) + \boldsymbol{\nu}_{2I} (\bar{p}_I - p_j)] \end{aligned} \quad (3.70)$$

for face 12 in Figure 3.5.

Applying this extension to all face fluxes in the interaction volume and inserting them into the system of Equations (3.26) or (3.34), \mathbf{T}_{tI} can be obtained similarly as:

$$\mathbf{T}_{tI} = \mathbf{C}_{tI} \mathbf{A}_{tI}^{-1} \mathbf{B}_{tI} - \mathbf{D}_{tI}. \quad (3.71)$$

A general disadvantage of the described transmissibility calculation is that the matrix \mathbf{A} has to be invertible. Thus, additional modifications are necessary to get a transmissibility matrix if a flux across an interface becomes zero and hence \mathbf{A} becomes singular (*Aavatsmark et al.*, 1998c; *Aavatsmark*, 2002). Zero-flux-faces can occur if coefficients which enter the flux calculation become zero (e.g. permeability). Zero absolute permeabilities usually occur rarely. Two-phase properties like phase mobilities, however, become zero whenever a phase is not present. Thus, the proposed method includes only the total mobility, which is always defined and greater than zero, into the transmissibility calculation (Equations (3.63)-(3.68)). Besides the non-singularity of \mathbf{A} , a second advantage of this choice is a gain in efficiency. Instead of calculating three transmissibilities, one for the total flux, one for the wetting phase flux and one for the non-wetting phase flux, the computationally expansive calculation only has to be performed once to get \mathbf{T}_{tI} . Although this flux approximation is different to one including all coefficients into the transmissibility matrix the error is justifiable compared to the aforementioned advantages. The diffusive pressure (potential) term (Equation (3.66)) is well approximated. The capillary potential term (Equation (3.67)) as well as the wetting

phase flux term (Equation (3.68)) are of parabolic character and strongly dependent on the transported variable, namely the saturation. Thus, it is reasonable that the direct influence of the strongly saturation dependent coefficients is limited to one flux face instead of all faces via the transmissibility. However, in order to get conservative fluxes and to preserve the hyperbolic character an upwinding scheme is applied. For the flux interface between sub-control-volumes 1 and 2 this results in the fluxes:

$$\mathbf{f}_{c12} = f_{n12}^{\text{upw}} \mathbf{f}_{tc12} = \mathbf{f}_{c21} \quad (3.72)$$

$$\mathbf{f}_{w12} = f_{w12}^{\text{upw}} \mathbf{f}_{t12} = \mathbf{f}_{w21} \quad (3.73)$$

where $\mathbf{f}_{tc12} = (\mathbf{T}_{tI} \Phi_{cI})_{12}$ and $\mathbf{f}_{t12} = (\mathbf{T}_{tI} \Phi_{wI})_{12}$ and

$$f_{\alpha 12} = \begin{cases} f_{\alpha i}, & \text{if } \mathbf{f}_{\alpha 12} \geq 0 \\ f_{\alpha j}, & \text{else} \end{cases} \quad (3.74)$$

3.1.7 Tests

The numerical methods described in this section and their implementation in DuMu^x are tested by simulating three different test cases. In the case of two-phase flow, the correct and conservative transport of phases, described by the parabolic saturation transport equation, is important. Therefore, physical features like saturation discontinuities at fluid fronts or at heterogeneous material interfaces have to be reproduced by the numerical scheme as well as the diffusive character of fluxes driven by a capillary pressure gradient. The test cases are the Buckley-Leverett problem (advection dominated, (*Buckley and Leverett*, 1942)), the McWhorter problem (capillary diffusion dominated, (*McWhorter and Sunada*, 1990)), and the setup of *Helmig and Huber* (1998) (focus on capillary pressure heterogeneity). In all test cases, an IMPES scheme (e.g. *Aziz and Settari*, 1979) is applied where the stability of the scheme is guaranteed by the time-step condition of *Coats* (2003).

Buckley-Leverett Problem

The setup of the Buckley-Leverett problem is shown in Figure 3.12. The domain with the size of $30 \times 6 \times 3$ meters (30×3 meters in 2-d) has a constant porosity, a constant permeability ($\phi = 0.2$; $\mathbf{K} = k\mathbf{I}$, where $k = 10^{-7}$ m², \mathbf{I} is the identity matrix) and

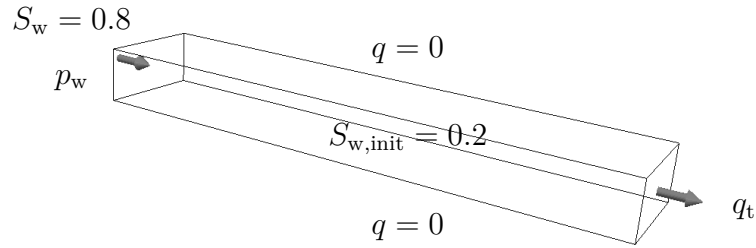


Figure 3.12: Setup of the Buckley-Leverett problem. The arrows mark the wetting fluid inflow and the non-wetting fluid outflow.

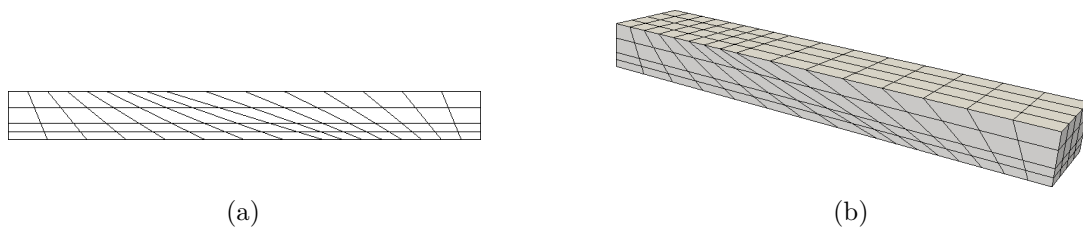


Figure 3.13: Simulation grid of level 1 in the two-dimensional case (a) (64 cells) and in the three-dimensional case (b) (256 cells) of the Buckley-Leverett problem.

is initially saturated by a non-wetting fluid. From one side a wetting fluid is injected and displaces the non-wetting fluid. The outflow boundary condition is set to q_t with $v_t = 3 \times 10^{-6}$ m/s. Both fluids have the same fluid properties. The relative permeabilities are calculated using the Brooks-Corey parameterization (*Brooks and Corey, 1964*) with $\lambda = 2.0$ and residual saturations $S_{wr} = S_{nr} = 0.2$. Gravity as well as capillary effects are neglected. To test the capabilities of the MPFA methods, unstructured two-dimensional as well as three-dimensional grids are used (Figure 3.13). The grids are hierarchically refined from level 1 (64 cells 2-d, 256 cells 3-d) to level 4 (4096 cells 2-d, 131072 cells 3-d) to analyze the convergence behavior of the methods. The Buckley-Leverett problem can also be solved analytically (*Buckley and Leverett, 1942; Helmig, 1997*). The analytic solution is calculated for each cell of the simulation grids and used to quantify errors of the numerical solution.

The resulting saturation distributions of the two-dimensional simulations are shown in Figure 3.14 and 3.15. The solutions of both MPFA methods (O-method Figure 3.14a, L-method Figure 3.14b) are similar and agree very well with the analytic solution in Figure 3.15a, although numerical diffusion leads to stronger smearing effects around the saturation discontinuity for the coarser grids. In comparison, a simple TPFA method is not able to sufficiently approximate the fluxes on the unstructured grid. This leads to a

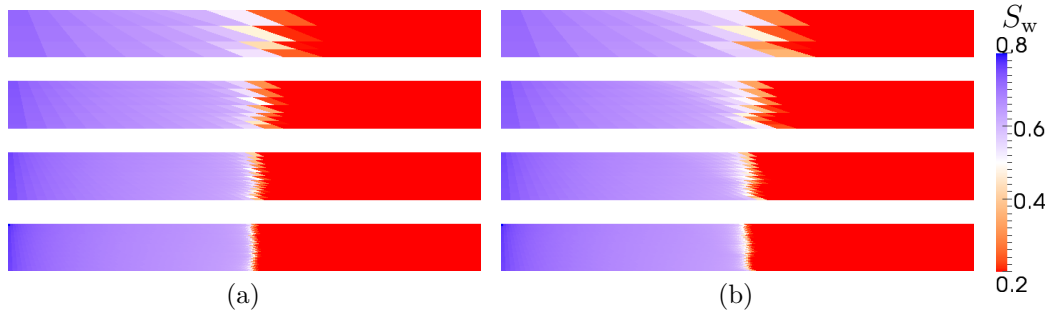


Figure 3.14: Wetting phase saturation at $t = 2 \times 10^5$ s. The results are shown for the grid levels 1-4 (top to bottom) using the MPFA O-method (a) and the MPFA L-method (b).

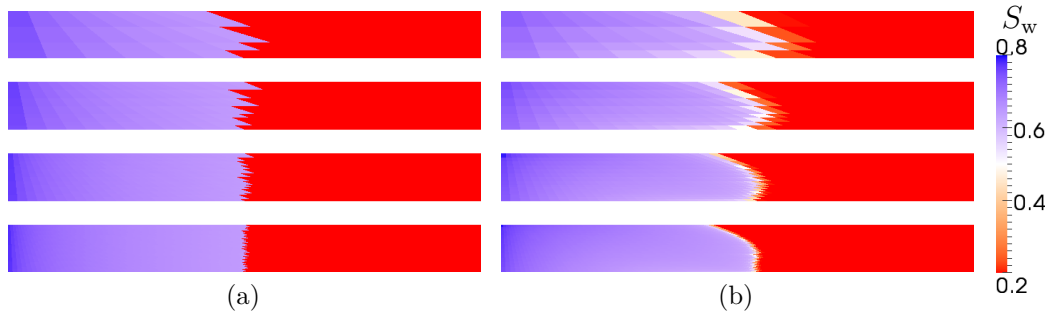


Figure 3.15: Wetting phase saturation at $t = 2 \times 10^5$ s. The results are shown for the grid levels 1-4 (top to bottom) using an analytic solution (a) and a simple TPFA model (b).

curvature of the shock front (Figure 3.15b), which does not vanish if the grid is refined.

This observation is confirmed by an analysis of the errors. In Figure 3.16 the cell saturation errors $e_{S_{wi}} = S'_{wi} - S_{wi}$ (S'_{wi} = analytic solution) are plotted. On the finest grid the error of the MPFA solutions concentrates on a very limited area around the saturation discontinuity (Figure 3.16b), while it is more distributed on the coarse grid (Figure 3.16a). The TPFA solution exhibits the largest absolute local error as well as the largest range of errors.

In Figure 3.17 the global error

$$\bar{e}_g = \frac{1}{V_\Omega^2} \sqrt{\sum_i^{n_c} V_i (S'_{wi} - S_{wi})^2} \quad (3.75)$$

is plotted over the number of cells n_c (V_Ω = volume of the area covered by the moving fluid fronts). As expected it is almost equal for O-method and L-method and considerably

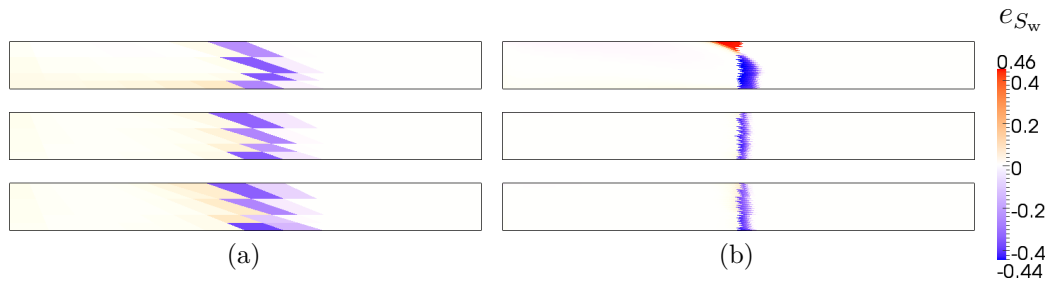


Figure 3.16: Wetting phase saturation error at $t = 2 \times 10^5$ s. From top to bottom the results are shown for TPFA, O-method, and L-method, for grid level 1 (a) and 4 (b).

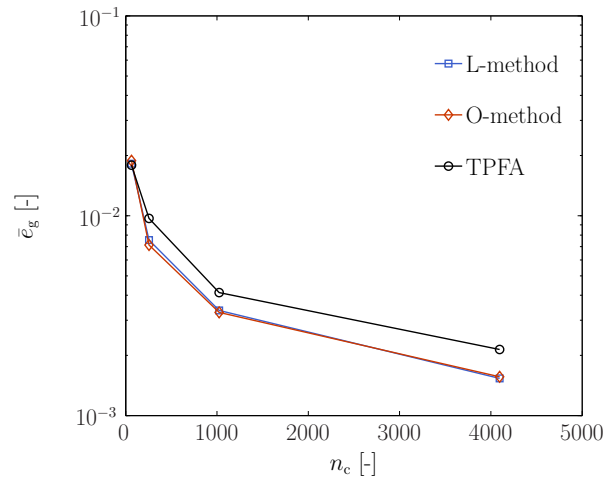


Figure 3.17: Global error of the transport solution of the Buckley-Leverett problem at $t = 2 \times 10^5$ s over the number of cells.

smaller than for the simple TPFA approach, especially for the finer grids. Further, the MPFA methods show a faster grid convergence.

The results for three-dimensional simulations using the MPFA L-method are shown in Figure 3.18. At all grid levels the saturation distributions are very similar to the two-dimensional solutions shown before. For better validation a slice of the three-dimensional solution of the level 4 grid in Figure 3.18d is compared to the two-dimensional solution of the MPFA L-method and to the analytic solution (Figure 3.19). Both L-method solutions match very well and are in good agreement with the analytic solution.

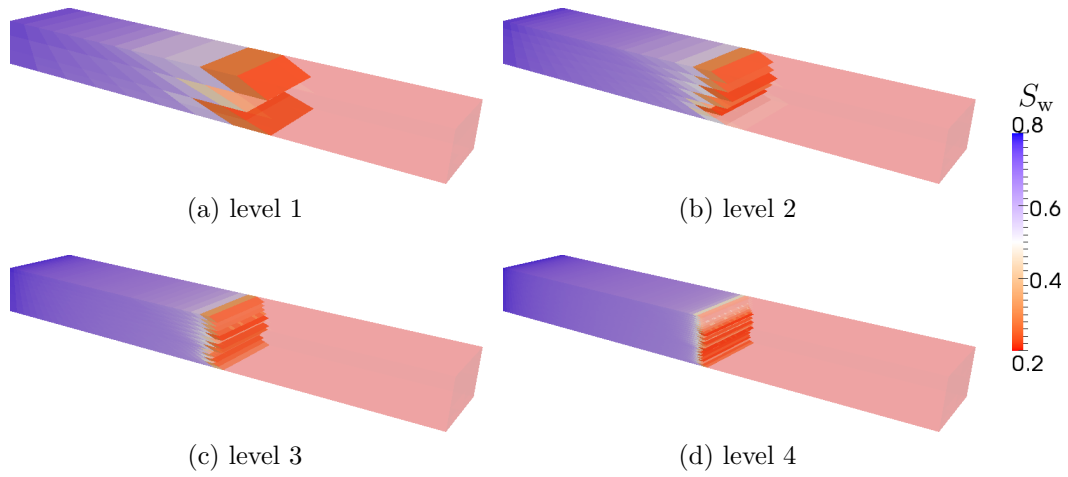


Figure 3.18: Wetting phase saturation at $t = 2 \times 10^5$ s using the 3-d MPFA L-method.

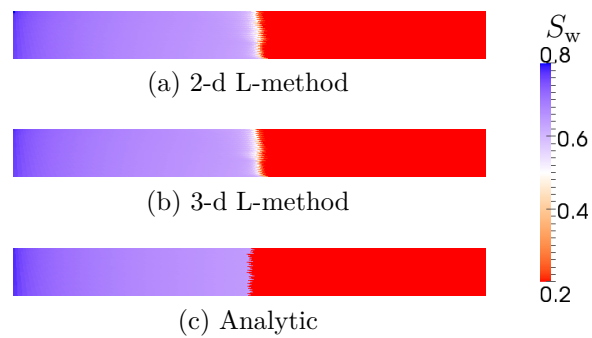


Figure 3.19: Comparison of the 2-d solution (a) and a 2-d slice of the 3-d solution (b) of the L-method with the analytic solution (c).

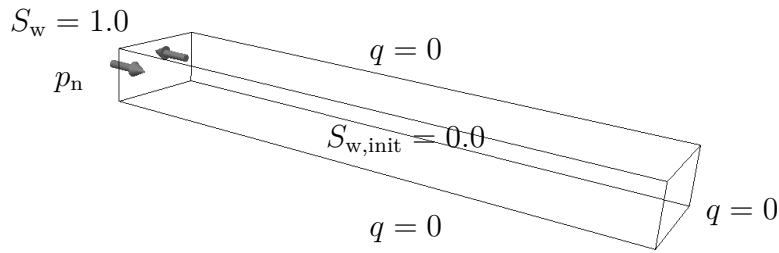


Figure 3.20: Setup of the McWhorter problem. The arrows mark the wetting fluid inflow and the non-wetting fluid outflow.

McWhorter Problem

The model domain for the McWhorter problem again has a size of $30 \times 6 \times 3$ meters (30×3 meters in 2-d), and is initially fully saturated by a non-wetting fluid (Figure 3.20). All boundaries except one are no flow boundaries. The open boundary is a contact area between the non-wetting fluid inside the domain and a wetting fluid outside the domain. Due to the capillary-pressure gradient, counter-current flow develops. Porosity as well as permeability are constant ($\phi = 0.3$; $\mathbf{K} = k\mathbf{I}$, where $k = 10^{-10} \text{ m}^2$). Again both fluids have the same fluid properties and the relative permeabilities are parameterized by Brooks-Corey functions ($\lambda = 2.0$, $S_{\text{wr}} = S_{\text{nr}} = 0$) (*Brooks and Corey*, 1964). Gravity is neglected. The unstructured grids used for the simulations are equal to those of the Buckley-Leverett problem (Figure 3.13). As the Buckley-Leverett problem the McWhorter problem can be solved analytically (*McWhorter and Sunada*, 1990; *Fučík et al.*, 2007). The analytic solution is calculated for each cell of the simulation grids and used to quantify errors of the numerical solution.

The simulation results using the O-method and the L-method are shown in Figure 3.21. The simulations are carried out on five grid levels where the maximum level (level 5) results in a grid of 16384 cells. It can be observed that numerical diffusion influences the solution much stronger in the capillary diffusion dominated case than in the advection dominated Buckley-Leverett problem discussed before. On the coarser grid the front is almost twice as fast as on the finest grid. However, it finally converges to the correct solution shown in Figure 3.22a. For comparison the results obtained with a simple TPFA method are again plotted in Figure 3.22b. The front remains tilted following the direction of the skew grid although it, in average, converges against the analytic front.

The global error trend (Equation (3.75)) is plotted in Figure 3.24. Against the expectation, the L-method produces the largest global errors for the grid levels 1-3. At level 4 the

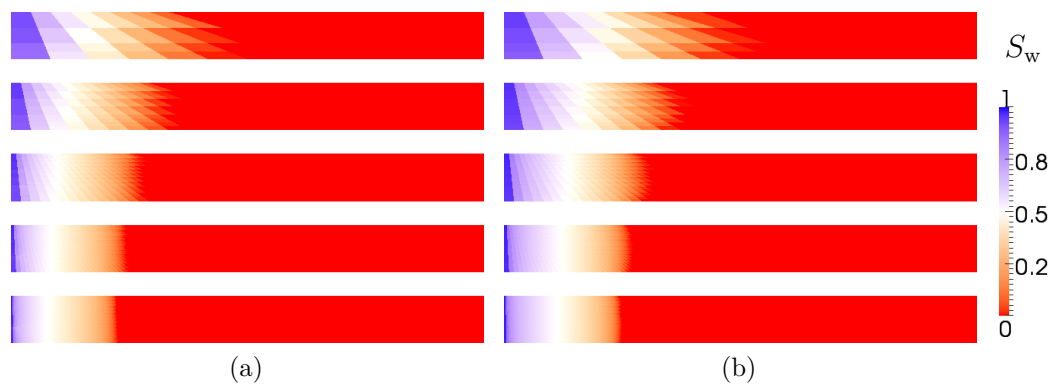


Figure 3.21: Wetting phase saturation at $t = 2 \times 10^5$ s. The results are shown for the grid levels 1-5 (top to bottom) using the MPFA O-method (a) and the MPFA L-method (b).

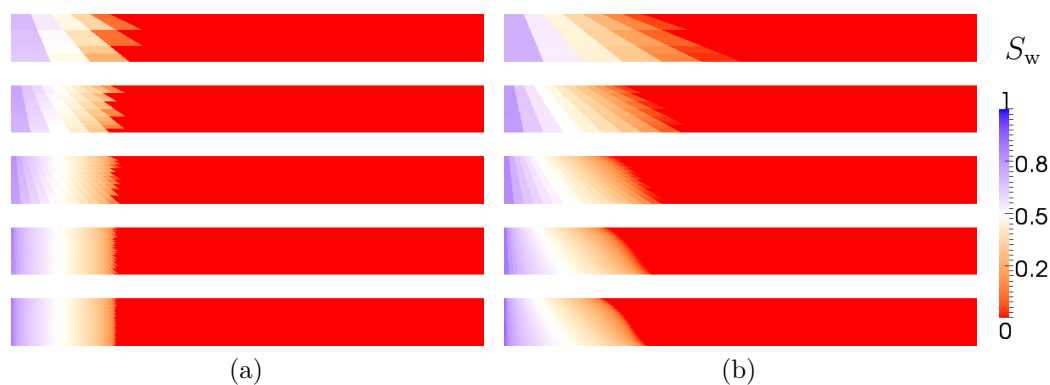


Figure 3.22: Wetting phase saturation at $t = 2 \times 10^5$ s. The results are shown for the grid levels 1-5 (top to bottom) using an analytic solution (a) and a simple TPFA model (b).

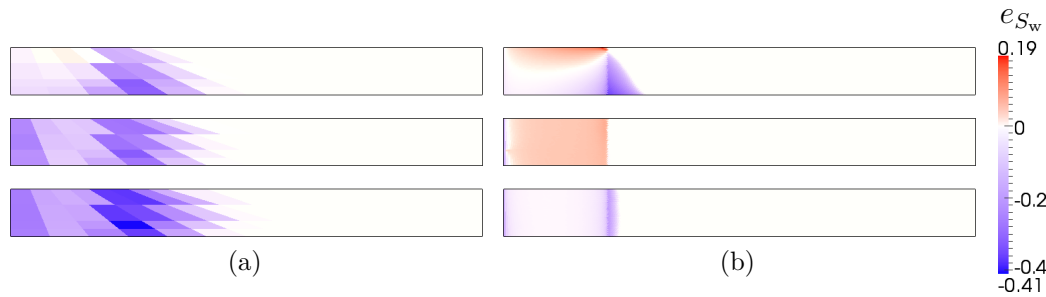


Figure 3.23: Wetting phase saturation error at $t = 2 \times 10^5$ s. From top to bottom the results are shown for TPFA, O-method, and L-method, for grid level 1 (a) and 5 (b).

error becomes slightly smaller than that of the TPFA method. Afterwards it is strongly decreasing almost reaching the error of the O-method at level 5. This behavior can also be observed considering the local errors (Figure 3.23). At level 1 the saturation distribution of the L-method shows the largest local errors, at level 5 the exact solution is approximated well with comparably small errors at the saturation discontinuity.

Comparing the saturation distributions of the O-method and the L-method (Figure 3.21), the L-method shows slightly higher front speeds inside the domain compared to the near boundary regions. Obviously, the error due to the simplified boundary treatment explained in Section 3.1.5 has a noticeable effect in case of the L-method. At faces intersecting a boundary the flux stencil is reduced to that of a half face (2-d). However, in case of the O-method it is still large enough to give a sufficiently accurate approximation, also for the skew unstructured grid. In case of the L-method, which uses smaller flux stencils, the L-stencil selected for the half face can be insufficient with regard to the complete face. This leads to under- or overestimation of the fluxes along the boundaries. With an increasing refinement level the influence of the boundaries decreases leading to the convergence behavior discussed before.

In the three-dimensional case the negative effect of the boundaries is reduced (Figure 3.25). On the one hand, the ratio of inner cells and boundary cells is different. On the other hand, also fluxes along the boundary are mostly approximated by flux-stencils consisting of more than one L-stencil. This reduces the negative effect of a single, badly chosen L-stencil. For validation again a slice of the result of grid level 4 (Figure 3.25d) is plotted in Figure 3.26 and compared to the two-dimensional case. The results show that also in the capillary pressure dominated case both MPFA-L-models agree very well and are able to approximate the exact solution sufficiently accurate.

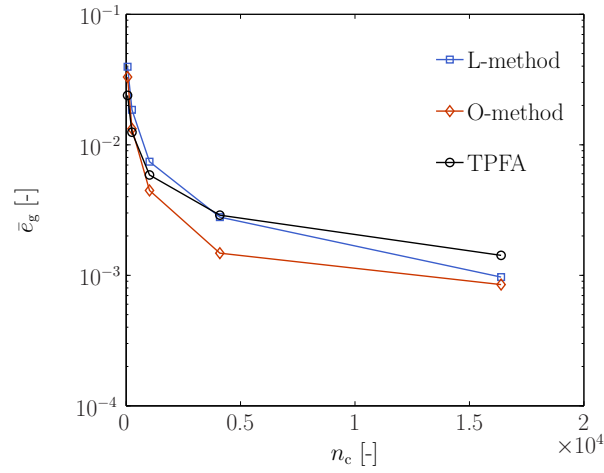


Figure 3.24: Global error of the transport solution of the McWhorter problem at $t = 2 \times 10^5$ s over the number of cells.

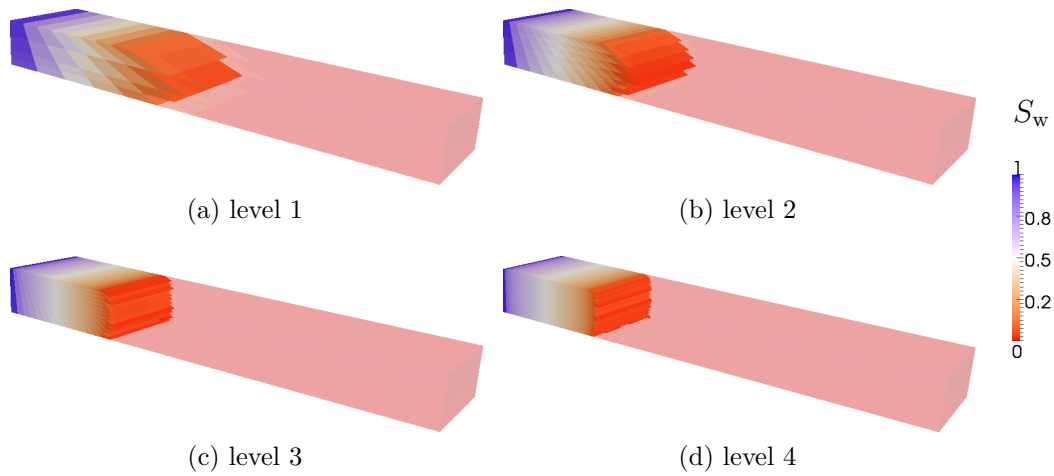


Figure 3.25: Wetting phase saturation at $t = 2 \times 10^5$ s using the 3-d MPFA L-method.

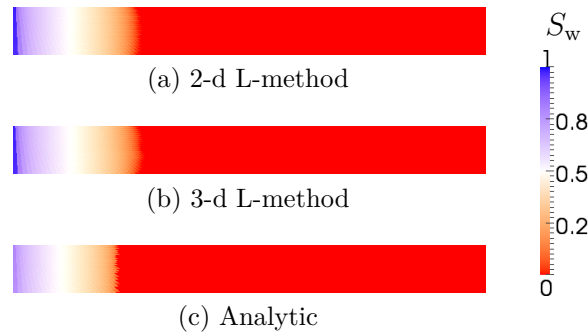


Figure 3.26: Comparison of the 2-d solution (a) and a 2-d slice of the 3-d solution (b) of the L-method with the analytic solution (c).

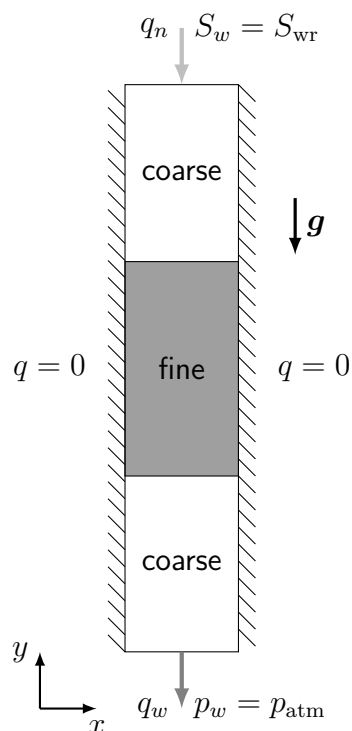


Figure 3.27: Setup of the capillary pressure heterogeneity problem. The arrows mark the non-wetting fluid inflow and the wetting fluid outflow. In the vertical column a fine material is surrounded by coarse material.

Capillary Pressure Heterogeneity Problem

Often only permeability and porosity are considered heterogeneous, while capillary pressure is neglected. However, capillary pressure heterogeneities can dramatically change the flow behavior. Different entry pressures can lead to zones which are completely impermeable for the non-wetting phase. As a result, more distinct flow paths or regions of a trapped phase can develop. To model such effects, the numerical scheme has to account for the different capillary-pressure-saturation relationships at material interfaces correctly. Figure 3.28 shows the capillary pressure functions of a fine sand and a coarse sand. As a pressure is a continuous quantity, the capillary pressure in the coarse material at least has to reach the entry pressure of the fine material if the non-wetting phase is present on both sides of the interface. From Figure 3.28 it is obvious that a continuous capillary pressure necessitates a saturation jump at the interface. The numerical treatment of the capillary pressure interface condition has been studied in *Helmig and Huber (1998)*. Following, the capabilities of the MPFA models with regard to this interface condition is tested by simulating the test case of *Helmig and Huber (1998)*.

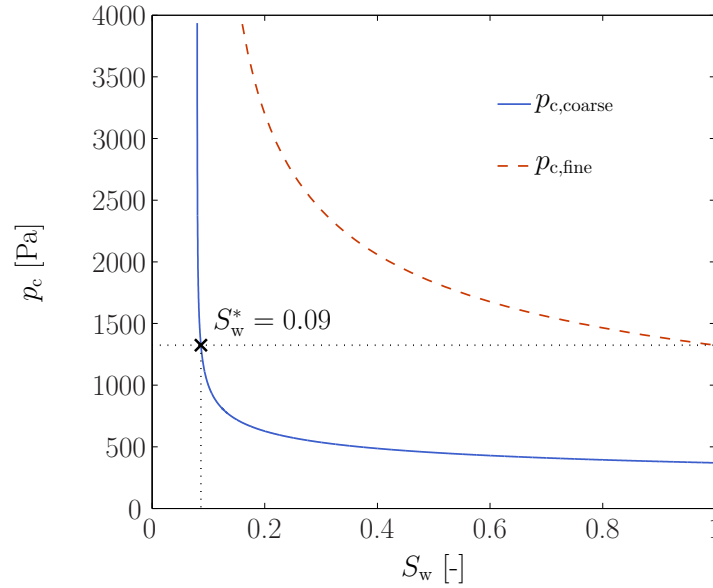


Figure 3.28: Function plots of the p_c - S_w -functions illustrating the interface saturation S_w^* , where $p_c^c(S_w^*) = p_d^f$.

Material	Parameters					
	\mathbf{K} [m ²]	ϕ	S_w	S_n	p_d [Pa]	λ
coarse (c)	5.04×10^{-10}	0.40	0.08	0	370	3.86
fine (f)	5.26×10^{-11}	0.39	0.1	0	1324	2.49

Table 3.1: Porous media properties of the column experiment (Figure 3.27).

The setup is sketched in Figure 3.27. The vertical column is filled by a fine sand surrounded by coarse sand. The material properties are shown in Table 3.1. The capillary-pressure-saturation curves resulting from the Brooks-Corey parameterization (*Brooks and Corey, 1964*) are plotted in Figure 3.28. The column is initially fully saturated by the wetting fluid. A DNAPL (Dense Non-Aqueous Phase Liquid) is injected at the top of the column ($q_n = -0.05$ kg/(m² s)) flowing in direction of gravity. A structured grid of 2×100 cells and an unstructured grid of 16×64 cells (Figure 3.13a, level 3) are used for the simulations.

The resulting saturation distributions are shown in Figure 3.29. On the structured grid the O-method (Figure 3.29a) and the L-method (Figure 3.29c) show identical results. For a better comparison the saturation profiles of the center of the column along the y -axis are plotted. Figure 3.30a shows the profiles according to the 2-d saturation plots (Figure 3.29). It confirms that the O- and L-method give equal solutions on the

structured grid. Further, the effects of the material interfaces are clearly visible. The DNAPL is pooling on top of the fine sand. This results in the saturation discontinuity at the interface discussed before. At the transition from fine to coarse material the opposite behavior can be observed. The saturation in the fine material decreases such that the capillary pressure of the coarse material can be reached. Again this leads to a saturation discontinuity.

From the Brooks-Corey capillary-pressure-saturation parameterization the theoretical interface saturation for the breakthrough from the coarse to the fine material can be calculated as:

$$S_n^* = (1 - S_{wr} - S_{nr})(1 - S_{we}), \quad S_{we} = \left(\frac{p_{dc}}{p_{df}} \right)^{-\lambda_f}. \quad (3.76)$$

Inserting the parameters of Table 3.1 yields $S_n^* = 0.91$. To validate the MPFA models, the saturation profiles at the breakthrough are shown in Figure 3.30b. The theoretical value is almost met by the numerical approximations, and thus, the capillary pressure interface condition is well accounted for.

In case of the unstructured grid, the saturation distributions shown in Figures 3.29b and 3.29d are similar to those of the structured grid. Both show the pooling on top of the fine sand and the decrease of saturation at the transition from fine to coarse sand. In average, the front speed also matches. However, as already discussed for the McWhorter problem, the result using the L-method shows an increased error due to insufficient approximation of the near boundary fluxes. As the level 3 grid discretizes the domain with only 16 cells in x -direction, it can be assumed that negative boundary effects have a noticeable influence on the solution. The McWhorter test has shown that these effects vanish if the grid is refined. However, refinement would smooth the material interface line and soften the test conditions. It is therefore avoided. The saturation profiles using the unstructured grid (Figure 3.31a) are similar than those using the structured grid and both methods account for the important features discussed before. However, in both Figure 3.29b and Figure 3.31a, it can be observed that the O-method systematically produces an unphysical saturation undershot in the first row of cells in the fine material. Here, the L-method gives a better approximation for the unstructured grid. Considering the breakthrough into the fine material both methods cannot reach the theoretical saturation in the coarse sand. The saturation distribution is less homogeneous in x -direction due to the unstructured grid. This leads to different breakthrough times

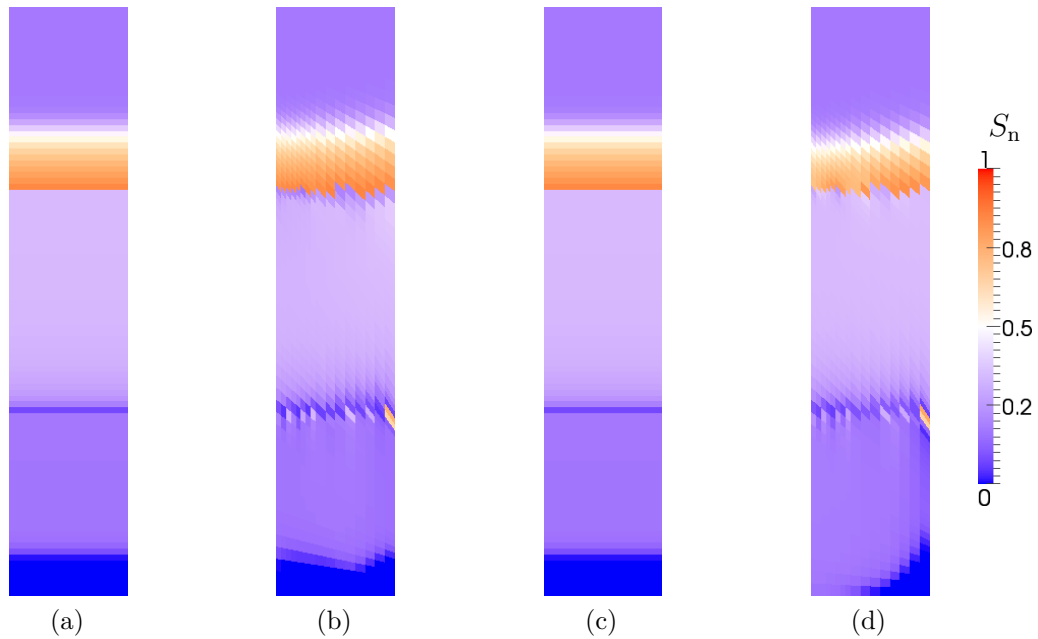


Figure 3.29: Non-wetting phase saturation at $t = 1.5 \times 10^3$ s using the O-method: (a) (structured grid), (b) (unstructured grid), and the L-method, (c) (structured grid), (d) (unstructured grid).

for the different cells. The plots in Figure 3.31 indicate that the first breakthrough does not appear in the center of the column from where the saturation profile is shown. At the location of the real first breakthrough a saturation similar than for the structured grid is reached.

The tests showed that the proposed MPFA models are able to account for the important aspects of two-phase flow including the approximation of shock fronts, the diffusive character of capillary pressure driven flow and the correct treatment of capillary pressure heterogeneities for both structured and unstructured grids. The L-method approximates the saturation discontinuity forced by the capillary pressure interface condition better. However, it is more sensitive to errors due to the simplified approximation of fluxes at the boundary in the case of non- \mathbf{K} -orthogonal grids. In the three-dimensional case, this sensitivity is reduced. Considering the applicability of the method, this error becomes important if important processes occur directly at a boundary which is discretized by strongly non- \mathbf{K} -orthogonal oriented cells. In real applications this is rarely the case.

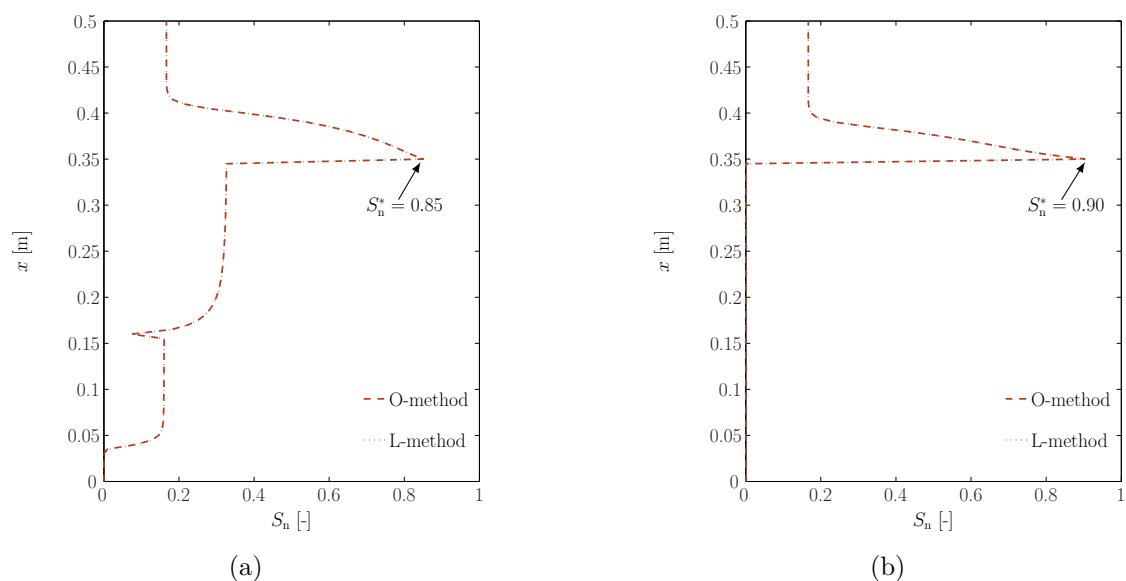


Figure 3.30: Non-wetting phase saturation plot along the y -axis at $x = 0.05$ m at the end of the simulation (a) and at the time of the breakthrough into the fine material (b) (structured grid).

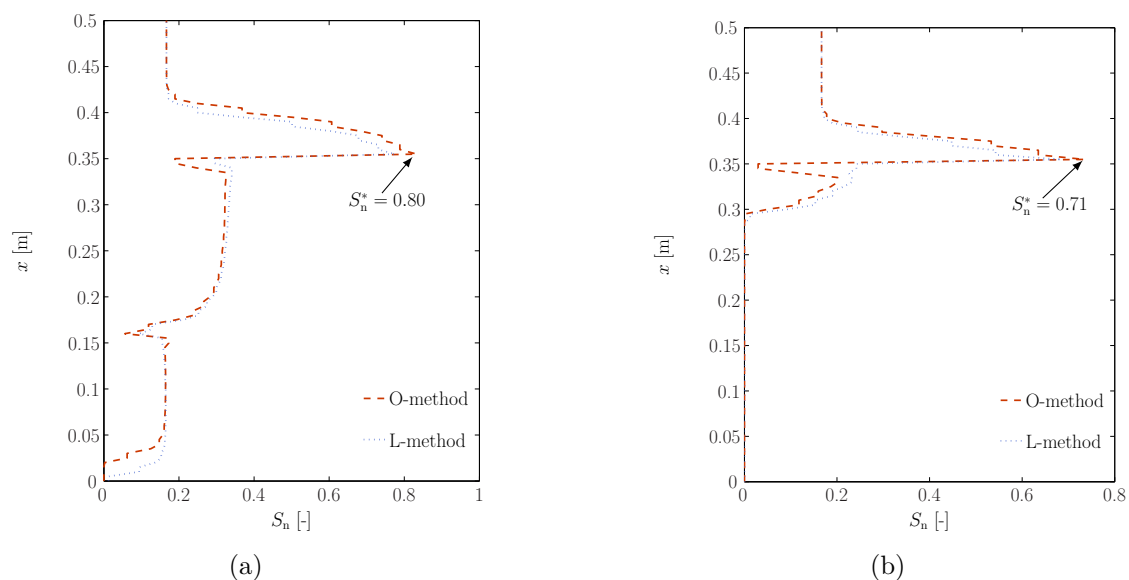


Figure 3.31: Non-wetting phase saturation plot along the y -axis at $x = 0.05$ m at the end of the simulation (a) and at the time of the breakthrough into the fine material (b) (unstructured grid).

3.2 Non-Conforming Adaptive Grids

Regarding time-dependent coupled transport problems like multi-phase flow in porous media, the efficiency of the numerical method is crucial. Complex discretization schemes, for example MPFA methods, might not be applicable for large-scale problems on very fine meshes. One way for increasing efficiency is the use of locally refined grids. Considering the previously introduced MPFA methods an advantage of the L-method is that the treatment of hanging nodes is straight forward. For grids of quadrilaterals or quadrilaterally faced hexahedra the case of one hanging node per face can be treated directly by applying one of the L-interaction-volumes described in Sections 3.1.2 and 3.1.3. The convergence of the L-method for non-conforming grids has been shown in *Aavatsmark et al. (2010)*. For the O-method a new interaction volume type as well as a different pressure approximation is necessary in order to get an acceptable flux approximation (see e.g. *Aavatsmark et al., 2001*). Thus, we adapt the grid by a non-conforming grid refinement allowing one hanging node per cell face and approximate the fluxes between grid cells applying the MPFA L-method. The macro grid is assumed to be conforming.

The interaction volume at a hanging node in the two-dimensional case is sketched in Figure 3.32. The fluxes can be approximated as explained in Section 3.1.2 with the hanging node being the vertex I . For the flux between cell 2 and 3 the type of L-shape (left (a), right (b)) has to be chosen applying one of the L-selection criteria. For the fluxes across the hanging node faces only one of the L-shapes can be used. Referring to Figure 3.32 this is a right L-stencil for the flux between cell 1 and 2 (a) and a left L-stencil for the flux between cell 1 and 3 (b).

Figure 3.33 shows the basic types of interaction volumes which can occur around

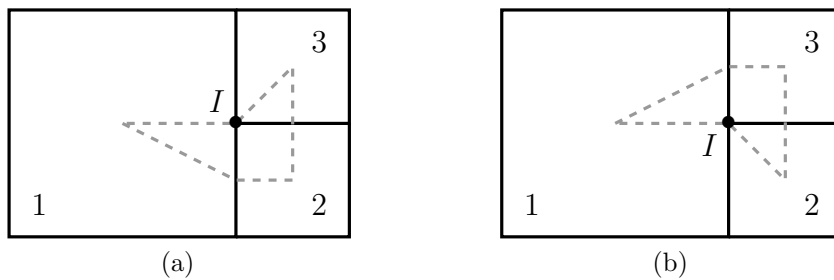


Figure 3.32: Flux stencil around a hanging node (2-d).

a hanging node in the three-dimensional case. The flux faces corresponding to these interaction-volume shapes are sketched in Figure 3.34. For each flux face of an interaction volume around a hanging-node the flux can be calculated by applying one of the four L-stencils introduced in Figure 3.6. However, compared to a regular node only one or one of two of these L-shapes can be suitable for certain flux faces. For the volume Type 1, for instance, all four L-cases could be used for the flux calculation through faces 1-4, while only the stencil (a) or (b) could be used for the flux faces 9-12 (see Figure 3.34). Let us consider the L-stencil for face 9 of the volume Type 1 where cell number 5 is cell 1 according to the numbering of Figure 3.6 and cell number 1 is cell 2. In this case only cells 5, 1, 3, and 2 can be combined to the regular L-shape (b). The remaining three L-shapes respectively combine cells 5 and 1 for the construction of the L-stencil (a), cells 5, 1, and 3 for the L-stencil (c), and cells 5, 1, and 2 for the L-stencil (d). This leads to stencils consisting of less than four cells. Obviously, these degenerated stencils are not feasible to derive a closed local system for the flux approximation through face 9.

3.2.1 Boundary Handling

As explained in Section 3.1.5, a two-point flux approximation is used at Dirichlet boundaries and a weighting factor is used to obtain the fluxes through the faces intersecting with the boundary. The weighting becomes more complex, if hanging nodes occur. Considering two neighboring cells of the interaction volume around a hanging node, the intersecting face of one (coarser) cell could touch a boundary while the intersecting face of the other (finer) cell could be completely inside the domain.

Figure 3.35 exemplarily shows such a situation for the two-dimensional case and Figure 3.36 for the three-dimensional case. The dashed lines and hatched areas respectively mark boundary faces. The gray lines and gray shaded areas respectively mark the sub-interfaces through which the flux is calculated by the MPFA interaction volumes inside the model domain (volumes that do not touch the boundary). Each of the arrows in Figures 3.35a or 3.36a represents the flux \mathbf{f}_i through a sub-interface i of the interface x_2x_3 or $x_5x_6x_3x_4$ calculated from one L-stencil. As for the non-adaptive case explained before we now want to weight the flux through a sub-interface such that it approximates the flux through the whole cell interface x_1x_2 or $x_1x_2x_3x_4$. According to Section 3.1.5 we can define:

$$\mathbf{f} = \frac{|s|}{\sum_i |s_i|} \sum_i \mathbf{f}_i \quad (3.77)$$

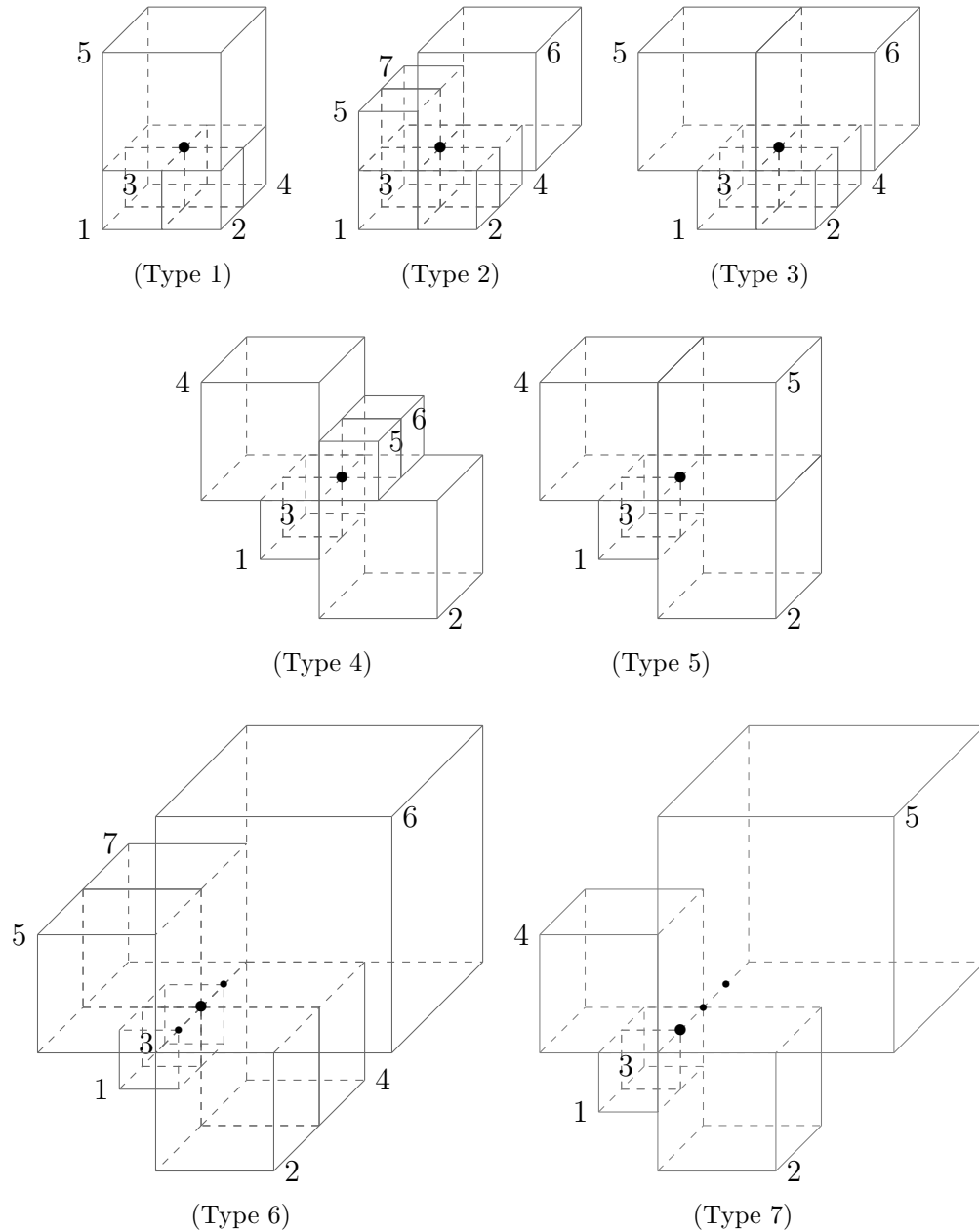


Figure 3.33: Interaction-volume-types around hanging nodes allowing only one hanging node (HN) per cell face. (Type 1): one face HN; (Type 2): one edge HN, one coarser cell; (Type 3): one edge HN, two coarser cells; (Type 4): one edge HN, two coarser cells, diagonal configuration; (Type 5): one edge HN, three coarser cells; (Type 6): three edge HNs, special case of (Type 2); (Type 7): three edge HNs, special case of (Type 5).

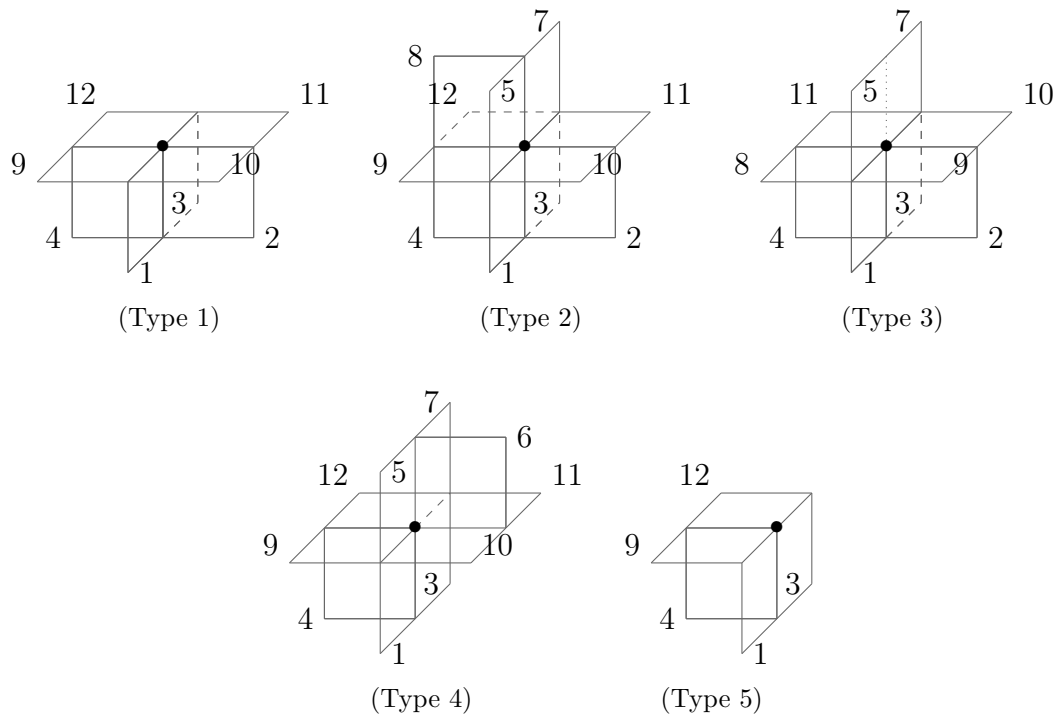


Figure 3.34: Flux faces of the different interaction-volume-types shown in Figure 3.33. The numbering of the faces relates to the general case without hanging nodes (12 faces per interaction-volume). (Type 1): 8 flux faces; (Type 2): 11 flux faces; (Type 3): 10 flux faces; (Type 4): 10 flux faces; (Type 5): 5 flux faces; (Type 6): see (Type 2); (Type 7): see (Type 5).

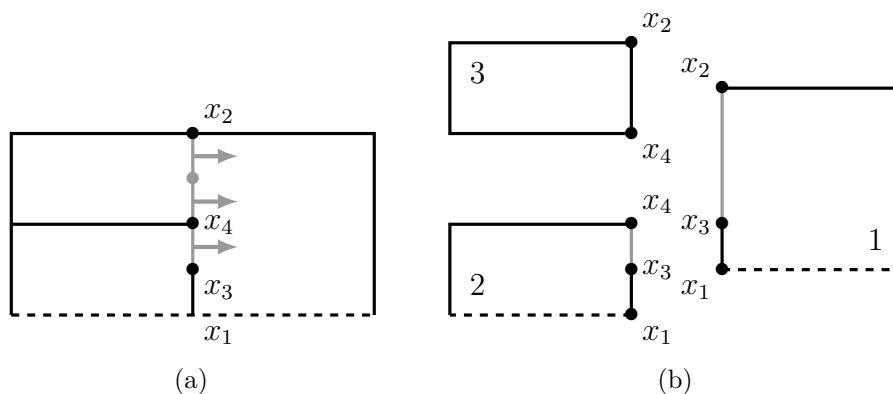


Figure 3.35: Example for boundary treatment with hanging nodes (2-d). The dashed line marks the boundary faces. (a) MPFA flux area (gray) and sub-fluxes (arrows) - Fluxes are not calculated by the MPFA for the whole cell face! (b) MPFA flux area (gray) only for the boundary cells.

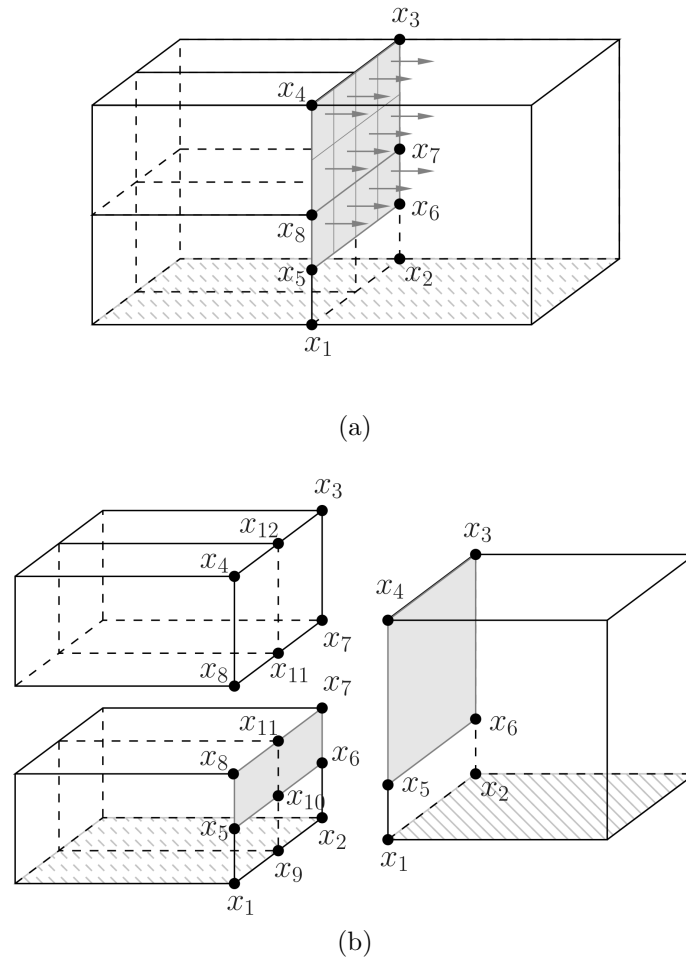


Figure 3.36: Example for boundary treatment with hanging nodes (3-d). The hatched area marks the boundary faces. (a) MPFA flux area (gray) and sub-fluxes (arrows) - Fluxes are not calculated by the MPFA for the whole cell face! (b) MPFA flux area (gray) only for the boundary cells.

where $|s_i|$ is the area of the flux sub-interface i and $|s|$ the reference face area. However, instead of two cells sharing one face we now have 3 cells in the two-dimensional case and five cells in the three-dimensional case. Thus, the fluxes are weighted separately for each of the cells (Figure 3.35b or 3.36b).

In the two-dimensional case only cells 1 and 2 are located at the boundary. For cell 3 the fluxes can be completely approximated by the MPFA on interaction volumes around inner vertices. Referring to Equation (3.77), this means that $\sum_i \frac{|s|}{|s_i|} = 1.0$. For cell 1 the flux is calculated using Equation (3.77) where $i = i \in x_2x_3$ and $|s| = \text{area of face } x_1x_2$. Cell 2 can be treated like boundary cells on regular boundary interaction volumes (Equation (3.61)). This means that f_i is the flux through face x_3x_4 and $|s|$ is equal to the area of face x_1x_4 .

In the three-dimensional case the two upper left cells intersecting at sub-faces $x_8x_{11}x_{12}x_4$ and $x_{11}x_7x_3x_{12}$ are not located directly at the boundary. For these cells, the weight is $\sum_i \frac{|s|}{|s_i|} = 1.0$. For the remaining cells, the flux is approximated by Equation (3.77) with:

- one right coarse cell: $i = i \in x_5x_6x_3x_4$ and $|s| = \text{area of face } x_1x_2x_3x_4$;
- two lower left fine cells:

$$i = i \in x_5x_{10}x_{11}x_8 \text{ and } |s| = \text{area of face } x_1x_9x_{11}x_8, \text{ and}$$

$$i = i \in x_{10}x_6x_7x_{11} \text{ and } |s| = \text{area of face } x_9x_2x_7x_{11}.$$

Equation (3.77) is general and can be applied to any kind of boundary configuration, with f_i being the sub-flux through one sub-interface calculated from non-boundary interaction volumes, $|s|$ the cell face area and $|s_i|$ the area of sub-interface i . If a face does not intersect with a boundary, $|s| = \sum_i |s_i|$ and $f = \sum_i f_i$.

3.2.2 Tests

The adaptive grid method is tested on two test-scenarios for the two-dimensional model and the three-dimensional model. In both scenarios the model domain sketched in Figure 3.37 is initially saturated with water. DNAPL infiltrates from the top of the domain at the location marked by the arrow. In the two-dimensional case $q_n = 0.2 \text{ kg}/(\text{ms})$, in the three-dimensional case $q_n = 0.1 \text{ kg}/(\text{m}^2\text{s})$. The bottom and top

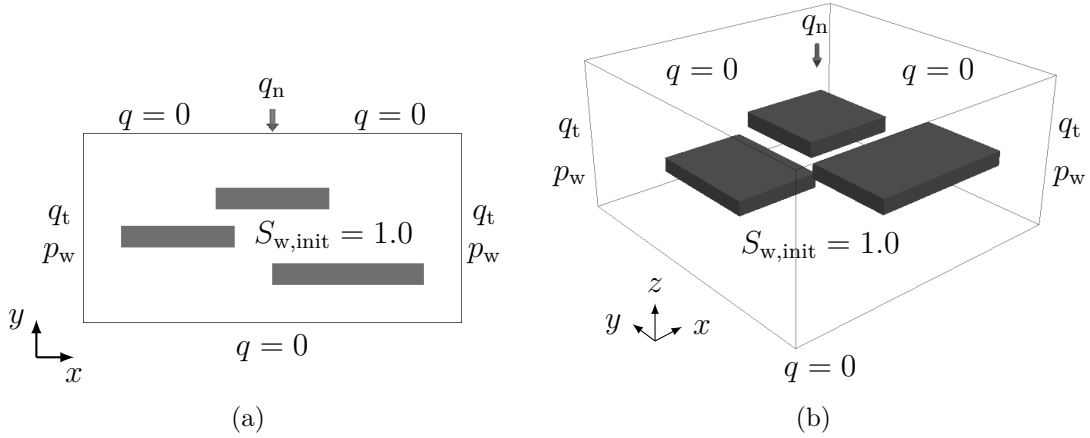


Figure 3.37: Problem setup of the DNAPL infiltration example in 2-d (a) and 3-d (b). The arrow indicates where the DNAPL is released. The gray boxes are lenses of lower permeability and higher entry pressure.

(except the infiltration area) are impermeable. On the side boundaries hydrostatic pressure distributions are assumed, allowing free fluid outflow (or inflow). In both scenarios the MPFA methods are compared to a standard TPFA method. In the two-dimensional tests the MPFA O-method, the L-method and the adaptive L-method, in the three-dimensional case only the adaptive MPFA L-method are applied.

In the first scenario three low permeable lenses, marked by the anthracite boxes, are embedded in a homogeneous background material. The background permeability and entry pressure are $\mathbf{K}_b = k_b \mathbf{I}$ with $k_b = 10^{-10} \text{ m}^2$, $p_{d,b} = 500 \text{ Pa}$. Permeabilities and entry pressures of the lenses are $\mathbf{K}_l = k_l \mathbf{I}$ with $k_l = 10^{-14} \text{ m}^2$, $p_{d,l} = 5000 \text{ Pa}$. The relative permeabilities and the capillary pressure are parameterized by Brooks-Corey functions (*Brooks and Corey*, 1964). The porosity as well as the Brooks-Corey parameter λ are constant through the whole domain ($\lambda = 2.0$, $\phi = 0.4$). The domain size is chosen to be 20×10 meters in two dimensions and $20 \times 20 \times 10$ meters in three dimensions.

The results of the two-dimensional test case are shown in Figure 3.38. The simulation grid for the TPFA (Figure 3.38a), the O-method (Figure 3.38b) and the L-method (Figure 3.38c) is a structured grid of 40×35 cells. The results agree very well and the heterogeneities are well accounted for. Especially, the interaction of gravity and capillary entry pressure heterogeneities, which leads to a pooling on top of the lenses and to a bypassing of the lenses and thus, to a kind of macro dispersion, is consistently modeled. As the grid is \mathbf{K} -orthogonal the TPFA solution can be viewed as a reference solution for the validation of the MPFA methods. Figure 3.38d shows the saturation distribution of

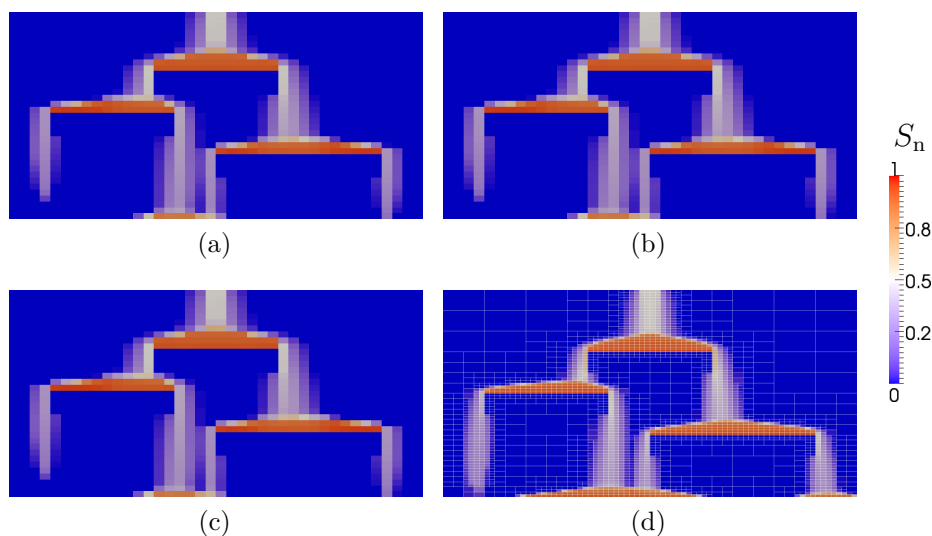


Figure 3.38: Saturation distributions of the lense scenario at $t = 6 \times 10^4$ s using a TPFA method (a), the O-method (b), the L-method (c), and the adaptive L-method (d).

a grid adaptive simulation using the L-method. A macro grid of 10×10 cells is applied and 3 refinement levels are allowed. Therefore, the front resolution is increased, while the number of cells is similar or lower.

For the three-dimensional case, a structured coarse grid of $10 \times 10 \times 10$ cells is generated, which just resolves the lenses. For the TPFA model this grid is globally refined twice leading to a grid of $40 \times 40 \times 40$ cells. The adaptive MPFA L-model uses the coarse grid, but is allowed to locally refine the grid twice. The results are plotted in Figure 3.39. The upper row shows the results of the TPFA method and the lower row the results of the adaptive MPFA L-method. Both methods show similar DNAPL saturation distributions. They account for the heterogeneities and also satisfy the interface condition due to the capillary-pressure heterogeneity. However, in the three-dimensional case the TPFA is more diffusive than the L-method. Considering the pooling on top of the lenses, the DNAPL layer from the L-model mainly consists of one cell layer while the DNAPL layer from the TPFA model consists of two or more cell layers. A possible reason is that due to the larger flux stencil the ability of the L-method to deflect the flow at the lense is higher. The same effect can be observed where the DNAPL flows around the corners of the lenses. Additionally, the circular propagation of the pool on top of the lenses can be better approximated by the MPFA method. The adaptive local grid refinement of the L-model is visualized in Figure 3.40. As can be observed from Figure 3.40a, mostly the

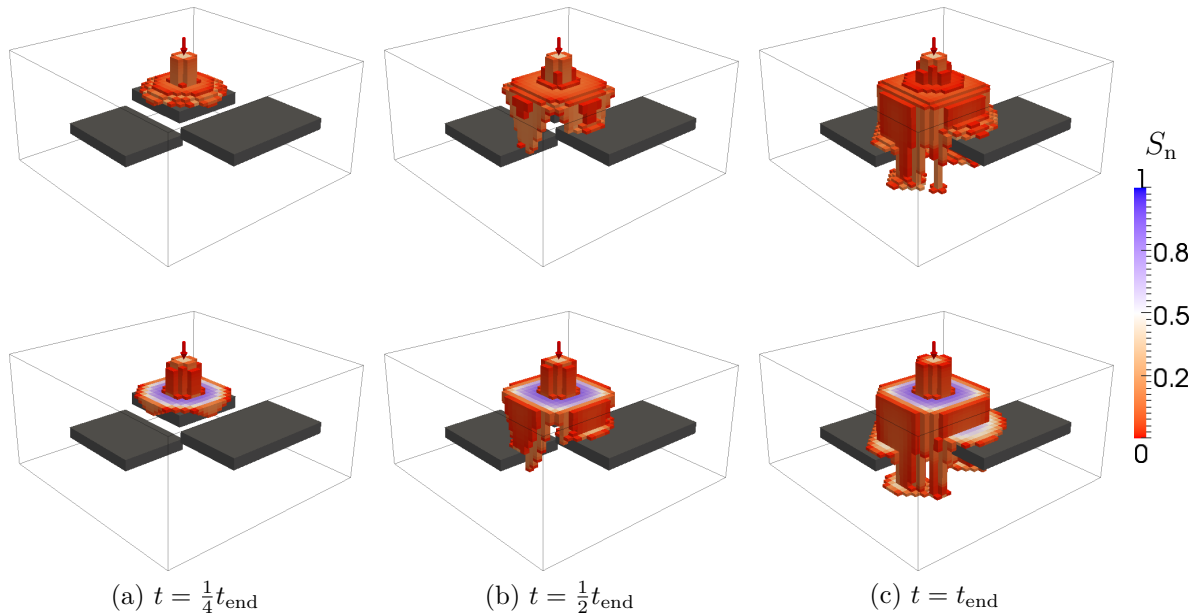


Figure 3.39: Saturation distributions of the three-dimensional lense scenario for 1.8×10^5 simulated time: The upper row shows the results of the TPF method, the lower row the results of the adaptive MPFA L-method.

coarsest grid cells are used at the early time of the simulation. Later, more and more cells are refined following the DNAPL distribution.

The setup of the second scenario is similar. DNAPL still infiltrates from the top at the location marked by the arrow (Figure 3.37). The boundary conditions remain the same. However, instead of the heterogeneities we now introduce anisotropy. The homogeneous

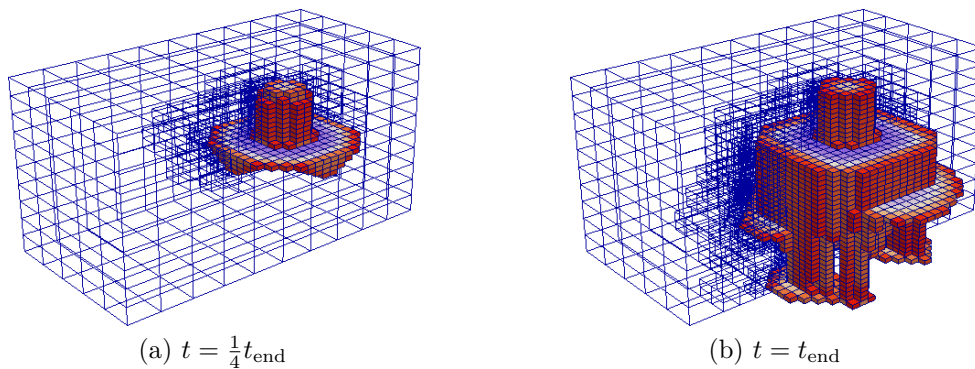


Figure 3.40: Locally adapted grids of the adaptive MPFA model for the lense scenario.

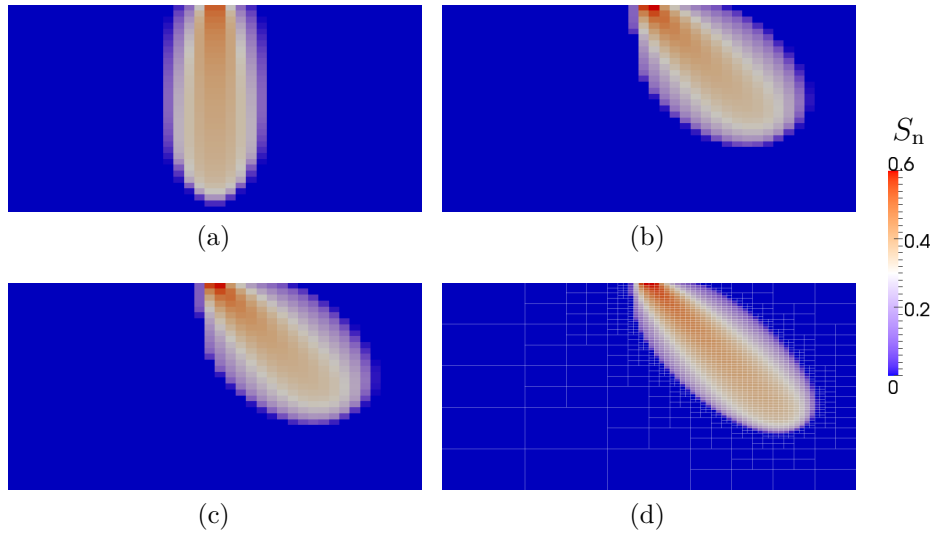


Figure 3.41: Saturation distributions of the anisotropic scenario at $t = 3.4 \times 10^4$ s using a TPFA method (a), the O-method (b), the L-method (c), and the adaptive L-method (d).

anisotropic permeability tensor is defined as

$$\mathbf{K} = \begin{pmatrix} 10^{-10} & 0 & -5 \times 10^{-11} \\ 0 & 10^{-10} & 5 \times 10^{-11} \\ -5 \times 10^{-11} & 5 \times 10^{-11} & 5 \times 10^{-11} \end{pmatrix} \text{ m}^2.$$

Using this permeability tensor the grid is no longer \mathbf{K} -orthogonal. Thus, the TPFA method is expected to fail. In the entire domain a constant entry pressure $p_d = 5000$ Pa is used.

The saturation distributions resulting from the two-dimensional simulations are plotted in Figure 3.41. Again a simulation grid of 40×35 cells is used for the simulations applying TPFA (Figure 3.41a), the O-method (Figure 3.41b) and the L-method (Figure 3.41c). The O- and L-method yield equal saturation distributions while the result obtained by the TPFA model strongly differs. As expected, TPFA can not account for the off-diagonal entries of the full permeability tensor. Therefore, the DNAPL flows straight downwards, following the direction of gravity. Using the MPFA methods, the fluid propagation is deflected following the preferred direction given by the off-diagonal tensor coefficients. Figure 3.41d shows the results using an adaptive grid method. In this case, the cells of a macro grid of 5×5 cells are allowed to be refined four times. As can be observed, the finer front resolution reduces numerical diffusion and therefore has

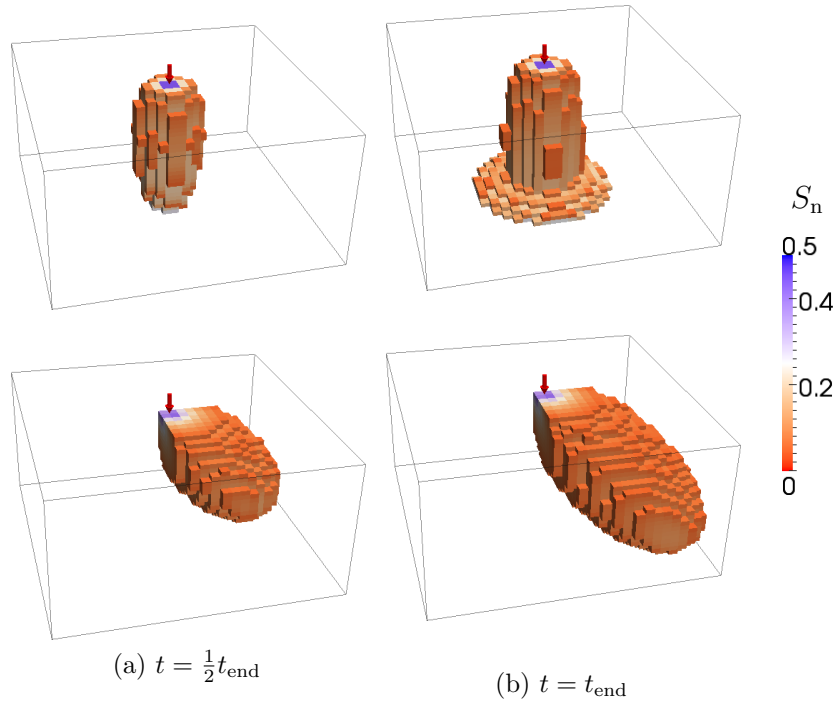


Figure 3.42: Saturation distributions of the three-dimensional anisotropic scenario for 2×10^5 s simulated time: The upper row shows the results of the TPFA method, the lower row the results of the adaptive MPFA L-method.

a visible effect on the accuracy of the approximation. At the same time the number of cells of the simulation grid is reduced below the number of the coarser static grid used before.

In the three-dimensional case the absence of heterogeneities allows a minimal macro grid size of $2 \times 2 \times 2$ cells. This grid is globally refined to a $32 \times 32 \times 32$ grid for the TPFA model. The adaptive MPFA L-model again uses the coarse grid but is allowed to refine four times. Figure 3.42 shows the results of the anisotropic scenario. The results of the TPFA model are visualized in the upper row and those of the adaptive L-model in the lower row. As observed in the two-dimensional test, the TPFA fails to account for the anisotropy in the off-diagonal direction. The DNAPL just follows the direction of gravity, which is the driving force, and pools at the impermeable bottom. The DNAPL distribution calculated by the L-model also flows towards the bottom of the domain but following the diagonal direction given by the off-diagonal entries of the anisotropic permeability tensor. Obviously, the TPFA can not be used to validate the adaptive L-method in this case. Thus, the results of the adaptive model are compared to a reference solution using the L-method calculated on a structured grid of $32 \times 32 \times$

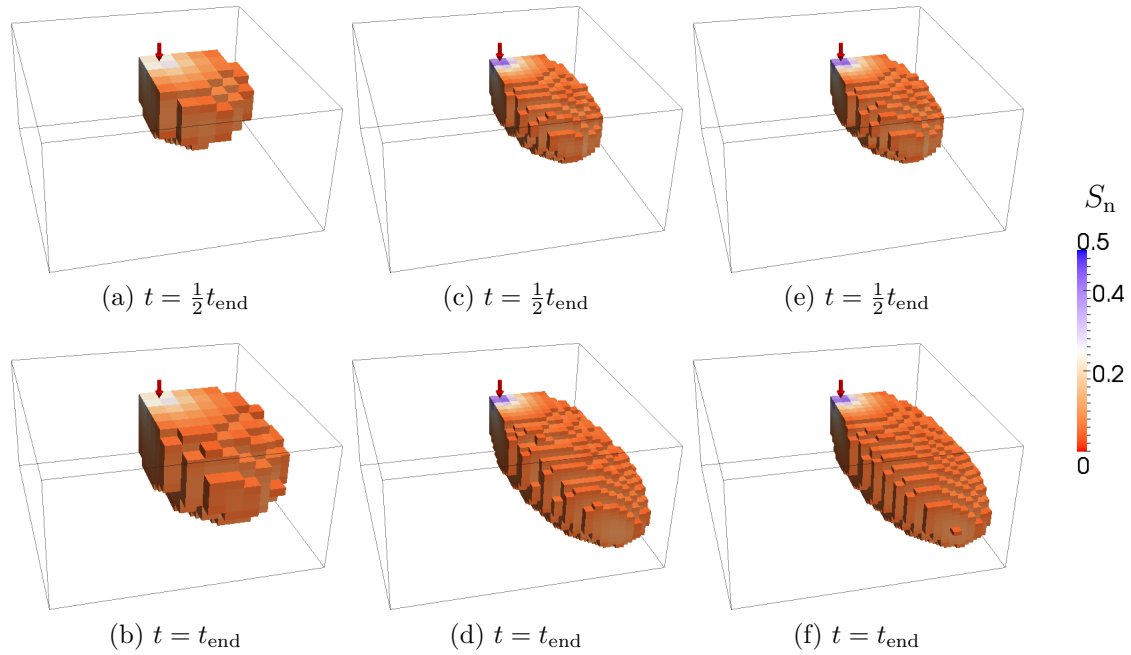


Figure 3.43: Saturation distributions of the three-dimensional anisotropic scenario for 2×10^5 s simulated time: Comparison of the results using a locally refined grid (c) - (d), a coarse structured grid (a) - (b), and a fine structured grid (e) - (f).

32 cells, which have the same size as the finest cells of the adapted grid. Additionally, a coarser structured grid of $16 \times 16 \times 16$ cells is used where the number of degrees of freedom is in the order of the averaged number of degrees of freedom of the adapted grid. Figure 3.43 clearly shows that the adaptive scheme obtains the accuracy of the fine structured grid which can not be achieved by the coarser structured grid of a similar size. As an example, two grids of the adaptive L-model for the anisotropic case at $t = \frac{1}{2}t_{\text{end}}$ and $t = t_{\text{end}}$ are shown in Figure 3.44.

Two different DNAPL infiltration scenarios are used in a two-dimensional and in a three-dimensional setup to test the previously introduced two-phase models, which are based on the MPFA L-method and allow non-conforming grid refinement. In the case of a \mathbf{K} -orthogonal grid, the MPFA method could be validated against a standard TPFA model. Important two-phase features like the treatment of capillary pressure heterogeneities are well accounted for. Especially in the three-dimensional case, the multi-dimensional flux approximation leads to a more accurate approximation of the fluid movement, for example, of the circular spreading on top of the lenses. In the case of an anisotropic permeability leading to a non- \mathbf{K} -orthogonal grid, the MPFA model

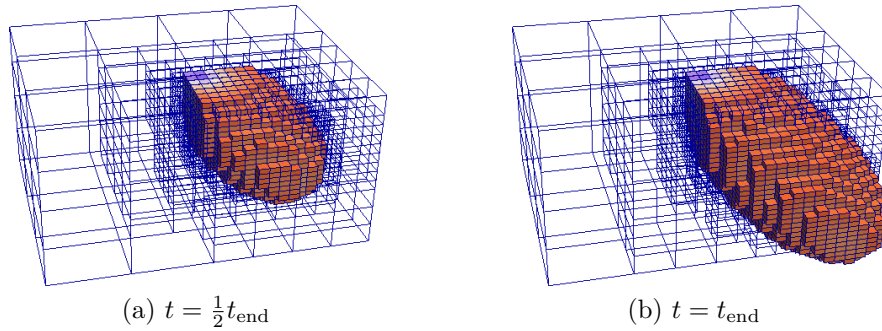


Figure 3.44: Locally adapted grids of the MPFA model for the anisotropic scenario.

clearly shows its superiority. In such cases the standard TPFA approach fails. Further, the potential of grid adaptive methods with respect to efficiency becomes obvious. When large parts of a model domain are not affected by moving fluid fronts, the local grid refinement and coarsening can provide a fine resolution of the fronts while still having feasible grid sizes. This increased efficiency also allows us to use more complex methods like MPFA methods for realistic scenarios where they otherwise could be too expensive.

3.3 The Treatment of Tensorial Solution Dependent Coefficients

In this section, the methods introduced before are transferred to a more general case of modelling two-phase flow in porous media in which also the relative permeabilities are tensors. A fundamental difference compared to the case of scalar relative permeabilities is that the phase dependent quantities have to remain in the MPFA operator in order to account for anisotropy effects correctly. The resulting transmissibilities \mathbf{T}_t (advective wetting phase flux \mathbf{f}_{aw}), \mathbf{T}_n (capillary flux \mathbf{f}_c) and \mathbf{T}_w (wetting phase flux \mathbf{f}_w) are either related to the total flow (\mathbf{T}_t) or to the phase flow (\mathbf{T}_n , \mathbf{T}_w). In particular, the phase related quantities require a special treatment. One reason is that in the case of advection-dominated problems the hyperbolic character has to be preserved. Another reason is that phase dependent properties like \mathbf{F}_α become zero if the phase is not present. The flux continuity at the cell interfaces, which is a basic concept of MPFA methods, produces a behavior similar to a harmonic averaging of the interface fluxes: a flux between two cells can only occur if the fluxes from both sides of the interface are not zero. This means that a fluid α could never enter a cell if $S_\alpha = 0$ and therefore $\mathbf{F}_\alpha = 0$. Moreover, the

equations for continuity of fluxes (e.g. Equation (3.26), (3.34), or (3.44)) can degenerate to the trivial statement $0 = 0$ and the system of equations that has to be solved to get a transmissibility matrix would be under-determined. Therefore, upwind schemes are usually applied. In the case of scalar relative permeability functions, upstream weighting is straightforward, because the direction of flow can be directly determined from the single phase transmissibilities. However, in the case of tensorial relative permeabilities, the determination of an upwind direction is challenging. In the following, the multi-point flux approximations of the different flux terms are derived. From Equation (2.62) and Equation (2.66) or (2.67) they are defined as:

$$\mathbf{f}_{\text{aw}} = (-\mathbf{\Lambda}_t \mathbf{K} \nabla \Phi_w) \cdot \mathbf{n} A \quad (3.78)$$

$$\mathbf{f}_c = (-\mathbf{F}_n \mathbf{\Lambda}_t \mathbf{K} \nabla \Phi_c) \cdot \mathbf{n} A \quad (3.79)$$

$$\mathbf{f}_w = (-\mathbf{F}_w \mathbf{\Lambda}_t \mathbf{K} \nabla \Phi_w) \cdot \mathbf{n} A \quad (3.80)$$

Special emphasis is given to upwinding in case of tensorial phase-dependent coefficients. Formulations are given such that they could be used with different types of MPFA methods (e.g. O-method or L-method).

3.3.1 Advective Flux

Equations (3.78) and (3.63) only differ regarding the definition of the total mobility. As the scalar total mobility λ_t , the total mobility $\mathbf{\Lambda}_t$ is a property of the total flux. Thus, no upwinding scheme is necessary. Moreover, as long as one of the fluids is flowing the total mobility can not become zero, because it is the sum of the phase mobilities. The extension of the advective flux approximation for tensorial total mobilities is straight forward. Referring to Equations (3.69) and (3.70) the flux balance for face 12 in Figure 3.4 is written as:

$$\begin{aligned} & \frac{-\Gamma_{ij} \mathbf{n}_{ij}^T \mathbf{\Lambda}_{ti} \mathbf{K}_i}{T_1} \left[\nu_{12} (\bar{\Phi}_{12} - \Phi_i) + \nu_{14} (\bar{\Phi}_{14} - \Phi_i) \right] \\ &= \frac{\Gamma_{ij} \mathbf{n}_{ij}^T \mathbf{\Lambda}_{tj} \mathbf{K}_j}{T_2} \left[\nu_{21} (\bar{\Phi}_{21} - \Phi_j) + \nu_{23} (\bar{\Phi}_{23} - \Phi_j) \right] \end{aligned} \quad (3.81)$$

for the O-method and for face 12 in Figure 3.5 as:

$$\begin{aligned} & \frac{-\Gamma_{ij} \mathbf{n}_{ij}^T \boldsymbol{\Lambda}_{ti} \mathbf{K}_i}{T_1} [\boldsymbol{\nu}_{12} (\bar{p}_{12} - p_i) + \boldsymbol{\nu}_{14} (\bar{p}_{14} - p_i)] \\ \stackrel{!}{=} & \frac{\Gamma_{ij} \mathbf{n}_{ij}^T \boldsymbol{\Lambda}_{tj} \mathbf{K}_j}{T_2} [\boldsymbol{\nu}_{21} (\bar{p}_{21} - p_j) + \boldsymbol{\nu}_{2I} (\bar{p}_I - p_j)] \end{aligned} \quad (3.82)$$

for the L-method .

3.3.2 Capillary Flux

The second flux term, that has to be approximated, is the term \mathbf{f}_c , which includes the product $\mathbf{F}_n \boldsymbol{\Lambda}_t$. Thus, instead of the total transmissibility, a phase transmissibility is required and the capillary fluxes of an interaction volume can be calculated as:

$$\mathbf{f}_c = \mathbf{T}_n \boldsymbol{\Phi}_c. \quad (3.83)$$

However, there exist two main problems for the calculation of the phase transmissibility \mathbf{T}_n . First, the fractional flow function tensor has to be approximated at the cell face. Since the capillary flux term in this formulation includes both capillary and gravity effects, where the flux driven by gravity has advective character, an upwinding scheme is necessary ($\mathbf{F}_n = \mathbf{F}_n^{\text{upw}}$). Second, in contrast to the total mobility, the phase mobility can become zero if the phase is at or below residual saturation. As discussed before, this would lead to a degeneration of the system of equations, that has to be solved to get the transmissibility matrix.

Upwinding can cause problems in the context of tensorial coefficients: by adding $\mathbf{F}_n^{\text{upw}}$ into Equation (3.81) or (3.82), we multiply $\boldsymbol{\Lambda}_n$ and \mathbf{K} and thus the relative permeability with the absolute permeability. Depending on $\text{upw} = 1$ or $\text{upw} = 2$, one of the products of relative and absolute permeability (from cell 1 or 2) is a product where both types of permeability come from the same cell whereas the other product is a mixed product. For the latter case, it is not guaranteed that the phase permeability satisfies the criteria discussed in Section 2.1.3. Even if both, the absolute permeability as well as the relative permeability are symmetric and positive definite, the phase permeability resulting from the mixed product does not have to satisfy these properties, because the principal directions could be completely different. An entirely unphysical behavior could be the result, for example, a flow in the direction of increasing potential. Furthermore, we

multiply Λ_t^T and Λ_t . This may result in similar problems although the total mobility is supposed to be more smooth and easier to handle numerically.

The following solutions to these problems are suggested: Instead of applying an upstream weighting of the mobilities, only the transported quantity the mobility depends on, namely, the saturation, is weighted. Accordingly, one can write:

$$\mathbf{F}_{nij} = \mathbf{F}_{nij}^{\text{upw}} = \mathbf{F}_{ni}(S^{\text{upw}}). \quad (3.84)$$

Considering the flux balances in Equations (3.81) and (3.82), this means that $\mathbf{F}_{n12} = \mathbf{F}_{n1}(S^{\text{upw}})$ for \mathbf{f}_{12} and $\mathbf{F}_{n21} = \mathbf{F}_{n2}(S^{\text{upw}})$ for \mathbf{f}_{21} . It is assumed that it is not necessary to apply an upwinding scheme to the total mobility Λ_t to calculate the advective flux. To be consistent this assumption is applied also for the other flux terms. For the capillary flux this means that only the fractional flow function is calculated from an upwind saturation S^{upw} . The determination of an upwind direction, which is quite simple for scalar fractional flow functions, however is nontrivial for tensor functions. The reason is that a tensor coefficient like \mathbf{F} can lead to a phase normal flux in opposite direction than the total normal flux or the phase potential difference of two neighboring cells. Therefore, the following procedure is suggested:

1. calculate the phase transmissibilities without upwinding;
2. calculate phase fluxes using the pressure field of the old time step (this is reasonable as in the sequential solution strategy the capillary flux term is also assumed to be known from the old time step and thus completely moved to the right hand side);
3. calculate upwind fractional flow functions, where the directions of the previously calculated phase fluxes determine the upwind direction.

The second problem of possibly ill-posed linear systems for the calculation of the phase transmissibilities, can be addressed as follows: the coefficients \mathbf{f}_{cij} of the vector \mathbf{f}_c are given by

$$\mathbf{f}_{cij} = \mathbf{n}_{ij}^T \mathbf{F}_{nij}^\epsilon \mathbf{n}_{ij} \mathbf{f}_{cij}^{\text{mpfa}} \quad (3.85)$$

where $\mathbf{f}_{cij}^{\text{mpfa}}$ are the coefficients of the flux vector:

$$\mathbf{f}_c^{\text{mpfa}} = \mathbf{T}_n \Phi_c. \quad (3.86)$$

The transmissibility \mathbf{T}_n has to be additionally calculated. Therefore, the flux continuity equations of the MPFA method have to be reformulated to include the fractional flow tensor. As done before the flux balance for face 12 in Figures 3.4 and 3.5 is written as an example, for the O-method:

$$\begin{aligned} & \frac{-\Gamma_{ij} \mathbf{n}_{ij}^T \mathbf{F}_{n12}^{\text{mpfa}} \Lambda_{ti} \mathbf{K}_i}{T_1} \left[\boldsymbol{\nu}_{12} (\bar{\Phi}_{12} - \Phi_i) + \boldsymbol{\nu}_{14} (\bar{\Phi}_{14} - \Phi_i) \right] \\ &= \frac{\Gamma_{ij} \mathbf{n}_{ij}^T \mathbf{F}_{n21}^{\text{mpfa}} \Lambda_{tj} \mathbf{K}_j}{T_2} \left[\boldsymbol{\nu}_{21} (\bar{\Phi}_{21} - \Phi_j) + \boldsymbol{\nu}_{23} (\bar{\Phi}_{23} - \Phi_j) \right] \end{aligned} \quad (3.87)$$

and for the L-method:

$$\begin{aligned} & \frac{-\Gamma_{ij} \mathbf{n}_{ij}^T \mathbf{F}_{n12}^{\text{mpfa}} \Lambda_{ti} \mathbf{K}_i}{T_1} \left[\boldsymbol{\nu}_{12} (\bar{p}_{12} - p_i) + \boldsymbol{\nu}_{14} (\bar{p}_{14} - p_i) \right] \\ & \stackrel{!}{=} \frac{\Gamma_{ij} \mathbf{n}_{ij}^T \mathbf{F}_{n21}^{\text{mpfa}} \Lambda_{tj} \mathbf{K}_j}{T_2} \left[\boldsymbol{\nu}_{21} (\bar{p}_{21} - p_j) + \boldsymbol{\nu}_{2I} (\bar{p}_I - p_j) \right] \end{aligned} \quad (3.88)$$

To ensure that the system of flux balances can always be solved to get a transmissibility matrix we add the condition:

$$\mathbf{F}_n^{\text{mpfa}} = \begin{cases} \varepsilon \mathbf{I}, & \text{if } \lambda(\mathbf{F}_n) < \varepsilon \\ \mathbf{F}_n, & \text{else} \end{cases}, \quad \mathbf{F}_n^\varepsilon = \begin{cases} \mathbf{I}, & \text{if } \lambda(\mathbf{F}_n) \geq \varepsilon \\ \mathbf{F}_n, & \text{else} \end{cases} \quad (3.89)$$

where $\lambda(\mathbf{F}_n)$ are the eigenvalues of \mathbf{F}_n . The condition ensures that no fluxes of zero occur in the system of flux continuity as long as ε is greater than zero. In this case the Matrix \mathbf{A} (Equation (3.1.6)) is always invertible. However, the real fluxes still can become zero or approach zero due to the threshold fractional flow function \mathbf{F}^ε .

3.3.3 Wetting Phase Flux

From Equation (3.80) it is obvious that the wetting phase flux has the same form than the capillary flux (Equation (3.79)). Thus, the MPFA approximation can be written by substituting the capillary potential in Equation (3.86) by the wetting phase potential, the non-wetting phase fractional flow functions of Equations (3.85), and (3.87) or (3.88) by the wetting phase fractional flow function, and the capillary flux by the advective flux:

$$\mathbf{f}_{wij} = \mathbf{n}_{ij}^T \mathbf{F}_{wij}^\varepsilon \mathbf{n}_{ij} \mathbf{f}_{wij}^{\text{mpfa}}, \quad (3.90)$$

$$\mathbf{f}_w^{\text{mpfa}} = \mathbf{T}_w \Phi_w. \quad (3.91)$$

The crucial points concerning the tensorial phase quantities in the MPFA method have already been discussed for the approximation of the capillary flux. The same problems occur for the approximation of the phase fluxes. Thus, according to Equation (3.84), we approximate the wetting phase fractional flow function tensor at a face ij as:

$$\mathbf{F}_{wij} = \mathbf{F}_{wij}^{\text{upw}} = \mathbf{F}_{wi}(S^{\text{upw}}). \quad (3.92)$$

Compared to the capillary flux, which has to be determined for the solution of the pressure equation, the wetting phase flux is needed to solve the saturation transport equation. This means that in a sequential solution strategy the pressure field of the new time step is already known. Thus, the scheme for determining the upwind directions given in Section 3.3.2 for the capillary flux is also applied to the phase fluxes with the exception that the pressure of the old time step in step 2 is substituted by the pressure of the new time step.

If a MPFA method is applied to one-phase flow, the transmissibilities have to be calculated only once in a preprocessing step and do not change during a simulation. Of course, this is different if saturation dependent quantities are included into the transmissibility. In the case of scalar relative permeabilities, the transmissibilities have to be recalculated for every time step, because the total mobility influences the transmissibility matrices. In the case of tensorial relative permeabilities, as discussed in this section, different terms such as the advective term, the gravity term or the capillary pressure term require a different treatment. This leads to different MPFA operators or transmissibilities and increases the computational costs. In the proposed method we need to calculate three different transmissibilities to calculate the different fluxes (advective flux, capillary flux, wetting/non-wetting phase flux). Further, four additional transmissibilities are needed to determine the upwind directions (wetting and non-wetting phase direction for each potential and saturation transport calculation). Using the O-method this leads to seven transmissibility calculations for each grid vertex, for the L-method to seven transmissibilities per MPFA sub-interface. In comparison with the O-method, a system of equations to calculate one transmissibility using the L-method is smaller in the two-dimensional case and much smaller in the three-dimensional case. Thus, the overall costs can be assumed to be comparable, although much more transmissibilities have to be computed for the L-method. Depending on the flow problem, it can be reasonable to determine the upwind directions only once each time step (for both equations).

This would reduce the transmissibility calculations to five, but could also reduce the accuracy. To make further statements about the efficiency different methods have to be investigated. One alternative can be found in *Keilegavlen et al. (2012)* where the authors approximate the phase fluxes using an approximate Riemann solver.

3.3.4 Some Remarks on Upwinding

There exists one crucial difficulty for upwinding in presence of tensorial coefficients, such as the relative permeability, which are saturation dependent and therefore change with time. In general, not only the absolute value but also the direction of such coefficients is saturation dependent and hence the direction of flow can change from one time step to another as the saturation changes. Thus, it is, in general, not possible to base the upwinding decision on the solution of the old time step.

The challenge for a MPFA concept for modelling multi-phase flow is to avoid upwinding whenever this is possible and to find a solution procedure that is sufficiently accurate and computationally efficient if upwind can not be avoided. If Equations (2.54) and (2.55) are solved simultaneously applying a fully implicit scheme the only way out of the upwinding dilemma seems to be the following: First, calculate transmissibility matrices for every possible upwind combination for every interaction volume ($2e4 = 16$ combinations (2-d), $2e12 = 4096$ combinations (3-d)). Second, find and apply kind of heuristic criteria to decide which is the most likely combination. It is obvious, that, on the one hand, the formulation of reasonable criteria can be difficult and, on the other hand, recalculation of the transmissibilities is very expensive (already in 2-d). This consideration is one motivation to use a different model formulation. The reformulation into one equation for the potentials and one equation for the transport of saturation accompanied with a sequential solution strategy allows for the decoupling of some steps. Thus, the upwinding decisions described before are not based on the old solution, but always on information of the new time step that is already available. Of course, this concept also includes some necessary assumptions:

- It is common to use the total mobility without any upwinding because it is a property of the total flow which uses to behave quite smooth within the model domain. We assume that this still holds for tensorial total mobilities. This allows the calculation of the advective flux (Equation (3.78)) without any upwinding.

- The capillary pressure as well as the gravity part are assumed to be known from the old time step and put to the right hand side of the system of equations. This treatment is common if a pressure (or potential) equation and a transport equation (e.g. for saturation) are solved sequentially. Thus, it is assumed that it is also sufficient to base the upwind decision for this flux term on the solution of the old time step.
- In the procedure for determining the upwind directions cell values of the phase quantities are used for the transmissibility calculation. Thus, it is assumed that the upwinding has no influence on the direction of flow but only on the amount of fluid that crosses a cell face.
- Saturation upwinding is applied instead of direct upwinding of the relative permeability. In the homogeneous case this equals relative permeability upwinding. However, saturation upwinding also ensures that the flux approximation accounts for heterogeneous anisotropies and thus, helps to prevent unphysical fluxes (e.g. in opposite direction to the potential gradient).

3.3.5 Tests

In this section, the numerical experiments of *Wolff et al. (2012)* for the O-method and additional results for the L-method are presented to demonstrate and test the capabilities of the proposed treatment of anisotropic relative permeabilities. The first test case from *Eichel et al. (2005)* applies a diagonal relative permeability tensor derived for a horizontally layered system. In such systems, layers of different entry pressures can lead to anisotropic relative permeabilities at a larger scale (e.g. *Saad et al., 1995; Pickup and Sorbie, 1996; Braun et al., 2005; Eichel et al., 2005*). In a second test, full tensor relative permeabilities are used. Considering a layered system, a full tensor could result from an upscaling if the layers are not horizontal but rotated. Of course, there are also other effects that might cause anisotropy of large scale relative permeability functions.

In *Eichel et al. (2005)* flow experiments and numerical simulations of a horizontally layered system are compared. The layers consist of three different soil types (permeability $\mathbf{K}_{\text{fine}} = 6.38 \times 10^{-11} \text{ m}^2$, $\mathbf{K}_{\text{medium}} = 1.22 \times 10^{-10} \text{ m}^2$, $\mathbf{K}_{\text{coarse}} = 2.55 \times 10^{-10} \text{ m}^2$, porosity $\Phi = 0.38$). The setup is shown in Figure 3.45. A DNAPL (Denser Non-Aqueous-Phase Liquid, here TCE) is injected from the top into a domain of 1.2 m length and 0.5 m

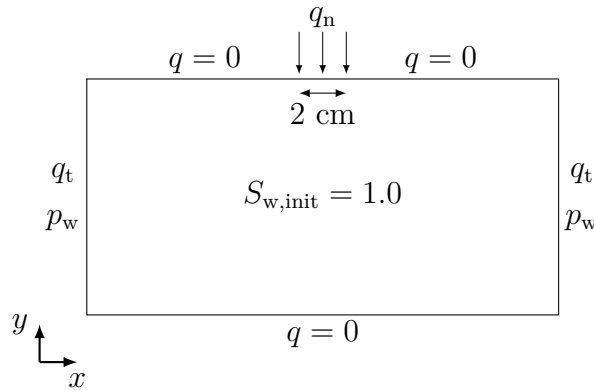


Figure 3.45: Setup of the infiltration experiment.



Figure 3.46: Model domain with the discrete lenses showing the different entry pressures.

height. The upper and lower boundaries are closed for flow, except for the injection area. On the right as well as on the left boundary a hydrostatic pressure profile is assumed. The domain is initially fully water saturated. The location of the layers as well as the entry pressures of the differently permeable layers (entry pressure $p_{d_{\text{fine}}} = 882.9$ Pa, $p_{d_{\text{medium}}} = 539.55$ Pa, $p_{d_{\text{coarse}}} = 353.16$ Pa) are shown in Figure 3.46. On this scale (fine scale) Brooks-Corey parameterizations are used for the capillary pressure-saturation and the relative-permeability-saturation relations (*Brooks and Corey*, 1964). The capillary pressure-saturation curves of the different layers are correlated to the permeabilities according to a Leverett J-function (*Leverett*, 1941). The upscaled capillary pressure function for this system is plotted in Figure 3.47a, the effective relative permeability functions for the two fluids in different coordinate directions are shown in Figure 3.47b (details, see *Eichel et al.*, 2005). The simulated time is 1 hour while the injection is stopped after ~ 50 minutes.

Figure 3.48 shows the saturation distribution of the fine-scale reference solution, which resolves the discrete system of layers on a grid of 60×50 cells (*Wolff et al.*, 2012). For the coarse scale simulations using the proposed MPFA methods for the treatment of

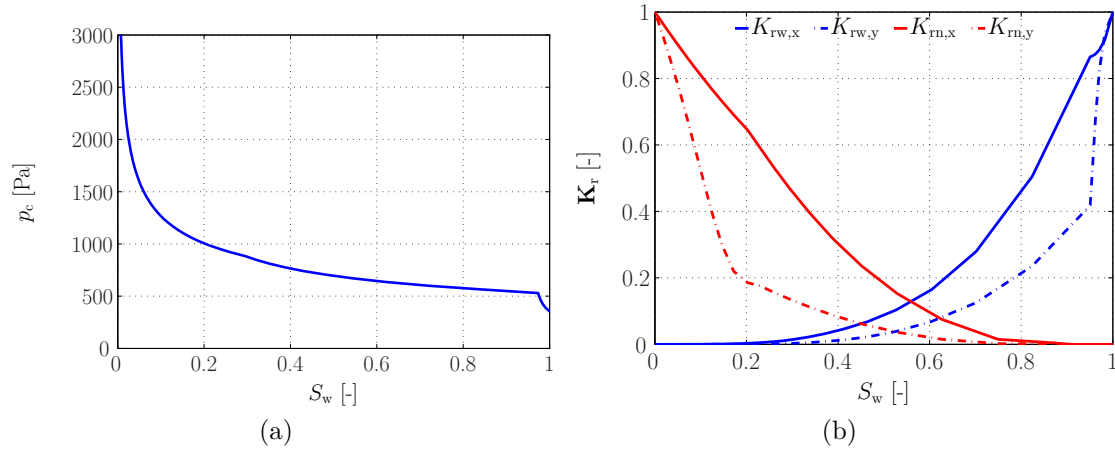


Figure 3.47: Coarse scale constitutive relations (*Eichel et al.*, 2005).

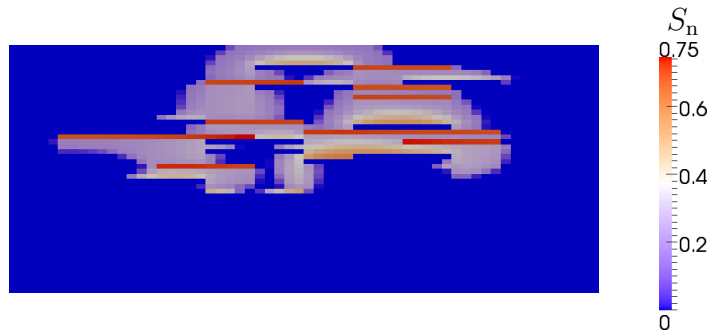


Figure 3.48: Saturation distributions calculated with the fine-scale parameter distribution resolving the lenses.

the anisotropic relative permeability functions three different grid types are applied. All grids, a structured grid and two unstructured grids (Figure 3.49), consist of 60×50 cells. The unstructured grids are chosen to test the case of a non- \mathbf{K} -orthogonal grid. The same amount of TCE is injected in all cases. The results are shown in Figure 3.50 where the results of both methods O- and L-method, are equal. This demonstrates that the proposed approach for treating anisotropic solution dependent parameters is independent of the type of the MPFA. As discussed in more detail in *Wolff et al.* (2012), qualitatively, the numerical models account for the anisotropy well and capture the main features of the discretely layered model. Quantitatively, the horizontal spreading of the infiltrating non-wetting phase is underestimated, whereas the vertical spreading is overestimated. One possible reason are the simplifications applied for the upscaling of the coarse-scale functions in *Eichel et al.* (2005) where gravity effects, for example, are completely neglected. Thus, the qualitative distribution behavior is not further

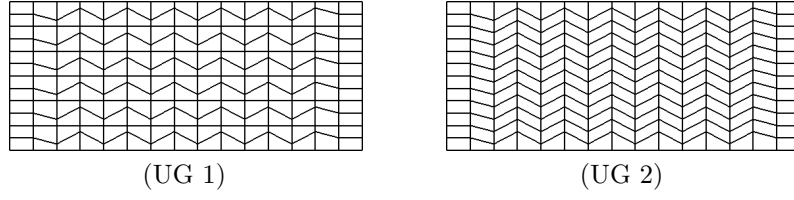


Figure 3.49: The types of unstructured grids used to test the mpfa methods.

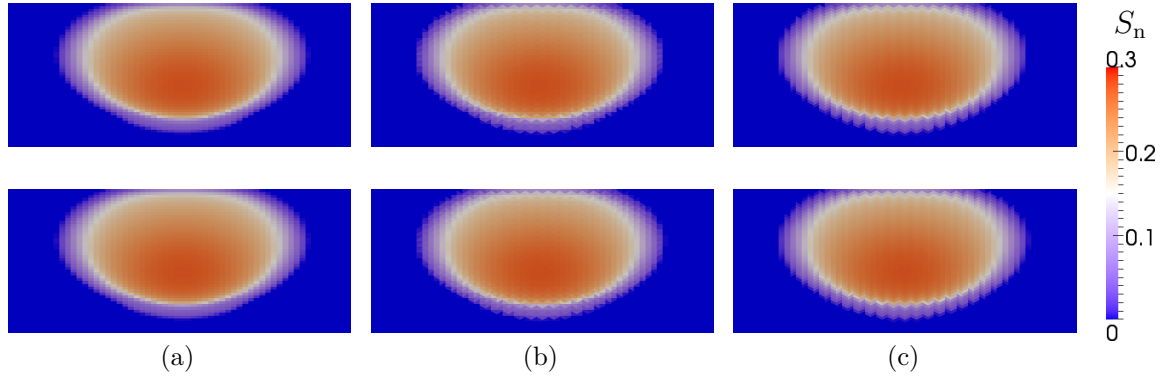


Figure 3.50: Saturation distributions obtained using the O-method (upper row) and the L-method (lower row), on a structured grid (a), an unstructured grid of type UG 1 (b), and an unstructured grid of type UG 2 (c).

investigated here.

Next, the case of a full tensor relative permeability is investigated. A rotation of the orientation of the lenses (Figure 3.46) would result in non-diagonal, full tensor relative permeability functions. However, no validated test scenario like the previous one for the case of the diagonal tensors is available. Thus, the same experimental setup is chosen to test the method (Figure 3.45) and only the relative permeability functions are replaced by the functions derived in *Keilegavlen et al.* (2012), which result from the consideration of vertically segregated upscaling:

$$\mathbf{K}_{r_\alpha} = S_\alpha \begin{pmatrix} 1 & \frac{0.9}{2\pi S_\alpha} (1 - \cos(2\pi S_\alpha)) \\ \frac{0.9}{2\pi S_\alpha} (1 - \cos(2\pi S_\alpha)) & S_\alpha^{\frac{1}{2}} \end{pmatrix}, \quad \alpha \in \{w, n\}. \quad (3.93)$$

The relative permeability function of Equation (3.93) has no physical meaning in the context of this test case, although its derivation is physically motivated. It can be considered a artificially generated full tensor relative permeability function for testing the capabilities of the numerical model and for demonstrating the influence of off-diagonal effects. In comparison to the previous examples not only the anisotropy ratio is

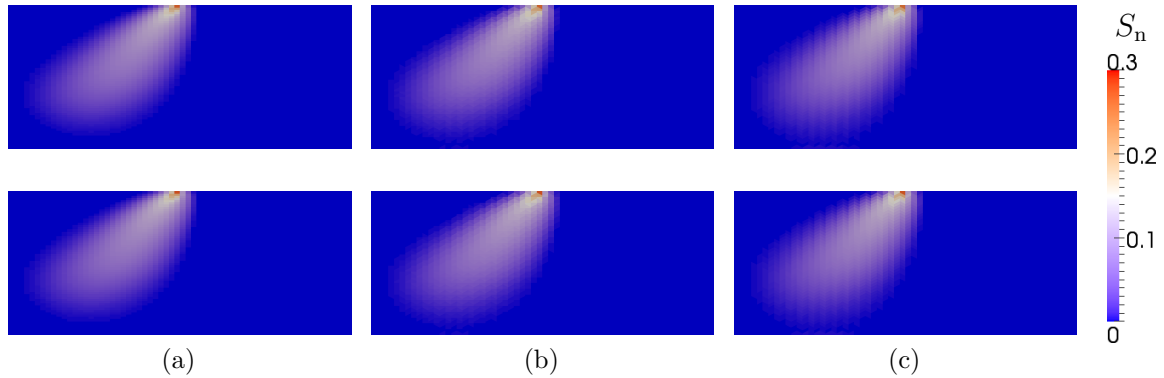


Figure 3.51: Saturation distributions obtained using the O-method (upper row) and the L-method (lower row), on a structured grid (a), an unstructured grid of type UG 1 (b), and an unstructured grid of type UG 2 (c).

saturation dependent, but also the direction of the eigenvectors of the matrices resulting from Equation (3.93). For the O-method this test case has already been investigated in *Wolff et al.* (2012). Again, the simulations are carried out on one structured grid and two unstructured grids (Figure 3.49), which consist of 60×50 elements. The results are plotted in Figure 3.51. Comparing these results with the results of the diagonal tensor case (Figure 3.50) it is obvious that off-diagonal effects can have a major impact and that this effect is described well by both numerical methods. The infiltrating non-wetting phase only spreads into the left side of the domain, whereas the spreading in the diagonal case is symmetric. The results are similar for the different types of grids chosen for these calculations where none of the grids is \mathbf{K} -orthogonal in the case of the full tensor relative permeability functions.

Finally, the method is combined with local grid adaption (Section 3.2). The results are shown in Figure 3.52 for both test cases and for a structured (Figure 3.52a) and an unstructured grid (Figure 3.52b). The structured macro grid consists of 15×12 cells, allowing two refinement levels, the unstructured macro grid of 5×4 cells, allowing 4 refinement levels. For the previous cases without grid adaption the cell size is chosen such that the discretization length in x -direction is exactly the injection width (2 cm). This is also the case for the adaptive structured grid and ensures that the same amount of fluid is injected and a similar pressure gradient develops. The result for both tests (Figure 3.52a) are equal to the results without grid adaption, but using considerably less cells. The cells of the finest grid level of the unstructured grids are smaller with a discretization length in x -direction of only 1.5 cm. Thus, the injection rate is slightly increased to inject the same amount of fluid. However, this results in slightly different

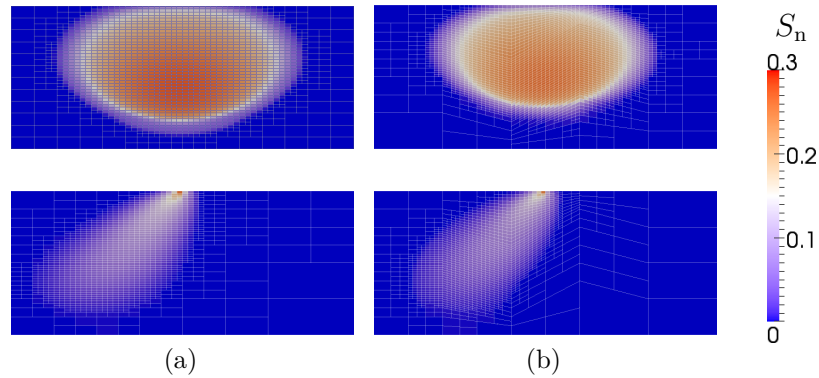


Figure 3.52: Saturation distributions obtained using the adaptive L-method for the case of the diagonal relative permeability tensor (upper row) and full relative permeability tensor (lower row), on a structured grid (a), and an unstructured grid of type UG 1 (b).

pressure gradients and therefore velocities. Additionally, the finer grid leads to a reduced numerical diffusion. In consequence, the fluid distribution is slightly different to the distributions shown before, although the behavior is qualitatively equal.

The tests showed that the proposed treatment strategy for tensorial solution dependent coefficients, namely relative (phase) permeabilities, enables us to describe the anisotropic character of diagonal as well as full tensors, and for \mathbf{K} -orthogonal as well as non- \mathbf{K} -orthogonal grids. Further, it is demonstrated that the concept is applicable for different types of MPFA methods (here, O-method and L-method) and can also be combined with the extension for non-conforming adaptive grids presented in Section 3.2. This allows to considerably increase the efficiency of the method.

Summary In this chapter, numerical methods based on MPFA for modeling the two-phase flow equations introduced in Chapter 2 were developed and validated on various test problems. The tests showed that the methods are able to approximate important two-phase flow features such as saturation discontinuities due to shock fronts or material interfaces, or capillary diffusion very well. Moreover, they are able to account for the effects of anisotropic coefficients which, for example, appear in the coarse-scale equations very well. Finally, the ability of the MPFA L-method to treat hanging nodes which appear in non-conforming adaptive grids could be clearly demonstrated. This is important, in particular, regarding the selection of a method for the subsequent use in a multi-scale

approach. Thus, the MPFA L-method which is available for the two-dimensional and the three-dimensional case is used in the following for the multi-scale modeling.

4 Upscaling and Multi-Scale Modeling

In Chapter 2 the mathematical models for describing immiscible two-phase flow are introduced for a fine and a coarse Darcy scale. In Chapter 3 numerical methods for solving the two-phase flow equations are introduced and developed which are capable of treating non-conforming adaptive grids as well as tensorial relative permeability functions which appear in the coarse-scale equations.

In the following chapter, a set of upscaling algorithms is introduced which allows the calculation of the coarse-scale parameters appearing in Equations (2.54) - (2.58) (Section 4.1). Moreover, a novel multi-scale approach is developed which combines the numerical upscaling method with an adaptive grid where the focus is on the development of an appropriate adaptation strategy (Section 4.2). Sections 4.1 and 4.2 are to a large extent part of *Wolff et al.* (2013b). Both the numerical upscaling and the multi-scale concept are validated and tested by means of several test scenarios.

4.1 Upscaling

This section, describes how the different effective coarse-scale quantities appearing in Equations (2.54), (2.55) and (2.60) can be determined. Assuming that a fine-scale distribution of parameters is known, the model domain is discretized using a coarse-scale mesh (Figure 4.1). All effective quantities are now calculated for each coarse grid block. Thus, the porous medium can also be heterogeneous on the coarse scale. The choice of a single method is at first motivated by efficiency. The solution of the global flow problem by the multi-scale method including upscaling (or downscaling) steps should be computationally much cheaper than the direct solution on the fine scale. Second, the efficient parameters should be able to account for important fine-scale flow features.

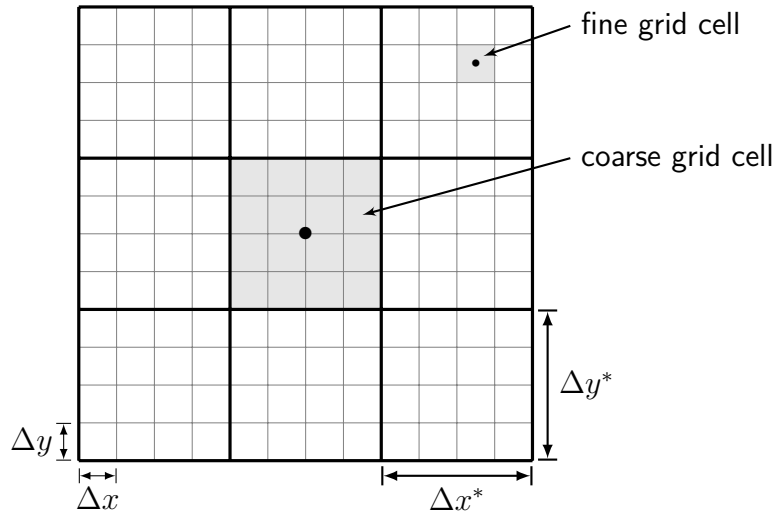


Figure 4.1: Sketch of a multi-scale grid.

4.1.1 Effective Porosity

Porosity is defined as the volume fraction of pore space:

$$\phi = \frac{V_p}{V} \quad (4.1)$$

where V is the representative elementary volume (REV) of the porous medium and V_p is the pore volume in the REV. Similar, the coarse-scale porosity is defined as:

$$\phi^* = \frac{V_p^*}{V^*}. \quad (4.2)$$

The coarse-scale pore volume can be calculated from the fine-scale porosity as:

$$V_p^* = \int_{V^*} \phi dV. \quad (4.3)$$

Inserting Equation (4.3) in Equation (4.2) yields an effective (averaged) coarse-scale porosity

$$\phi^* = \frac{1}{V^*} \int_{V^*} \phi dV. \quad (4.4)$$

The porosity of each coarse grid block of a simulation grid can then be calculated from high-resolution fine-scale quantities as:

$$\phi^* = \frac{1}{V^*} \sum_{n^*} \phi V \quad (4.5)$$

where n^* is the number of fine grid cells in a coarse grid block and ϕ and V are the porosity and volume respectively of a fine grid cell.

4.1.2 Effective Capillary Pressure

The calculation of effective capillary pressure functions is based on the assumption of local capillary equilibrium. This is a common assumption for determining capillary pressure curves for fine-scale models, either experimentally, or by upscaling pore-scale models. It allows us to use a macroscopic percolation approach such as that suggested and investigated in *Kueper and McWhorter (1992)* or *Yortsos et al. (1993)*. The macroscopic percolation theory is similar to the percolation theory used in pore network modeling. However, instead of different pores and/or pore throats, the points of the percolation lattice are assigned to blocks of a heterogeneous porous medium, which have a certain porosity, permeability, and capillary pressure function. The key idea of a percolation method is to check if and how a physical process can propagate from one grid point to a neighboring point. The origin of as well as the criteria for the propagation depend on the process and on the kind of problem that is to be modeled. By definition a pressure is a scalar quantity. Thus, the effective capillary pressure must not depend on direction. To ensure this, we allow the complete surroundings of a coarse grid block to be the origin of a propagation, instead of choosing, for example, one boundary side as the inlet and another as the outlet. Further, two processes are distinguished – drainage and imbibition.

Figure 4.2 schematically shows one coarse grid block. At the boundary, a uniform pressure boundary condition p_{bc} is specified. Starting from the boundary, the invasion condition is checked. Two examples are illustrated by the hatched cells in Figure 4.2. The arrows indicate cell-cell interfaces for which the invasion condition has to be checked once the hatched cells are invaded. The grey cells mark the propagation path. Cells inside the domain can only be invaded if a path to the boundary exists.

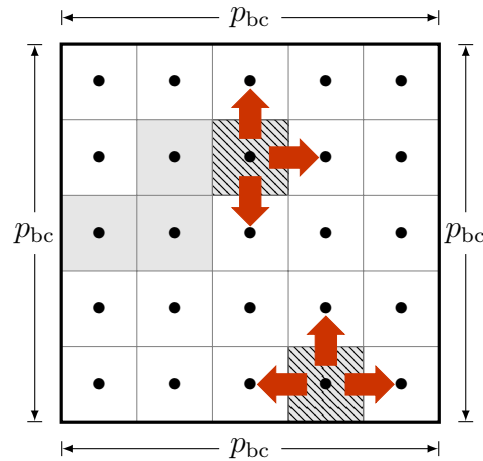


Figure 4.2: Schematic of percolation for capillary pressure upscaling.

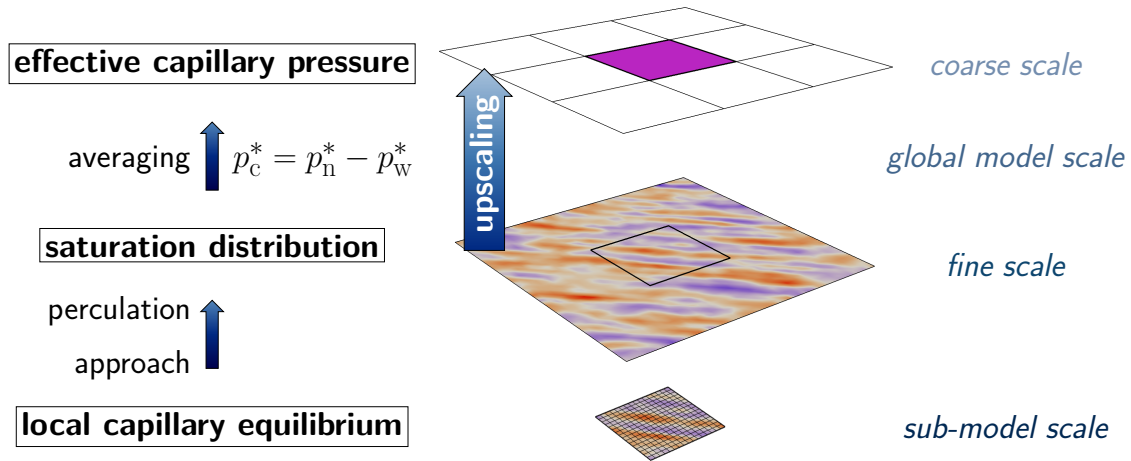


Figure 4.3: Workflow of the capillary pressure upscaling.

The procedure of the capillary pressure upscaling is sketched in Figure 4.3. Based on the assumption of capillary equilibrium, a saturation distribution for a coarse grid block can be obtained from the percolation approach. The effective capillary pressure results as the difference between the phase pressures for the given saturation distribution. In more detail, the macroscopic percolation algorithm for both drainage and imbibition works as follows:

- 1) Determine the initial pressure boundary condition (p_{bc}) from the capillary-pressure-saturation functions of the fine-scale cells along the boundary of a coarse grid block.

- 2) Check whether the boundary cells are invaded at the given boundary pressure.
- 3) For all boundary cells which are invaded, check whether their neighboring cells are invaded.
- 4) For all neighboring cells which are invaded, check whether their neighboring cells are invaded.
- 5) Repeat step 4) until no more neighboring cells can be invaded.
- 6) Calculate and store the averaged coarse-scale saturation S_w^* and the effective coarse-scale capillary pressure p_c^* .
- 7) Increase/decrease the boundary pressure p_{bc} and restart at step 2) until a sufficient number of data points for the $p_c^*(S_w^*)$ function is available.

Once the percolation paths are determined (step 6), the saturation distribution is defined by the inverse capillary-pressure-saturation function:

$$S_{ei} = p_{ci}^{-1}(p_{bc}), \quad S_{wi} = S_e^{-1}(S_{ei}) \quad (4.6)$$

All cells that are not invaded are still fully saturated with the displaced fluid. The effective coarse-scale parameters can now be calculated as a volume average of the fine-scale distribution as:

$$S_w^* = \frac{1}{\phi^* V^*} \int_{V^*} S_w \phi dV \quad (4.7)$$

$$p_c^* = \frac{1}{S_n^* \phi^* V^*} \int_{V^*} p_n S_n \phi dV - \frac{1}{S_w^* \phi^* V^*} \int_{V^*} p_w S_w \phi dV \quad (4.8)$$

Taking advantage of the capillary equilibrium assumption, we can simplify the effective capillary pressure definition to:

$$p_c^* = \frac{1}{S_n^* \phi^* V^*} \int_{V^*} p_c S_n \phi dV. \quad (4.9)$$

In discrete notation, the effective capillary pressure and saturation of a coarse grid block

are calculated as

$$S_w^* = \frac{1}{\phi^* V^*} \sum_{n^*} S_w \phi V \quad (4.10)$$

$$p_c^* = \frac{1}{S_n^* \phi^* V^*} \sum_{n^*} p_c S_n \phi V \quad (4.11)$$

where n^* is the number of fine grid cells in a coarse grid block and ϕ , V , S_w , and S_n are the porosity, volume, wetting saturation, and non-wetting saturation respectively of the fine grid cells. The average used for the pressure is the intrinsic phase average, which is commonly used for pressure averaging and assumes that the centroid of the phase is equal to the centroid of the coarse grid block. More complicated approaches also exist which, for example, include geometric information on the fluid distribution inside the coarse grid block in the averaging (e.g. *Nordbotten et al.*, 2008). Depending on the structure of the porous medium such approaches could increase the quality of the upscaling. However, the assumption of having the same centroid for phase volume and grid block also seems to be quite reasonable if we assume we have an REV (Representative Elementary Volume). The question whether we can really get an REV is indeed crucial and is discussed in more detail in Section 4.1.5.

Drainage

In the case of drainage, the domain is initially saturated by the wetting phase and the percolation is controlled by the entry (displacement) pressure $p_d = p_c(S_e = 1)$. The coarse-scale entry pressure is given by the lowest fine-scale entry pressure along a coarse grid-block boundary. As soon as the boundary pressure exceeds this coarse-scale entry pressure, non-wetting fluid can invade (Figure 4.2). Thus, starting from this entry pressure, the boundary pressure is increased step by step until the domain is saturated by the displacing non-wetting phase. The invasion condition for drainage is: A fine-scale cell i is invaded by the non-wetting fluid if a neighboring cell j has a non-wetting phase connection to the domain boundary, which means its effective wetting phase saturation S_{ej} is less than 1, and

$$p_{ci}(S_{ei} = 1) < p_{bc}. \quad (4.12)$$

Imbibition

During imbibition, the non-wetting phase is displaced by the wetting phase. Thus, the domain is initially saturated by the non-wetting fluid. In the drainage case, the displaced wetting phase is continuously connected to the boundary. By contrast, in the case of imbibition the connection of the displaced non-wetting phase to the boundary is controlled by the maximum capillary pressure of a cell $p_{c,\max} = p_c(S_e = 0)$. The lowest fine-scale $p_{c,\max}$ along a coarse grid-block boundary determines the maximum of the effective capillary pressure function. If the boundary pressure is decreased below this maximum, non-wetting fluid can leave the domain and wetting phase can invade (Figure 4.2). Thus, starting from the maximum pressure, the boundary pressure is decreased step by step until the non-wetting phase is displaced. However, as pointed out before, the displaced phase is not necessarily continuous in the case of imbibition and can be disconnected from the boundary. This can lead to trapping if cells containing the non-wetting phase become completely surrounded by cells fully saturated by the invading wetting phase. In this case, the boundary pressure is decreased until a residual saturation of the non-wetting phase is reached. The invasion condition for imbibition is: A fine-scale cell i can be invaded by the wetting fluid if a neighboring cell j has a wetting phase connection to the domain boundary, which means its effective wetting phase saturation S_{ej} is greater than 0. Additionally, the non-wetting fluid must be able to leave the cell. Therefore, a non-wetting phase connection to the boundary is necessary and the pressure condition

$$p_c(S_{ei} = 0) > p_{bc} \quad (4.13)$$

has to be fulfilled. If cells contain trapped non-wetting phase their state is frozen and they are not considered further in the percolation procedure.

4.1.3 Effective Absolute Permeability

In recent decades, many methods for determining the effective permeabilities of heterogeneous porous media have been developed and investigated. An overview is given in for example *Renard and de Marsily* (1997). In this work, the focus is on numerical upscaling techniques which use local fine-scale solutions of a single-phase pressure equation. To account for heterogeneous fine-scale structures, an effective permeability should in general be a tensor. A method for calculating symmetric and positive definite effective permeability tensors was developed in *Durlofsky* (1991). To guarantee these properties of

the tensor, periodic boundary conditions are applied to the local fine-scale problems. In *Wen et al.* (2003), the method is improved by the use of border regions, i. e. by including the fine cells surrounding the coarse grid block for which an effective permeability is calculated. Thus, effects of connectivity are accounted for better and local boundary condition effects are weakened. The latter is crucial, especially for an accurate calculation of a full effective permeability tensor. In this work, the method proposed in *Wen et al.* (2003) is combined with effective flux boundary conditions derived in *Wallstrom et al.* (2002a) and *Wallstrom et al.* (2002b) to include global effects in the local calculations. Both methods will be explained in more detail in Section 4.1.4, where they are extended for the calculation of full relative permeability tensors.

4.1.4 Effective Relative Permeability

The effective coarse-scale relative permeability is assumed to be a full second-order tensor (Equation 2.57). The basic ideas of the numerical upscaling are similar to those proposed in *Pickup and Sorbie* (1996). As mentioned before, one of the main requirements for the upscaling step is efficiency. Thus, time-consuming unsteady two-phase flow simulations on the fine scale have to be avoided. Additionally, it should be possible to separate the complete coarse-scale parameter calculation from the large-scale solution procedure in a preprocessing step. The method introduced in the following combines ideas of *Pickup and Sorbie* (1996) with two-phase flow extensions of the methods of *Wen et al.* (2003) and *Wallstrom et al.* (2002a) and a macroscopic percolation method (see Section 4.1.2).

Steady-state methods still have a wide application for determining relative permeability curves experimentally (e.g. *Honarpour and Mahmood*, 1988). The setup for the numerical measurements presented in the following is based on the idea of experimental steady-state measurements. Of course, the acting forces on the core scale are not comparable to those on the field scale. On the core scale, the steady state for a given flux is dominated by capillary forces. On larger scales, forces like gravitational forces gain a stronger influence. However, investigation of flow through heterogeneous porous media shows that, if capillary effects are not negligible, capillary pressure heterogeneities still locally dominate the preferred directions of flow, although the fluxes can be driven by a pressure gradient or by gravity. The natural parameter to include the directional effects induced by capillary pressure heterogeneities is the effective phase permeability and hence the relative permeability.

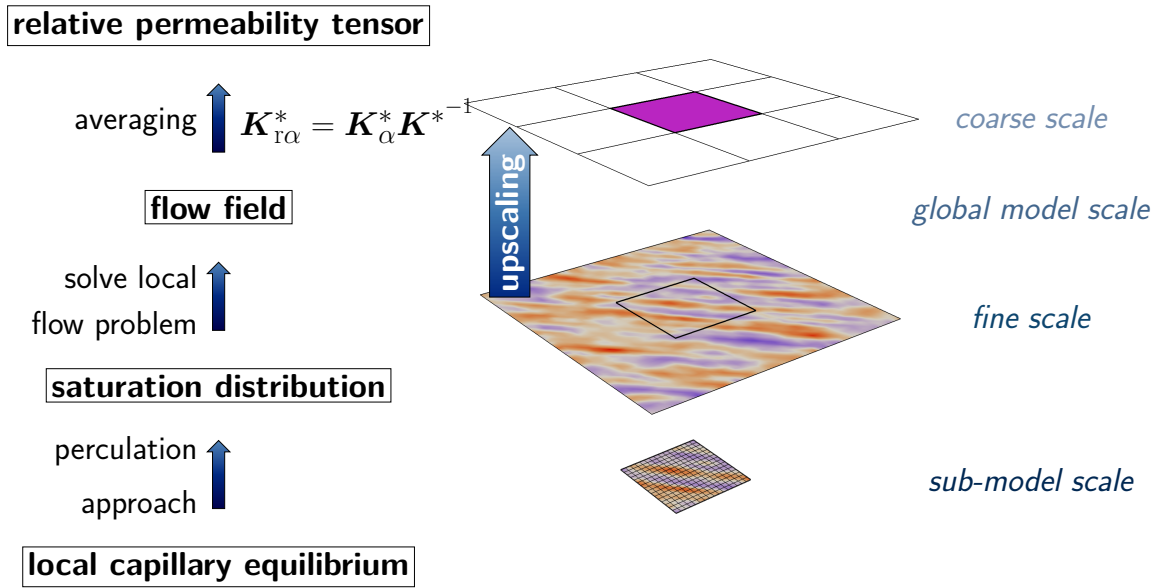


Figure 4.4: Workflow of the relative permeability upscaling.

On this basis, the idea of this method is to construct the effective phase permeabilities based on saturation patterns whose preferential flow paths account for the capillary pressure heterogeneities. If capillary pressure is neglected and the relative permeability distribution is homogeneous (this is a meaningful assumption if capillary pressure is neglected), there will always be a uniform saturation distribution at steady state, which only depends on the assumed boundary condition. Following the idea of border regions introduced in *Wen et al. (2003)*, the sub-domains for the calculation of the effective relative permeability are also extended. An exemplary setup is shown in Figure 4.5 where the dashed rectangle around coarse cell i represents the local sub-domain used for the fine-scale calculations. The size of the border region can be varied. The influence of the size of the border regions on the parameter upscaling is investigated in, for example, *Wen et al. (2003)* or *Chen et al. (2003)*. In general, a larger radius reduces boundary effects and increases the amount of information about the fine-scale parameter distribution and hence, increases the quality of the upscaled parameters. However, it also increases the number of degrees of freedom of the local fine-scale system. Therefore, the choice of the radius is always a choice between accuracy and efficiency. In this work, border regions with a radius between 0.5 and 1 coarse-scale discretization widths are used.

As described for the capillary pressure upscaling in Section 4.1.2, the macroscopic percolation method is used to construct the saturation distributions. Thus, expensive time-dependent fine-scale simulations can be avoided. The general procedure is similar

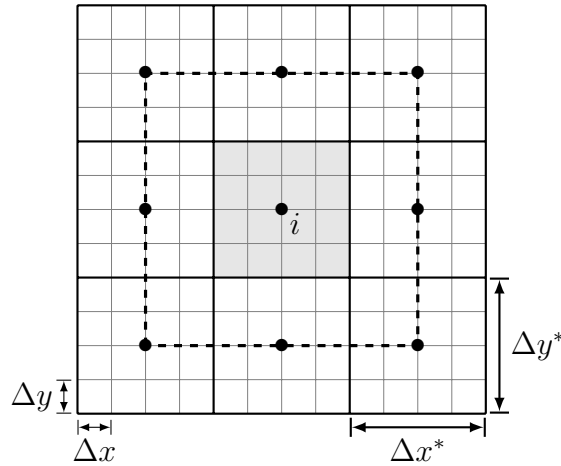


Figure 4.5: Sketch of a multi-scale grid. The dashed square marks a potential local sub-domain for the numerical permeability upscaling.

to the one described in Section 4.1.2. However, the requirements for the calculation of effective relative permeabilities are slightly different.

First, the local sub-domain can be larger than the coarse grid block. This is a problem, because it is not the border region that should control the invasion behavior, but the coarse grid block for which the effective parameter is determined. Thus, the propagation of the invading fluid is again initialized at the coarse grid-block boundary instead of the local sub-domain boundary (Figure 4.6). This means that the percolation procedure works as described for the effective capillary pressure, but the propagation of the invading fluid can be in both directions, into the coarse grid block, or into the border region. In doing so, we ensure that entry effects at the coarse grid block boundary are accounted for correctly.

Second, relative permeability is a quantity which is related to flow. Fluxes through a coarse grid block can only appear if boundaries of the block are connected by flow paths. Thus, in a second step the percolation paths have to be checked with regard to connectivity and only connected paths are further considered for the calculation of the relative permeability tensor (Figure 4.7). If only disconnected paths exist, this leads to a kind of coarse-scale residual saturation.

The general workflow for the relative permeability upscaling is sketched in Figure 4.4. A macroscopic percolation approach is applied for constructing a fine-scale saturation distribution for a coarse grid-block and the surrounding border region. Given the

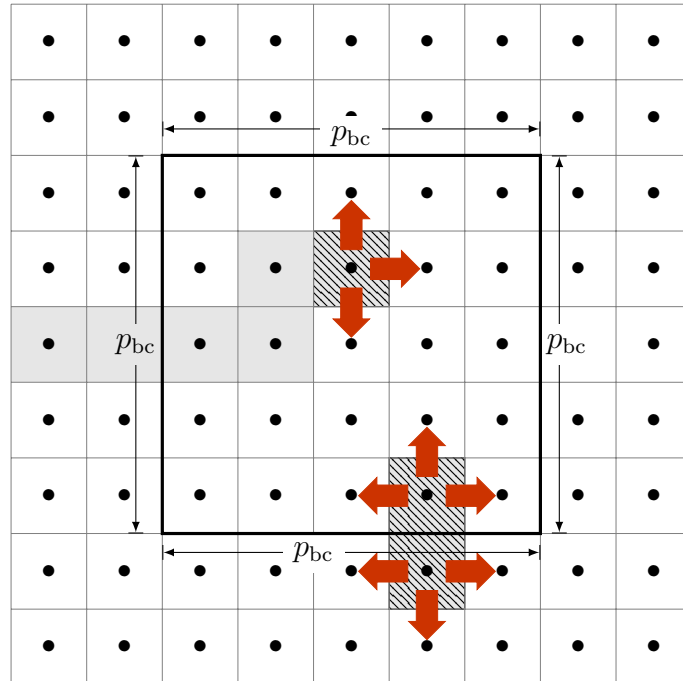


Figure 4.6: Schematic of percolation for a relative permeability upscaling.

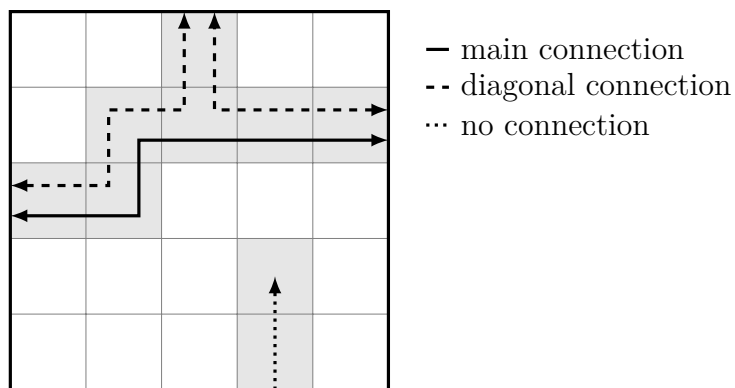


Figure 4.7: Sketch of the percolation pattern after one percolation step.

saturation distribution, a flow problem is solved on the local sub-domain and an effective relative permeability can be constructed from the fine-scale results.

In more detail, the algorithm for the effective relative permeability calculation can be summarized as follows:

- 1) Determine the saturation distribution:
 - a) Set the pressure boundary condition (p_{bc}) along the boundary of a coarse grid block.
 - b) Check whether the cells intersecting at this boundary are invaded.
 - c) For all cells which are invaded, check whether their neighboring cells are invaded.
 - d) For all neighboring cells which are invaded, check whether their neighboring cells are invaded.
 - e) Repeat step d) until no more neighboring cells can be invaded.
 - f) Calculate and store the averaged coarse-scale saturation S_w^* (Equation 4.7).
- 2) Check the connectivity of the saturation paths.
- 3) Given the saturation distribution, calculate the effective flux boundary conditions.
- 4) Solve the fine-scale pressure equation:

$$\nabla \cdot [-\lambda_t \mathbf{K} (\nabla p_w + f_n \nabla p_c)] = 0$$

- 5) Calculate the effective grid-block velocity \mathbf{v}_α^* and pressure gradient ∇p_α^* from the fine-scale solution.
- 6) Calculate the effective relative permeability tensor.
- 7) Restart at step 1) until a sufficient number of data points for the $\mathbf{K}_{r,\alpha}^*(S_w^*)$ function is available.

Construction of the Relative Permeability Tensor

Second-order phase permeability tensors can be calculated by an extension of the method of *Wen et al.* (2003), which was originally derived for absolute permeability upscaling and single-phase flow. The data base for the calculation is generated by solving several local fine-scale problems, one for each space dimension. The local boundary conditions are chosen accordingly (see Section 4.1.4). In the general three-dimensional case the following system of equations has to be solved for the components of the phase permeability tensors:

$$\begin{pmatrix}
 \frac{\partial p_\alpha^{*x}}{\partial x} & \frac{\partial p_\alpha^{*x}}{\partial y} & \frac{\partial p_\alpha^{*x}}{\partial z} & 0 & 0 & 0 & 0 & 0 & 0 \\
 0 & 0 & 0 & \frac{\partial p_\alpha^{*x}}{\partial x} & \frac{\partial p_\alpha^{*x}}{\partial y} & \frac{\partial p_\alpha^{*x}}{\partial z} & 0 & 0 & 0 \\
 0 & 0 & 0 & 0 & 0 & 0 & \frac{\partial p_\alpha^{*x}}{\partial x} & \frac{\partial p_\alpha^{*x}}{\partial y} & \frac{\partial p_\alpha^{*x}}{\partial z} \\
 \frac{\partial p_\alpha^{*y}}{\partial x} & \frac{\partial p_\alpha^{*y}}{\partial y} & \frac{\partial p_\alpha^{*y}}{\partial z} & 0 & 0 & 0 & 0 & 0 & 0 \\
 0 & 0 & 0 & \frac{\partial p_\alpha^{*y}}{\partial x} & \frac{\partial p_\alpha^{*y}}{\partial y} & \frac{\partial p_\alpha^{*y}}{\partial z} & 0 & 0 & 0 \\
 0 & 0 & 0 & 0 & 0 & 0 & \frac{\partial p_\alpha^{*y}}{\partial x} & \frac{\partial p_\alpha^{*y}}{\partial y} & \frac{\partial p_\alpha^{*y}}{\partial z} \\
 \frac{\partial p_\alpha^{*z}}{\partial x} & \frac{\partial p_\alpha^{*z}}{\partial y} & \frac{\partial p_\alpha^{*z}}{\partial z} & 0 & 0 & 0 & 0 & 0 & 0 \\
 0 & 0 & 0 & \frac{\partial p_\alpha^{*z}}{\partial x} & \frac{\partial p_\alpha^{*z}}{\partial y} & \frac{\partial p_\alpha^{*z}}{\partial z} & 0 & 0 & 0 \\
 0 & 0 & 0 & 0 & 0 & 0 & \frac{\partial p_\alpha^{*z}}{\partial x} & \frac{\partial p_\alpha^{*z}}{\partial y} & \frac{\partial p_\alpha^{*z}}{\partial z} \\
 0 & 1 & 0 & -1 & 0 & 0 & 0 & 0 & 0 \\
 0 & 0 & 1 & 0 & 0 & 0 & -1 & 0 & 0 \\
 0 & 0 & 0 & 0 & 0 & 1 & 0 & -1 & 0
 \end{pmatrix}
 \begin{pmatrix}
 K_{\alpha,xx}^* \\
 K_{\alpha,xy}^* \\
 K_{\alpha,xz}^* \\
 K_{\alpha,yx}^* \\
 K_{\alpha,yy}^* \\
 K_{\alpha,yz}^* \\
 K_{\alpha,zx}^* \\
 K_{\alpha,zy}^* \\
 K_{\alpha,zz}^*
 \end{pmatrix}
 = \mu_\alpha
 \begin{pmatrix}
 v_{\alpha,x}^{*x} \\
 v_{\alpha,y}^{*x} \\
 v_{\alpha,z}^{*x} \\
 v_{\alpha,x}^{*y} \\
 v_{\alpha,y}^{*y} \\
 v_{\alpha,z}^{*y} \\
 v_{\alpha,x}^{*z} \\
 v_{\alpha,y}^{*z} \\
 v_{\alpha,z}^{*z} \\
 0 \\
 0 \\
 0
 \end{pmatrix}
 \quad (4.14)$$

Lines 1 to 9 of Equation (4.14) relate average velocities $v_{\alpha,i}$ to average pressure gradients $\frac{\partial p_\alpha^*}{\partial i}$ via effective phase permeabilities $K_{\alpha,ij}^*$, $i = x, y, z$ and $j = x, y, z$. The averages result from the local fine-scale simulations in different space directions ($()^x$, $()^y$, $()^z$), and μ_α is the phase viscosity. Lines 10 to 12 of Equation (4.14) include conditions which ensure that the permeability tensor is symmetric. The overdetermined system of equations can be solved as a linear least-squares problem (*Wen et al.*, 2003). Besides symmetry, positive definiteness is an important property. If a phase is present and hence its saturation S_α is greater than 0, a phase permeability tensor which is not positive definite can lead to unphysical flow behavior. Such tensors mostly occur if the local sub-problem is not properly defined or bad average volumes are chosen. However, experience shows that in most cases the tensors are positive definite. In the two-dimensional case the system size reduces to five equations: one for each entry of the 2×2 permeability matrix and one for the symmetry condition. Once the phase permeability is calculated, the relative

permeability can be obtained from

$$\mathbf{K}_{r\alpha}^* = \mathbf{K}_\alpha^* \mathbf{K}^{*-1}. \quad (4.15)$$

The crucial point in the upscaling procedure is the calculation of the average pressure gradients and the average velocities. A straightforward approach, which is also used for single phase flow methods, is applying a simple volume averaging to the fine-scale velocities and gradients:

$$\nabla p_\alpha^* = \frac{1}{V^*} \int_{V^*} \nabla p_\alpha dV \quad (4.16)$$

$$\mathbf{v}_\alpha^* = \frac{1}{V^*} \int_{V^*} \mathbf{v}_\alpha dV. \quad (4.17)$$

The definition of an upscaled velocity as volume average of fine-scale velocities is, although this approach is rather simple, in line with a variety of theoretical works addressing upscaling of single-phase or multi-phase flow in porous media (e.g. *Quintard and Whitaker, 1988; Whitaker, 1998; Nordbotten et al., 2007b*). In comparison with the velocity, one obvious approach for defining a coarse-scale pressure gradient does not exist. Equation (4.16) defines the effective pressure gradient as the average of the fine-scale gradients. Darcy's law is based on the potential theory where a velocity is defined as the gradient of a potential field. In case of Darcy's law the potential field is the pressure potential field and the gradients are multiplied with supplementary coefficients including material properties to result the Darcy velocity. Nevertheless, the pressure gradient itself like the Darcy velocity is a potential velocity. Thus, a treatment of the pressure gradient analogous to the velocity is justifiable. An alternative approach is motivated by the coarse-scale equations resulting from averaging theory, where the effective pressure gradient is, per definition, the gradient of an average pressure:

$$\nabla p_\alpha^* = \nabla \{p_\alpha\}. \quad (4.18)$$

A common definition for the averaging operator $\{\cdot\}$ is the intrinsic phase average:

$$\{p_\alpha\} = \langle p_\alpha \rangle_\alpha = \left(\frac{1}{S_\alpha^* \phi^* V^*} \int_{V^*} p_\alpha S_\alpha \phi dV \right) \quad (4.19)$$

Inserting Equation (4.19) in Equation (4.18), an effective coarse-scale pressure gradient can be defined as derived in *Korteland et al.* (2010) as:

$$\nabla p_\alpha^* = \frac{1}{S_\alpha^* \phi^* V^*} \left(- \langle p_\alpha \rangle_\alpha \int_{\partial V^*} \mathbf{n} S_\alpha \phi dA + \int_{\partial V^*} \mathbf{n} p_\alpha S_\alpha \phi dA \right) \quad (4.20)$$

where \mathbf{n} is the normal vector along the surface of an average volume (along the faces of a coarse grid block). In Equation (4.20) the pressure and saturation distribution along the boundary of a coarse grid block determines the effective coarse-scale gradient. It is obvious that this can result in gradients which are different from gradients calculated from Equation (4.16). Due to the reformulation, the coarse-scale gradient operator has vanished from the right hand side of Equation (4.20). Thus, the coarse-scale pressure gradient can be directly calculated from the scalar fine-scale quantities. More complex approaches to define the averaging operator $\{\cdot\}$, for example the approach of *Nordbotten et al.* (2008), may not allow such a reformulation and thus require alternative reconstruction strategies. A possible approach is presented in *Nordbotten et al.* (2010), where the authors explicitly discuss the choice of the pressure average with regard to numerical upscaling.

Following, an alternative approach to reconstructing effective velocities and gradients is proposed, which is fundamentally different, although it is motivated by the aforementioned methods and work. To be consistent, both effective velocity and pressure gradient are calculated applying the same method. As explained before this can be justified by the potential theory, which defines a velocity as the gradient of a potential field. Thus, a pressure gradient is a potential velocity and a Darcy velocity which is just an extended pressure gradient is a quantity of the same type. The basic idea is that numerical upscaling should never be considered in isolation but in combination with a numerical method. In a finite volume context, fluxes at cell faces are crucial. Thus, the reconstruction is based on fluxes through coarse cell faces:

$$q_{\alpha n}^* = \sum_i \mathbf{v}_{\alpha i} \mathbf{n}_i A_i \quad (4.21)$$

$$q_{\nabla \alpha n}^* = \sum_i (\nabla p_\alpha)_i \mathbf{n}_i A_i \quad (4.22)$$

Equations (4.21) and (4.22) give the fluxes through coarse cell face n , which are the sum of fine-scale fluxes through the fine cell faces i . Given these coarse-scale fluxes, we can construct a coarse-scale velocity and pressure gradient at a reference element. Figure 4.8a exemplary shows the coarse cell face fluxes from a top view on the x-z plane.

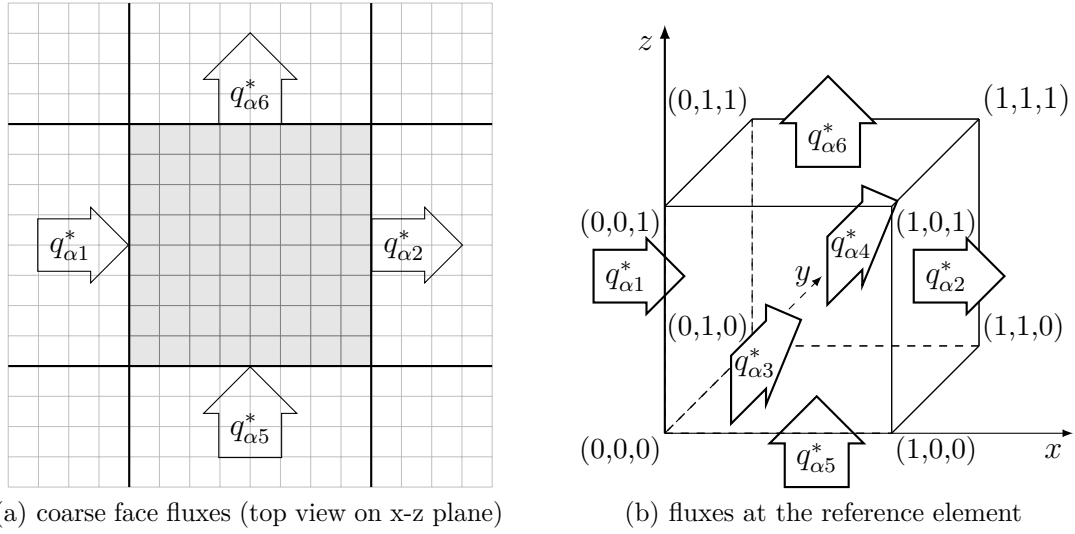


Figure 4.8: Transfer of average face fluxes from a coarse grid cell (a) to a reference element (b).

The corresponding fluxes at the reference element are sketched in Figure 4.8b. The resulting reference velocities and reference gradients can be calculated as:

$$\tilde{v}_{\alpha,x}^* = \frac{q_{\alpha 1}^* + q_{\alpha 2}^*}{2}, \quad \tilde{v}_{\alpha,y}^* = \frac{q_{\alpha 3}^* + q_{\alpha 4}^*}{2}, \quad \tilde{v}_{\alpha,z}^* = \frac{q_{\alpha 5}^* + q_{\alpha 6}^*}{2}, \quad (4.23)$$

$$\frac{\partial p_{\alpha}^*}{\partial x} = \frac{q_{\nabla \alpha 1}^* + q_{\nabla \alpha 2}^*}{2}, \quad \frac{\partial p_{\alpha}^*}{\partial y} = \frac{q_{\nabla \alpha 3}^* + q_{\nabla \alpha 4}^*}{2}, \quad \frac{\partial p_{\alpha}^*}{\partial z} = \frac{q_{\nabla \alpha 5}^* + q_{\nabla \alpha 6}^*}{2} \quad (4.24)$$

The reference quantities \tilde{v}_{α}^* and $\widetilde{\nabla p_{\alpha}^*}$ are finally transferred back to the real coarse grid block applying a Piola transformation (e.g. *Marsden and Hughes, 1983*).

Effective Flux Boundary Conditions for Two-Phase Parameters

The local fine-scale flow problems that have to be solved in order to calculate effective relative permeabilities are formulated using effective flux boundary conditions (EFBC) introduced in *Wallstrom et al. (2002a)* and *Wallstrom et al. (2002b)*. In the following, the EFBCs are explained by means of the local problem aligned to the x-axis of the global coordinate system (Figure 4.9). In this case, only domain boundaries which have a normal component in x-direction can be an inlet or an outlet. The remaining boundaries are closed by defining Neumann no-flow conditions. At the inlet and outlet, Neumann EFBCs are set. In the original formulation, the flux weight includes local heterogeneities of permeability and a global background permeability. Thus, it accounts

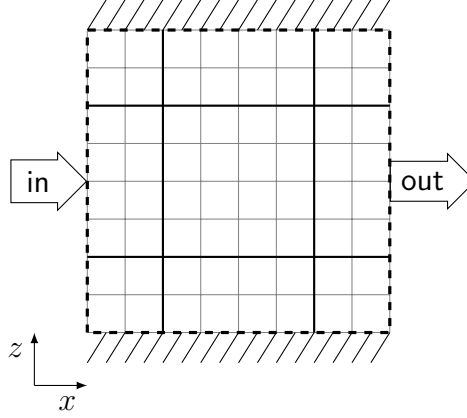


Figure 4.9: Local fine-scale problem for relative permeability upscaling in x-direction.

for local fluctuations, but also in some sense allows to incorporate global features, for example, in the case of high permeability channels. Additionally, we now want to account for effects due to capillary pressure heterogeneities. These are implicitly included in the saturation distribution obtained from the percolation method. Thus, we multiply the flux expression given in *Wallstrom et al.* (2002b) by the phase fractional flow functions $f_\alpha(S_w)$:

$$q_{\alpha i, x}^{\text{in}} = \frac{f_{\alpha i} k_i}{k_i + \bar{k}_x (R'_x - 1)} A_i \quad (4.25)$$

$$q_{\alpha i, x}^{\text{out}} = -\frac{f_{\alpha i} k_i}{k_i + \bar{k}_x (R'_x - 1)} A_i. \quad (4.26)$$

Subscript i indicates cells at the inlet or outlet (Figure 4.9), k_i is the fine-scale permeability, \bar{k}_x an effective global permeability in x-direction, R'_x a parameter accounting for the heterogeneity aspect ratio in x-direction and A_i the boundary face area. The idea of this extension is that, assuming an equilibrium, $\frac{k_i}{k_i + \bar{k}_x (R'_x - 1)} A_i$ gives an approximation of the total flux which can be multiplied by $f_\alpha(S_w)$ to get a phase flux. The net total flux into the domain has to be zero. However, as we assume equilibrium, the net phase fluxes also have to be zero. Thus, we scale the outlet fluxes such that their sum is equal to the sum of the inlet fluxes:

$$q_{\alpha i, x}^{\text{out}'} = q_{\alpha i, x}^{\text{out}} \frac{\sum_n q_{\alpha n, x}^{\text{in}}}{\sum_m q_{\alpha m, x}^{\text{out}}}. \quad (4.27)$$

Using EFBCs, only Neumann boundary conditions are defined. To get a uniquely solvable system, a single pressure value has to be fixed somewhere inside the domain. In the

two-dimensional case, an analytic solution for \mathbf{R}' can be derived (Wallstrom *et al.*, 2002a):

$$\mathbf{R}' = \begin{pmatrix} 1 + \sqrt{\frac{\bar{k}_y}{\bar{k}_x} \frac{\lambda_x}{\lambda_y}} \\ 1 + \left(\sqrt{\frac{\bar{k}_y}{\bar{k}_x} \frac{\lambda_x}{\lambda_y}} \right)^{-1} \end{pmatrix} \quad (4.28)$$

where λ_x and λ_y are correlation lengths of the heterogeneous permeability distribution. In the general three-dimensional case, the entries R'_i , $i = x, y, z$, of \mathbf{R}' are given by the elliptic integral:

$$\frac{1}{R'_i} = \frac{a_x a_y a_z}{2} \int_0^\infty \frac{ds}{(s + a_i^2) \sqrt{(s + a_x^2)(s + a_y^2)(s + a_z^2)}} \quad (4.29)$$

where $a_x = \lambda_x$, $a_y = \frac{\lambda_y}{\sqrt{\frac{\bar{k}_y}{\bar{k}_x}}}$ and $a_z = \frac{\lambda_z}{\sqrt{\frac{\bar{k}_z}{\bar{k}_x}}}$. An analytic solution of Equation (4.29) can only be obtained for specific simplified cases, for example, if at least two correlation lengths are assumed to be equal (see Wallstrom *et al.*, 2002a). In the general case, R'_i can be approximated by a numerical integration of the infinite integral.

4.1.5 Limitations of Upscaling

There is no need for further discussion of the limitation of upscaling with respect to spatial resolution. It is obvious, that a coarse-scale model results in coarse-scale solutions and can, for example, not resolve saturation fronts on the fine scale. Considering the numerical upscaling algorithms themselves, three important aspects regarding limitation can be identified: the assumptions of the upscaling, the quality of the numerical upscaling algorithm, and the complexity of the effective parameters.

Assumptions

Two major assumptions have to be discussed in more detail. The first is the assumption of a representative elementary volume (REV), the second the assumption of local capillary equilibrium.

The REV assumption is crucial. It is closely connected to the assumption of scale separation, which is important in the theoretical derivation of upscaled equations using volume averaging or homogenization. Only if we have sufficient scale separation can

we define coarse grid blocks which are an REV for the coarse-scale model parameters. The required size of the REV can certainly vary for the different effective parameters. In real-world problems, the assumption of scale separation is often violated. So the important questions are: do we have an REV for the coarse-scale parameter? If not, what are the consequences?

Regarding the permeability tensors, strong violation of the REV leads to ill-posed local fine-scale problems. On the one hand, the system of equations to get the components of the permeability tensor might not be solvable at all (e.g. because the symmetry condition cannot be fulfilled). On the other hand, the resulting tensors might be not positive definite. Regarding the effective capillary pressure, the $p_c^*(S_w^*)$ function can become direction dependent. To avoid the choice of the direction, the percolation algorithm invades a coarse grid block simultaneously from all sides. Thus, we always get a unique function, but most likely underestimate the entry pressure if the REV assumption is strongly violated.

For both the effective capillary pressure upscaling as well as the effective relative permeability upscaling, the saturation distributions are reconstructed based on the assumption of local capillary equilibrium. Depending on the global flow regime, this assumption can still be reasonable in the presence of viscous forces if capillary forces still dominate. Otherwise, important dynamic fine-scale effects are neglected.

Quality of the Numerical Upscaling Algorithm

The design and quality of the solution of the local fine-scale flow problems is essential for the quality of the numerical upscaling. Only representative setups in combination with reliable numerical methods can lead to meaningful fine-scale solutions for calculating representative coarse-scale quantities. More sophisticated discretization schemes such as multi-point flux approximation schemes (e.g. *Aavatsmark*, 2002) may increase the accuracy and minimize the numerical error when solving the heterogeneous fine-scale problems. In addition, iterative linear solvers can be a source of error. It has to be ensured that the linear solver, which is used for solving the local fine-scale systems, converges towards the correct solution. Considering the number of degrees of freedom of a local fine-scale flow problem, a direct linear solver is often a good choice for minimizing potential errors (e.g. *Demmel et al.*, 1999). The selection of the appropriate numerical methods, however, always depends on the complexity of the local fine-scale problems.

The most important design parameters are the size and shape of the local sub-domains and the boundary conditions.

Besides the setup of the local flow problems, the choice of the averaging operators is important. Depending on the current situation, the use of one operator could result in an averaged flux while the other operator gives an averaged flux of zero. Thus, the effective coarse-scale quantity will be different for different averaging operators. As pointed out before, a good choice may depend on the numerical scheme of the coarse-scale model. However, it is also connected to the aforementioned local boundary conditions which should not directly affect the averaging. A volume average, for example, is less sensitive to the boundary conditions than the approach based on the averaged coarse-face fluxes presented in Section 4.1.4. For this approach, it is essential to have a sufficient border region and properly chosen boundary conditions like the EFBCs. At regions where a border region is not possible (e.g. at the global boundary), a different averaging operator (e.g. Equations 4.16, 4.17) is recommended.

Finally, in order to get a numerically stable coarse-scale model, the effective parameters and functions have to be post-processed carefully. This includes filtering the parameters to avoid unphysical values but also constructing smooth and continuous functions from the data points that result from the upscaling algorithm. The most difficult part is the post-processing of the relative permeability sampling points. It is done as follows:

1. Eliminate sampling points with non-positive-definite phase permeability matrices.
2. Choose the sampling points for the interpolation of a relative permeability saturation function such that the functions of the eigenvalues are monotonous.
3. Interpolate the sampling points to get a continuous function by a method which ensures monotony (e.g. monotonous cubic spline interpolation, *Fritsch and Carlson*, 1980).

Complexity of the Effective Parameters

In order to account for certain important fine-scale effects, a certain complexity of the effective parameters is required. Compared with the fine-scale equations (Equation 2.33), the complexity of the relative permeability is increased from a scalar function to a second-order tensor function on the coarse scale (Equation 2.60). This allows us to account for changes in the flow direction induced by fine-scale capillary effects. However,

even with this increased complexity, only a limited range of processes can be reproduced correctly. A positive definite second-order tensor requires, for example, that a pressure gradient in x-direction, which leads to a flux, always leads to a flux in x-direction. For a diagonally layered system, it could be that, given a pressure gradient in x-direction, flow out of a coarse grid block only occurs in y-direction. In the case depicted in Figure 4.7, this would mean that only diagonal connections exist. In that case, the main diagonal entry would have to be zero and the matrix would no longer be positive definite. One possible solution could be to increase the order of the tensors further. In analogy to material science, the authors of *Dmitriev and Maksimov (1998)* or *Dmitriev et al. (2005)* suggest, for example, using fourth-order relative permeability tensors. However, it is already challenging to set up an efficient upscaling algorithm which provides meaningful second-order tensors. This is essential to get a numerically stable and converging coarse-scale solution. It is not clear if and how a similar algorithm could be set up to calculate higher-order tensors efficiently for general heterogeneous porous media. Additionally, the numerical coarse-scale model would have to be able to treat these higher-order tensors.

4.1.6 Tests

In Section 4.1, a set of parameter upscaling methods is described which allows us the coarse-scale simulation of two-phase flow. The limitations of the parameter upscaling were already discussed in the previous section (Section 4.1.5). As the upscaling approach only serves as the basis for a multi-scale method, which is introduced in the second part of this chapter (Section 4.2), it is not the intention of the following tests to investigate these limits but to test the method on a model setup and in a physical regime in which it is supposed to be valid.

Two setups are investigated which are sketched in Figure 4.10. Both setups consider a quadratic domain of a size of $100 \times 100 \text{ m}^2$ and are selected such that boundary influences are minimized. In setup 1 (Figure 4.10a) flow between an injection well (q_i) and a production well (q_p) is modeled. In setup 2 (Figure 4.10b) an injection well (q_i) is placed in the center of the model domain leading to a radial distribution of the injected fluid. For a fair comparison to a fine-scale reference solution, avoiding any special treatment of the near well area, it is injected and produced in the complete area of a coarse grid block. Two types of processes are investigated: drainage and imbibition. In the case of drainage the domain is initially saturated with the wetting phase in the

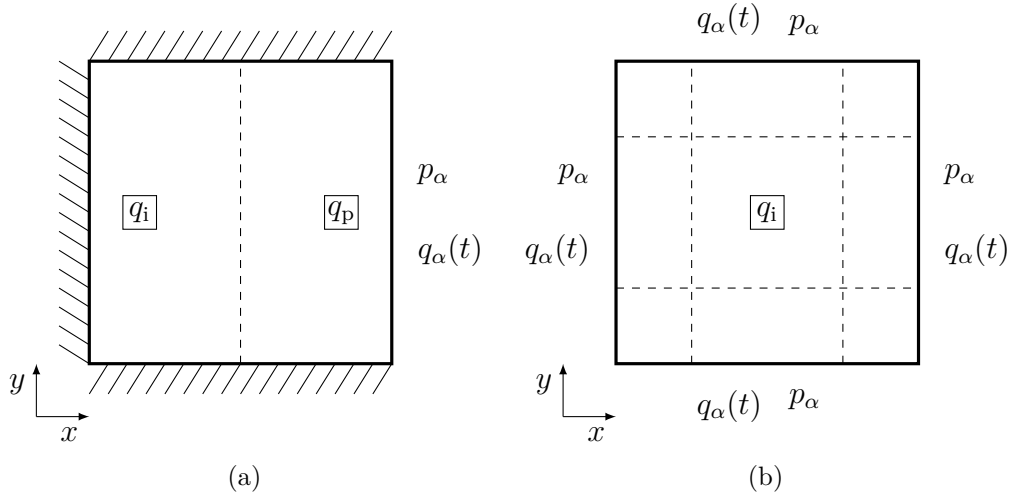


Figure 4.10: Problem setup 1 (a) (two-well setup) and 2 (b) (one-well setup) for testing the upscaling method. The dashed lines mark the positions for the evaluation of breakthrough curves.

case of imbibition with the non-wetting phase. The fluid viscosity ratio is set to $\frac{\mu_n}{\mu_w} = 0.5$ and the porosity is assumed to be constant ($\phi = 0.2$).

The heterogeneous permeability distribution (Figure 4.11) is obtained using the geostatistical modelling tool *gstat* (Pebesma and Wesseling, 1998). The correlations lengths are set in a order of magnitude of a fine grid cell size leading to a heterogeneous parameter distribution which shows no larger scale structures. Thus, scale separation can be assumed. The permeability in the area of the wells is set to a constant value to achieve a better comparability to the reference solution - as mentioned before no special well treatment is applied. A corresponding entry pressure distribution is obtained by a Leverett-J-scaling as:

$$p_{ci}(S_w) = p'_d \sqrt{\frac{\phi_i \bar{k}}{\bar{\phi} k_i}} J(S_w), \quad (4.30)$$

where i is the cell index, p'_d is a reference displacement or entry pressure and \bar{k} and $\bar{\phi}$ are the mean permeability and porosity. For both setups Brooks-Corey parameterizations are used for the J-function $J(S_w)$ and the relative permeability functions (Brooks and Corey, 1964). In the case of drainage the J-function is defined as:

$$J(S_w) = S_w^{\frac{-1}{\lambda}}. \quad (4.31)$$

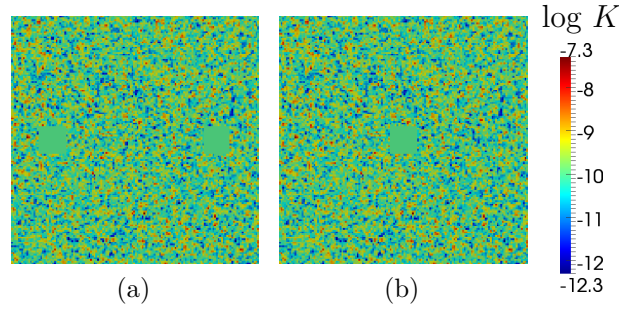


Figure 4.11: Permeability distributions for setup 1 (a) and setup 2 (b).

In the case of imbibition it is slightly modified to avoid entry pressures:

$$J(S_w) = S_w^{-\frac{1}{\lambda}} - 1. \quad (4.32)$$

The relative-permeability-saturation functions are defined as:

$$k_{rw} = S_w^{\frac{2+3\lambda}{\lambda}} \quad (4.33)$$

$$k_{rn} = (1 - S_w)^2 (1 - S_w^{\frac{2+\lambda}{\lambda}}). \quad (4.34)$$

The Brooks-Corey parameter appearing in the J-functions and in the relative permeability functions is set to $\lambda = 2$. The heterogeneities are defined on a fine-scale grid of 144×144 cells. On the coarse scale the domain is discretized by a grid of 9×9 cells.

As explained in Section 4.1.4 the definition of the averaging operator used in the upscaling algorithms might considerably influence the upscaled coarse scale parameters. Thus, the three introduced types of averaging operators: av1 (Equations (4.16) and (4.17)); av2 (Equations (4.20) and (4.17)); av3 (Equations (4.21) - (4.24)), are applied for the permeability and relative permeability upscaling and compared in the following tests. To compare and verify the results, coarse-scale breakthrough curves are calculated and plotted where the breakthrough saturation is defined as

$$S_b(\mathbf{x}) = \frac{1}{n} \sum_{i=1}^n S_{\alpha_i}^*(\mathbf{x}). \quad (4.35)$$

In Equation 4.35, n is the number of coarse grid cells along the breakthrough-line at position \mathbf{x} , and $S_{\alpha_i}^*$ is the phase saturation which is averaged to the coarse grid resolution (Equation 4.10).

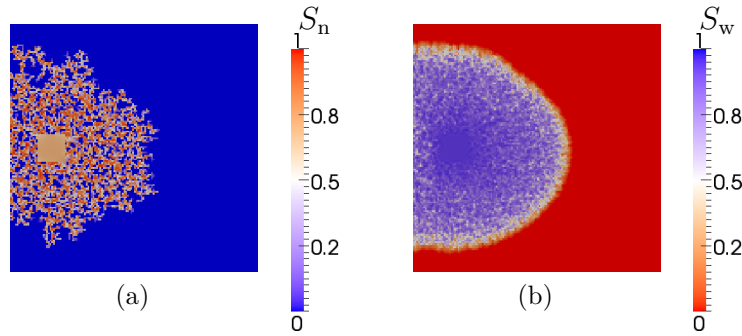


Figure 4.12: Saturation distribution of the fine-scale reference simulations of setup 1: (a) drainage ($t = 2.4 \times 10^6$ s); (b) imbibition ($t = 5 \times 10^6$ s).

Setup 1

In this setup all boundaries except the eastern boundary are impermeable (Figure 4.10a). The eastern boundary conditions are a Dirichlet boundary condition for the pressure (drainage: $p_n = 10^6$ Pa, imbibition: $p_w = 10^6$ Pa) and a free outflow condition for the saturation transport equation. The injection and production rate are set to a value of $q_i = q_p = 0.01$ kg/(m³ s). The flow rates are chosen low enough to ensure a capillary dominated flow regime for which the capillary equilibrium assumption of the upscaling approach is meaningful.

The fine-scale saturation results are shown in Figure 4.12. They convincingly demonstrate the effect of an entry pressure dominated drainage process, leading to high local saturation contrasts and areas which are effectively impermeable for the invading fluid (Figure 4.12a). In contrast, an imbibition process leads to a much smoother saturation distribution (Figure 4.12b).

In Figures 4.13 and 4.14 the coarse scale saturation solutions of the drainage and imbibition case respectively are plotted and compared to the fine-scale solution. To improve the comparability the fine-scale solution is averaged to the coarse grid resolution (Figures 4.13a and 4.14a). In the drainage case, the effective coarse-scale parameters applying av1 and av2 result in more or less equal saturation distributions. Compared to the reference solution, the fluid distribution is more diffusive, although the the general flow behavior is well captured. The coarse-scale parameters applying av3 lead to a less diffusive fluid distribution and, neglecting the boundary cells, very well approximate the reference saturation pattern. As discussed in Section 4.1.5, the upscaling as well as the numerical method tend to increase the error of the solution at the domain boundaries.

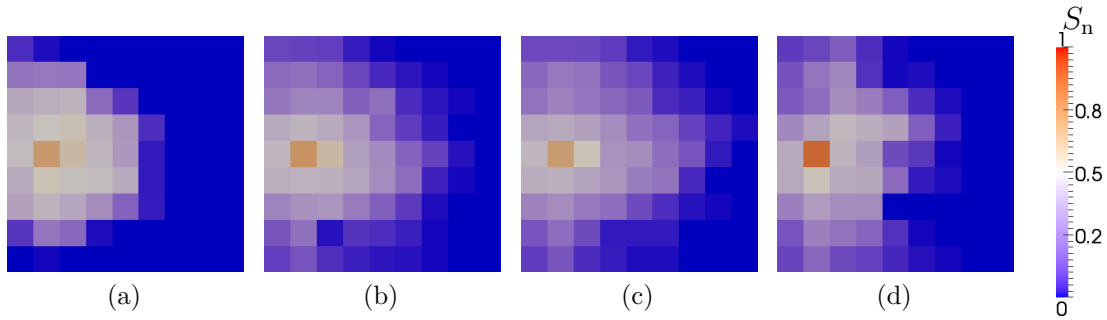


Figure 4.13: Saturation distributions of setup 1 for the case of drainage at $t = 2.4 \times 10^6$ s: (a) fine-scale reference solution (averaged to the coarse grid resolution); (b) upscaling using average operator 1 (av1);(c) upscaling using average operator 2 (av2);(d) upscaling using average operator 3 (av3).

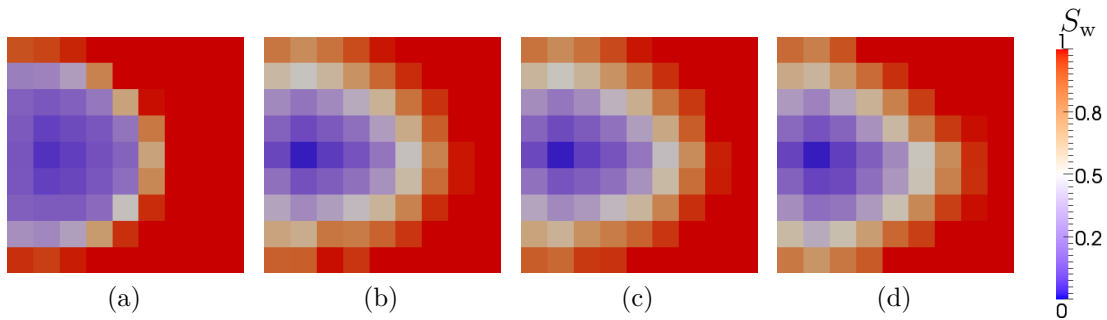


Figure 4.14: Saturation distributions of setup 1 for the case of imbibition at $t = 5 \times 10^6$ s: (a) fine-scale reference solution (averaged to the coarse grid resolution); (b) upscaling using average operator 1 (av1);(c) upscaling using average operator 2 (av2);(d) upscaling using average operator 3 (av3).

In the imbibition case, the variations in the saturation results using the different types of averaging operators are negligible. Compared to the reference solution, the general flow and transport behavior is well approximated, although the coarse scale solutions again are more diffusive. However, this had to be expected, because a coarsening of the grid usually enhances the error due to numerical diffusion. The saturation breakthrough curves plotted in Figure 4.15 confirm the analysis of the saturation distributions. In the case of imbibition, all coarse-scale solutions in average sufficiently match the reference solution. In the case of drainage, only the coarse scale parameters resulting from av3 lead to a breakthrough curve that agrees well with the reference breakthrough curve. Using av1 and av2, the saturation plateau which is reached towards the end of the simulation is considerably lower or reached much later than in the reference solution. The driving forces for flow in setup 1 are capillary forces and the pressure gradient

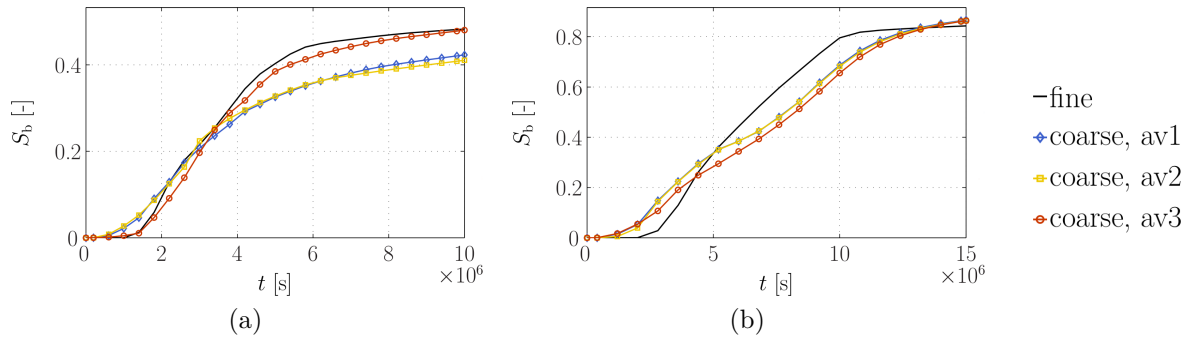


Figure 4.15: Saturation breakthrough curves for setup 1 (Figure 4.10a) at $x = 0.5x_{\max}$ along the y-axis: (a) drainage, (b) imbibition.

between the two wells. The pressure gradient still has an influence, especially in the cells directly connecting the wells, although the regime is capillary dominated. At the coarse scale the wells are directly connected by one row consisting of only five cells. Thus, the influence of the wells might be stronger compared to the fine-scale simulation and lead to an increased error of the approximation. In order to avoid such effects the second setup was developed.

Setup 2

In the second setup a fluid injection at the center of the model domain is simulated. To minimize boundary influences and avoid an accumulation of fluid at the boundaries, all boundaries are free outflow boundaries for the saturation transport (Figure 4.10b). For pressure, a Dirichlet boundary condition is defined (drainage: $p_n = 10^6$ Pa, imbibition: $p_w = 10^6$ Pa). The injection rate is set to a value of $q_i = 0.005$ kg/(m³ s). As in setup 1 the injection rates are chosen low enough to ensure a capillary dominated flow regime.

The fine-scale saturation distributions after $t = 1 \times 10^6$ seconds of injection are shown in Figure 4.16. The radial distribution of the injected fluid is quite regular for both kinds of processes. As already observed in the previous test case the difference between drainage and imbibition is, however, quite obvious. If entry pressures influence the flow paths, the saturation pattern is dominated by high local saturation contrasts and areas which are effectively impermeable for the invading fluid (drainage). Otherwise, the saturation is distributed more smoothly (imbibition). The coarse-scale saturation distributions as well as the averaged fine-scale saturation are shown in Figure 4.17 for the case of drainage and in Figure 4.18 for the case of imbibition. They qualitatively show a similar

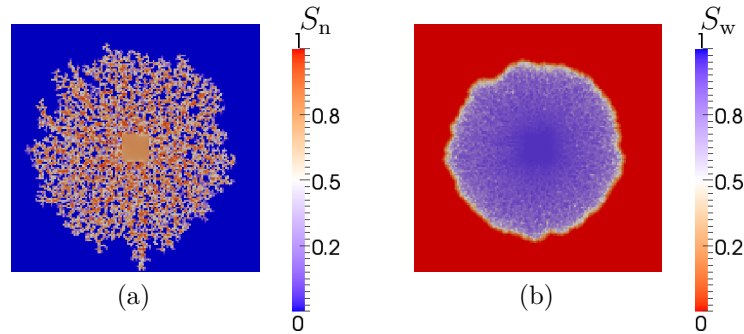


Figure 4.16: Saturation distribution of the fine-scale reference simulations of setup 2: (a) drainage ($t = 1 \times 10^6$ s); (b) imbibition ($t = 1 \times 10^6$ s).

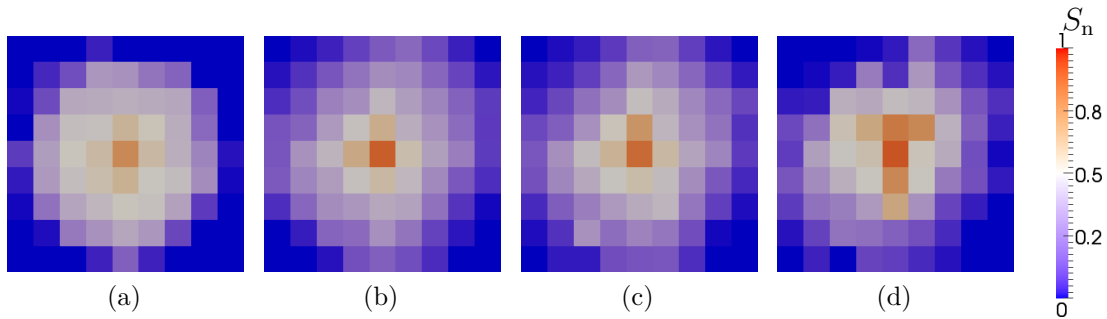


Figure 4.17: Saturation distributions of setup 2 for the case of drainage at $t = 1 \times 10^6$ s: (a) fine-scale reference solution (averaged to the coarse grid resolution); (b) upscaling using average operator 1 (av1); (c) upscaling using average operator 2 (av2); (d) upscaling using average operator 3 (av3).

behavior of the different variants of the upscaling method (av1-3) than observed for setup 1. In the case of imbibition, the results using the different coarse-scale parameters are very similar (Figures 4.18b - 4.18d). In comparison to the averaged fine-scale result (Figure 4.18a), the fluid propagation is more diffusive. This could be expected because the error due numerical diffusion increases if a grid is coarsened. A similar behavior can be observed in the case of drainage if the coarse-scale parameters resulting from the average operators av1 and av2 are applied. The effective parameters calculated using the third averaging operator (av3), as shown for setup 1, result in a less diffusive distribution of the injected fluid. Again, the values of the boundary cells have to be considered with caution because the upscaling as well as the numerical method are less accurate at global domain boundaries (see Section 4.1.5).

The saturation breakthrough curves plotted in Figure 4.19 confirm the results of setup 1. The positions of the breakthrough lines around the injection well are illustrated in

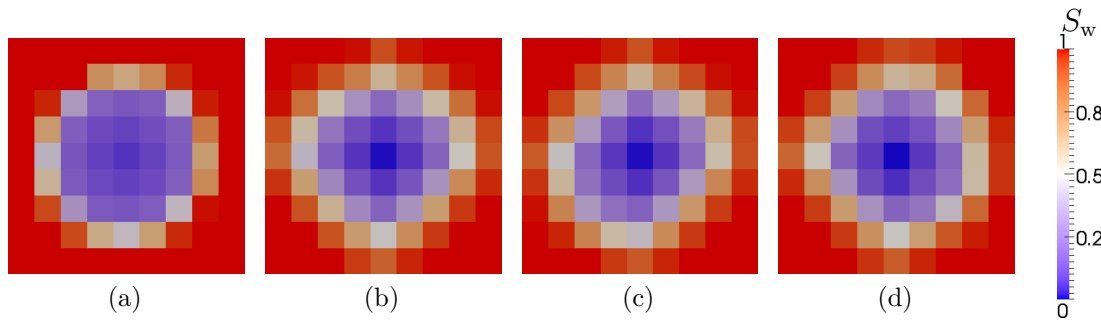


Figure 4.18: Saturation distributions of setup 2 for the case of imbibition at $t = 1 \times 10^6$ s: (a) fine-scale reference solution (averaged to the coarse grid resolution); (b) upscaling using average operator 1 (av1); (c) upscaling using average operator 2 (av2); (d) upscaling using average operator 3 (av3).

Figure 4.10b. In the case of imbibition (Figure 4.19b) all variants of the parameter upscaling lead to similar breakthrough curves which match well with the averaged fine-scale breakthrough. In the case of drainage, the breakthrough curves using averaging operator av3 for the parameter upscaling agree slightly better with the fine-scale results than using av1 and av2.

Finally, some examples of the coarse-scale constitutive relations calculated in this test series are plotted in Figures 4.20 - 4.22. The expected main difference between the capillary-pressure-saturation function for drainage (Figure 4.20a) and imbibition (Figure 4.20b) is the entry pressure in the case of drainage. Considering all coarse-grid cells, the functions slightly vary in the entry pressures (only drainage) and the average capillary pressure magnitude. Two examples of relative-permeability-saturation functions for the case of imbibition are shown in Figure 4.21. For the fine-scale permeability distribution of these test scenarios, the functions are very smooth. The curves of eigenvalues are similar to the fine-scale relative-permeability-saturation functions. The functions vary from cases with small off-diagonal entries (Figure 4.21b) to cases with approximately zero off-diagonal entries (Figure 4.21a). For the drainage example the curves are completely different. They vary from quite smooth functions similar to the imbibition example (Figure 4.22a) over functions showing stepwise (Figure 4.22b) or even non-monotonous (Figure 4.22c) variations of the single entries of the tensors to functions showing a convex instead of a concave shape (Figure 4.22d). This is caused by the heterogeneous saturation distribution in the case of drainage (see for example Figure 4.16) which may lead to continuously changing patterns of available flow paths depending on the phase saturation. Thus, the preferred flow direction related to a coarse

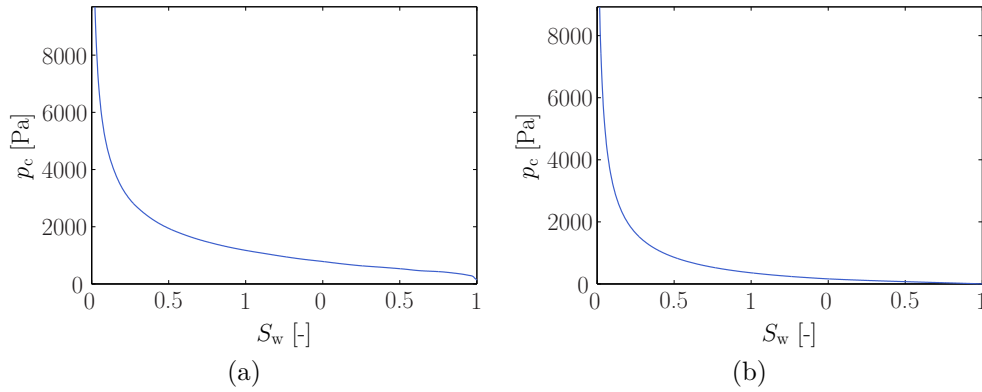


Figure 4.20: Comparison of two coarse-scale capillary-pressure-saturation functions: (a) drainage, (b) imbibition.

grid-block may also vary continuously. Nevertheless, except for cases of convexly shaped main-diagonal functions, the curves of the eigenvalues are most often similar to the fine-scale functions. By the application of different averaging operators (Section 4.1.4), only the details of the functions vary while the main features are similar. For different distributions of fine-scale parameters the characteristics of the coarse-scale functions may, of course, be different.

Summarizing, the tests showed that the introduced set of numerical parameter-upscaling methods approximate the fine-scale results sufficiently well if conditions and setups are chosen so that the assumptions included in the single upscaling approaches are valid. In particular, the newly developed concept to include the effects of capillary pressure, which can differ depending on the process (e.g. drainage or imbibition), in the coarse scale parameters is tested successfully. In Section 4.1.4 the choice of a suitable averaging operator, which is used to calculate coarse-scale parameters from local fine-scale results in a numerical upscaling procedure, is identified to be crucial. Thus, three different operators are applied and compared in the tests. Especially in the case of drainage, the reconstruction from the fluxes at the faces of a coarse grid block described in Equations (4.21) - (4.24) (av3) results in the best approximation of the fine-scale transport. Thus, this averaging operator is further used for the parameter upscaling. Of course, the quality of the coarse-scale solution decreases if the conditions and setups are less favorable. However, as mentioned at the beginning of this section the numerical upscaling only serves as a basis for the multi-scale approach which is introduced in the following section. Against this background, a further separate validation of the upscaling method on more difficult tests scenarios is not necessary.

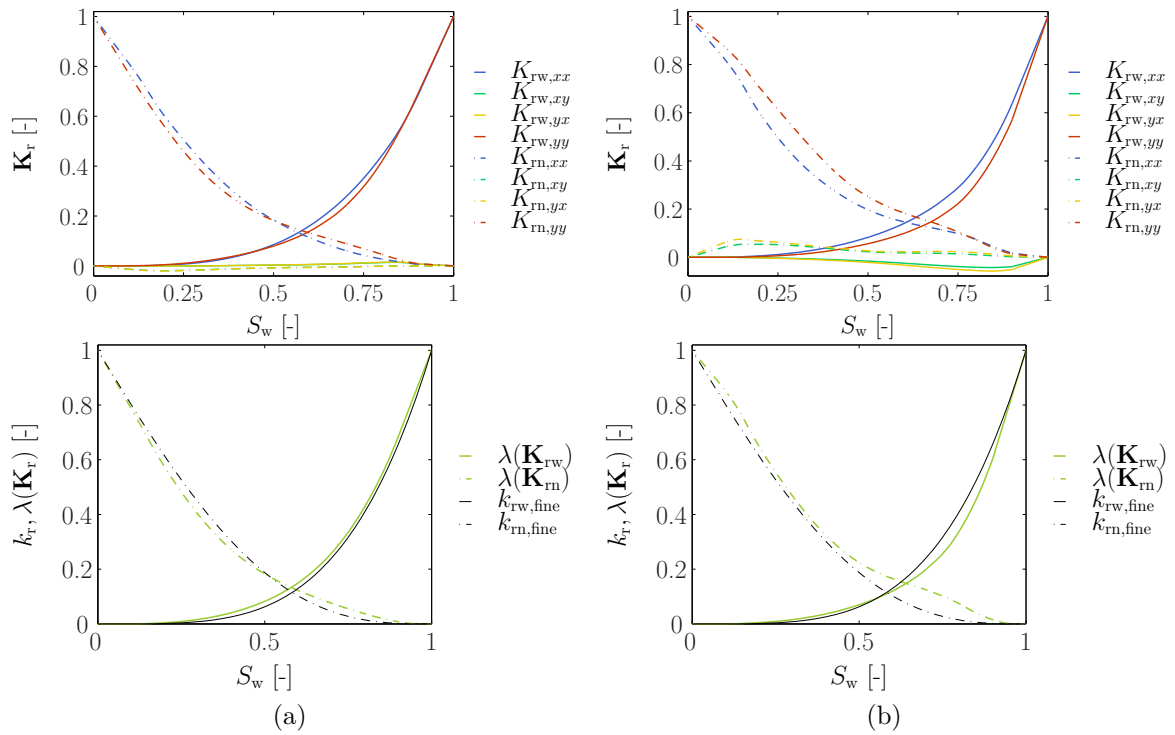


Figure 4.21: Comparison of two coarse-scale relative-permeability-saturation functions for the case of imbibition: \mathbf{K}_r is the tensorial coarse-scale function, $\lambda(\mathbf{K}_r)$ are the averaged eigenvalues of \mathbf{K}_r , and k_r is the fine-scale function (Equations (4.33) and (4.34)).

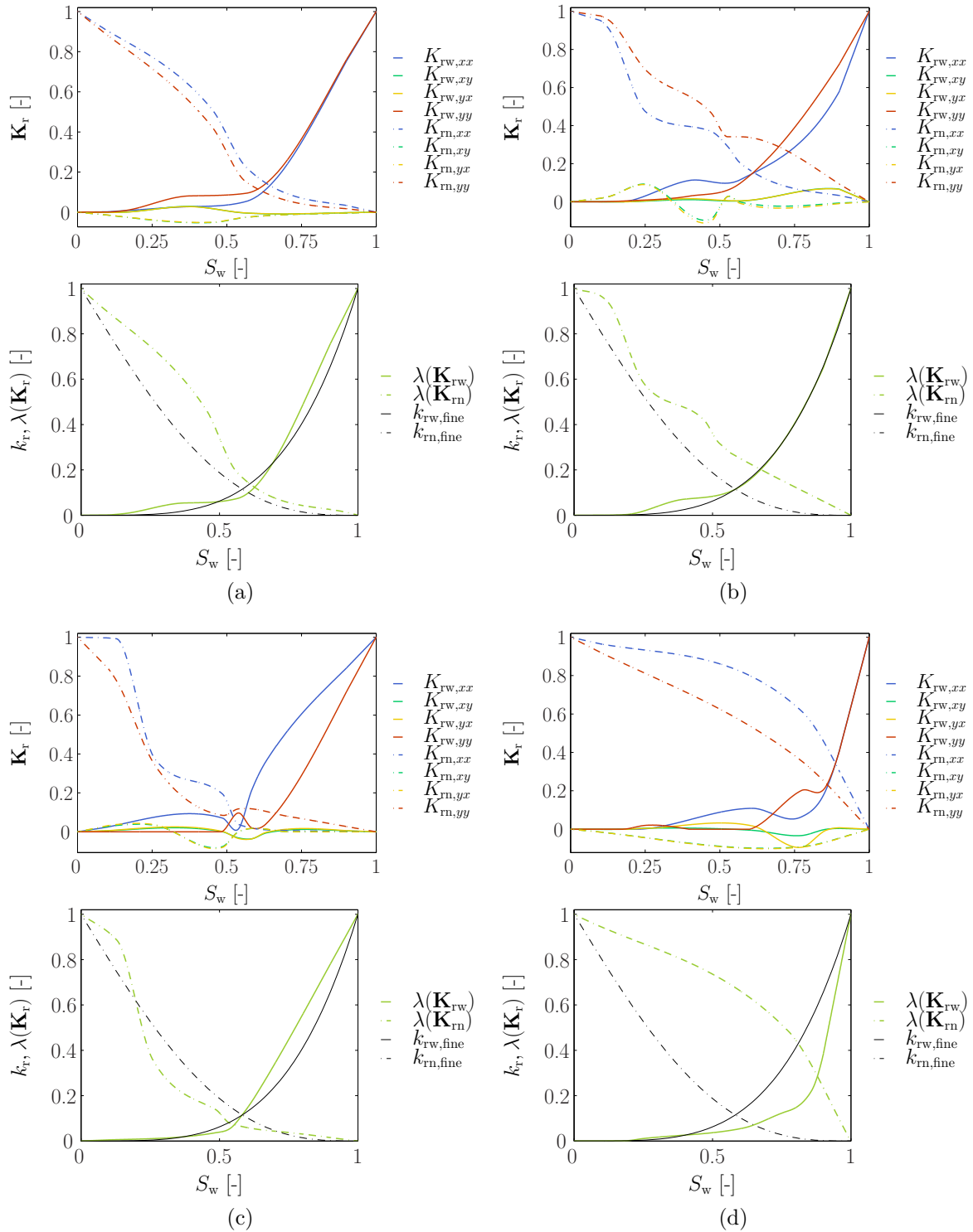


Figure 4.22: Comparison of four coarse-scale relative-permeability-saturation functions for the case of drainage: \mathbf{K}_r is the tensorial coarse-scale function, $\lambda(\mathbf{K}_r)$ are the averaged eigenvalues of \mathbf{K}_r , and k_r is the fine-scale function (Equations (4.33) and (4.34)).

4.2 Multi-Scale Modeling

The motivation for using upscaled (large-scale) models is to save computation time by decreasing the number of degrees of freedom. In this way, it is possible to simulate larger domains with sufficient accuracy. However, upscaling methods are limited on the one hand to coarse spatial resolutions and on the other hand to a certain spectrum of applications which is given by the underlying assumptions. The limitations of the numerical upscaling method are discussed in detail in Section 4.1.5. Knowledge of these limitations is the key to identifying sources of errors. To some extent the limitations can be overcome and errors thus reduced by multi-scale modeling. Multi-scale in that context means that the scale transfer can be in both directions, from fine to coarse (upscaling) and from coarse to fine (downscaling). As introduced in Chapter 1, various multi-scale methods exist which have proven to work well for advection-dominated problems. However, the problem of flow influenced or dominated by capillary pressure has not been solved. Thus, a novel approach is provided in this work.

The upscaling step was already discussed in detail in the last section. To extend the method to a multi-scale approach, the downscaling step has to be added. The problem of downscaling compared to upscaling is that it is not unique. This means that, given a certain parameter distribution, one averaging operator results in exactly one averaged quantity, while various parameter distributions could result in one given averaged quantity. Downscaling in the case of two-phase flow would mean that fine-scale pressure and saturation distributions are reconstructed from given coarse-scale solutions. This is usually done by solving local fine-scale problems where the boundary conditions are interpolated from the coarse-scale solution. However, in the case of capillary pressure heterogeneities, both quantities are coupled and can vary strongly or even be discontinuous on comparatively small length scales. On the one hand, due to the coupling, the interpolation of the pressure and saturation boundary condition is also coupled; on the other hand, extreme values due to capillary pressure effects are quite important to get a meaningful distribution. These extreme values are naturally averaged out on the coarse scale and can therefore hardly be obtained by interpolation between the coarse-scale values. This leads to the conclusion that local downscaling is very difficult and may not be possible at all if capillary pressure effects cannot be neglected. Thus, an h-adaptive grid method is combined with our upscaling approach. The adaptive grid can be interpreted as an efficient and natural way of global downscaling. Compared to

the local downscaling, this way of global downscaling is also advantageous with regard to efficiency as one has to keep in mind that each of the local fine-scale problems that would have to be solved is time-dependent.

In the following sections, the multi-scale modeling strategy is described and various criteria to control the local grid adaptation are introduced. Afterwards, the effects of the application of the different adaptation criteria on the multi-scale solution are investigated on several test examples where the physical regime ranges from a purely viscous dominated to a capillary dominated regime.

4.2.1 Grid adaptation – Switching Scales

The concept of the multi-scale algorithm is relatively simple. It is assumed that a fine-scale parameter distribution (highest grid level) as well as an upscaled coarse-scale parameter distribution (zeroth grid level) are known. Wherever possible, the grid consists of level zero cells, otherwise it can be refined up to the highest level (fine scale, Figure 4.23). Only one level difference is allowed between neighboring cells. This leads to a transfer region if there is more than one level difference between the fine scale and the coarse scale. At the highest level, the fine-scale parameters can be used directly. At all other levels, the upscaled parameters calculated for the zeroth grid level are used and intermediate-scale parameters are not upscaled separately. Experience with realistic problems shows that even on the coarsest grid level the grid cells often are not sufficiently large to have an REV for the upscaled parameters. Thus, upscaling of intermediate-scale parameters usually does not make sense because it is even more questionable whether there is a chance of having an REV on this length scale. However, there are two exceptions:

1. to get a correct scaling of the speed of propagation of the saturation, the porosity is averaged separately for every grid level. This is justifiable because it is only a volume ratio and the volumes are known.
2. to account for entry pressure effects better and to avoid artificial gradients, an entry pressure is also determined separately for each level. The intermediate-scale entry pressures are then used to scale the coarse-scale capillary-pressure-saturation function.

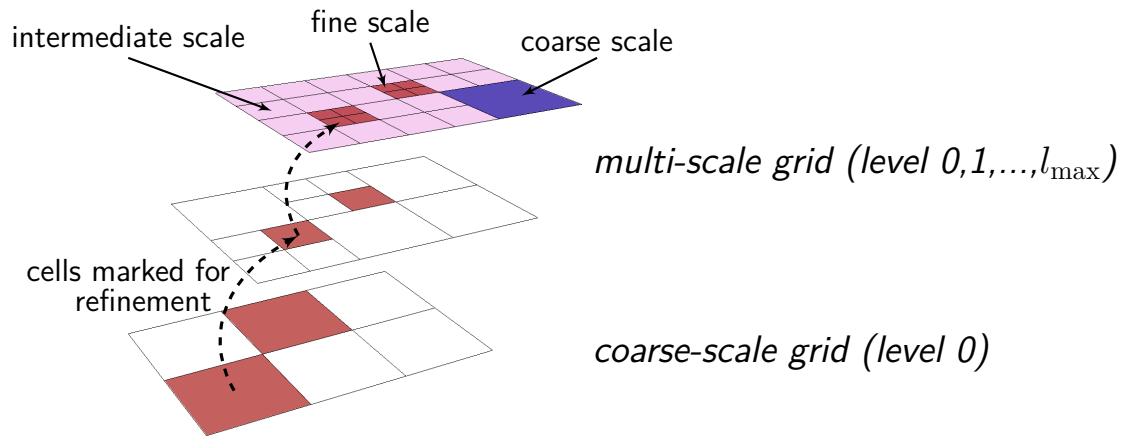


Figure 4.23: Sketch of the multi-scale adaptation procedure. The coarse grid (level 0) is refined up to the fine scale (level l_{\max}) depending on the adaptation indicators.

The grid is adapted using a non-conforming refinement strategy. To get a correct approximation of fluxes, especially at hanging nodes, the MPFA L-method derived in Chapter 3 is used. An advantage of the MPFA L-method is that it easily allows the treatment of hanging nodes. The extension of the method for modeling two-phase flow with anisotropic relative permeabilities and for using non-conforming adaptive grids is described in detail in Chapter 3.

4.2.2 Criteria

The objective of grid adaptation is to reduce the error of the solution. Thus, an efficient adaptation algorithm has to identify regions where a reduction of the local error leads to the required reduction of the global error. In Figure 4.23 such regions are shown in red. In the multi-scale model, adaptation indicators which we call standard adaptation indicators are combined with so-called multi-scale indicators. Standard indicators adapt the grid in dependence on specific flow or transport features. Multi-scale indicators try to identify regions where the upscaling might lead to increased errors.

One standard indicator is used to account for each equation of the two-phase system. The solution of the pressure equation should provide a flow field that accounts for important fine-scale flow features. Especially if the assumption of scale separation is strongly violated, effects of important structures like channels can be estimated insufficiently.

Thus, a flux-based criterion, the v_t -indicator, is used as indicator which scans the flow field for preferred larger-scale flow paths. A cell i is marked for refinement if

$$\frac{|\mathbf{v}_i| - |\mathbf{v}_{\min}|}{|\mathbf{v}_{\max}| - |\mathbf{v}_{\min}|} \geq \varepsilon_{v,r} \quad (4.36)$$

and for coarsening if

$$\frac{|\mathbf{v}_i| - |\mathbf{v}_{\min}|}{|\mathbf{v}_{\max}| - |\mathbf{v}_{\min}|} < \varepsilon_{v,c} \quad (4.37)$$

where \mathbf{v} is the total velocity of cell i , $|\mathbf{v}_{\max}|$ and $|\mathbf{v}_{\min}|$ are the global extremes of the absolute total velocity, and $\varepsilon_{v,r}$ and $\varepsilon_{v,c}$ are threshold values for refinement and coarsening respectively.

Regarding the transport equation, the aim is a high resolution of the moving fluid fronts. To track the fronts, a local-gradient-based criterion, the S -indicator, is used similar to the one described in *Wolff et al. (2013a)*: a cell i is marked for refinement if

$$\frac{\max(\Delta S_{ij})_i - \Delta S_{\min}}{\Delta S_{\max} - \Delta S_{\min}} \geq \varepsilon_{S,r} \quad (4.38)$$

and for coarsening if

$$\frac{\max(\Delta S_{ij})_i - \Delta S_{\min}}{\Delta S_{\max} - \Delta S_{\min}} < \varepsilon_{S,c} \quad (4.39)$$

where ΔS_{ij} is the saturation difference between neighbor cells i and j and ΔS_{\max} is the global maximum of ΔS_{ij} , and $\varepsilon_{S,r}$ and $\varepsilon_{S,c}$ are again threshold values which usually differ from those of the flux-based criterion. The choice of the thresholds, which can range between zero and one, is problem-dependent. If meaningful values can be estimated a priori, they can be set directly. Otherwise, it may be more reasonable to define percentiles for refinement and coarsening and recalculate the threshold values during the simulation.

The idea of multi-scale indicators is to identify regions in which the limiting assumptions of the numerical upscaling method discussed in Section 4.1.5 can lead to noticeable errors or even convergence towards a wrong solution. A violation of the REV assumption as well as an insufficient complexity of the effective parameters is already partly compensated for by the standard indicators described previously. The particular multi-scale indicator, the Ca -indicator, described in the following addresses the problem of the capillary pressure equilibrium assumption. A cell i is marked for refinement if

$$Ca_i \geq \varepsilon_{Ca,r} \quad (4.40)$$

and for coarsening, if

$$Ca_i < \varepsilon_{Ca,c} \quad (4.41)$$

where $Ca_i = |\mathbf{Ca}_i|$ is the local capillary number of cell i and \mathbf{Ca}_i is defined according to *Hilfer and Øren (1996)*:

$$\mathbf{Ca}_i = \frac{\Delta x_i \mu_w v_i^c}{p_c^c} \mathbf{K}^{*-1}. \quad (4.42)$$

The key issue for applying this capillary number as meaningful multi-scale adaptation indicator is the definition of the characteristic quantities. They are chosen as follows:

- The characteristic length is defined by the local discretization length Δx_i .
- The characteristic velocity v_i^c is defined as the absolute advective phase velocity $v_i^c = f_{\alpha i} |\mathbf{v}_{ti}|$.
- A good choice of the characteristic capillary pressure most likely depends on the shape of the coarse scale capillary-pressure-saturation functions. Two possible choices are suggested here which are also investigated in the numerical tests at the end of this section: the coarse scale entry pressure $p_c^c = p_d^*$, and $p_c^c = p_c^*(\hat{S}_{w,\min}^*)$. The latter is illustrated in Figure 4.24. It is defined as the capillary pressure at a minimum saturation of a linear approximation of the lower part of a capillary-pressure-saturation function. This definition is similar to the definition of the breakthrough saturation defined in *Hilfer and Øren (1996)*, which is the saturation at $\frac{d^2 p_c(S_w)}{dS_w^2} = 0$, but it can also be applied to parameterizations which do not have an inflection point (e.g. Brooks-Corey parameterizations, *Brooks and Corey, 1964*).

If cell i is on the coarsest grid level, \mathbf{K}^* and p_d^* or $p_c^*(\hat{S}_{w,\min}^*)$ are the absolute permeability and capillary pressure of cell i , otherwise of the coarse grid block including cell i . In the upscaling step we assume capillary equilibrium. This assumption is fulfilled if $Ca \ll 1$, but it may also be justifiable if $Ca < 1$. In a physical interpretation, a capillary number of one means that capillary forces and viscous forces are in equilibrium. However, the relation between Ca and the real physical regime strongly depends on the choice of the characteristic quantities. Thus, the critical value of $Ca = 1$ and its interpretation should be treated with care. By choosing the threshold values $\varepsilon_{Ca,r}$ (refinement) and $\varepsilon_{Ca,c}$ (coarsening), we can define if and to which extent we allow violation of the capillary equilibrium assumption $Ca \ll 1$.

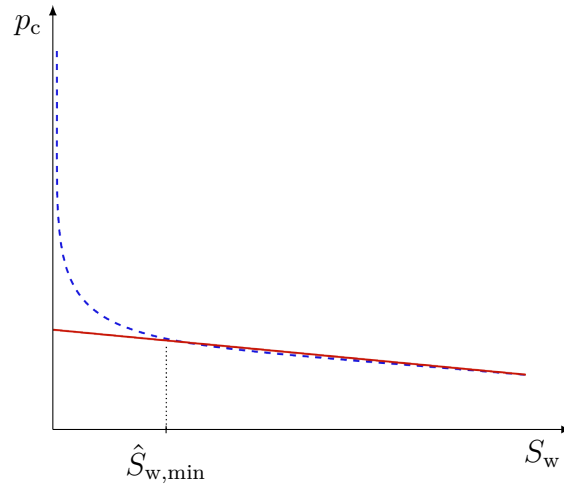


Figure 4.24: Illustration of the minimum saturation $\hat{S}_{w,\min}$ of the linear approximation (solid line) of the lower part of a capillary-pressure-saturation function (dashed line).

4.2.3 Tests

In the previous section, three different indicators for grid adaptation are presented, one for each balance equation and an additional multi-scale indicator. Especially regarding the multi-scale behavior, it is important to choose and combine meaningful indicators. This is demonstrated and analyzed in the following tests.

The test setup is sketched in Figure 4.25. The domain is initially saturated by a non-wetting phase (e.g. oil). A wetting phase (e.g. water) infiltrates from the southern domain boundary. The eastern and western sides are closed and a pressure gradient in y-direction is applied. On the fine scale, the domain is discretized by a grid of 128×256 cells and on the coarse scale by a grid of 4×8 cells, leading to a hierarchic refinement factor of five. The heterogeneous permeability and porosity distributions (Figure 4.26a and 4.26b) are taken from one layer (layer 15, top formation) of the three-dimensional geological model (model 2) of the SPE 10 benchmark study (*Christie and Blunt, 2001*). The corresponding entry pressure distribution is obtained by a Leverett-J-scaling from the permeability and porosity distribution (Equations (4.30) and (4.32)). The fine-scale relative permeabilities are calculated using quadratic laws

$$k_{rw} = S_w^2 \quad (4.43)$$

$$k_{rn} = (1 - S_w)^2 \quad (4.44)$$

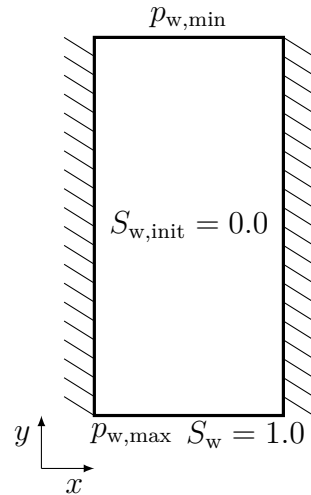


Figure 4.25: Problem setup for the indicator tests.

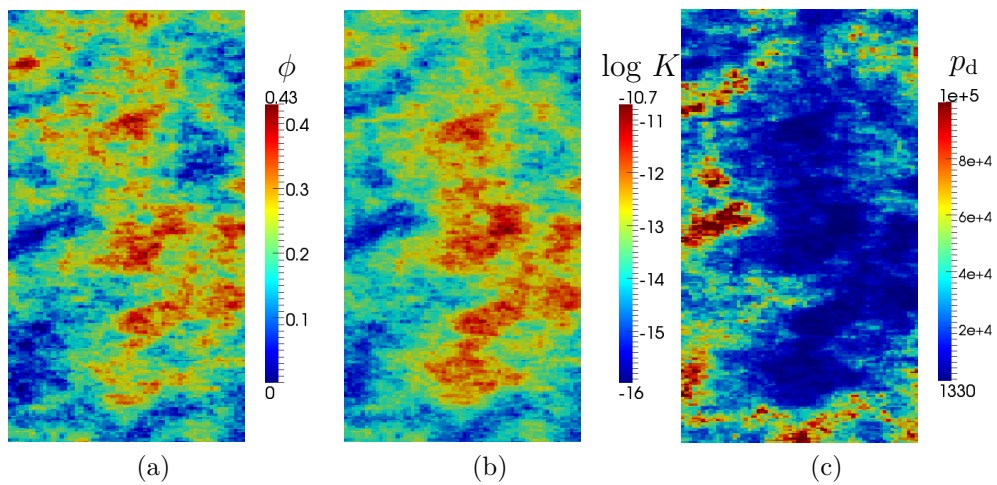


Figure 4.26: Porosity (a), permeability (b), and entry pressure (c) distribution according to layer 15 of the SPE 10 benchmark model 2 (top formation).

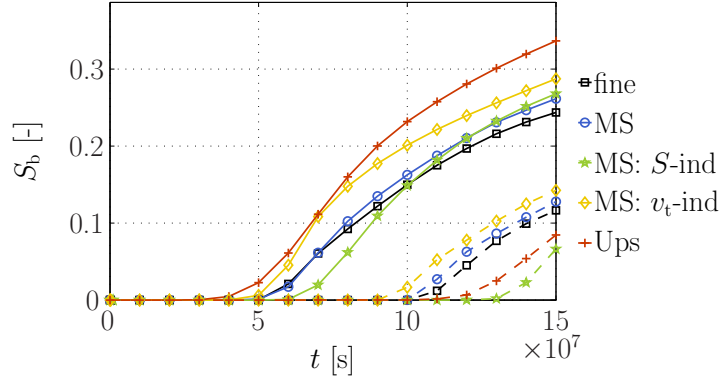


Figure 4.27: Saturation breakthrough curves along the x -axis at $y = \frac{1}{3}y_{\max}$ (solid lines) and at $y = \frac{2}{3}y_{\max}$ (dashed lines)

and the fluid viscosities are $\mu_w = 10^{-3}$ kg/(ms) and $\mu_n = 5 \times 10^{-3}$ kg/(ms). In the following, the effects using both kinds of indicators are investigated, where the first test focuses on the introduced standard indicators and the second test on the proposed multi-scale indicator.

Standard indicators

To simplify the analysis of the standard indicators which are the v_t -indicator (Equation (4.36) and (4.37)) and the S -indicator (Equation (4.38) and (4.39)), capillary effects are neglected in this test case. The pressure boundary conditions are set to $p_{\max} = 30$ MPa and $p_{\min} = 20$ MPa.

Figure 4.27 shows the saturation breakthrough curves (Equation (4.35)) of different model runs. The breakthrough time using only the upscaled coarse-scale model is strongly underestimated at the first breakthrough position (solid lines) and overestimated at the second position (dashed lines). Obviously, the assumption of scale separation is violated for the porous medium under consideration, which means that the REV assumption is also violated. This can be expected just from a visual analysis of the parameter fields shown in Figure 4.26. As a result, the global pressure gradient is underestimated due to the averaging, and the channel connecting inlet and outlet boundary, which can be clearly identified from the fine-scale velocity field (Figure 4.28a), is not well accounted for. The resulting saturation distribution is shown in Figure 4.29, where it is compared to the fine-scale saturation averaged to the coarse grid resolution.

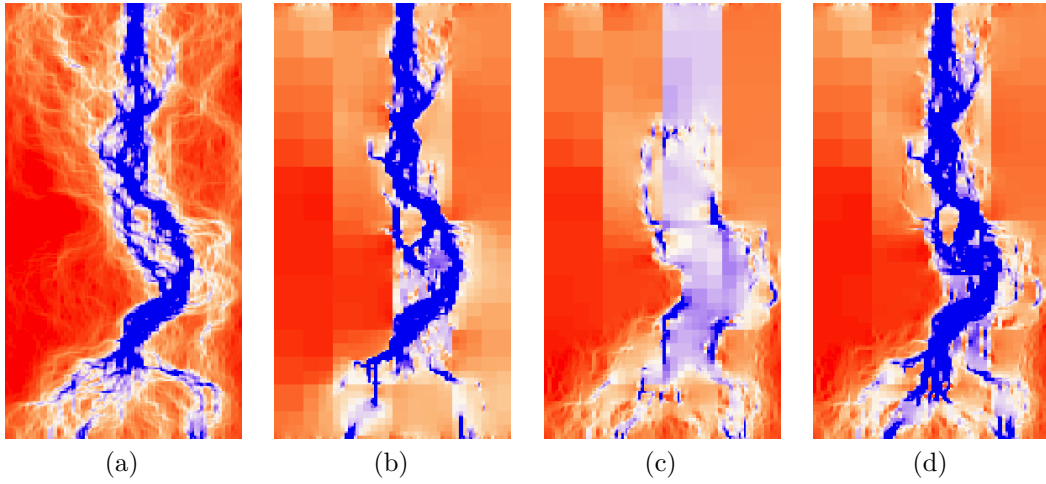


Figure 4.28: Total velocity distribution of the fine-scale simulation (a), the multi-scale simulation with v_t -indicator (b), with S -indicator (c), and using both indicators (d) at $t = 1.5 \times 10^8$ s.

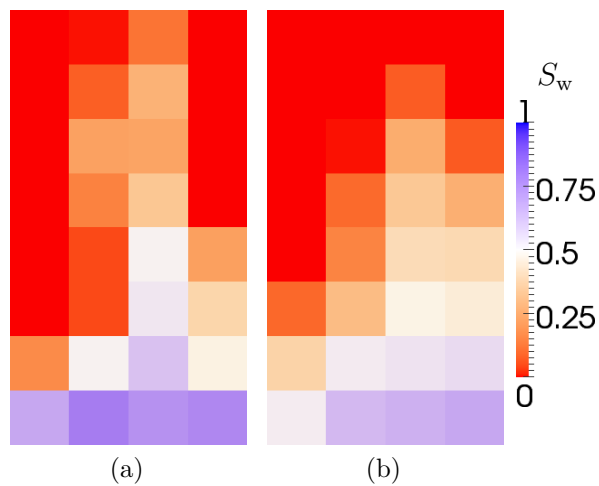


Figure 4.29: Saturation distribution of the fine-scale simulation (a) averaged to the coarse grid resolution, and the coarse-scale simulation using the upscaled parameters (b) at $t = 1.5 \times 10^8$ s.

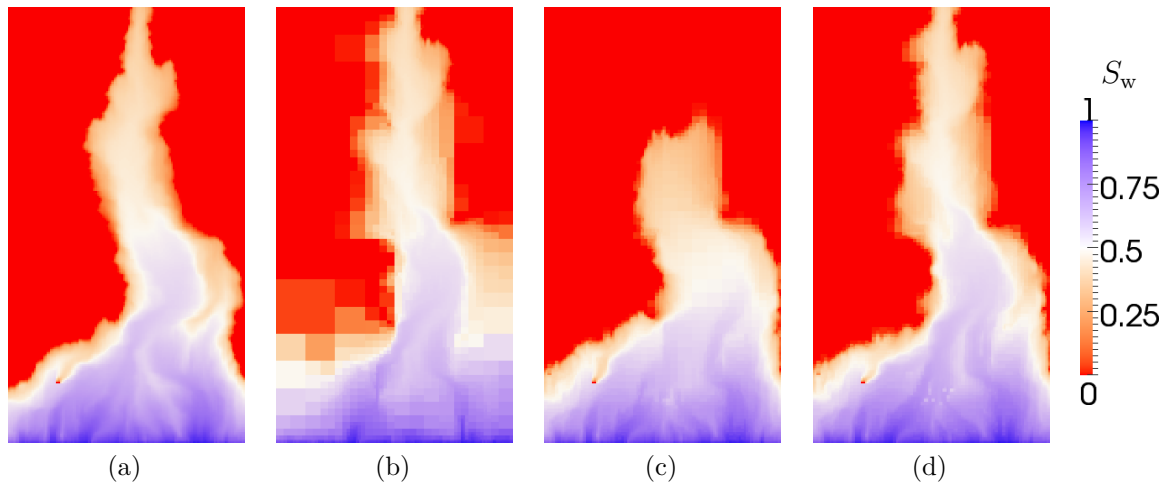


Figure 4.30: Saturation distribution of the fine-scale simulation (a), the multi-scale simulation with v_t -indicator (b), with S -indicator (c), and using both indicators (d) at $t = 1.5 \times 10^8$ s.

A similar behavior can be observed using the S -indicator. In this case, the error at the invading fluid front is reduced due to the higher resolution (Figure 4.30c), but the large scale pressure gradient is also underestimated. Figure 4.28c qualitatively shows the total velocity field at $t = t_{\text{end}}$. In comparison with the fine-scale solution (Figure 4.28a), the preferred flow paths are not sufficiently resolved to reduce the error of the flow field. With only the v_t -indicator, the solution shows the opposite behavior. At the first breakthrough position, the breakthrough time is overestimated. In that case, the invading fluid front is not explicitly refined (Figure 4.30b), leading to an error in the front propagation. However, at the second breakthrough position, the breakthrough time is closer to that of the reference solution, because the global pressure gradient is better approximated. Only a combination of both indicators and thus error reduction in both equations (pressure and transport) results in breakthrough curves which are very close to the reference breakthrough. The saturation distribution at $t = t_{\text{end}}$ (Figure 4.30 (a) and (d)) and the total velocity field are also in very good agreement (Figure 4.28 (a) and (d)). The corresponding grid at the end of the simulation is plotted in Figure 4.31. It nicely illustrates that the moving fluid-fluid front as well as paths of relatively high total velocity are refined while other parts of the plume are coarsened.

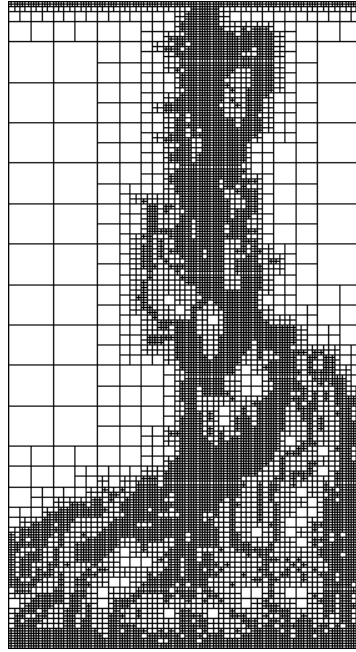


Figure 4.31: Locally adapted grid of the multi-scale solution shown in Figure 4.30d.

Multi-scale indicator

The multi-scale indicator described in Equations (4.40) - (4.42) uses a capillary number to estimate to what extent the flow regime is capillary or viscous dominated. Strictly speaking, the numerical upscaling approach is only valid in a capillary-dominated regime and the indicator should hence lead to a grid refinement if the flow is viscous dominated and to a coarsening if it is capillary dominated.

The adaptation behavior is tested applying two sets of boundary conditions resulting in a viscous-dominated and a capillary-dominated flow regime. For the viscous-dominated case the pressure boundary conditions are set to $p_{\max} = 30$ MPa and $p_{\min} = 20$ MPa, for the capillary-dominated case to $p_{\max} = 26$ MPa and $p_{\min} = 25$ MPa. In both cases, the reference entry pressure is set to $p'_d = 0.05$ MPa (Equation (4.30)). Moreover, the two definitions for the characteristic capillary pressure suggested in Section 4.2.2 are compared, which are for this specific setup defined as: $p_c^c = p_c(0.8) \approx p_d^*$ and $p_c^c = p_c^*(0.2)$.

Figure 4.32 shows selected results for the capillary-dominated case. They clearly show that the choice of the characteristic capillary pressure strongly influences the grid refinement. The results in Figures 4.32a and 4.32d are obtained using the same refinement and coarsening thresholds ($\varepsilon_{Ca,r} = 2$, $\varepsilon_{Ca,c} = 1$) which lead to completely different refinement of the grids (third row of the figure). However, independent of the choice of p_c^c and

ε_{Ca} and the resulting refinement level, the saturation distributions as well as the total velocity magnitudes are very similar.

Considering the saturation breakthrough curves (Equation (4.35)), a first important aspect is that the coarse-scale solution using the numerical upscaling method (Ups) is completely different from the fine-scale solution. In this setup, the global inflow and outflow at the domain boundaries is driven by the global pressure gradient due to the pressure boundary conditions. As an imbibition process is modeled the capillary pressure gradient at the inflow boundary points outwards the domain (in the opposite direction of the pressure gradient). Thus, upscaling errors at the domain boundary, which lead to an error in the capillary pressure gradient or to a wrong flux scaling via coarse-scale permeabilities, directly influence the amount of fluid that can enter the domain. As discussed in Section 4.1.5 the parameter upscaling is particularly difficult at the global domain boundaries. This explanation is supported by the multi-scale results visualized by the yellow curves (diamond marker). The cells at the inflow and outflow boundaries are refined, but the refinement thresholds are too large to cause any additional refinement inside the domain. The breakthrough curves are almost identical to the other multi-scale curves until the invading fluid approaches the outflow boundary, although no more cells are refined. Here, the capillary pressure gradients in the opposite direction to the global pressure gradient lead to a kind of equilibrium state, which is indicated by the constant plateau value of the saturation breakthrough curves. The reason of this behavior is the insufficient grid refinement, which leads to kind of artificial fluxes due to contrast between fine-scale and coarse-scale parameters. The results of Figure 4.32d show that even a small amount of additionally refined cells can avoid such problems. However, the breakthrough curves also shows that further refinement due to the multi-scale indicator does not significantly improve the approximation of the fine-scale result. As the regime is set up to be capillary dominated the multi-scale criterion should, per definition, not lead to a large amount of refined cells if the threshold values are defined around one. Thus, comparing the different definitions of the characteristic capillary pressure, the second definition $p_c^c = p_c^*(\hat{S}_{w,\min}^*) \approx p_c^*(0.2)$ seems to be more reasonable.

The results of the viscous-dominated case are shown in Figures 4.34 and Figures 4.35. As for the capillary-dominated case it can be observed that the choice of the characteristic capillary pressure considerably influences the grid adaptation. However, as the flow regime is viscous dominated a larger number of cells is refined in all four cases visualized in Figure 4.34. This is the expected behavior if the capillary number is chosen as

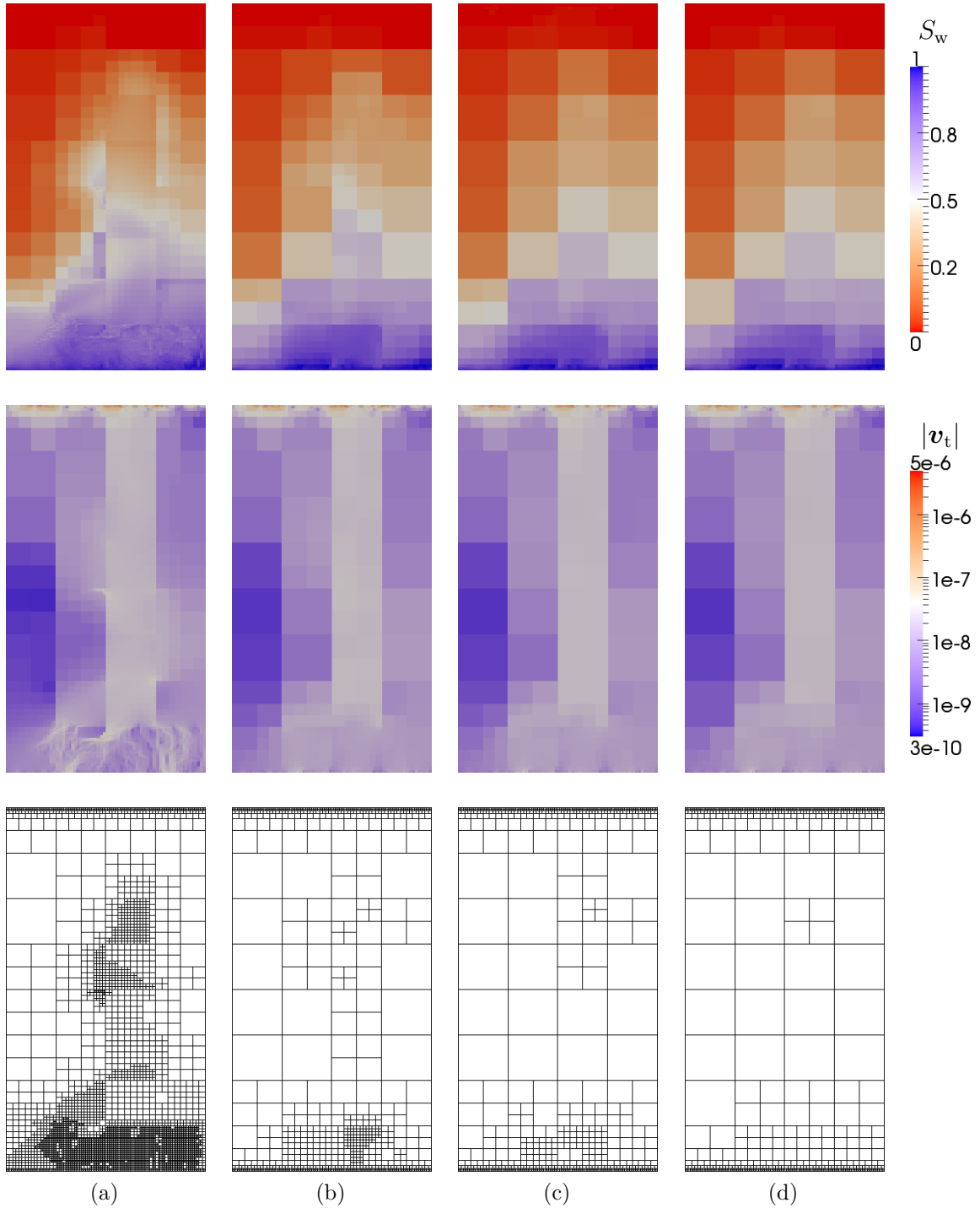


Figure 4.32: Saturation distributions (top row), total velocity distribution (middle row) and refined grids (bottom row) of the capillary-dominated case at $t = 6 \times 10^9$ s applying: (a) $p_c^c = p_c(0.8) \approx p_d^*$, $\varepsilon_{Ca,r} = 2$, $\varepsilon_{Ca,c} = 1$; (b) $p_c^c = p_c(0.8) \approx p_d^*$, $\varepsilon_{Ca,r} = 1$, $\varepsilon_{Ca,c} = 10$; (c) $p_c^c = p_c^*(0.2)$, $\varepsilon_{Ca,r} = 1.1$, $\varepsilon_{Ca,c} = 0.9$; (d) $p_c^c = p_c^*(0.2)$, $\varepsilon_{Ca,r} = 2$, $\varepsilon_{Ca,c} = 1$.

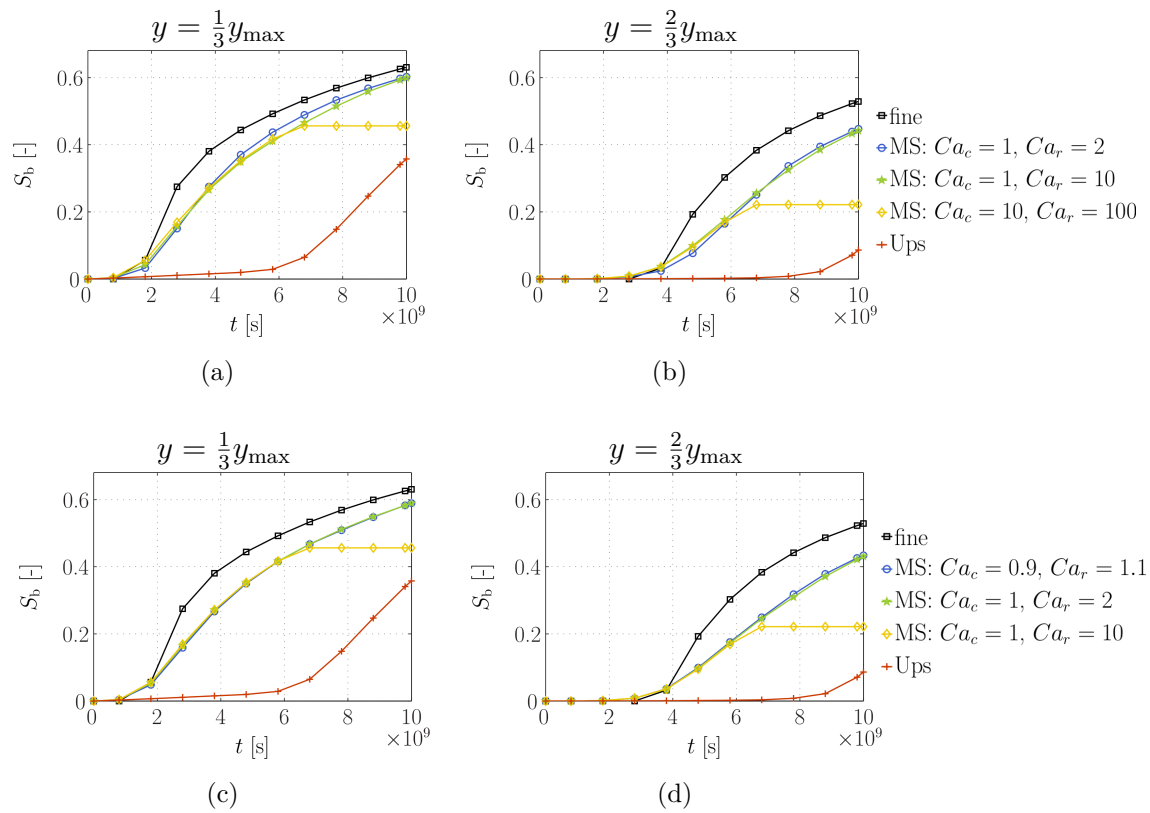


Figure 4.33: Saturation breakthrough curves along the x-axis for the capillary-dominated case: (a) and (b) $p_c^c = p_c(0.8) \approx p_d^*$; (c) and (d) $p_c^c = p_c^*(0.2)$.

the adaptation indicator. The breakthrough curves confirm the meaningful choice of the capillary number as multi-scale indicator. Compared to the coarse-scale solution (Ups) the accuracy of the approximation is significantly improved and the multi-scale breakthrough curves agree very well with the fine-scale curve. As discussed for the capillary-dominated case, an insufficient refinement due to large threshold values can lead to artificial fluxes caused by contrasts between fine-scale and coarse-scale parameters and functions. This can lead to an unphysical behavior. The refinement parameters of the yellow saturation breakthrough curves (diamond marker) in Figure 4.35, as an example, lead to the development of an equilibrium of gradients or fluxes which prevents further inflow or outflow and leads to a constant plateau value of the breakthrough saturation. As concluded from the capillary-dominated case, the definition of the characteristic capillary pressure as $p_c^c = p_c^*(\hat{S}_{w,\min}^*) \approx p_c^*(0.2)$ seems to be the preferable choice. It results in a good approximation of the fine-scale results and an efficient refinement pattern while allowing the definition of the threshold values for refinement and coarsening around a value of one.

This test showed that the proposed multi-scale indicator based on a capillary number can be a meaningful and efficient indicator for grid adaptation in the newly developed multi-scale approach. As expected, its application significantly improves the accuracy of the solution, especially in viscous-dominated regimes. However, additional indicators may be necessary depending on the specific problem setup and regime to avoid an unphysical behavior due to insufficient refinement. As explained in Section 4.2.1 the hierarchic refinement structure leads to a transition zone between fine scale and coarse scale. The transition between fine-scale and coarse-scale model parameters can only work if the indicators lead to a physically motivated and meaningful refinement pattern. Concerning the definition of the capillary number both test cases suggest to use $p_c^c = p_c^*(\hat{S}_{w,\min}^*)$ (Section 4.2.2) as the characteristic capillary pressure.

The grid adaptation has to be performed such that a minimum of cells is refined while the error is sufficiently reduced in order to get an efficient multi-scale model. Thus, additional indicators should first of all not just increase the number of refined cells, but lead to a more advantageous distribution of refined cells. These tests clearly demonstrate that a meaningful combination of different indicators can help to account better for different physical processes and effects. With increasing complexity, a higher number of indicators may be necessary.

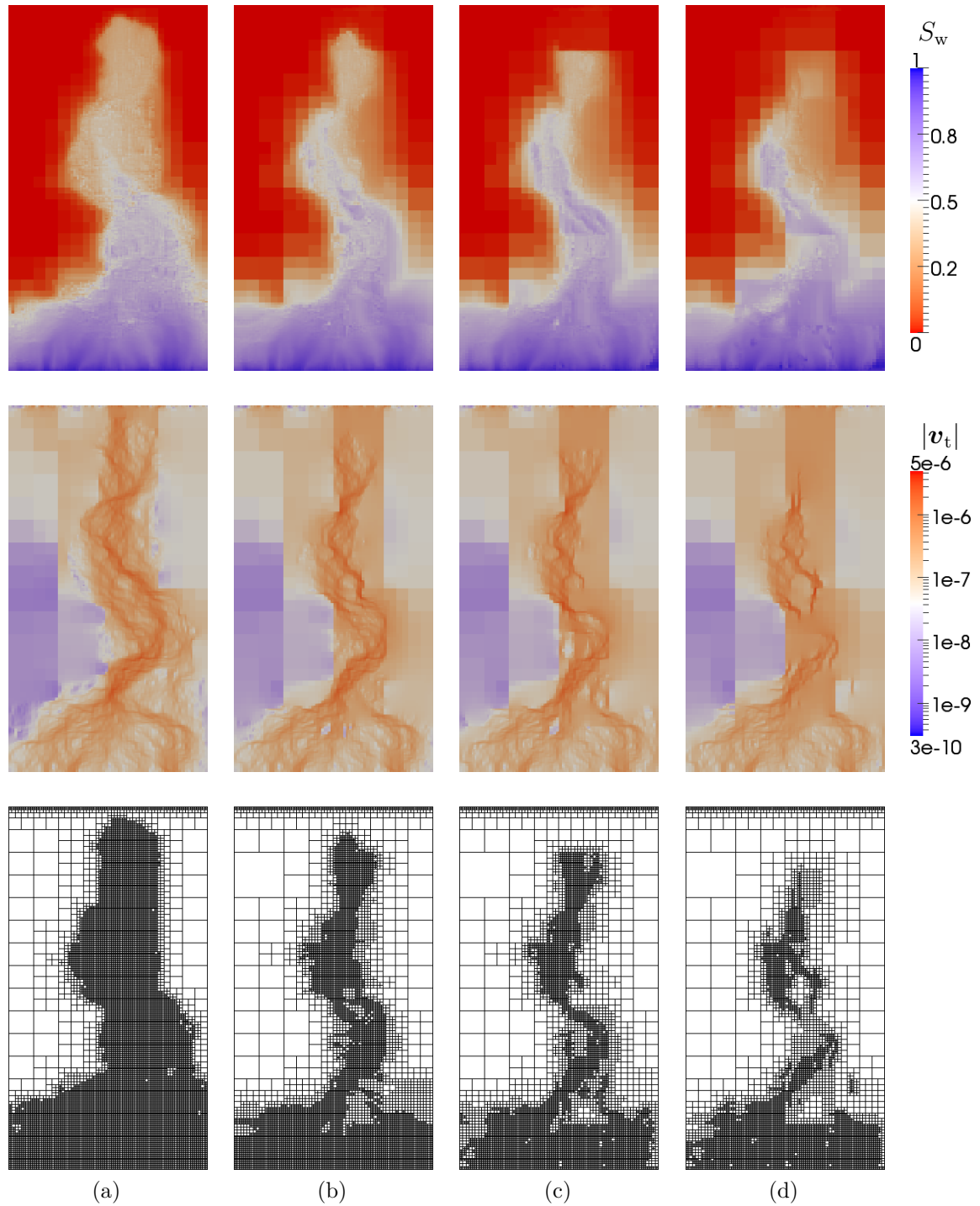


Figure 4.34: Saturation distributions (top row), total velocity distribution (middle row) and refined grids (bottom row) of the viscous-dominated case at $t = 4 \times 10^8$ s applying: (a) $p_c^c = p_c(0.8) \approx p_d^*$, $\varepsilon_{Ca,r} = 2$, $\varepsilon_{Ca,c} = 1$; (b) $p_c^c = p_c(0.8) \approx p_d^*$, $\varepsilon_{Ca,r} = 1$, $\varepsilon_{Ca,c} = 10$; (c) $p_c^c = p_c^*(0.2)$, $\varepsilon_{Ca,r} = 1.1$, $\varepsilon_{Ca,c} = 0.9$; (d) $p_c^c = p_c^*(0.2)$, $\varepsilon_{Ca,r} = 2$, $\varepsilon_{Ca,c} = 1$.

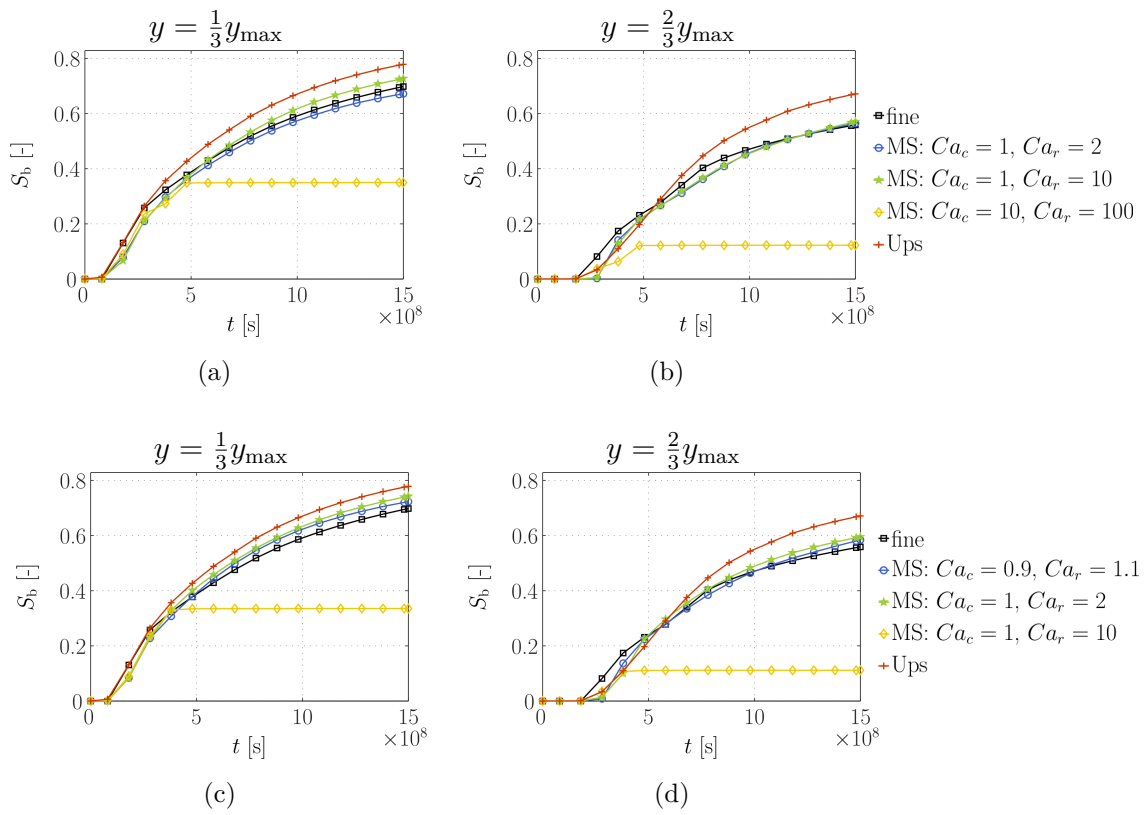


Figure 4.35: Saturation breakthrough curves along the x-axis for the viscous-dominated case: (a) and (b) $p_c^c = p_c(0.8) \approx p_d^*$; (c) and (d) $p_c^c = p_c^*(0.2)$.

Summary In this chapter different numerical upscaling techniques were combined and extended to get a set of methods which enables the calculation of the effective coarse scale parameters appearing in the coarse-scale equations for modeling incompressible immiscible two-phase flow. The numerical upscaling approach was tested and could be validated against fine-scale solutions on several test scenarios. They were designed so that the assumptions included in the upscaling methods can be assumed to be valid. To overcome the limitations of the numerical upscaling, which were discussed in some detail, an adaptive grid method based on multi-point flux approximation was combined with the numerical upscaling. The key factor of this novel multi-scale approach is an appropriate adaptation strategy, which aims to refine and coarsen the grid such that the method is efficient and sufficiently accurate. Therefore, different adaptation indicators were suggested. So-called standard indicators allow to control the numerical error of the solution of the pressure and the saturation transport equation. Further, the idea of special multi-scale indicators was proposed which allow to account for the validity of the upscaled parameters depending on the flow regime. Accounting for one of the basic assumptions of the upscaling, the capillary equilibrium assumption, a new multi-scale indicator based on the definition of a capillary number was introduced. The different indicators and their effect on the adaptation behavior was investigated in several numerical tests. They demonstrated that all suggested indicators can help to considerably improve the quality of the approximation. The choice of a certain indicator or combination of indicators has to be made in dependence on the specific problem and physical regime.

5 Application

In this chapter, the multi-scale method is tested and validated on various scenarios relating to realistic applications: a drainage scenario (two-dimensional) and two imbibition scenarios (two-dimensional and three-dimensional). The first application is motivated by remediation scenarios where the saturated or unsaturated zone is polluted by a Non-Aqueous Phase Liquid (Section 5.1). The second application considers a primary imbibition process into a geological formation (Section 5.2). Both scenarios are designed for the validation of the multi-scale approach against fine-scale simulations. The setups are varied with regard to parameter distribution and dominant physical processes. The two-dimensional applications investigated in Sections 5.1 and 5.2 are in large parts extracted from *Wolff et al. (2013b)*. The third application (Section 5.3) is the model 2 of the SPE 10 benchmark study (*Christie and Blunt, 2001*). Due to the complex geological fine-scale model this application is particularly suitable for demonstrating the capabilities of the multi-scale approach with respect to real three-dimensional applications.

As discussed in the previous chapter, one aim of multi-scale modeling is to overcome the limitations of pure upscaling methods. The multi-scale model can be forced to converge towards the fine-scale solution. However, in many cases, this will lead to disproportionally increasing costs and is contradictory to the aim of providing an efficient method. Thus, the multi-scale approximation is hereafter defined as sufficiently accurate in comparison to a fine-scale solution if the averaged coarse-scale behavior of the solutions is equal. The multi-scale results of the two-dimensional applications are validated by comparison to reference fine-scale solutions. Therefore, breakthrough curves at different positions are compared where the averaged breakthrough saturation is calculated following Equation (4.35). To avoid errors in the solution of the linear system the direct linear solver SuperLU (*Demmel et al., 1999*) is used in the two-dimensional applications in which the number of degrees of freedom is small enough. In the three-dimensional case with a higher number of degrees of freedom an iterative solver has to be applied.

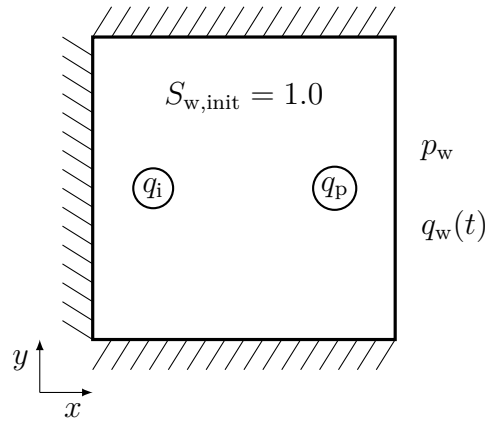


Figure 5.1: Problem setup of drainage scenario.

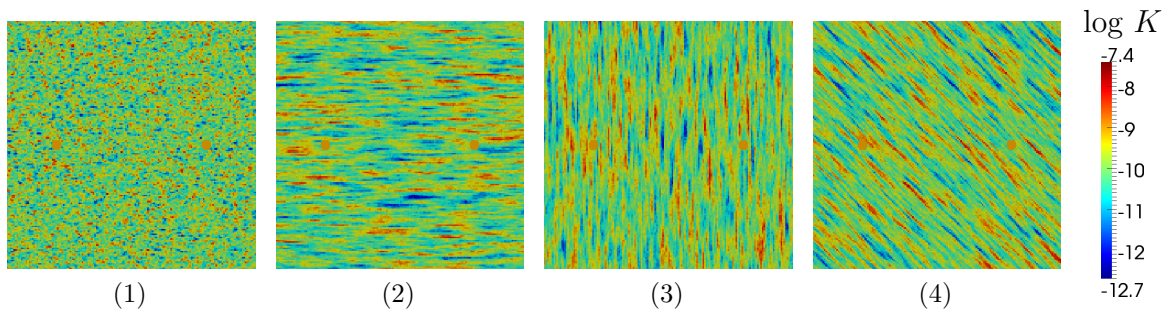


Figure 5.2: Permeability distributions of used for the drainage scenario.

5.1 Two-Dimensional Drainage Scenarios

The first example investigates the propagation of a Dense Non-Aqueous Phase Liquid (DNAPL, e.g. TCE) in a water-saturated porous medium (Figure 5.1). The domain has the size $100 \times 100 \text{ m}^2$. At the eastern boundary, a constant pressure boundary condition and a free outflow condition for the wetting phase are applied. The other boundaries are closed. The DNAPL source has an area of 4 meters diameter and is released with q_i . On the opposite side of the domain, water is produced with q_p . The DNAPL viscosity is $\mu_{\text{DNAPL}} = 0.5\mu_w$ and the porosity is assumed to be constant with $\phi = 0.2$. The permeability fields for this example are generated with the geostatistical modelling tool *gstat* (Pebesma and Wesseling, 1998) using a spherical variogram model. The resulting permeability distributions are shown in Figure 5.2. The permeabilities vary in a range of about two orders of magnitude around the mean $\bar{k} = 10^{-10} \text{ m}^2$. For field (1), a correlation length of $l_x = 2 \text{ m}$ in x-direction and of $l_y = 1 \text{ m}$ in y-direction is chosen. For fields (2), (3) and (4), the correlation length is $l_m = 15 \text{ m}$ in major

direction and $l_p = 1.5$ m in perpendicular direction. The major direction of field (2) is the x-direction, of field (3) the y-direction (rotated by 90°), and of field (4) the diagonal direction (rotated by 135°).

To obtain a heterogeneous field of capillary-pressure-saturation functions, a Leverett-J-function approach is used:

$$p_{ci}(S_w) = p'_d \sqrt{\frac{\phi_i \bar{k}}{\bar{\phi} k_i}} J(S_w). \quad (5.1)$$

It scales a reference entry pressure p'_d according to the permeability and porosity distribution to get one function for each cell i , where \bar{k} and $\bar{\phi}$ are the mean permeability and porosity. For the J-function $J(S_w)$ as well as for the relative permeability functions Brooks-Corey parameterizations are chosen (*Brooks and Corey*, 1964):

$$J(S_w) = S_w^{-\frac{1}{\lambda}} \quad (5.2)$$

$$k_{rw} = S_w^{\frac{2+3\lambda}{\lambda}} \quad (5.3)$$

$$k_{rn} = (1 - S_w)^2 (1 - S_w^{\frac{2+\lambda}{\lambda}}). \quad (5.4)$$

The domain is discretized by a fine-scale grid of 160×160 cells and a coarse-scale grid of 10×10 cells leading to a hierarchic refinement factor of four.

For the permeability field (1), it seems reasonable to assume that the coarse grid cells are an REV for the absolute permeability. Thus, in a first test, we neglect capillary pressure and only apply the absolute permeability upscaling. The simulation results are shown in Figure 5.3. On the one hand, the absolute permeability upscaling is quite reliable for this case; on the other hand, the relatively smooth propagation of the fluid fronts allows an efficient adaptation of the grid. Both the saturation plots in Figures 5.3a and 5.3b and the breakthrough curves shown in Figure 5.3c illustrate the fact that the multi-scale solution is in very good agreement with the fine-scale reference.

Next, a capillary pressure distribution is defined by setting $p'_d = 100$ Pa. The value of p'_d and an injection/production rate of $|q| = 1.25 \frac{m^3}{s}$ are chosen such that the flow regime is still viscous dominated. The results for the permeability fields (1) to (4) are shown in Figure 5.4. In all four cases, the multi-scale results are on average in very good agreement with the fine-scale solution. Compared with the case neglecting capillary effects, the saturation distributions are less smooth and show discontinuities due to entry pressure effects. Because of the small correlation lengths (at least in one

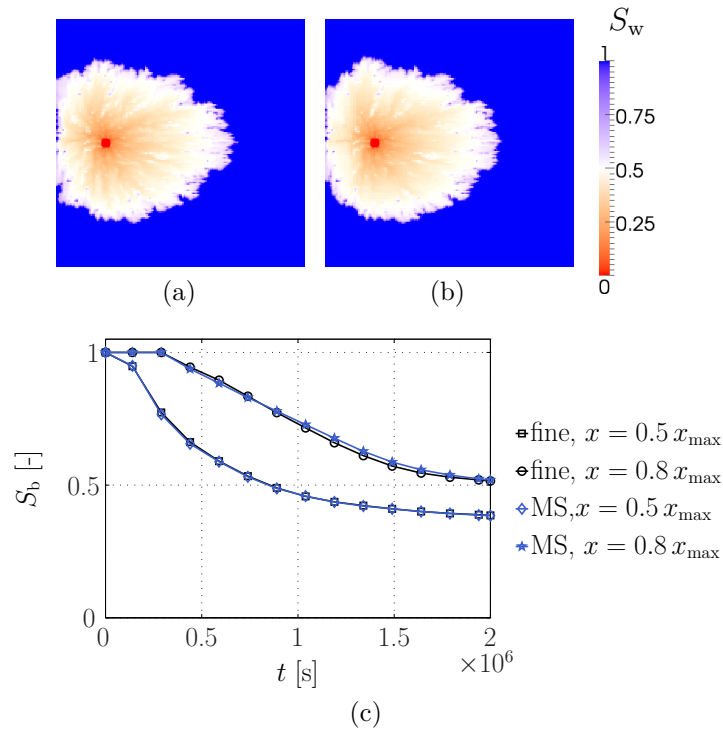


Figure 5.3: Saturation distribution of the fine-scale simulation (a) and the multi-scale simulation (b) at $t = 3 \times 10^5$ s and saturation breakthrough curves along the y-axis (c); permeability field (1) (Figure 5.2), $p_c = 0$.

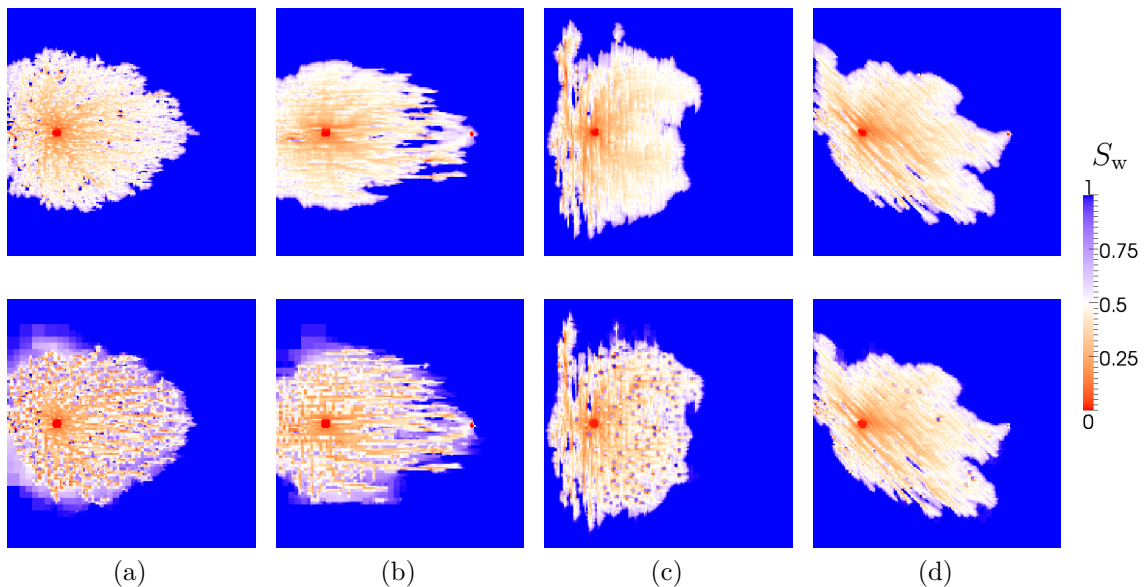


Figure 5.4: Saturation distributions of the fine-scale simulations (upper row) and the multi-scale simulations (lower row) at $t = 3 \times 10^5$ s using the permeability fields (1): (a), (2): (b), (3): (c), and (4): (d) ($p_c \neq 0$, viscous-dominated flow conditions).

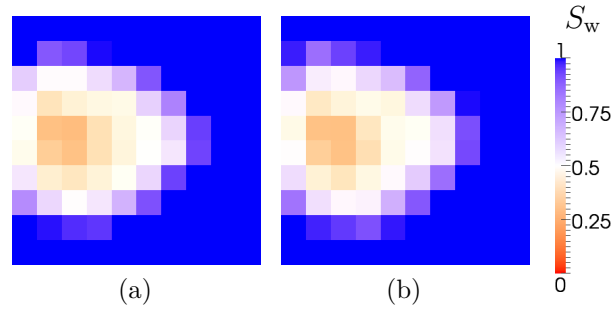


Figure 5.5: Saturation distribution of the fine-scale simulation (a) and the multi-scale simulation (b) at $t = 3 \times 10^5$ s averaged to the coarse grid resolution; permeability field (1) (Figure 5.2), $p_c = 0$.

direction), the heterogeneous parameters of the chosen fields show strong contrasts on a small length scale. Thus, the saturations and velocities also vary quite strongly on small length scales, making it difficult to adapt the grid in these regions efficiently and meaningfully. The result is small isolated areas in the DNAPL plume in which the grid is coarsened. Mixture of the quasi-averaged and fine-scale values leads to the slightly spotted saturation patterns in Figures 5.4a, 5.4b, 5.4c, and 5.4d. However, as pointed out before, we assume the multi-scale method to be sufficiently accurate if the averaged coarse-scale behavior is similar to that of the fine-scale solution. On average, these spotted patterns are negligible. This can be seen clearly in Figure 5.5, where the averaged solutions of Figure 5.4a (permeability (1)) are shown as examples. As regards the breakthrough curves in Figure 5.6, all multi-scale results match the fine-scale results for $x = 0.5x_{\max}$ very well. The agreement gets worse at later simulation times, although the breakthrough time agrees very well at the second breakthrough position. One possible reason is the boundary effect. Both the numerical upscaling methods as well as the MPFA method are less accurate at the boundaries. At coarser discretization widths, this can affect the solution more strongly due to higher numerical diffusion. A second reason is a limitation of the refinement. Especially in the case of permeability fields (1) and (3), the plume almost covers the whole domain at later simulation times. However, for reasons of efficiency, depending on the adaptation indicators, only a certain percentage of the cells is allowed to be refined. This can, of course, increase the error of the solution.

Finally, the reference entry pressure is increased to $p'_d = 1000$ Pa. The injection/production rate is decreased to $|q| = 0.06 \frac{m^3}{s}$ to reach a capillary-dominated flow regime ($Ca < 1$), which is much more realistic for the DNAPL scenario under investigation. In this case,

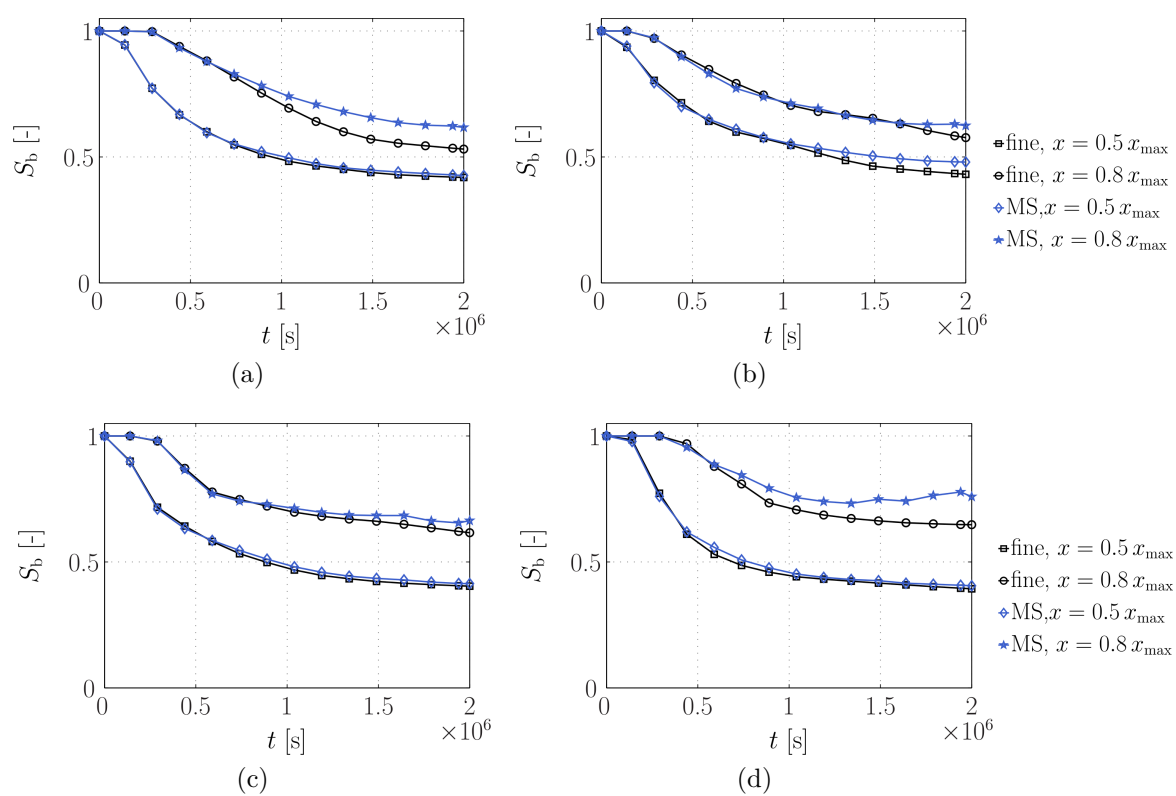


Figure 5.6: Saturation breakthrough curves along the y-axis using permeability fields (1): (a), (2): (b), (3): (c), and (4): (d) ($p_c \neq 0$, viscous-dominated flow conditions).

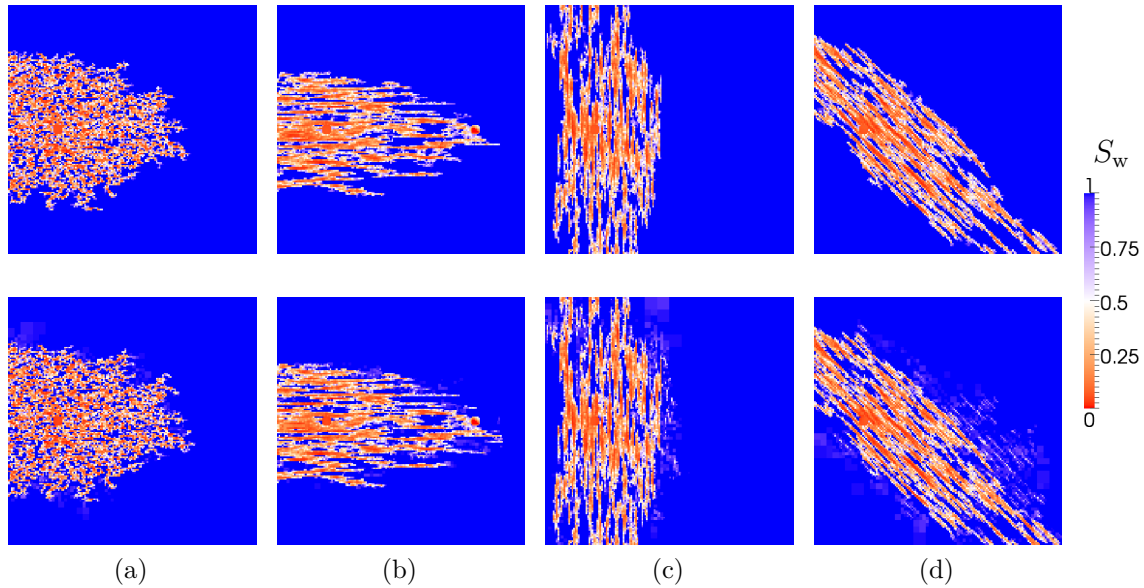


Figure 5.7: Saturation distributions of the fine-scale simulations (upper row) and the multi-scale simulations (lower row) at $t = 5 \times 10^6$ s using the permeability fields (1): (a), (2): (b), (3): (c), and (4): (d) ($p_c \neq 0$, capillary-dominated flow conditions).

the saturation patterns are completely dominated by entry pressure effects which lead to strong saturation discontinuities in the area of the DNAPL plume (Figure 5.7). Due to the strong discontinuities in the saturation, the adaptation indicators introduced previously tend to refine most parts of the DNAPL plume. Outside the plume, the grid is completely coarsened, because the propagation is dominated by the local capillary pressure gradients instead of the global pressure gradient. Thus, in all four cases, the multi-scale solution fits the fine-scale solution very well, except for some numerical diffusion effects. This is also confirmed by the breakthrough curves shown in Figure 5.8. At later simulation times as well, the error is small compared with the viscous-dominated case. This indicates that the amount of cells allowed to be refined is sufficient to cover all important effects. The negative influence of the right boundary is not visible. The reason, as pointed out before, is that the flow is more dominated by local effects than by global gradients.

To demonstrate how the flow regime influences the grid adaptation, as examples the adapted grids according to Figures 5.3b, 5.4a, and 5.7a are shown in Figure 5.9. If capillary effects are neglected and the saturation distribution is therefore smooth, it is comparatively simple to identify and to refine the moving front of the DNAPL plume

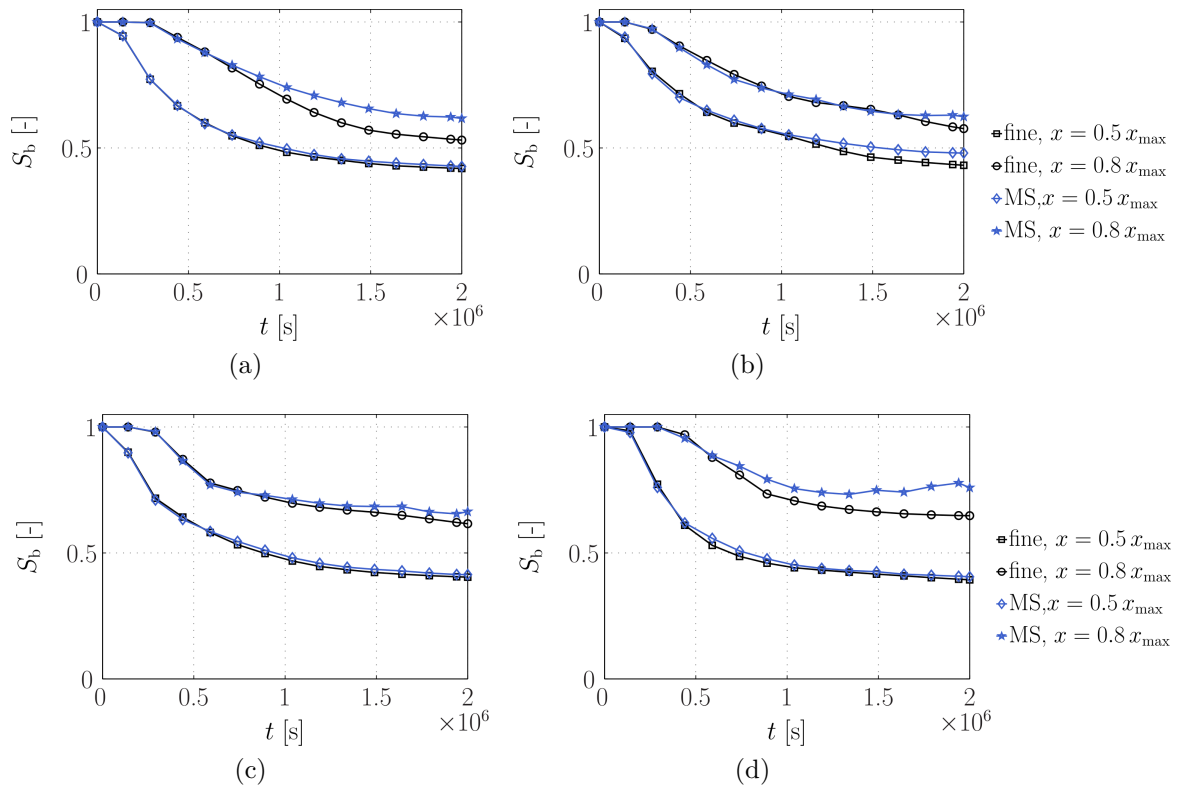


Figure 5.8: Saturation breakthrough curves along the y-axis using permeability fields (1): (a), (2): (b), (3): (c), and (4): (d) ($p_c \neq 0$, capillary-dominated flow conditions).

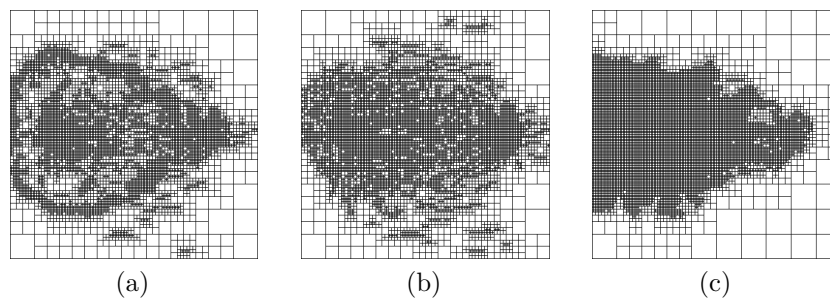


Figure 5.9: Grids of the multi-scale solutions shown in: (a) Figure 5.3b ($p_c = 0$), (b) Figure 5.4a ($p_c \neq 0$, viscous dominated), and (c) Figure 5.7a ($p_c \neq 0$, capillary dominated)

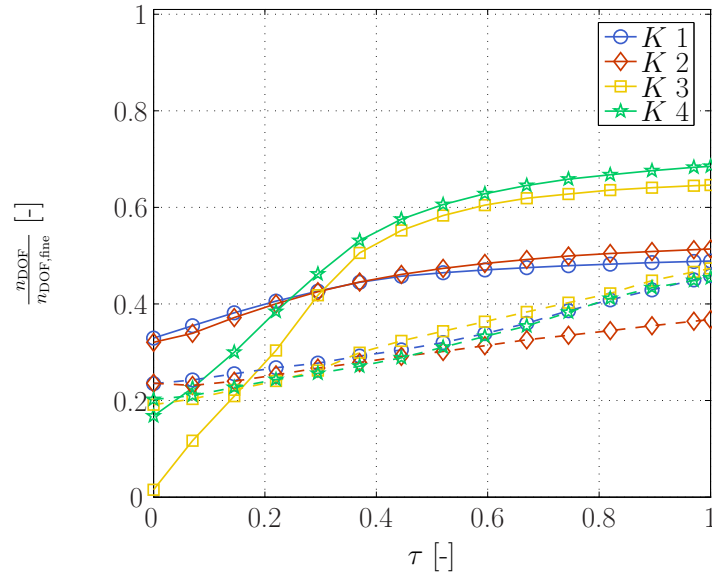


Figure 5.10: Ratio of multi-scale and fine-scale numbers of degrees of freedom (n_{DOF}) over dimensionless simulation time τ . Solid lines show the viscous-dominated cases, dashed lines the capillary dominated cases.

and to coarsen the other parts. The viscous-dominated case including capillary effects is in a kind of transition zone. Here, the adaptation is indicated by both the structure of the plume due to local effects, and global gradients and flow paths. Thus, it is difficult to identify clear structures. In the capillary-dominated case, it is obvious that the grid adaptation is mainly driven by local saturation and thus capillary pressure gradients. It is very challenging in this case to define an adaptation strategy which allows local coarsening inside the plume and still leads to a sufficient accuracy, because of the strongly heterogeneous and discontinuous plume.

Independent of the different adaptation behavior, the multi-scale approach clearly increases the efficiency in comparison with the fine-scale model. Figure 5.10 shows the development of the DOF (degrees of freedom) scaled by the DOF of the fine-scale model over a dimensionless simulation time. On average, the DOF are reduced to 30-50% of the fine-scale DOF. In the viscous-dominated case, the DOF are systematically higher than in the capillary-dominated case. The reason is that, in the latter, the refinement within the plume is sufficient while otherwise preferred flow paths have to be additionally refined to get a correct global flow behavior.

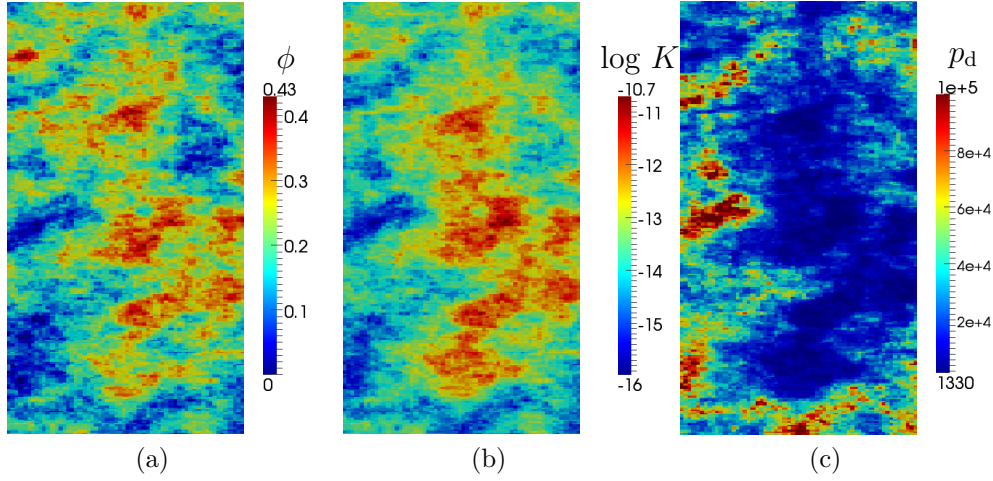


Figure 5.11: Porosity (a), permeability (b), and entry pressure (c) distribution according to layer 15 of the SPE 10 benchmark model 2 (top formation).

5.2 Two-Dimensional Imbibition Scenarios

The second example tests the multi-scale method on two layers of the three-dimensional geological model (model 2) of the SPE 10 benchmark study (*Christie and Blunt, 2001*). The permeability and porosity fields of layer 15 (top formation) are shown in Figure 5.11a and 5.11b and of layer 50 (bottom formation) in Figure 5.12a and 5.12b. Both fields show high parameter contrasts and different kinds of large scale features like channels, which massively strain the assumption of scale separation. The corresponding entry pressure distributions are again obtained following Equation (5.1). As we are now considering an imbibition process, the definition of the J-function is changed slightly to avoid entry pressures:

$$J(S_w) = S_w^{-\lambda} - 1. \quad (5.5)$$

The fine-scale relative permeabilities are calculated using the quadratic laws

$$k_{rw} = S_w^2 \quad (5.6)$$

$$k_{rn} = (1 - S_w)^2 \quad (5.7)$$

and the fluid viscosities are $\mu_w = 10^{-3}$ kg/(ms) and $\mu_n = 5 \times 10^{-3}$ kg/(ms). The problem setup is illustrated in Figure 5.13. The domain is initially saturated by a non-wetting phase (e.g. oil) and water infiltrates from the southern domain boundary. The eastern and western sides are closed and a pressure gradient in y-direction is applied. On the

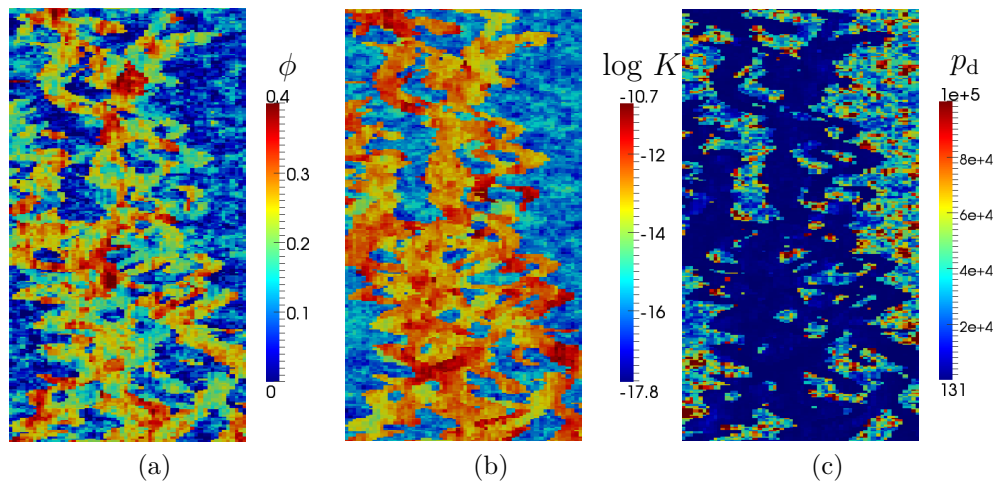


Figure 5.12: Porosity (a), permeability (b), and entry pressure (c) distribution according to layer 50 of the SPE 10 benchmark model 2 (bottom formation).

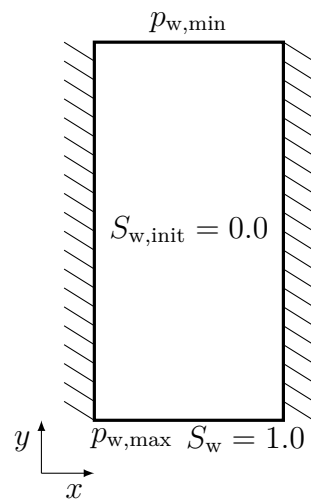


Figure 5.13: Problem setup of the imbibition scenario.

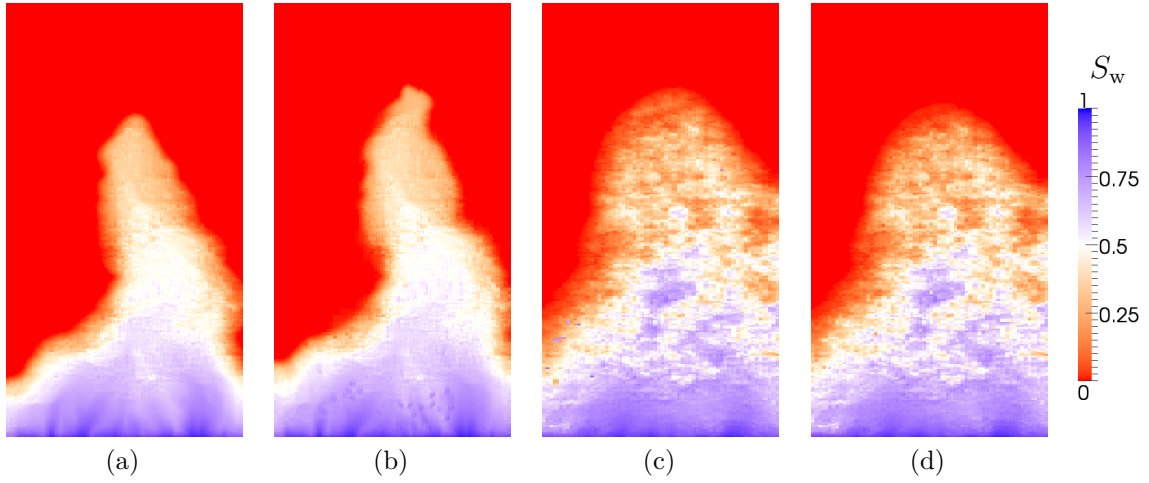


Figure 5.14: Saturation distribution of the fine-scale simulations: (a) viscous-dominated flow conditions, $t = 2.6 \times 10^8$ s; (c) capillary-dominated flow conditions, $t = 4.2 \times 10^9$ s, and the multi-scale simulations: (b) viscous-dominated flow conditions, $t = 2.6 \times 10^8$ s; (d) capillary-dominated flow conditions, $t = 4.2 \times 10^9$ s (layer 15, $p_c \neq 0$).

fine scale, the domain is discretized by a grid of 128×256 cells and on the coarse scale by a grid of 4×8 cells, leading to a hierarchic refinement factor of 5.

As already done in Section 5.1, we consider a viscous-dominated and a capillary-dominated flow regime. For the viscous-dominated case the pressure boundary conditions are set to $p_{\max} = 30$ MPa and $p_{\min} = 20$ MPa, for the capillary-dominated case to $p_{\max} = 26$ MPa and $p_{\min} = 25$ MPa. In both cases, the reference entry pressure is set to $p'_d = 0.05$ MPa.

The results for layer 15 are shown in Figures 5.14 and 5.15. The saturation plots show the situation approximately at the breakthrough time at the second breakthrough position. On average, the multi-scale solution agrees very well with the fine-scale solution (Figure 5.15), although the front speed in the multi-scale solution of the viscous-dominated regime is slightly overestimated (Figure 5.14 (a) and (b)). The results clearly show that the change in the flow regime results in quite different saturation patterns. In the viscous-dominated case, a large-scale finger develops, revealing a large-scale channel-like structure in the heterogeneous parameters. In the capillary dominated regime, the propagation is much more diffusive, revealing the local heterogeneous structures. As already observed in Section 5.1, the refinement in the area of the plume is sufficient in the capillary-dominated regime while the refinement in regions of global flow paths becomes

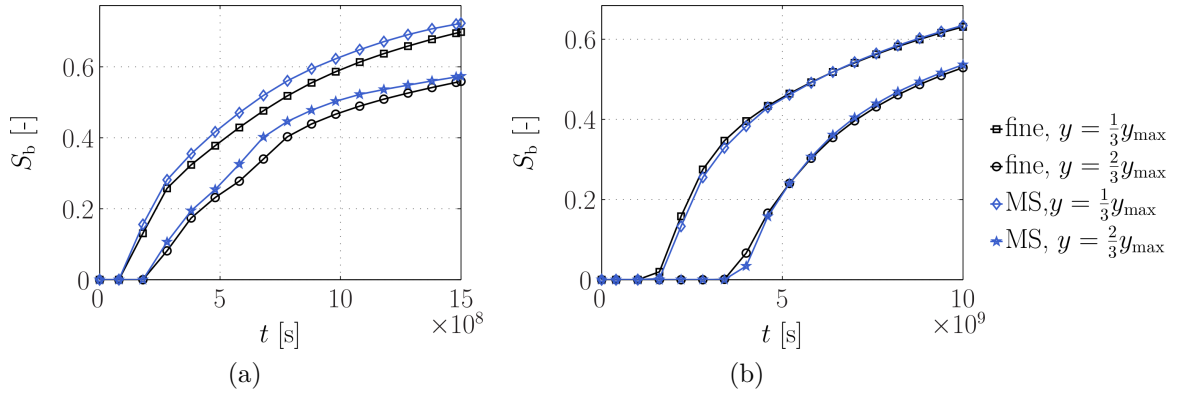


Figure 5.15: Saturation breakthrough curves along the x-axis: (a) viscous-dominated flow conditions; (b) capillary-dominated flow conditions (layer 15, $p_c \neq 0$).

more important to model the viscous-dominated case correctly. The breakthrough curves of the multi-scale solution approximate the fine-scale curves very well.

In comparison with layer 15 which exhibits a smooth transition between areas of high and low permeability and porosity and a more regular parameter distribution, layer 50 shows a highly channelized structure with high local contrasts in the heterogeneous parameters. The results for layer 50 are shown in Figures 5.16 and 5.17. The saturation patterns of the fine-scale and the multi-scale model at the beginning of the second breakthrough agree very well in the viscous-dominated regime. In the capillary-dominated regime, the speed of the propagation of the invading fluid is overestimated, although the distribution patterns in general are similar. At the first breakthrough position, the multi-scale solution is in very good agreement with the fine-scale solution in both the viscous and the capillary-dominated case. At the second position, the breakthrough times of the fine-scale model are well met in both cases and the breakthrough curves are similar at an early simulation time. However, with increasing time, the averaged breakthrough saturations of the multi-scale solutions increase much faster than those of the fine-scale solution. The limits of the numerical upscaling have been discussed before. Most examples discussed in this section violate important assumptions of the upscaling methods. However, resulting errors could mostly be corrected by the multi-scale approach. One can assume that, for the channelized structure of layer 50, the coarse-scale quantities cannot resolve the effects of the strong local contrasts in the capillary pressure functions given by the fine-scale structure, especially at the “channel walls”. Thus, the development of certain flow paths is completely dependent on the refinement strategy. If more cells are refined, additional flow paths might open, changing the effective cross section which is available

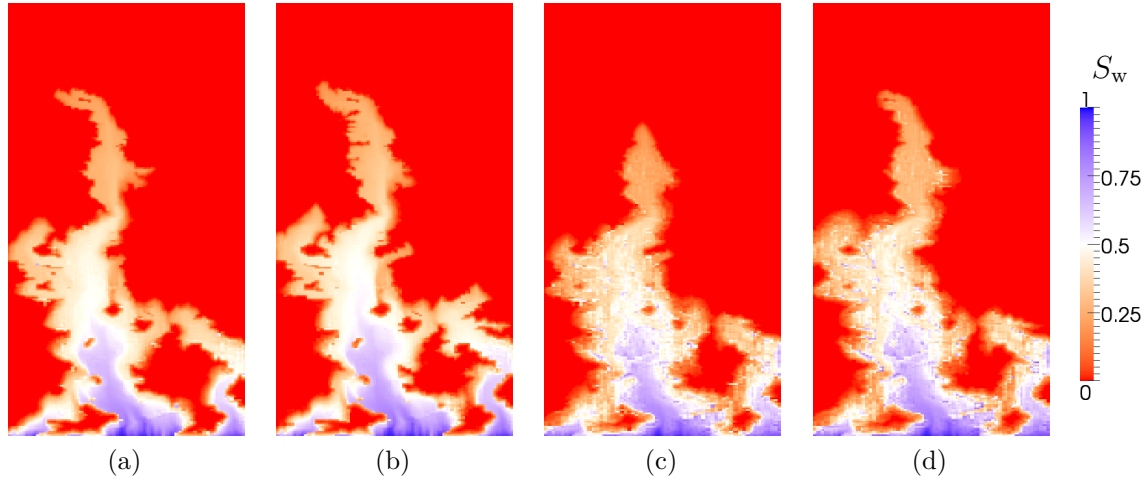


Figure 5.16: Saturation distribution of the fine-scale simulations: (a) viscous-dominated flow conditions, $t = 2 \times 10^8$ s; (c) capillary-dominated flow conditions, $t = 2 \times 10^9$ s, and the multi-scale simulations: (b) viscous-dominated flow conditions, $t = 2 \times 10^8$ s; (d) capillary-dominated flow conditions, $t = 2 \times 10^9$ s (layer 50, $p_c \neq 0$).

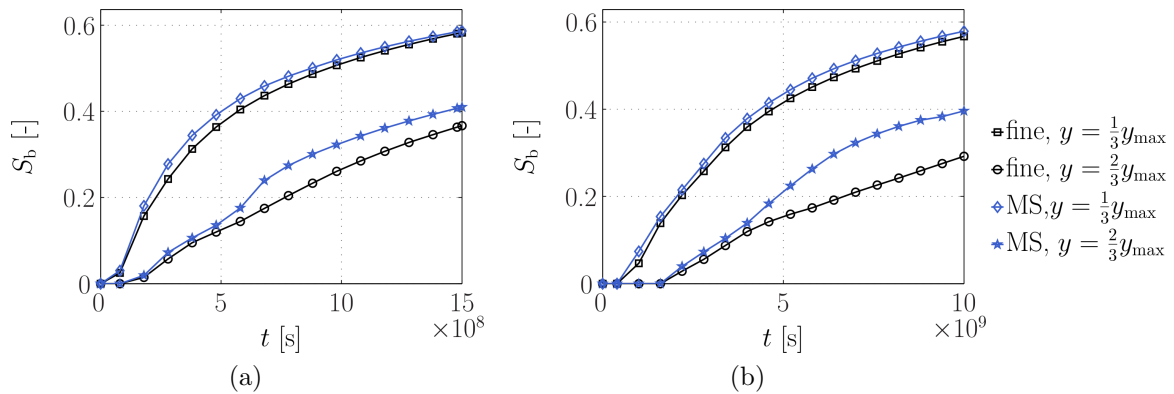


Figure 5.17: Saturation breakthrough curves along the x-axis: (a) viscous-dominated flow conditions; (b) capillary-dominated flow conditions (layer 50, $p_c \neq 0$).

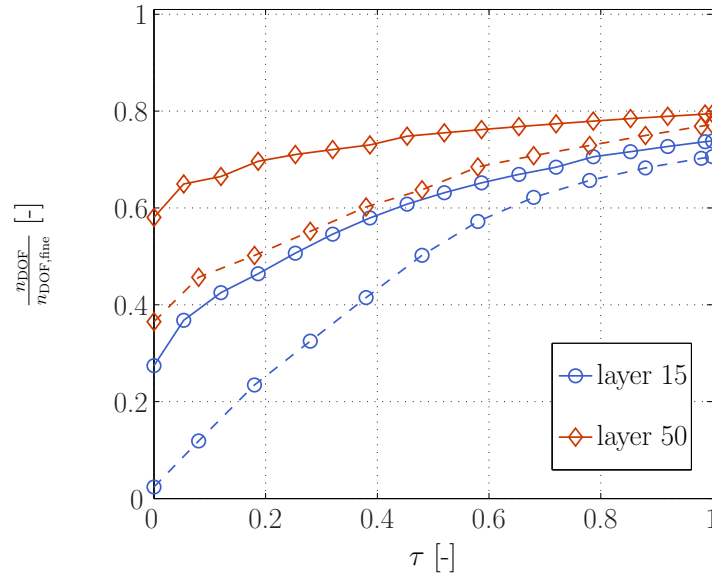


Figure 5.18: Ratio of multi-scale and fine-scale numbers of degrees of freedom (n_{DOF}) over dimensionless simulation time τ . Solid lines show the viscous-dominated cases, dashed lines the capillary dominated cases.

for flow. This strongly influences the global gradients and thus the amount of fluid that can be transported. From the results, it can be assumed that the refinement is sufficient until $t \approx 5 \times 10^8$ s in the viscous and $t \approx 4 \times 10^9$ s in the capillary-dominated case. Afterwards, more or different cells would have to be refined in order to decrease the error.

The number of degrees of freedom (DOF) scaled by the fine-scale DOF over simulation time are plotted in Figure 5.18. For layer 15, the multi-scale model needs approximately 50% of the DOF of the fine-scale model, while the accuracy is still sufficient. Thus, the efficiency can be clearly increased. The difference between the capillary and the viscous-dominated regime is negligible. For layer 50, approximately 70% of the DOF of the fine-scale model are used. While the multi-scale solution can be viewed as sufficiently accurate in the viscous dominated case, the accuracy in the capillary-dominated case decreases after a certain point in time (approximately half-time) is reached. Stronger refinement to decrease this error would increase the DOF further.

5.3 Application to the Three-Dimensional SPE10 Benchmark

In Sections 5.1 and 5.2 the multi-scale approach is tested and validated by means of different two-dimensional scenarios including various processes and regimes. However, for the employment on realistic applications it is essential that the method can be extended to three space dimensions. Both the numerical method (Chapter 3) and the parameter upscaling algorithms (Chapter 4) which are combined to the novel multi-scale approach are derived and introduced for the general three-dimensional case. In the following, a first application to a three-dimensional scenario is presented, which can be viewed as a kind of outlook to discuss the capabilities and the potential of the method with regard to realistic applications.

The setup is taken from the second problem of the SPE 10 benchmark (*Christie and Blunt, 2001*). The fine-scale geological model is originally described on a cartesian grid of $60 \times 220 \times 85$ (1,122,000) cells. For this test a coarse-scale grid of $4 \times 14 \times 6$ cells is used allowing for four hierarchic refinement levels. This yields a fine-scale grid of $64 \times 224 \times 96$ (1,376,256) cells. The simulation domain has a size of $365.8 \times 670.6 \times 51.8$ m. For visualization purposes the z-axis is scaled by factor five in all figures of this section showing the three-dimensional model domain.

The heterogeneous porosity and permeability distributions are shown in Figure 5.19. The model consists of two different formation types. The top 21 meters are a representation of a prograding near shore environment with a smooth Gaussian like parameter distribution, while the lower 30 meters are fluvial showing a clearly channelized structure. The domain is initially fully saturated by the oil phase. Water is injected through a vertical well in the center of the domain and oil is produced in the four corners (see Figure 5.20). As in the previous example, we assume a water viscosity of $\mu_w = 10^{-3}$ kg/(ms) and a oil viscosity of $\mu_n = 5 \times 10^{-3}$ kg/(ms), and use a quadratic law for the relative-permeability-saturation functions (Equations (5.6) and (5.7)). Capillary pressure and gravity are neglected. The wells are implemented using a Peaceman well model (*Peaceman, 1978*) which defines the source of a phase in a grid cell i including a well as

$$q_{\alpha i} = WI_i \lambda_{\alpha} (p_{bh} - p_{\alpha i}) \quad (5.8)$$

where WI_i is the well index ($[WI] = \text{m}^3$) and p_{bh} the well bottom hole pressure. In the

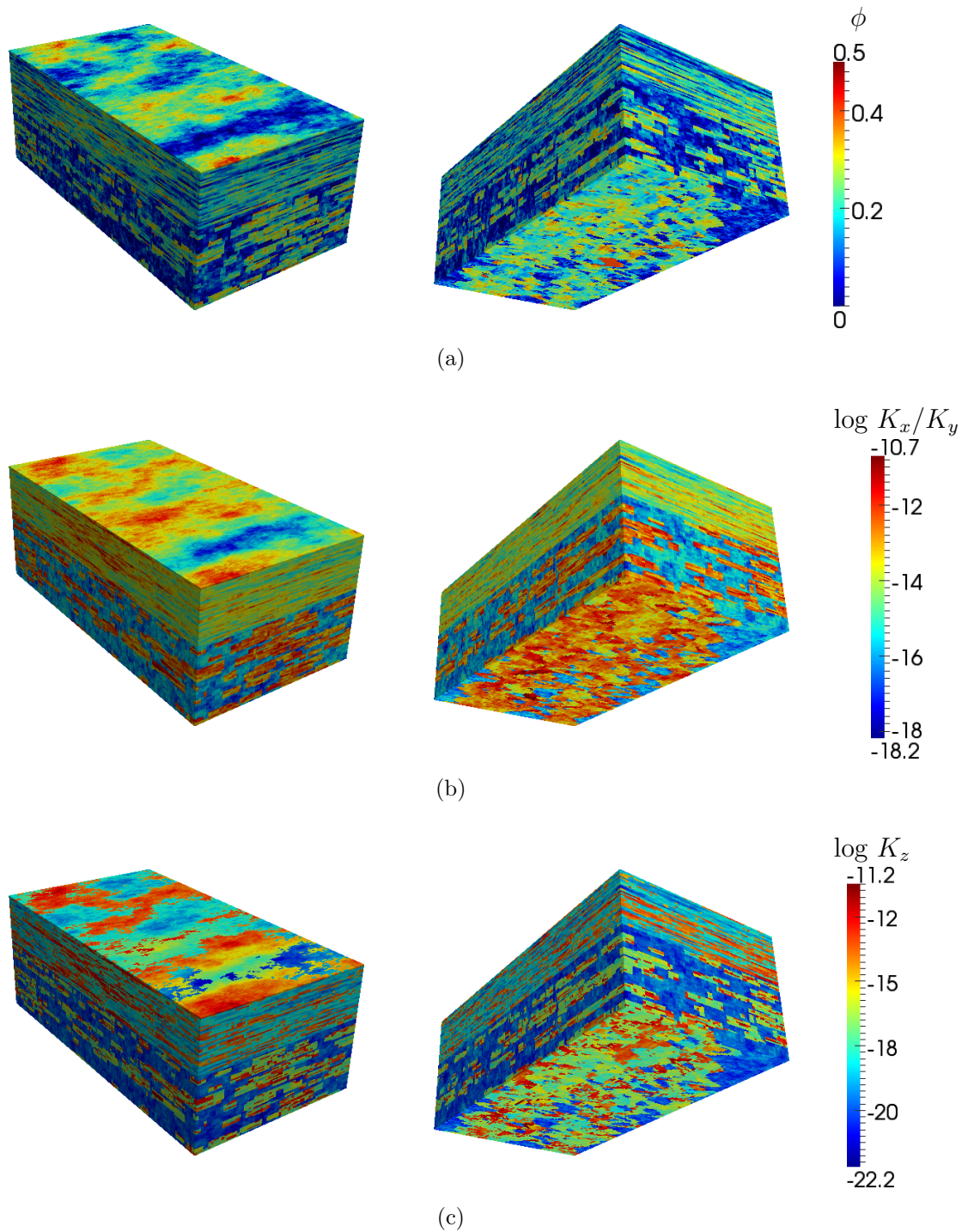


Figure 5.19: Porosity (a) and permeability (b)/(c) distribution according to model 2 of the SPE 10 benchmark. The left column shows a top view, the right column a bottom view (z-direction scaled by 5).

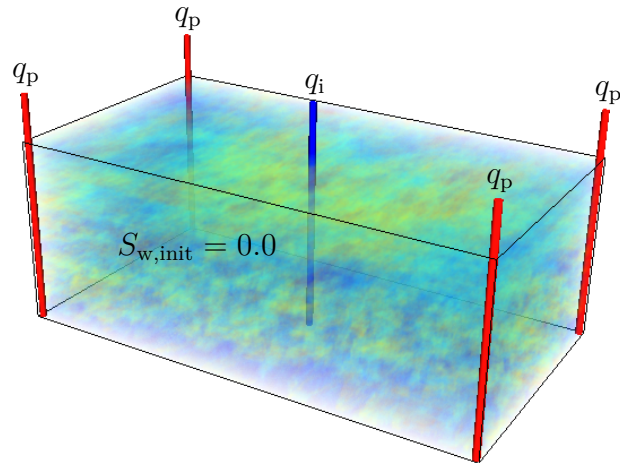


Figure 5.20: Problem setup: One vertical central injector (q_i) and one vertical producer in each corner of the domain (q_p); all wells are completed throughout the formation (z-direction scaled by 5).

following simulations we assume that the wells are controlled by a well bottom hole pressure of $p_{bhi} \approx 68.9$ MPa in the injector and $p_{bhp} \approx 27.6$ MPa in the producers. The domain boundaries are defined to be impermeable.

The strongly heterogeneous and anisotropic permeability distribution results in a complex global coefficient matrix of the linear system for calculating the pressure distribution. Compared to a TPFA method, using the MPFA method leads to a less sparse matrix. Thus, depending on the heterogeneity and anisotropy it is even more challenging for the linear solver to solve the system. In the following, a full MPFA L-method is compared with a combined MPFA-TPFA method. The latter applies the L-method for calculating the fluxes whenever coarse-scale permeabilities, which are not necessarily \mathbf{K} -orthogonal, are included and TPFA if only fine-scale permeabilities influence the flux. A restarted Generalized Minimal Residual (GMRes) solver with ILUn preconditioner (*Barrett et al.*, 1994) is used as linear solver.

The water saturation distributions for 920 days simulated time are shown in Figure 5.21. Especially at the beginning of the injection and during the initial third of the simulation the fluid distributions using the MPFA and MPFA-TPFA method differ. The use of TPFA for the fine-scale fluxes leads to a faster propagation of the injected water and hence a earlier arrival time of water in the producers.

The water saturation distribution inside the water plume and the evolution of the adaptive grid during the simulations is visualized in Figure 5.22. Besides the differences

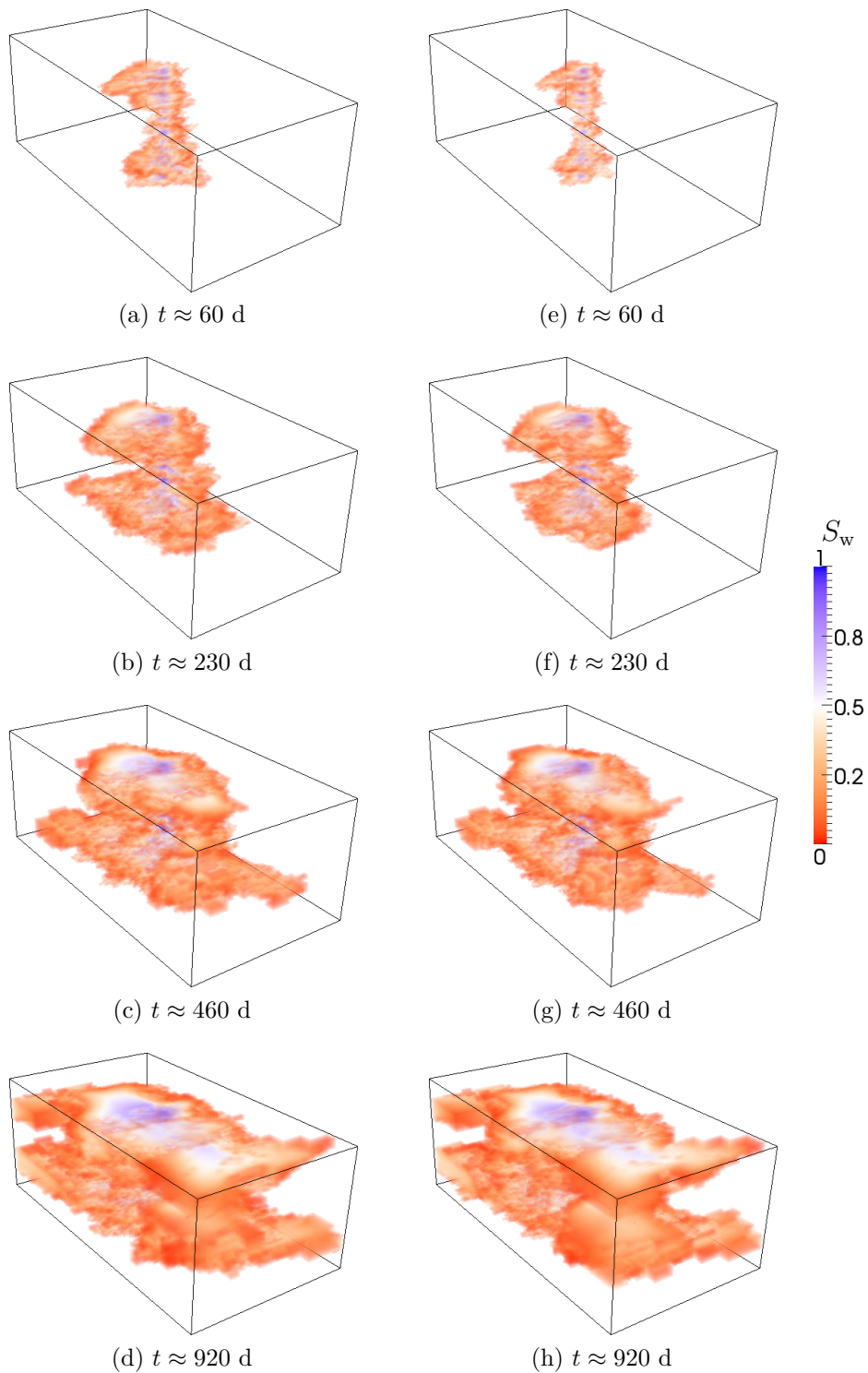


Figure 5.21: Saturation of the injected water plume using a mixed flux approximation scheme (TPFA + MPFA) (a) - (d), and using only MPFA (e) - (h) (z-direction scaled by 5).

in the speed of propagation the distribution inside the plume is very similar and the heterogeneous structure of the various layers is clearly visible.

Comparing the performance of the two methods there is hardly any difference considering the specific setup. The combined MPFA-TPFA method leads to faster convergence behavior of the linear solver. In contrast, less cells have to be refined using the MPFA method what leads to a smaller number of global degrees of freedom (Figure 5.23).

As outlined above, this three-dimensional application can be viewed as a kind of outlook to discuss the capabilities and the potential of the method with regard to realistic applications. A direct comparison to the results of the SPE 10 benchmark is not useful at the current stage of development and implementation of the model in DuMu^x. Some simplifications such as the purely bottom hole pressure controlled well and the constant fluid properties yield a slightly different model setup. Moreover, the implementation of the multi-scale model is not optimized and there exist no solvers in DuMu^x which are specialized for this very specific and complex scenario motivated by petroleum engineering. However, the test shows that the multi-scale method can be used to simulate complicated three-dimensional applications. The upscaling method works very efficiently, also in the three-dimensional case. This can still be expected if capillary pressure is not neglected, because all upscaling methods are based on steady state algorithms. The results show that the numerical MPFA method can be easily simplified to a MPFA-TPFA method if the fine-scale grid is \mathbf{K} -orthogonal. However, in the current test case the simplification could not significantly increase the efficiency. If a higher accuracy is required the MPFA method is superior. The potential savings of the multi-scale method regarding computational costs can be estimated from Figure 5.23. In average, it had to be solved for less than 10% of the number of fine-scale degrees of freedom (DOF). In dependence on the required accuracy this number may, of course, be increased. Even with an increase by four though, less than half of the fine-scale DOF would be necessary. The test, however, also showed that the bottle neck of the method in the current stage is the IMPES algorithm. The explicit solution of the saturation transport equation requires a time-step condition which guarantees the stability of the scheme (see, for example, *Coats*, 2001, 2003), where the cells on the smallest length-scale usually control the time step. In general a high local resolution results in small time steps. Thus, many solutions of the linear system are required during the simulation. This significantly reduces the overall performance even with the previously discussed savings. For the future development, improvements regarding the time discretization are

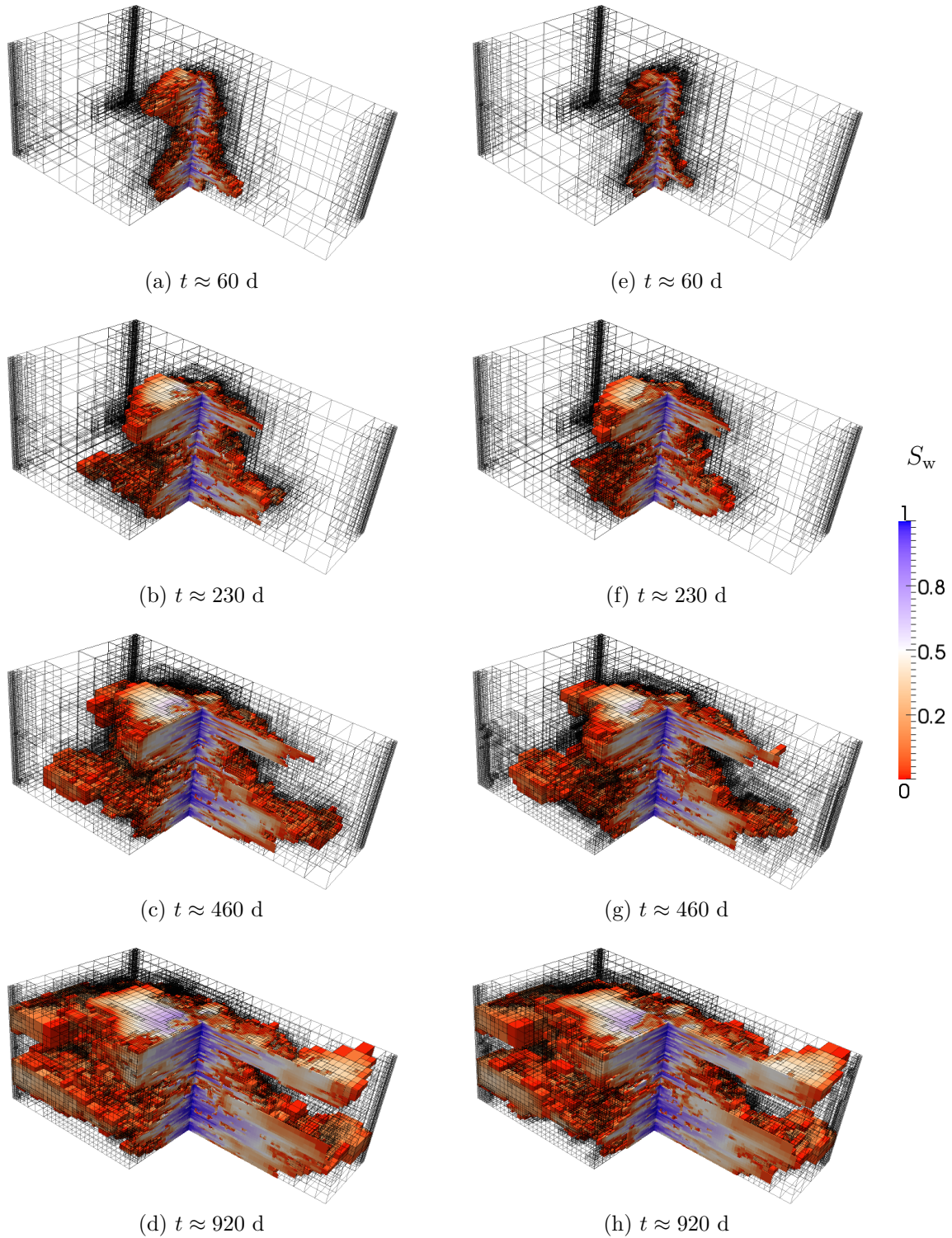


Figure 5.22: Saturation distribution in the injected water plume and the corresponding adapted grid using a mixed flux approximation scheme (TPFA + MPFA) (a) - (d), and using only MPFA (e) - (h) (z-direction scaled by 5).

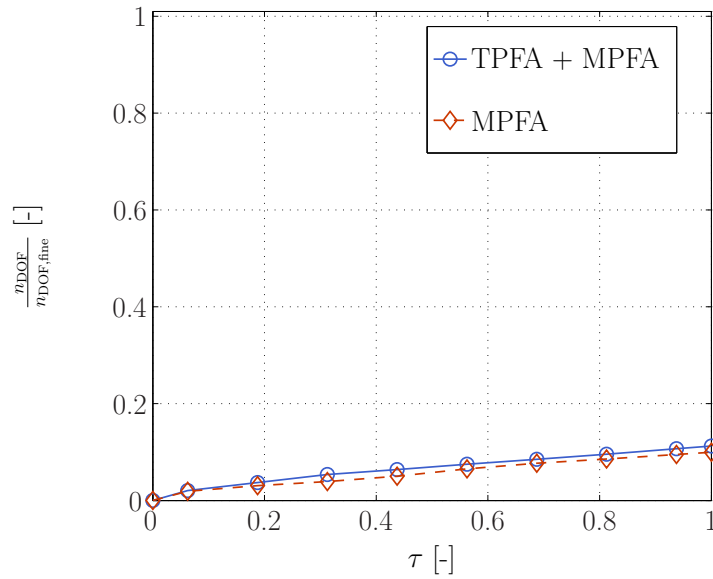


Figure 5.23: Ratio of multi-scale and fine-scale numbers of degrees of freedom (n_{DOF}) over dimensionless simulation time τ .

a key issue.

Summary In this chapter, the multi-scale concept was tested and validated on various two- and three-dimensional scenarios, relating to realistic applications.

The two-dimensional applications in Sections 5.1 and 5.2 showed that the multi-scale method performs very well for a variety of challenging heterogeneous parameter fields and for various flow regimes, ranging from the purely viscous dominated case ($p_c = 0$) to the capillary dominated case. The results show that the characteristic of saturation transport can dramatically change depending on the capillary pressure influence. Preferred flow paths can completely change due to capillary-pressure-induced blocking effects, although the permeability and porosity distribution remain the same. Thus, it is extremely important to have efficient multi-scale models which allow us to model large-scale problems and still correctly account for this effect. A limit of the proposed method was demonstrated using one of the extremely channelized layers of the bottom formation of model 2 of the SPE 10 benchmark (Section 5.2). In this case, the refinement indicators and strategies could not lead to a sufficient balance of accuracy and efficiency at the current stage of development in a capillary-pressure-dominated flow regime. However, in general, the simulation of this complicated geological structure is also feasible.

The application to the full three-dimensional model 2 of the SPE 10 benchmark in

Section 5.3 clearly demonstrated the capabilities of the multi-scale approach with respect to three-dimensional applications. This is essential for the employment on realistic scenarios. The application showed the potential and can be viewed as an outlook, although, a quantitative validation could not be presented in the current stage of development.

In most test problems, the two-dimensional as well as three-dimensional, the computational costs could be significantly reduced, usually below 50% of those of the fine-scale simulations. However, the test examples also show that the efficiency is much higher at the beginning of the simulations. The reason is that, at later simulation times, most parts of the simulated domain are important for the flow and especially for the transport processes. This leads to larger numbers of degrees of freedom because more cells have to be refined. In real large-scale applications, this is often not the case and important processes only appear in relatively small and isolated areas. This would be more comparable to the early stage of the test simulations where the multi-scale method is even more efficient (20-35% of the fine-scale costs). In this case, also for the simulation of more complex structures like the channelized formation in Section 5.2, the efficiency would increase considerably compared with the fine-scale solution.

6 Final Remarks

6.1 Summary

In this work, a novel approach for multi-scale modeling of two-phase flow in porous media is developed. The method can be applied in a wide range of regimes, in particular, in regimes in which capillary effects have a major impact on the flow processes. In such regimes many existing multi-scale techniques are not sufficiently accurate or even fail.

The model equations for the presented multi-scale method are phase-potential-saturation formulations. The equations are implemented using an IMPES algorithm. By solving for the potentials, the gravity term is not completely moved to the right-hand side of the linear system of equations that has to be solved. This can improve the solution behavior of the sequential IMPES solver which decouples the solution for the velocity field and for the transport of the phases. Another advantage of the potential formulation is the minimal number of different terms, namely, one advective and one capillary flux term in the potential equation and one phase flux term in the saturation equation. In contrast, a phase pressure formulation, as an example, includes additional gravity terms. Additionally, the different flux terms of a phase potential formulation have a similar form. Thus, a minimal number of different transmissibilities has to be calculated for the multi-point flux approximation.

For discretizing the two-phase flow equations, in particular the coarse-scale equations, a finite volume scheme based on the multi-point flux approximation L-method was developed and validated on various test problems. The tests showed that the method is able to approximate important two-phase flow features, to account for the effects of anisotropic coefficients, and to treat hanging nodes which appear in non-conforming adaptive grids.

The developed multi-scale method combines a local steady-state numerical upscaling method with an h-adaptive grid. In a first step, different numerical upscaling techniques were combined and extended to get a set of methods which enables the calculation of the effective parameters which appear in the coarse-scale equations. The numerical upscaling approach was tested and could be validated on several test scenarios. To overcome the limitations of the numerical upscaling, an adaptive grid method based on multi-point flux approximation was combined with the numerical upscaling. The key factor of this novel multi-scale approach is an appropriate adaptation strategy, which aims to refine and coarsen the grid such that the method is efficient and sufficiently accurate. Therefore, different adaptation indicators were suggested. Besides the so-called standard indicators, which try to minimize numerical errors in the solutions, the development of special multi-scale indicators has to be emphasized. The idea of such indicators is to take into account the validity of the upscaled parameters for the error estimation. One new multi-scale indicator based on the definition of a capillary number was introduced. Several numerical tests demonstrated that the multi-scale approach can significantly improve the quality of a solution in comparison to a pure upscaling method. Moreover, all suggested indicators can help to considerably improve the quality of the multi-scale approximation.

Finally, the multi-scale concept was tested and validated on various two- and three-dimensional scenarios, relating to realistic applications. The two-dimensional applications showed that the multi-scale method performs very well for a variety of challenging heterogeneous parameter fields and for various flow regimes, ranging from the purely viscous dominated case to the capillary dominated case. The results show that the characteristic of saturation transport can dramatically change depending on the capillary pressure influence. Thus, it is extremely important to have efficient multi-scale models which allow us to model large-scale problems and still account for this effect correctly. The application to the full three-dimensional model 2 of the SPE 10 benchmark clearly demonstrated the capabilities of the multi-scale approach with respect to three-dimensional applications. This is essential for the employment on realistic scenarios. In most of the test problems, the two-dimensional as well as three-dimensional, the computational costs could be significantly reduced, usually below 50% of those of the fine-scale simulations. Considering realistic large-scale applications, important transport processes often appear in relatively small and isolated areas. As can be concluded from the application examples, in such cases the multi-scale method may be even more efficient (20-35% of the fine-scale costs).

6.2 Discussion and Future Work

The focus of this thesis was on the development of a multi-scale approach which, in particular, can be used for modeling regimes which are capillary dominated or in which capillary pressure at least influences the flow and transport behavior considerably. Therefore, the influence of gravity was not explicitly considered in the context of the multi-scale method, although the method is derived and implemented for the general case including gravity.

An advantage of the developed concept is its flexibility and expandability. The decoupling of the numerical upscaling and the multi-scale modeling via the adaptive grid method facilitates the exchange of the single parts. As an example, alternative numerical methods may increase the flexibility with respect to challenging grids and geometries. In DuMu^x various methods are already available or will be available in the future. As regards the numerical parameter upscaling, different upscaling methods can be easily included for both existing or new coarse-scale parameters. Additionally, the complexity of the modeled physical processes can be increased easily and straightforward by including the ideas of a multi-physics method (see e.g. *Wheeler and Peszyńska, 2002; Fritz et al., 2012; Faigle et al., 2013*). Many applications may allow us to increase the complexity of the fine-scale equations without increasing the complexity on the coarse scale if a suitable adaptation strategy is applied.

So far, the basic concept of the multi-scale approach has been implemented and tested successfully. The long-term goal is a flexible and robust multi-scale method which can be used for modeling real world applications such as gas storage in the subsurface, thermal energy production from geothermal sources, or investigation of nuclear storage sites. The large-scale simulation of these current and important applications, which may become even more important in the future, is essential for the investigation of potentials and risks. In order to achieve this objective, the introduced multi-scale method has to be developed further, improved, and tested in the future:

Three-dimensional validation is crucial to verify the applicability for modelling realistic problems. The capabilities and the potential of the method for modeling complex three-dimensional scenarios was demonstrated. However, more detailed three-dimensional tests including different flow regimes, especially the capillary dominated case, and a

comparison to reference solutions is indispensable for a thorough validation of the method.

Support of complex grids is an important issue for the applicability of a simulator in practice. All tests of the multi-scale method, which are presented in this thesis, are defined on structured grids. In general, the numerical method as well as the upscaling can be applied also to unstructured grids. However, the problem of an appropriate treatment of more complex grids consisting of cells of complex geometry, for example corner-point grids, still has to be solved.

Improving the robustness of the method with regard to the solvability of the linear system and the time discretization may be necessary for modeling domains of complex geometry and parameter distributions. A method is defined to be robust in this context if it leads to a meaningful solution with a reasonable number of time steps and for a variety of problems. Thus, alternative spatial discretization schemes (e.g. mimetic finite differences, *Brezzi et al.*, 2005) have to be investigated and tested. The application to the three-dimensional SPE 10 model showed that a bottle neck of the method in the current stage is the IMPES algorithm. The time-step condition required for the stability of the scheme results in strongly decreasing time steps with increasing resolution. Thus, the potential to transfer the methods from the IMPET scheme (IMplicit Pressure Explicit Transport) to a sequential fully implicit or an adaptive implicit scheme (e.g. *Forsyth and Sammon*, 1986; *de Loubens et al.*, 2009), or to a fully implicit scheme have to be investigated.

Parallelization is another way for increasing the performance. Thus, the method has to be extended for a parallel application by exploiting the existing capabilities of DuMu^x and DUNE (*Bastian et al.*, 2008) for parallel computations.

Multi-physics modeling is one approach for increasing the complexity of the modeled processes locally. For simulation of many applications the incompressible isothermal immiscible two-phase model is sufficient. Nevertheless, considering the large-scale applications mentioned at the beginning of this section, more complex processes may have a major impact. A way for increasing the model complexity is the combination of the multi-scale method with a multi-physics approach. In recent years multi-physics

approaches have also been developed in DuMu^x (*Faigle et al.*, 2013; *Darcis*, 2012; *Darcis et al.*, 2013).

Benchmarking is an essential and supporting process for the development and, in particular, the implementation of numerical methods. In this work, only the number of global degrees of freedom is used as a measure for the efficiency. The linear solver often is the bottleneck with regard to computational costs and the linear solution time usually scales at least linearly with the numbers of degrees of freedom. Therefore, this is a reasonable indicator for potential savings. The costs for the upscaling step are negligible because only fast steady-state methods are used. An analysis of the overall computational costs confirmed that the number of degrees of freedom is a good measure of efficiency. However, a fair and meaningful direct comparison of fine-scale and multi-scale costs and a benchmark against other simulators would require a simulation code which is optimized similarly regarding both implementation and application. Hence, this is also part of future work.

Bibliography

- J. E. Aarnes, S. Krogstad, and K.-A. Lie, *A hierarchical multiscale method for two-phase flow based upon mixed finite elements and nonuniform coarse grids*. *Multiscale Modeling & Simulation*, 5 (2006)(2), 337–363.
- I. Aavatsmark, *An introduction to multipoint flux approximations for quadrilateral grids*. *Computational Geosciences*, 6 (2002), 405–432.
- I. Aavatsmark, *Interpretation of a two-point flux stencil for skew parallelogram grids*. *Computational Geosciences*, 11 (2007), 199–206.
- I. Aavatsmark, T. Barkve, O. Bøe, and T. Mannseth (1994). *Discretization on non-orthogonal curvilinear grids for multi-phase flow*. In *Proceedings of 4th European Conference on the Mathematics of Oil Recovery*. Røros, Norway.
- I. Aavatsmark, T. Barkve, O. Bøe, and T. Mannseth, *Discretization on non-orthogonal, quadrilateral grids for inhomogeneous, anisotropic media*. *Journal of Computational Physics*, 127 (1996), 2–14.
- I. Aavatsmark, T. Barkve, O. Bøe, and T. Mannseth, *Discretization on unstructured grids for inhomogeneous, anisotropic media. Part I: Derivation of the methods*. *Siam Journal on Scientific Computing*, 19 (1998a), 1700–1716.
- I. Aavatsmark, T. Barkve, O. Bøe, and T. Mannseth, *Discretization on unstructured grids for inhomogeneous, anisotropic media. Part II: Discussion and numerical results*. *Siam Journal on Scientific Computing*, 19 (1998b), 1717–1736.
- I. Aavatsmark, T. Barkve, and T. Mannseth, *Control-volume discretization methods for 3D quadrilateral grids in inhomogeneous, anisotropic reservoirs*. *SPE Journal*, 3 (1998c)(2), 146–154.

- I. Aavatsmark, G. Eigestad, and B. Heimsund, *A new finite-volume approach to efficient discretization on challenging grids. SPE Journal*, 15 (2010)(3), 658–669.
- I. Aavatsmark and G. T. Eigestad, *Numerical convergence of the mpfa o-method and u-method for general quadrilateral grids. International Journal for Numerical Methods in Fluids*, 51 (2006)(9-10), 939–961.
- I. Aavatsmark, G. T. Eigestad, R. A. Klausen, M. F. Wheeler, and I. Yotov, *Convergence of a symmetric MPFA method on quadrilateral grids. Computational Geosciences*, 11 (2007)(4), 333–345.
- I. Aavatsmark, G. T. Eigestad, B. T. Mallison, and J. M. Nordbotten, *A compact multipoint flux approximation method with improved robustness. Numerical Methods for Partial Differential Equations*, 24 (2008), 1329–1360.
- I. Aavatsmark, E. Reiso, and R. Teigland, *Control-volume discretization method for quadrilateral grids with faults and local refinements. Computational Geosciences*, 5 (2001)(1), 1–23.
- L. Agelas and R. Masson, *Convergence of the finite volume MPFA O scheme for heterogeneous anisotropic diffusion problems on general meshes. Comptes Rendus Mathematique*, 346 (2008)(17-18), 1007–1012.
- T. Arbogast, G. Pencheva, M. F. Wheeler, and I. Yotov, *A multiscale mortar mixed finite element method. Multiscale Modeling & Simulation*, 6 (2007)(1), 319–346.
- V. Artus and B. Noetinger, *Upscaling two-phase flow in heterogeneous reservoirs: current trends. Oil & Gas Science and Technology-Revue de l Institut Français du Pétrole*, 59 (2004)(2), 185–195.
- K. Aziz and A. Settari (1979). *Petroleum reservoir simulation*. Elsevier Applied Science.
- R. Barrett, M. Berry, T. F. Chan, J. Demmel, J. Donato, J. Dongarra, V. Eijkhout, R. Pozo, C. Romine, and H. van der Vorst (1994). *Templates for the solution of linear systems: building blocks for iterative methods*. SIAM.
- P. Bastian, M. Blatt, A. Dedner, C. Engwer, R. Klöforn, R. Kornhuber, M. Ohlberger, and O. Sander, *A Generic Grid Interface for Parallel and Adaptive Scientific Computing. Computing*, 82 (2008)(2–3), 103–138.
- J. Bear (1972). *Dynamics of fluids in porous media*. Dover Publications, inc, New York.

-
- P. Binning and M. A. Celia, *Practical implementation of the fractional flow approach to multi-phase flow simulation*. *Advances in Water Resources*, 22 (1999)(5), 461–478.
- C. Braun, R. Helmig, and S. Manthey, *Macro-scale effective constitutive relationships for two-phase flow processes in heterogeneous porous media with emphasis on the relative permeability-saturation relationship*. *Journal of Contaminant Hydrology*, 76 (2005)(1-2), 47–85.
- F. Brezzi, K. Lipnikov, and V. Simoncini, *A family of mimetic finite difference methods on polygonal and polyhedral meshes*. *Mathematical Models and Methods in Applied Science*, 15 (2005)(10), 1533–1551.
- R. Brooks and A. Corey, *Hydraulic properties of porous media*. *Hydrology Papers, Colorado State University*, (1964)(March).
- S. E. Buckley and M. C. Leverett, *Mechanisms of fluid displacement in sand*. *Petroleum Transactions, AIME*, 146 (1942), 107–116.
- Y. Cao, R. Helmig, and B. I. Wohlmuth, *Geometrical interpretation of the multi-point flux approximation L-method*. *International Journal for Numerical Methods in Fluids*, 60 (2009), 1173–1199.
- Y. Cao, R. Helmig, and B. I. Wohlmuth, *Convergence of the multipoint flux approximation l-method for homogeneous media on uniform grids*. *Numerical Methods for Partial Differential Equations*, 27 (2011), 329–350.
- G. Chavent (1976). *A new formulation of diphasic incompressible flows in porous media*, pages 258–270. Number 503 in *Lecture Notes in Mechanics*. Springer, Berlin.
- G. Chavent and J. Jaffré (1986). *Mathematical models and finite elements for reservoir simulation*.
- Q.-Y. Chen, J. Wan, Y. Yang, and R. T. Mifflin, *Enriched multi-point flux approximation for general grids*. *Journal of Computational Physics*, 227 (2008)(3), 1701–1721.
- Y. Chen and L. J. Durlofsky, *Adaptive local-global upscaling for general flow scenarios in heterogeneous formations*. *Transport in Porous Media*, 62 (2006)(2), 157–185.
- Y. Chen, L. J. Durlofsky, M. Gerritsen, and X. H. Wen, *A coupled local-global upscaling approach for simulating flow in highly heterogeneous formations*. *Advances in Water Resources*, 26 (2003)(10), 1041–1060.

- Y. Chen and Y. Li, *Local-global two-phase upscaling of flow and transport in heterogeneous formations. Multiscale Modeling & Simulation*, 8 (2009), 125–153.
- Z. Chen and T. Y. Hou, *A mixed multiscale finite element method for elliptic problems with oscillating coefficients. Mathematics of Computation*, 72 (2003)(242), 541–576.
- Z. Chen, G. Huan, and Y. Ma (2006). *Computational methods for multiphase flows in porous media*. SIAM, Computational Science & Engineering.
- M. A. Christie and M. J. Blunt, *Tenth SPE comparative solution project : a comparison of upscaling techniques. SPE Reservoir Evaluation & Engineering*, 4 (2001), 308–317.
- K. H. Coats, *IMPES stability: the stable step. SPE Journal*, (2001)(69225).
- K. H. Coats, *Impes stability: selection of stable timesteps. SPE Journal*, 8 (2003), 181–187.
- M. Darcis (2012). *Coupling Models of Different Complexity for the Simulation of CO₂ storage in Deep Saline Aquifers*. Ph.D. thesis, Institut für Wasser- und Umweltsystemmodellierung, Universität Stuttgart.
- M. Darcis, H. Class, B. Flemisch, and S. Müthing, *A spatially coupled model for simulating flow and geomechanical processes during CO₂ storage. Water Resources Research*, (2013). Submitted.
- H. Darcy (1856). *Les fontaines publiques de la ville de dijon*. Victor Dalmont, Paris.
- R. de Loubens, A. Riaz, and H. A. Tchelepi, *Error Analysis of an Adaptive Implicit Scheme for Hyperbolic Conservation Laws. SIAM Journal on Scientific Computing*, 31 (2009)(4), 2890–2914.
- J. Demmel, S. C. Eisenstat, J. R. Gilbert, X. S. Li, and J. W. H. Liu, *A supernodal approach to sparse partial pivoting. SIAM Journal on Matrix Analysis and Applications*, 20 (1999), 720–755.
- M. N. Dmitriev, N. M. Dmitriev, and V. M. Maksimov, *Representation of the functions of the relative phase permeabilities for anisotropic porous media. Fluid Dynamics*, 40 (2005), 439–445.
- N. M. Dmitriev and V. M. Maksimov, *Determining equations of two-phase flows through anisotropic porous media. Fluid Dynamics*, 33 (1998), 224–229.

-
- S. Doerr, R. Shakesby, and R. Walsh, *Soil water repellency: its causes, characteristics and hydro-geomorphological significance*. *Earth-Science Reviews*, 51 (2000)(1-4), 33–65.
- L. J. Durlofsky, *Numerical calculation of equivalent grid block permeability tensors for heterogeneous porous media*. *Water Resources Research*, 27 (1991)(5), 699–708.
- M. G. Edwards and C. F. Rogers (1994). *A flux continuous scheme for the full tensor pressure equation*. In *Proceedings of 4th European Conference on the Mathematics of Oil Recovery*. Røros, Norway.
- M. G. Edwards and C. F. Rogers, *Finite volume discretization with imposed flux continuity for the general tensor pressure equation*. *Computational Geosciences*, 2 (1998), 259–290.
- M. G. Edwards and H. Zheng, *A quasi-positive family of continuous Darcy-flux finite-volume schemes with full pressure support*. *Journal of Computational Physics*, 227 (2008)(22), 9333–9364.
- M. G. Edwards, H. Zheng, S. Lamine, and M. Pal, *Continuous elliptic and multi-dimensional hyperbolic Darcy-flux finite-volume methods*. *Computers & Fluids*, 46 (2011)(1), 12–22.
- Y. Efendiev and T. Hou, *Multiscale finite element methods for porous media flows and their applications*. *Applied Numerical Mathematics*, 57 (2007)(5-7), 577–596.
- H. Eichel, R. Helmig, I. Neuweiler, and O. A. Cirpka (2005). *Upscaling of two-phase flow processes in porous media*. In D. B. Das and S. M. Hassanizadeh, editors, *Upscaling multiphase flow in porous media*, pages 237–257. Springer.
- G. T. Eigestad and R. A. Klausen, *On the convergence of the multi-point flux approximation O-method: Numerical experiments for discontinuous permeability*. *Numerical Methods for Partial Differential Equations*, 21 (2005)(6), 1079–1098.
- S. Ekrann and J. Aasen, *Steady-state upscaling*. *Transport in Porous Media*, 41 (2000), 245–262.
- B. Faigle, R. Helmig, I. Aavatsmark, and B. Flemisch, *Efficient multi-physics modelling with adaptive grid-refinement using a MPFA method*. *Computational Geosciences*, (2013). Submitted.

- B. Flemisch, M. Darcis, K. Erbertseder, B. Faigle, A. Lauser, K. Mosthaf, S. Müthing, P. Nuske, A. Tatomir, M. Wolff, and R. Helmig, *DuMux: DUNE for multi-{phase,component,scale,physics,...} flow and transport in porous media. Advances in Water Resources*, 34 (2011)(9), 1102–1112.
- P. Forsyth and P. Sammon, *Practical considerations for adaptive implicit methods in reservoir simulation. Journal of Computational Physics*, 281 (1986), 265–281.
- J. Fořt, J. Fürst, J. Halama, R. Herbin, and F. Hubert (2011). *Finite volumes for complex applications VI problems & perspectives*. Springer Proceedings in Mathematics. Springer.
- F. N. Fritsch and R. E. Carlson, *Monotone piecewise cubic interpolation. {SIAM} Journal on numerical analysis*, 17 (1980)(2), 238–246.
- J. Fritz, B. Flemisch, and R. Helmig, *Decoupled and multiphysics models for non-isothermal compositional two-phase flow in porous media. International Journal of Numerical Analysis & Modeling*, 9 (2012)(1), 17–28.
- R. Fučík, J. Mikyška, M. Beneš, and T. H. Illangasekare, *An Improved Semi-Analytical Solution for Verification of Numerical Models of Two-Phase Flow in Porous Media. Vadose Zone Journal*, 6 (2007)(1), 93.
- M. Gerritsen and J. Lambers, *Integration of local–global upscaling and grid adaptivity for simulation of subsurface flow in heterogeneous formations. Computational Geosciences*, 12 (2008), 193–208.
- D. Gunasekera, P. Childs, J. Herring, and J. Cox (1998). *A multi-point flux discretization scheme for general polyhedral grids*. In *SPE International Oil and Gas Conference and Exhibition in China*, page SPE 48855. Beijing, China.
- H. Hajibeygi, G. Bonfigli, M. A. Hesse, and P. Jenny, *Iterative multiscale finite-volume method. Journal of Computational Physics*, 227 (2008), 8604–8621.
- H. Hajibeygi and P. Jenny, *Multiscale finite-volume method for parabolic problems arising from compressible multiphase flow in porous media. Journal of Computational Physics*, 228 (2009)(14), 5129–5147.
- V. L. Hauge, K.-A. Lie, and J. R. Natvig, *Flow-based coarsening for multiscale simulation of transport in porous media. Computational Geosciences*, 16 (2011)(2), 391–408.

-
- C. He and L. Durlafsky, *Structured flow-based gridding and upscaling for modeling subsurface flow*. *Advances in Water Resources*, 29 (2006)(12), 1876–1892.
- R. Helmig (1997). *Multiphase flow and transport processes in the subsurface: a contribution to the modeling of hydrosystems*. Springer, Berlin.
- R. Helmig, B. Flemisch, M. Wolff, A. Ebigbo, and H. Class, *Model coupling for multiphase flow in porous media*. *Advances in Water Resources*, 51 (2012), 52–66.
- R. Helmig and R. Huber, *Comparison of Galerkin-type discretization techniques for two-phase flow in heterogeneous porous media*. *Advances in Water Resources*, 21 (1998)(8), 697–711.
- R. Hilfer and P. E. Øren, *Dimensional analysis of pore scale and field scale immiscible displacement*. *Transport in Porous Media*, (1996), 53–72.
- M. Honarpour and S. Mahmood, *Relative-permeability measurements: an overview*. *Journal of Petroleum Technology*, 40 (1988), 963–966.
- H. Hoteit and A. Firoozabadi, *Numerical modeling of two-phase flow in heterogeneous permeable media with different capillarity pressures*. *Advances in Water Resources*, 31 (2008)(1), 56–73.
- T. Y. Hou and X.-H. Wu, *A multiscale finite element method for elliptic problems in composite materials and porous media*. *Journal of Computational Physics*, 134 (1997)(1), 169–189.
- P. Jenny, S. Lee, and H. Tchelepi, *Multi-scale finite-volume method for elliptic problems in subsurface flow simulation*. *Journal of Computational Physics*, 187 (2003)(1), 47–67.
- P. Jenny, S. H. Lee, and H. A. Tchelepi, *Adaptive multiscale finite-volume method for multiphase flow and transport in porous media*. *Multiscale Modeling & Simulation*, 3 (2004), 50–64.
- P. Jenny, S. H. Lee, and H. A. Tchelepi, *Adaptive fully implicit multi-scale finite-volume method for multi-phase flow and transport in heterogeneous porous media*. *Journal of Computational Physics*, 217 (2006)(2), 627–641.
- S. Jonoud and M. Jackson, *Validity of steady-state upscaling techniques*. *SPE Reservoir Evaluation & Engineering*, 11 (2008)(2), 405–416.

- E. Keilegavlen, J. M. Nordbotten, and A. Stephansen, *Tensor relative permeabilities: Origins, modeling and numerical discretization. International Journal of Numerical Analysis & Modeling*, 9 (2012)(3), 701–724.
- V. Kippe, J. E. Aarnes, and K.-A. Lie, *A comparison of multiscale methods for elliptic problems in porous media flow. Computational Geosciences*, 12 (2008)(3), 377–398.
- R. A. Klausen and R. Winther, *Convergence of multipoint flux approximations on quadrilateral grids. Numerical Methods for Partial Differential Equations*, 22 (2006), 1438–1454.
- S. Korteland, S. Bottero, S. M. Hassanizadeh, and C. W. J. Berentsen, *What is the correct definition of average pressure? Transport in Porous Media*, 84 (2010), 153–175.
- A. R. Kovscek, H. Wong, and C. J. Radke, *A pore-level scenario for the development of mixed wettability in oil reservoirs. AIChE Journal*, 39 (1993)(6), 1072–1085.
- B. H. Kueper and D. B. McWhorter, *The use of macroscopic percolation theory to construct large-scale capillary pressure curves. Water Resources Research*, 28 (1992), 2425–2436.
- J. R. Kyte and D. W. Berry, *New pseudo functions to control numerical dispersion. SPE Journal*, 15 (1975)(4), 269–276.
- S. Lee, H. Zhou, and H. Tchelepi, *Adaptive multiscale finite-volume method for nonlinear multiphase transport in heterogeneous formations. Journal of Computational Physics*, 228 (2009)(24), 9036–9058.
- S. H. Lee, H. A. Tchelepi, P. Jenny, and L. J. DeChant, *Implementation of a flux-continuous finite-difference method for stratigraphic, hexahedron grids. SPE Journal*, 7 (2002)(3), 267–277.
- M. C. Leverett, *Capillary behavior in porous solids. Transactions of the American Institute of Mining and Metallurgical Engineers*, 142 (1941), 152–169.
- K. Lipnikov, J. D. Moulton, and D. Svyatskiy, *A multilevel multiscale mimetic (m3) method for two-phase flows in porous media. Journal of Computational Physics*, 227 (2008), 6727–6753.
- A. Lohne, G. Virnovsky, and L. J. Durlofsky, *Two-stage upscaling of two-phase flow: from core to simulation scale. SPE Journal*, 11 (2006), 304–316.

-
- J. E. Marsden and T. J. R. Hughes (1983). *Mathematical foundations of elasticity*. Prentice-Hall, Englewood Cliffs, NJ.
- D. McWhorter and D. Sunada, *Exact integral solutions for two-phase flow*. *Water Resources Research*, 26 (1990)(3), 399–413.
- S. Mundal, I. Aavatsmark, and D. A. Di Pietro (2008). *Compact-stencil MPFA method for heterogeneous highly anisotropic second-order elliptic problems*. In R. Eymard and J.-M. Hérard, editors, *Finite Volumes for Complex Applications V (Problems & Perspectives)*, pages 905–918. Wiley.
- J. Nordbotten, *Adaptive variational multiscale methods for multiphase flow in porous media*. *Multiscale Modeling & Simulation*, 7 (2009)(3), 1455.
- J. M. Nordbotten and I. Aavatsmark, *Monotonicity conditions for control volume methods on uniform parallelogram grids in homogeneous media*. *Computational Geosciences*, 9 (2005)(1), 61–72.
- J. M. Nordbotten, I. Aavatsmark, and G. T. Eigestad, *Monotonicity of control volume methods*. *Numerische mathematik*, 106 (2007a), 255–288.
- J. M. Nordbotten and P. E. Bjørstad, *On the relationship between the multiscale finite-volume method and domain decomposition preconditioners*. *Computational Geosciences*, 12 (2008)(3), 367–376.
- J. M. Nordbotten, M. A. Celia, H. K. Dahle, and S. M. Hassanizadeh, *Interpretation of macroscale variables in darcy’s law*. *Water Resources Research*, 43 (2007b), W08430.
- J. M. Nordbotten, M. A. Celia, H. K. Dahle, and S. M. Hassanizadeh, *On the definition of macroscale pressure for multiphase flow in porous media*. *Water Resources Research*, 44 (2008), W06S02.
- J. M. Nordbotten and G. T. Eigestad, *Discretization on quadrilateral grids with improved monotonicity properties*. *Journal of Computational Physics*, 203 (2005), 744–760.
- J. M. Nordbotten, J. P. Noguees, and M. A. Celia, *Appropriate choice of average pressure for upscaling relative permeability in dynamic flow conditions*. *SPE Journal*, 15 (2010), 228–237.

- M. Pal and M. G. Edwards, *Anisotropy favoring triangulation CVD(MPFA) finite-volume approximations. International Journal for Numerical Methods in Fluids*, 67 (2011)(10), 1247–1263.
- M. Pal, M. G. Edwards, and A. R. Lamb, *Convergence study of a family of flux-continuous, finite-volume schemes for the general tensor pressure equation. International Journal for Numerical Methods in Fluids*, 51 (2006), 1177–1203.
- D. Peaceman, *Interpretation of well-block pressures in numerical reservoir simulation. SPE Journal*, 18 (1978)(3).
- J. E. Pebesma and C. G. Wesseling, *Gstat: a program for geostatistical modelling, prediction and simulation. Computers & Geosciences*, 24 (1998), 17–31.
- G. E. Pickup and K. S. Sorbie (1996). *The scaleup of two-phase flow in porous media using phase permeability tensors. In SPE Journal*, volume 1, pages 369–382.
- G. E. Pickup and K. D. Stephen, *An assessment of steady-state scale-up for small-scale geological models. Petroleum Geoscience*, 6 (2000), 203–210.
- M. Quintard and S. Whitaker, *Two-phase flow in heterogeneous porous media: the method of large-scale averaging. Transport in Porous Media*, 3 (1988)(4), 357–413.
- P. Renard and G. de Marsily, *Calculating equivalent permeability: a review. Advances in Water Resources*, 20 (1997), 253–278.
- N. Saad, A. S. Cullick, and M. M. Honarpour (1995). *Effective relative permeability in scale-up and simulation. In SPE Rocky Mountain Regional/Low-Permeability Reservoirs Symposium, 20-22 March, Denver, Colorado.*
- A. E. Sáez, C. J. Otero, and I. Rusinek, *The effective homogeneous behavior of heterogeneous porous media. Transport in Porous Media*, 4 (1989)(3), 213–238.
- A. Scheidegger (1974). *The physics of flow through porous media.* University of Toronto Press, 3d edition.
- Z. Sheng and G. Yuan, *A Nine Point Scheme for the Approximation of Diffusion Operators on Distorted Quadrilateral Meshes. Siam Journal on Scientific Computing*, 30 (2008)(3), 1341–1361.

-
- A. F. Stephansen, *Convergence of the multipoint flux approximation l-method on general grids*. *SIAM Journal on Numerical Analysis*, 50 (2012)(6), 3163–3187.
- H. L. Stone (1991). *Rigorous black oil pseudo functions*. In *SPE Symposium on Reservoir Simulation, 17-20 February, Anaheim, California*.
- M. T. van Genuchten, *A closed-form equation for predicting the hydraulic conductivity of unsaturated soils*. *Soil Science Society of America Journal*, 44 (1980)(5), 892–898.
- G. A. Virnovsky, H. A. Friis, and A. Lohne, *A steady-state upscaling approach for immiscible two-phase flow*. *Transport in Porous Media*, 54 (2004), 167–192.
- T. C. Wallstrom, M. A. Christie, L. J. Durlofsky, and D. H. Sharp, *Effective flux boundary conditions for upscaling porous media equations*. *Transport in Porous Media*, 46 (2002a)(2), 139–153.
- T. C. Wallstrom, S. Hou, M. A. Christie, L. J. Durlofsky, D. H. Sharp, and Q. Zou, *Application of effective flux boundary conditions to two-phase upscaling in porous media*. *Transport in Porous Media*, 46 (2002b)(2), 155–178.
- X. H. Wen, L. J. Durlofsky, and M. G. Edwards, *Use of border regions for improved permeability upscaling*. *Mathematical Geology*, 35 (2003)(5), 521–547.
- M. F. Wheeler and M. Peszyńska, *Computational engineering and science methodologies for modeling and simulation of subsurface applications*. *Advances in Water Resources*, 25 (2002)(8–12), 1147 – 1173.
- S. Whitaker (1998). *The method of volume averaging*. Kluwer Academic Publishers.
- M. Wolff, Y. Cao, B. Flemisch, R. Helmig, and B. Wohlmuth (2013a). *Multi-point flux approximation L-method in 3D: numerical convergence and application to two-phase flow through porous media*. In P. Bastian, J. Kraus, R. Scheichl, and M. Wheeler, editors, *Simulation of Flow in Porous Media - Applications in Energy and Environment*. De Gruyter.
- M. Wolff, B. Flemisch, and R. Helmig, *An adaptive multi-scale approach for modeling two-phase flow in porous media including capillary pressure*. *Water Resources Research*, (2013b). Submitted.

- M. Wolff, B. Flemisch, R. Helmig, and I. Aavatsmark, *Treatment of tensorial relative permeabilities with multipoint flux approximation. International Journal of Numerical Analysis & Modeling*, 9 (2012)(3), 725–744.
- X. Wu and R. Parashkevov, *Effect of grid deviation on flow solutions. SPE Journal*, 14 (2009)(1), 67–77.
- Y. C. Yortsos, C. Satik, J.-C. Bacri, and D. Salin, *Large-scale percolation theory of drainage. Transport in Porous Media*, 10 (1993), 171–195.

Lebenslauf

Persönliche Daten

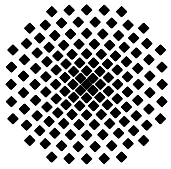
Name: Markus Wolff
Geburtsdatum: 9.11.1981
Geburtsort: Stuttgart
Staatsangehörigkeit: deutsch

Ausbildung

1988 - 2001 Wagenburg-Gymnasium Stuttgart
2002 - 2008 Studium der Umweltschutztechnik an der Universität Stuttgart
2006 Studium an der Chalmers University of Technology, Göteborg, Schweden

Berufstätigkeit

seit 2008 Wissenschaftlicher Mitarbeiter am Institut für Wasser- und Umweltsystemmodellierung der Universität Stuttgart, Lehrstuhl für Hydromechanik und Hydrosystemmodellierung



Institut für Wasser- und Umweltsystemmodellierung Universität Stuttgart

Pfaffenwaldring 61
70569 Stuttgart (Vaihingen)
Telefon (0711) 685 - 64717/64749/64752/64679
Telefax (0711) 685 - 67020 o. 64746 o. 64681
E-Mail: iws@iws.uni-stuttgart.de
<http://www.iws.uni-stuttgart.de>

Direktoren

Prof. Dr. rer. nat. Dr.-Ing. András Bárdossy
Prof. Dr.-Ing. Rainer Helmig
Prof. Dr.-Ing. Silke Wieprecht

Vorstand (Stand 19.08.2013)

Prof. Dr. rer. nat. Dr.-Ing. A. Bárdossy
Prof. Dr.-Ing. R. Helmig
Prof. Dr.-Ing. S. Wieprecht
Prof. Dr. J.A. Sander Huisman
Jürgen Braun, PhD
apl. Prof. Dr.-Ing. H. Class
Dr.-Ing. H.-P. Koschitzky
Dr.-Ing. M. Noack
Jun.-Prof. Dr.-Ing. W. Nowak, M.Sc.
Dr. rer. nat. J. Seidel
Dr.-Ing. K. Terheiden

Emeriti

Prof. Dr.-Ing. habil. Dr.-Ing. E.h. Jürgen Giesecke
Prof. Dr.h.c. Dr.-Ing. E.h. Helmut Kobus, PhD

Lehrstuhl für Wasserbau und Wassermengenwirtschaft

Leiter: Prof. Dr.-Ing. Silke Wieprecht
Stellv.: Dr.-Ing. Kristina Terheiden
Versuchsanstalt für Wasserbau
Leiter: Dr.-Ing. Markus Noack

Lehrstuhl für Hydromechanik und Hydrosystemmodellierung

Leiter: Prof. Dr.-Ing. Rainer Helmig
Stellv.: apl. Prof. Dr.-Ing. Holger Class
**Jungwissenschaftlergruppe: Stochastische
Modellierung von Hydrosystemen**
Leiter: Jun.-Prof. Dr.-Ing. Wolfgang Nowak, M.Sc.

Lehrstuhl für Hydrologie und Geohydrologie

Leiter: Prof. Dr. rer. nat. Dr.-Ing. András Bárdossy
Stellv.: Dr. rer. nat. Jochen Seidel
Hydrogeophysik der Vadosen Zone
(mit Forschungszentrum Jülich)
Leiter: Prof. Dr. J.A. Sander Huisman

VEGAS, Versuchseinrichtung zur Grundwasser- und Altlastensanierung

Leitung: Jürgen Braun, PhD, AD
Dr.-Ing. Hans-Peter Koschitzky, AD

Verzeichnis der Mitteilungshefte

- 1 Röhnisch, Arthur: *Die Bemühungen um eine Wasserbauliche Versuchsanstalt an der Technischen Hochschule Stuttgart*, und Fattah Abouleid, Abdel: *Beitrag zur Berechnung einer in lockeren Sand gerammten, zweifach verankerten Spundwand*, 1963
- 2 Marotz, Günter: *Beitrag zur Frage der Standfestigkeit von dichten Asphaltbelägen im Großwasserbau*, 1964
- 3 Gurr, Siegfried: *Beitrag zur Berechnung zusammengesetzter ebener Flächen-tragwerke unter besonderer Berücksichtigung ebener Stauwände, mit Hilfe von Randwert- und Lastwertmatrizen*, 1965
- 4 Plica, Peter: *Ein Beitrag zur Anwendung von Schalenkonstruktionen im Stahlwasserbau*, und Petrikat, Kurt: *Möglichkeiten und Grenzen des wasserbaulichen Versuchswesens*, 1966

- 5 Plate, Erich: *Beitrag zur Bestimmung der Windgeschwindigkeitsverteilung in der durch eine Wand gestörten bodennahen Luftschicht*, und
Röhnisch, Arthur; Marotz, Günter: *Neue Baustoffe und Bauausführungen für den Schutz der Böschungen und der Sohle von Kanälen, Flüssen und Häfen; Gesteigungskosten und jeweilige Vorteile*, sowie Unny, T.E.: *Schwingungsuntersuchungen am Kegelstrahlschieber*, 1967
- 6 Seiler, Erich: *Die Ermittlung des Anlagenwertes der bundeseigenen Binnenschiffahrtsstraßen und Talsperren und des Anteils der Binnenschifffahrt an diesem Wert*, 1967
- 7 *Sonderheft anlässlich des 65. Geburtstages von Prof. Arthur Röhnisch mit Beiträgen von* Benk, Dieter; Breitling, J.; Gurr, Siegfried; Haberhauer, Robert; Honekamp, Hermann; Kuz, Klaus Dieter; Marotz, Günter; Mayer-Vorfelder, Hans-Jörg; Miller, Rudolf; Plate, Erich J.; Radomski, Helge; Schwarz, Helmut; Vollmer, Ernst; Wildenhahn, Eberhard; 1967
- 8 Jumikis, Alfred: *Beitrag zur experimentellen Untersuchung des Wassernachschubs in einem gefrierenden Boden und die Beurteilung der Ergebnisse*, 1968
- 9 Marotz, Günter: *Technische Grundlagen einer Wasserspeicherung im natürlichen Untergrund*, 1968
- 10 Radomski, Helge: *Untersuchungen über den Einfluß der Querschnittsform wellenförmiger Spundwände auf die statischen und rammtechnischen Eigenschaften*, 1968
- 11 Schwarz, Helmut: *Die Grenztragfähigkeit des Baugrundes bei Einwirkung vertikal gezogener Ankerplatten als zweidimensionales Bruchproblem*, 1969
- 12 Erbel, Klaus: *Ein Beitrag zur Untersuchung der Metamorphose von Mittelgebirgsschneedecken unter besonderer Berücksichtigung eines Verfahrens zur Bestimmung der thermischen Schneequalität*, 1969
- 13 Westhaus, Karl-Heinz: *Der Strukturwandel in der Binnenschifffahrt und sein Einfluß auf den Ausbau der Binnenschiffskanäle*, 1969
- 14 Mayer-Vorfelder, Hans-Jörg: *Ein Beitrag zur Berechnung des Erdwiderstandes unter Ansatz der logarithmischen Spirale als Gleitflächenfunktion*, 1970
- 15 Schulz, Manfred: *Berechnung des räumlichen Erddruckes auf die Wandung kreiszylindrischer Körper*, 1970
- 16 Mobasseri, Manoutschehr: *Die Rippenstützmauer. Konstruktion und Grenzen ihrer Standsicherheit*, 1970
- 17 Benk, Dieter: *Ein Beitrag zum Betrieb und zur Bemessung von Hochwasserrückhaltebecken*, 1970

- 18 Gàl, Attila: *Bestimmung der mitschwingenden Wassermasse bei überströmten Fischbauchklappen mit kreiszylindrischem Staublech*, 1971, vergriffen
- 19 Kuz, Klaus Dieter: *Ein Beitrag zur Frage des Einsetzens von Kavitationserscheinungen in einer Düsenströmung bei Berücksichtigung der im Wasser gelösten Gase*, 1971, vergriffen
- 20 Schaak, Hartmut: *Verteilleitungen von Wasserkraftanlagen*, 1971
- 21 *Sonderheft zur Eröffnung der neuen Versuchsanstalt des Instituts für Wasserbau der Universität Stuttgart mit Beiträgen von* Brombach, Hansjörg; Dirksen, Wolfram; Gàl, Attila; Gerlach, Reinhard; Giesecke, Jürgen; Holthoff, Franz-Josef; Kuz, Klaus Dieter; Marotz, Günter; Minor, Hans-Erwin; Petrikat, Kurt; Röhnisch, Arthur; Rueff, Helge; Schwarz, Helmut; Vollmer, Ernst; Wildenhahn, Eberhard; 1972
- 22 Wang, Chung-su: *Ein Beitrag zur Berechnung der Schwingungen an Kegelstrahlschiebern*, 1972
- 23 Mayer-Vorfelder, Hans-Jörg: *Erdwiderstandsbeiwerte nach dem Ohde-Variationsverfahren*, 1972
- 24 Minor, Hans-Erwin: *Beitrag zur Bestimmung der Schwingungsanfachungsfunktionen überströmter Stauklappen*, 1972, vergriffen
- 25 Brombach, Hansjörg: *Untersuchung strömungsmechanischer Elemente (Fluidik) und die Möglichkeit der Anwendung von Wirbelkammerelementen im Wasserbau*, 1972, vergriffen
- 26 Wildenhahn, Eberhard: *Beitrag zur Berechnung von Horizontalfilterbrunnen*, 1972
- 27 Steinlein, Helmut: *Die Eliminierung der Schwebstoffe aus Flußwasser zum Zweck der unterirdischen Wasserspeicherung, gezeigt am Beispiel der Iller*, 1972
- 28 Holthoff, Franz Josef: *Die Überwindung großer Hubhöhen in der Binnenschifffahrt durch Schwimmerhebwerke*, 1973
- 29 Röder, Karl: *Einwirkungen aus Baugrundbewegungen auf trog- und kastenförmige Konstruktionen des Wasser- und Tunnelbaues*, 1973
- 30 Kretschmer, Heinz: *Die Bemessung von Bogenstaumauern in Abhängigkeit von der Talform*, 1973
- 31 Honekamp, Hermann: *Beitrag zur Berechnung der Montage von Unterwasserpipelines*, 1973
- 32 Giesecke, Jürgen: *Die Wirbelkammertriode als neuartiges Steuerorgan im Wasserbau*, und Brombach, Hansjörg: *Entwicklung, Bauformen, Wirkungsweise und Steuereigenschaften von Wirbelkammerverstärkern*, 1974

- 33 Rueff, Helge: *Untersuchung der schwingungserregenden Kräfte an zwei hintereinander angeordneten Tiefschützen unter besonderer Berücksichtigung von Kavitation*, 1974
- 34 Röhnisch, Arthur: *Einpreßversuche mit Zementmörtel für Spannbeton - Vergleich der Ergebnisse von Modellversuchen mit Ausführungen in Hüllwellrohren*, 1975
- 35 *Sonderheft anlässlich des 65. Geburtstages von Prof. Dr.-Ing. Kurt Petrikat mit Beiträgen von:* Brombach, Hansjörg; Erbel, Klaus; Flinspach, Dieter; Fischer jr., Richard; Gàl, Attila; Gerlach, Reinhard; Giesecke, Jürgen; Haberhauer, Robert; Hafner Edzard; Hausenblas, Bernhard; Horlacher, Hans-Burkhard; Hutarew, Andreas; Knoll, Manfred; Krummet, Ralph; Marotz, Günter; Merkle, Theodor; Miller, Christoph; Minor, Hans-Erwin; Neumayer, Hans; Rao, Syamala; Rath, Paul; Rueff, Helge; Ruppert, Jürgen; Schwarz, Wolfgang; Topal-Gökceli, Mehmet; Vollmer, Ernst; Wang, Chung-su; Weber, Hans-Georg; 1975
- 36 Berger, Jochum: *Beitrag zur Berechnung des Spannungszustandes in rotations-symmetrisch belasteten Kugelschalen veränderlicher Wandstärke unter Gas- und Flüssigkeitsdruck durch Integration schwach singulärer Differentialgleichungen*, 1975
- 37 Dirksen, Wolfram: *Berechnung instationärer Abflußvorgänge in gestauten Gerinnen mittels Differenzenverfahren und die Anwendung auf Hochwasserrückhaltebecken*, 1976
- 38 Horlacher, Hans-Burkhard: *Berechnung instationärer Temperatur- und Wärmespannungsfelder in langen mehrschichtigen Hohlzylindern*, 1976
- 39 Hafner, Edzard: *Untersuchung der hydrodynamischen Kräfte auf Baukörper im Tiefwasserbereich des Meeres*, 1977, ISBN 3-921694-39-6
- 40 Ruppert, Jürgen: *Über den Axialwirbelkammverstärker für den Einsatz im Wasserbau*, 1977, ISBN 3-921694-40-X
- 41 Hutarew, Andreas: *Beitrag zur Beeinflußbarkeit des Sauerstoffgehalts in Fließgewässern an Abstürzen und Wehren*, 1977, ISBN 3-921694-41-8, vergriffen
- 42 Miller, Christoph: *Ein Beitrag zur Bestimmung der schwingungserregenden Kräfte an unterströmten Wehren*, 1977, ISBN 3-921694-42-6
- 43 Schwarz, Wolfgang: *Druckstoßberechnung unter Berücksichtigung der Radial- und Längsverschiebungen der Rohrwandung*, 1978, ISBN 3-921694-43-4
- 44 Kinzelbach, Wolfgang: *Numerische Untersuchungen über den optimalen Einsatz variabler Kühlsysteme einer Kraftwerkskette am Beispiel Oberrhein*, 1978, ISBN 3-921694-44-2
- 45 Barczewski, Baldur: *Neue Meßmethoden für Wasser-Luftgemische und deren Anwendung auf zweiphasige Auftriebsstrahlen*, 1979, ISBN 3-921694-45-0

- 46 Neumayer, Hans: *Untersuchung der Strömungsvorgänge in radialen Wirbelkammerverstärkern*, 1979, ISBN 3-921694-46-9
- 47 Elalfy, Youssef-Elhassan: *Untersuchung der Strömungsvorgänge in Wirbelkammerdiolen und -drosseln*, 1979, ISBN 3-921694-47-7
- 48 Brombach, Hansjörg: *Automatisierung der Bewirtschaftung von Wasserspeichern*, 1981, ISBN 3-921694-48-5
- 49 Geldner, Peter: *Deterministische und stochastische Methoden zur Bestimmung der Selbstdichtung von Gewässern*, 1981, ISBN 3-921694-49-3, vergriffen
- 50 Mehlhorn, Hans: *Temperaturveränderungen im Grundwasser durch Brauchwasser-einleitungen*, 1982, ISBN 3-921694-50-7, vergriffen
- 51 Hafner, Edzard: *Rohrleitungen und Behälter im Meer*, 1983, ISBN 3-921694-51-5
- 52 Rinnert, Bernd: *Hydrodynamische Dispersion in porösen Medien: Einfluß von Dichteunterschieden auf die Vertikalvermischung in horizontaler Strömung*, 1983, ISBN 3-921694-52-3, vergriffen
- 53 Lindner, Wulf: *Steuerung von Grundwasserentnahmen unter Einhaltung ökologischer Kriterien*, 1983, ISBN 3-921694-53-1, vergriffen
- 54 Herr, Michael; Herzer, Jörg; Kinzelbach, Wolfgang; Kobus, Helmut; Rinnert, Bernd: *Methoden zur rechnerischen Erfassung und hydraulischen Sanierung von Grundwasserkontaminationen*, 1983, ISBN 3-921694-54-X
- 55 Schmitt, Paul: *Wege zur Automatisierung der Niederschlagsermittlung*, 1984, ISBN 3-921694-55-8, vergriffen
- 56 Müller, Peter: *Transport und selektive Sedimentation von Schwebstoffen bei gestautem Abfluß*, 1985, ISBN 3-921694-56-6
- 57 El-Qawasmeh, Fuad: *Möglichkeiten und Grenzen der Tropfbewässerung unter besonderer Berücksichtigung der Verstopfungsanfälligkeit der Tropfelemente*, 1985, ISBN 3-921694-57-4, vergriffen
- 58 Kirchenbaur, Klaus: *Mikroprozessorgesteuerte Erfassung instationärer Druckfelder am Beispiel seegangsbelasteter Baukörper*, 1985, ISBN 3-921694-58-2
- 59 Kobus, Helmut (Hrsg.): *Modellierung des großräumigen Wärme- und Schadstofftransports im Grundwasser*, Tätigkeitsbericht 1984/85 (DFG-Forschergruppe an den Universitäten Hohenheim, Karlsruhe und Stuttgart), 1985, ISBN 3-921694-59-0, vergriffen
- 60 Spitz, Karlheinz: *Dispersion in porösen Medien: Einfluß von Inhomogenitäten und Dichteunterschieden*, 1985, ISBN 3-921694-60-4, vergriffen
- 61 Kobus, Helmut: *An Introduction to Air-Water Flows in Hydraulics*, 1985, ISBN 3-921694-61-2

- 62 Kaleris, Vassilios: *Erfassung des Austausches von Oberflächen- und Grundwasser in horizontalebene Grundwassermodellen*, 1986, ISBN 3-921694-62-0
- 63 Herr, Michael: *Grundlagen der hydraulischen Sanierung verunreinigter Porengrundwasserleiter*, 1987, ISBN 3-921694-63-9
- 64 Marx, Walter: *Berechnung von Temperatur und Spannung in Massenbeton infolge Hydratation*, 1987, ISBN 3-921694-64-7
- 65 Koschitzky, Hans-Peter: *Dimensionierungskonzept für Sohlbelüfter in Schußrinnen zur Vermeidung von Kavitationsschäden*, 1987, ISBN 3-921694-65-5
- 66 Kobus, Helmut (Hrsg.): *Modellierung des großräumigen Wärme- und Schadstofftransports im Grundwasser*, Tätigkeitsbericht 1986/87 (DFG-Forscherguppe an den Universitäten Hohenheim, Karlsruhe und Stuttgart) 1987, ISBN 3-921694-66-3
- 67 Söll, Thomas: *Berechnungsverfahren zur Abschätzung anthropogener Temperaturanomalien im Grundwasser*, 1988, ISBN 3-921694-67-1
- 68 Dittrich, Andreas; Westrich, Bernd: *Bodenseeufererosion, Bestandsaufnahme und Bewertung*, 1988, ISBN 3-921694-68-X, vergriffen
- 69 Huwe, Bernd; van der Ploeg, Rienk R.: *Modelle zur Simulation des Stickstoffhaushaltes von Standorten mit unterschiedlicher landwirtschaftlicher Nutzung*, 1988, ISBN 3-921694-69-8, vergriffen
- 70 Stephan, Karl: *Integration elliptischer Funktionen*, 1988, ISBN 3-921694-70-1
- 71 Kobus, Helmut; Zilliox, Lothaire (Hrsg.): *Nitratbelastung des Grundwassers, Auswirkungen der Landwirtschaft auf die Grundwasser- und Rohwasserbeschaffenheit und Maßnahmen zum Schutz des Grundwassers*. Vorträge des deutsch-französischen Kolloquiums am 6. Oktober 1988, Universitäten Stuttgart und Louis Pasteur Strasbourg (Vorträge in deutsch oder französisch, Kurzfassungen zweisprachig), 1988, ISBN 3-921694-71-X
- 72 Soyeaux, Renald: *Unterströmung von Stauanlagen auf klüftigem Untergrund unter Berücksichtigung laminarer und turbulenter Fließzustände*, 1991, ISBN 3-921694-72-8
- 73 Kohane, Roberto: *Berechnungsmethoden für Hochwasserabfluß in Fließgewässern mit überströmten Vorländern*, 1991, ISBN 3-921694-73-6
- 74 Hassinger, Reinhard: *Beitrag zur Hydraulik und Bemessung von Blocksteinrampen in flexibler Bauweise*, 1991, ISBN 3-921694-74-4, vergriffen
- 75 Schäfer, Gerhard: *Einfluß von Schichtenstrukturen und lokalen Einlagerungen auf die Längsdispersion in Porengrundwasserleitern*, 1991, ISBN 3-921694-75-2
- 76 Giesecke, Jürgen: *Vorträge, Wasserwirtschaft in stark besiedelten Regionen; Umweltforschung mit Schwerpunkt Wasserwirtschaft*, 1991, ISBN 3-921694-76-0

- 77 Huwe, Bernd: *Deterministische und stochastische Ansätze zur Modellierung des Stickstoffhaushalts landwirtschaftlich genutzter Flächen auf unterschiedlichem Skalenniveau*, 1992, ISBN 3-921694-77-9, vergriffen
- 78 Rommel, Michael: *Verwendung von Kluftdaten zur realitätsnahen Generierung von Kluftnetzen mit anschließender laminar-turbulenter Strömungsberechnung*, 1993, ISBN 3-92 1694-78-7
- 79 Marschall, Paul: *Die Ermittlung lokaler Stofffrachten im Grundwasser mit Hilfe von Einbohrloch-Meßverfahren*, 1993, ISBN 3-921694-79-5, vergriffen
- 80 Ptak, Thomas: *Stofftransport in heterogenen Porenaquiferen: Felduntersuchungen und stochastische Modellierung*, 1993, ISBN 3-921694-80-9, vergriffen
- 81 Haakh, Frieder: *Transientes Strömungsverhalten in Wirbelkammern*, 1993, ISBN 3-921694-81-7
- 82 Kobus, Helmut; Cirpka, Olaf; Barczewski, Baldur; Koschitzky, Hans-Peter: *Versucheinrichtung zur Grundwasser und Altlastensanierung VEGAS, Konzeption und Programmrahmen*, 1993, ISBN 3-921694-82-5
- 83 Zang, Weidong: *Optimaler Echtzeit-Betrieb eines Speichers mit aktueller Abflußregenerierung*, 1994, ISBN 3-921694-83-3, vergriffen
- 84 Franke, Hans-Jörg: *Stochastische Modellierung eines flächenhaften Stoffeintrages und Transports in Grundwasser am Beispiel der Pflanzenschutzmittelproblematik*, 1995, ISBN 3-921694-84-1
- 85 Lang, Ulrich: *Simulation regionaler Strömungs- und Transportvorgänge in Karst-aquiferen mit Hilfe des Doppelkontinuum-Ansatzes: Methodenentwicklung und Parameteridentifikation*, 1995, ISBN 3-921694-85-X, vergriffen
- 86 Helmig, Rainer: *Einführung in die Numerischen Methoden der Hydromechanik*, 1996, ISBN 3-921694-86-8, vergriffen
- 87 Cirpka, Olaf: *CONTRACT: A Numerical Tool for Contaminant Transport and Chemical Transformations - Theory and Program Documentation -*, 1996, ISBN 3-921694-87-6
- 88 Haberlandt, Uwe: *Stochastische Synthese und Regionalisierung des Niederschlages für Schmutzfrachtberechnungen*, 1996, ISBN 3-921694-88-4
- 89 Croisé, Jean: *Extraktion von flüchtigen Chemikalien aus natürlichen Lockergesteinen mittels erzwungener Luftströmung*, 1996, ISBN 3-921694-89-2, vergriffen
- 90 Jorde, Klaus: *Ökologisch begründete, dynamische Mindestwasserregelungen bei Ausleitungskraftwerken*, 1997, ISBN 3-921694-90-6, vergriffen
- 91 Helmig, Rainer: *Gekoppelte Strömungs- und Transportprozesse im Untergrund - Ein Beitrag zur Hydrosystemmodellierung-*, 1998, ISBN 3-921694-91-4, vergriffen

- 92 Emmert, Martin: *Numerische Modellierung nichtisothermer Gas-Wasser Systeme in porösen Medien*, 1997, ISBN 3-921694-92-2
- 93 Kern, Ulrich: *Transport von Schweb- und Schadstoffen in staugeregelten Fließgewässern am Beispiel des Neckars*, 1997, ISBN 3-921694-93-0, vergriffen
- 94 Förster, Georg: *Druckstoßdämpfung durch große Luftblasen in Hochpunkten von Rohrleitungen* 1997, ISBN 3-921694-94-9
- 95 Cirpka, Olaf: *Numerische Methoden zur Simulation des reaktiven Mehrkomponententransports im Grundwasser*, 1997, ISBN 3-921694-95-7, vergriffen
- 96 Färber, Arne: *Wärmetransport in der ungesättigten Bodenzone: Entwicklung einer thermischen In-situ-Sanierungstechnologie*, 1997, ISBN 3-921694-96-5
- 97 Betz, Christoph: *Wasserdampfdestillation von Schadstoffen im porösen Medium: Entwicklung einer thermischen In-situ-Sanierungstechnologie*, 1998, ISBN 3-921694-97-3
- 98 Xu, Yichun: *Numerical Modeling of Suspended Sediment Transport in Rivers*, 1998, ISBN 3-921694-98-1, vergriffen
- 99 Wüst, Wolfgang: *Geochemische Untersuchungen zur Sanierung CKW-kontaminierter Aquifere mit Fe(0)-Reaktionswänden*, 2000, ISBN 3-933761-02-2
- 100 Sheta, Hussam: *Simulation von Mehrphasenvorgängen in porösen Medien unter Einbeziehung von Hysterese-Effekten*, 2000, ISBN 3-933761-03-4
- 101 Ayros, Edwin: *Regionalisierung extremer Abflüsse auf der Grundlage statistischer Verfahren*, 2000, ISBN 3-933761-04-2, vergriffen
- 102 Huber, Ralf: *Compositional Multiphase Flow and Transport in Heterogeneous Porous Media*, 2000, ISBN 3-933761-05-0
- 103 Braun, Christopherus: *Ein Upscaling-Verfahren für Mehrphasenströmungen in porösen Medien*, 2000, ISBN 3-933761-06-9
- 104 Hofmann, Bernd: *Entwicklung eines rechnergestützten Managementsystems zur Beurteilung von Grundwasserschadensfällen*, 2000, ISBN 3-933761-07-7
- 105 Class, Holger: *Theorie und numerische Modellierung nichtisothermer Mehrphasenprozesse in NAPL-kontaminierten porösen Medien*, 2001, ISBN 3-933761-08-5
- 106 Schmidt, Reinhard: *Wasserdampf- und Heißluftinjektion zur thermischen Sanierung kontaminierter Standorte*, 2001, ISBN 3-933761-09-3
- 107 Josef, Reinhold.: *Schadstoffextraktion mit hydraulischen Sanierungsverfahren unter Anwendung von grenzflächenaktiven Stoffen*, 2001, ISBN 3-933761-10-7

- 108 Schneider, Matthias: *Habitat- und Abflussmodellierung für Fließgewässer mit unscharfen Berechnungsansätzen*, 2001, ISBN 3-933761-11-5
- 109 Rathgeb, Andreas: *Hydrodynamische Bemessungsgrundlagen für Lockerdeckwerke an überströmbaren Erddämmen*, 2001, ISBN 3-933761-12-3
- 110 Lang, Stefan: *Parallele numerische Simulation instationärer Probleme mit adaptiven Methoden auf unstrukturierten Gittern*, 2001, ISBN 3-933761-13-1
- 111 Appt, Jochen; Stumpp Simone: *Die Bodensee-Messkampagne 2001, IWS/CWR Lake Constance Measurement Program 2001*, 2002, ISBN 3-933761-14-X
- 112 Heimerl, Stephan: *Systematische Beurteilung von Wasserkraftprojekten*, 2002, ISBN 3-933761-15-8, vergriffen
- 113 Iqbal, Amin: *On the Management and Salinity Control of Drip Irrigation*, 2002, ISBN 3-933761-16-6
- 114 Silberhorn-Hemming, Annette: *Modellierung von Kluftaquifersystemen: Geostatistische Analyse und deterministisch-stochastische Kluftgenerierung*, 2002, ISBN 3-933761-17-4
- 115 Winkler, Angela: *Prozesse des Wärme- und Stofftransports bei der In-situ-Sanierung mit festen Wärmequellen*, 2003, ISBN 3-933761-18-2
- 116 Marx, Walter: *Wasserkraft, Bewässerung, Umwelt - Planungs- und Bewertungsschwerpunkte der Wasserbewirtschaftung*, 2003, ISBN 3-933761-19-0
- 117 Hinkelmann, Reinhard: *Efficient Numerical Methods and Information-Processing Techniques in Environment Water*, 2003, ISBN 3-933761-20-4
- 118 Samaniego-Eguiguren, Luis Eduardo: *Hydrological Consequences of Land Use / Land Cover and Climatic Changes in Mesoscale Catchments*, 2003, ISBN 3-933761-21-2
- 119 Neunhäuserer, Lina: *Diskretisierungsansätze zur Modellierung von Strömungs- und Transportprozessen in geklüftet-porösen Medien*, 2003, ISBN 3-933761-22-0
- 120 Paul, Maren: *Simulation of Two-Phase Flow in Heterogeneous Poros Media with Adaptive Methods*, 2003, ISBN 3-933761-23-9
- 121 Ehret, Uwe: *Rainfall and Flood Nowcasting in Small Catchments using Weather Radar*, 2003, ISBN 3-933761-24-7
- 122 Haag, Ingo: *Der Sauerstoffhaushalt staugeregelter Flüsse am Beispiel des Neckars - Analysen, Experimente, Simulationen -*, 2003, ISBN 3-933761-25-5
- 123 Appt, Jochen: *Analysis of Basin-Scale Internal Waves in Upper Lake Constance*, 2003, ISBN 3-933761-26-3

- 124 Hrsg.: Schrenk, Volker; Batereau, Katrin; Barczewski, Baldur; Weber, Karolin und Koschitzky, Hans-Peter: *Symposium Ressource Fläche und VEGAS - Statuskolloquium 2003, 30. September und 1. Oktober 2003*, 2003, ISBN 3-933761-27-1
- 125 Omar Khalil Ouda: *Optimisation of Agricultural Water Use: A Decision Support System for the Gaza Strip*, 2003, ISBN 3-933761-28-0
- 126 Batereau, Katrin: *Sensorbasierte Bodenluftmessung zur Vor-Ort-Erkundung von Schadensherden im Untergrund*, 2004, ISBN 3-933761-29-8
- 127 Witt, Oliver: *Erosionsstabilität von Gewässersedimenten mit Auswirkung auf den Stofftransport bei Hochwasser am Beispiel ausgewählter Stauhaltungen des Oberrheins*, 2004, ISBN 3-933761-30-1
- 128 Jakobs, Hartmut: *Simulation nicht-isothermer Gas-Wasser-Prozesse in komplexen Kluft-Matrix-Systemen*, 2004, ISBN 3-933761-31-X
- 129 Li, Chen-Chien: *Deterministisch-stochastisches Berechnungskonzept zur Beurteilung der Auswirkungen erosiver Hochwasserereignisse in Flusstauhaltungen*, 2004, ISBN 3-933761-32-8
- 130 Reichenberger, Volker; Helmig, Rainer; Jakobs, Hartmut; Bastian, Peter; Niessner, Jennifer: *Complex Gas-Water Processes in Discrete Fracture-Matrix Systems: Upscaling, Mass-Conservative Discretization and Efficient Multilevel Solution*, 2004, ISBN 3-933761-33-6
- 131 Hrsg.: Barczewski, Baldur; Koschitzky, Hans-Peter; Weber, Karolin; Wege, Ralf: *VEGAS - Statuskolloquium 2004*, Tagungsband zur Veranstaltung am 05. Oktober 2004 an der Universität Stuttgart, Campus Stuttgart-Vaihingen, 2004, ISBN 3-933761-34-4
- 132 Asie, Kemal Jabir: *Finite Volume Models for Multiphase Multicomponent Flow through Porous Media*. 2005, ISBN 3-933761-35-2
- 133 Jacoub, George: *Development of a 2-D Numerical Module for Particulate Contaminant Transport in Flood Retention Reservoirs and Impounded Rivers*, 2004, ISBN 3-933761-36-0
- 134 Nowak, Wolfgang: *Geostatistical Methods for the Identification of Flow and Transport Parameters in the Subsurface*, 2005, ISBN 3-933761-37-9
- 135 Süß, Mia: *Analysis of the influence of structures and boundaries on flow and transport processes in fractured porous media*, 2005, ISBN 3-933761-38-7
- 136 Jose, Surabhin Chackiath: *Experimental Investigations on Longitudinal Dispersive Mixing in Heterogeneous Aquifers*, 2005, ISBN: 3-933761-39-5
- 137 Filiz, Fulya: *Linking Large-Scale Meteorological Conditions to Floods in Mesoscale Catchments*, 2005, ISBN 3-933761-40-9

- 138 Qin, Minghao: *Wirklichkeitsnahe und recheneffiziente Ermittlung von Temperatur und Spannungen bei großen RCC-Staumauern*, 2005, ISBN 3-933761-41-7
- 139 Kobayashi, Kenichiro: *Optimization Methods for Multiphase Systems in the Sub-surface - Application to Methane Migration in Coal Mining Areas*, 2005, ISBN 3-933761-42-5
- 140 Rahman, Md. Arifur: *Experimental Investigations on Transverse Dispersive Mixing in Heterogeneous Porous Media*, 2005, ISBN 3-933761-43-3
- 141 Schrenk, Volker: *Ökobilanzen zur Bewertung von Altlastensanierungsmaßnahmen*, 2005, ISBN 3-933761-44-1
- 142 Hundecha, Hirpa Yeshewatersfa: *Regionalization of Parameters of a Conceptual Rainfall-Runoff Model*, 2005, ISBN: 3-933761-45-X
- 143 Wege, Ralf: *Untersuchungs- und Überwachungsmethoden für die Beurteilung natürlicher Selbstreinigungsprozesse im Grundwasser*, 2005, ISBN 3-933761-46-8
- 144 Breiting, Thomas: *Techniken und Methoden der Hydroinformatik - Modellierung von komplexen Hydrosystemen im Untergrund*, 2006, 3-933761-47-6
- 145 Hrsg.: Braun, Jürgen; Koschitzky, Hans-Peter; Müller, Martin: *Ressource Untergrund: 10 Jahre VEGAS: Forschung und Technologieentwicklung zum Schutz von Grundwasser und Boden*, Tagungsband zur Veranstaltung am 28. und 29. September 2005 an der Universität Stuttgart, Campus Stuttgart-Vaihingen, 2005, ISBN 3-933761-48-4
- 146 Rojanschi, Vlad: *Abflusskonzentration in mesoskaligen Einzugsgebieten unter Berücksichtigung des Sickerraumes*, 2006, ISBN 3-933761-49-2
- 147 Winkler, Nina Simone: *Optimierung der Steuerung von Hochwasserrückhaltebecken-systemen*, 2006, ISBN 3-933761-50-6
- 148 Wolf, Jens: *Räumlich differenzierte Modellierung der Grundwasserströmung alluvialer Aquifere für mesoskalige Einzugsgebiete*, 2006, ISBN: 3-933761-51-4
- 149 Kohler, Beate: *Externe Effekte der Laufwasserkraftnutzung*, 2006, ISBN 3-933761-52-2
- 150 Hrsg.: Braun, Jürgen; Koschitzky, Hans-Peter; Stuhmann, Matthias: *VEGAS-Statuskolloquium 2006*, Tagungsband zur Veranstaltung am 28. September 2006 an der Universität Stuttgart, Campus Stuttgart-Vaihingen, 2006, ISBN 3-933761-53-0
- 151 Niessner, Jennifer: *Multi-Scale Modeling of Multi-Phase - Multi-Component Processes in Heterogeneous Porous Media*, 2006, ISBN 3-933761-54-9
- 152 Fischer, Markus: *Beanspruchung eingeeerdeter Rohrleitungen infolge Austrocknung bindiger Böden*, 2006, ISBN 3-933761-55-7

- 153 Schneck, Alexander: *Optimierung der Grundwasserbewirtschaftung unter Berücksichtigung der Belange der Wasserversorgung, der Landwirtschaft und des Naturschutzes*, 2006, ISBN 3-933761-56-5
- 154 Das, Tapash: *The Impact of Spatial Variability of Precipitation on the Predictive Uncertainty of Hydrological Models*, 2006, ISBN 3-933761-57-3
- 155 Bielinski, Andreas: *Numerical Simulation of CO₂ sequestration in geological formations*, 2007, ISBN 3-933761-58-1
- 156 Mödinger, Jens: *Entwicklung eines Bewertungs- und Entscheidungsunterstützungssystems für eine nachhaltige regionale Grundwasserbewirtschaftung*, 2006, ISBN 3-933761-60-3
- 157 Manthey, Sabine: *Two-phase flow processes with dynamic effects in porous media - parameter estimation and simulation*, 2007, ISBN 3-933761-61-1
- 158 Pozos Estrada, Oscar: *Investigation on the Effects of Entrained Air in Pipelines*, 2007, ISBN 3-933761-62-X
- 159 Ochs, Steffen Oliver: *Steam injection into saturated porous media – process analysis including experimental and numerical investigations*, 2007, ISBN 3-933761-63-8
- 160 Marx, Andreas: *Einsatz gekoppelter Modelle und Wetterradar zur Abschätzung von Niederschlagsintensitäten und zur Abflussvorhersage*, 2007, ISBN 3-933761-64-6
- 161 Hartmann, Gabriele Maria: *Investigation of Evapotranspiration Concepts in Hydrological Modelling for Climate Change Impact Assessment*, 2007, ISBN 3-933761-65-4
- 162 Kebede Gurmessa, Tesfaye: *Numerical Investigation on Flow and Transport Characteristics to Improve Long-Term Simulation of Reservoir Sedimentation*, 2007, ISBN 3-933761-66-2
- 163 Trifković, Aleksandar: *Multi-objective and Risk-based Modelling Methodology for Planning, Design and Operation of Water Supply Systems*, 2007, ISBN 3-933761-67-0
- 164 Göttinger, Jens: *Distributed Conceptual Hydrological Modelling - Simulation of Climate, Land Use Change Impact and Uncertainty Analysis*, 2007, ISBN 3-933761-68-9
- 165 Hrsg.: Braun, Jürgen; Koschitzky, Hans-Peter; Stuhmann, Matthias: *VEGAS – Kolloquium 2007*, Tagungsband zur Veranstaltung am 26. September 2007 an der Universität Stuttgart, Campus Stuttgart-Vaihingen, 2007, ISBN 3-933761-69-7
- 166 Freeman, Beau: *Modernization Criteria Assessment for Water Resources Planning; Klamath Irrigation Project, U.S.*, 2008, ISBN 3-933761-70-0

- 167 Dreher, Thomas: *Selektive Sedimentation von Feinstschwebstoffen in Wechselwirkung mit wandnahen turbulenten Strömungsbedingungen*, 2008, ISBN 3-933761-71-9
- 168 Yang, Wei: *Discrete-Continuous Downscaling Model for Generating Daily Precipitation Time Series*, 2008, ISBN 3-933761-72-7
- 169 Kopecki, Ianina: *Calculational Approach to FST-Hemispheres for Multiparametrical Benthos Habitat Modelling*, 2008, ISBN 3-933761-73-5
- 170 Brommundt, Jürgen: *Stochastische Generierung räumlich zusammenhängender Niederschlagszeitreihen*, 2008, ISBN 3-933761-74-3
- 171 Papafotiou, Alexandros: *Numerical Investigations of the Role of Hysteresis in Heterogeneous Two-Phase Flow Systems*, 2008, ISBN 3-933761-75-1
- 172 He, Yi: *Application of a Non-Parametric Classification Scheme to Catchment Hydrology*, 2008, ISBN 978-3-933761-76-7
- 173 Wagner, Sven: *Water Balance in a Poorly Gauged Basin in West Africa Using Atmospheric Modelling and Remote Sensing Information*, 2008, ISBN 978-3-933761-77-4
- 174 Hrsg.: Braun, Jürgen; Koschitzky, Hans-Peter; Stuhmann, Matthias; Schrenk, Volker: *VEGAS-Kolloquium 2008 Ressource Fläche III*, Tagungsband zur Veranstaltung am 01. Oktober 2008 an der Universität Stuttgart, Campus Stuttgart-Vaihingen, 2008, ISBN 978-3-933761-78-1
- 175 Patil, Sachin: *Regionalization of an Event Based Nash Cascade Model for Flood Predictions in Ungauged Basins*, 2008, ISBN 978-3-933761-79-8
- 176 Assteerawatt, Anongnart: *Flow and Transport Modelling of Fractured Aquifers based on a Geostatistical Approach*, 2008, ISBN 978-3-933761-80-4
- 177 Karnahl, Joachim Alexander: *2D numerische Modellierung von multifraktionalem Schwebstoff- und Schadstofftransport in Flüssen*, 2008, ISBN 978-3-933761-81-1
- 178 Hiester, Uwe: *Technologieentwicklung zur In-situ-Sanierung der ungesättigten Bodenzone mit festen Wärmequellen*, 2009, ISBN 978-3-933761-82-8
- 179 Laux, Patrick: *Statistical Modeling of Precipitation for Agricultural Planning in the Volta Basin of West Africa*, 2009, ISBN 978-3-933761-83-5
- 180 Ehsan, Saqib: *Evaluation of Life Safety Risks Related to Severe Flooding*, 2009, ISBN 978-3-933761-84-2
- 181 Prohaska, Sandra: *Development and Application of a 1D Multi-Strip Fine Sediment Transport Model for Regulated Rivers*, 2009, ISBN 978-3-933761-85-9

- 182 Kopp, Andreas: *Evaluation of CO₂ Injection Processes in Geological Formations for Site Screening*, 2009, ISBN 978-3-933761-86-6
- 183 Ebigbo, Anozie: *Modelling of biofilm growth and its influence on CO₂ and water (two-phase) flow in porous media*, 2009, ISBN 978-3-933761-87-3
- 184 Freiboth, Sandra: *A phenomenological model for the numerical simulation of multiphase multicomponent processes considering structural alterations of porous media*, 2009, ISBN 978-3-933761-88-0
- 185 Zöllner, Frank: *Implementierung und Anwendung netzfreier Methoden im Konstruktiven Wasserbau und in der Hydromechanik*, 2009, ISBN 978-3-933761-89-7
- 186 Vasin, Milos: *Influence of the soil structure and property contrast on flow and transport in the unsaturated zone*, 2010, ISBN 978-3-933761-90-3
- 187 Li, Jing: *Application of Copulas as a New Geostatistical Tool*, 2010, ISBN 978-3-933761-91-0
- 188 AghaKouchak, Amir: *Simulation of Remotely Sensed Rainfall Fields Using Copulas*, 2010, ISBN 978-3-933761-92-7
- 189 Thapa, Pawan Kumar: *Physically-based spatially distributed rainfall runoff modeling for soil erosion estimation*, 2010, ISBN 978-3-933761-93-4
- 190 Wurms, Sven: *Numerische Modellierung der Sedimentationsprozesse in Retentionsanlagen zur Steuerung von Stoffströmen bei extremen Hochwasserabflussereignissen*, 2011, ISBN 978-3-933761-94-1
- 191 Merkel, Uwe: *Unsicherheitsanalyse hydraulischer Einwirkungen auf Hochwasserschutzdeiche und Steigerung der Leistungsfähigkeit durch adaptive Strömungsmodellierung*, 2011, ISBN 978-3-933761-95-8
- 192 Fritz, Jochen: *A Decoupled Model for Compositional Non-Isothermal Multiphase Flow in Porous Media and Multiphysics Approaches for Two-Phase Flow*, 2010, ISBN 978-3-933761-96-5
- 193 Weber, Karolin (Hrsg.): *12. Treffen junger WissenschaftlerInnen an Wasserbauinstituten*, 2010, ISBN 978-3-933761-97-2
- 194 Bliedernicht, Jan-Geert: *Probability Forecasts of Daily Areal Precipitation for Small River Basins*, 2011, ISBN 978-3-933761-98-9
- 195 Hrsg.: Koschitzky, Hans-Peter; Braun, Jürgen: *VEGAS-Kolloquium 2010 In-situ-Sanierung - Stand und Entwicklung Nano und ISCO -*, Tagungsband zur Veranstaltung am 07. Oktober 2010 an der Universität Stuttgart, Campus Stuttgart-Vaihingen, 2010, ISBN 978-3-933761-99-6

- 196 Gafurov, Abror: *Water Balance Modeling Using Remote Sensing Information - Focus on Central Asia*, 2010, ISBN 978-3-942036-00-9
- 197 Mackenberg, Sylvia: *Die Quellstärke in der Sickerwasserprognose: Möglichkeiten und Grenzen von Labor- und Freilanduntersuchungen*, 2010, ISBN 978-3-942036-01-6
- 198 Singh, Shailesh Kumar: *Robust Parameter Estimation in Gauged and Ungauged Basins*, 2010, ISBN 978-3-942036-02-3
- 199 Doğan, Mehmet Onur: *Coupling of porous media flow with pipe flow*, 2011, ISBN 978-3-942036-03-0
- 200 Liu, Min: *Study of Topographic Effects on Hydrological Patterns and the Implication on Hydrological Modeling and Data Interpolation*, 2011, ISBN 978-3-942036-04-7
- 201 Geleta, Habtamu Itefa: *Watershed Sediment Yield Modeling for Data Scarce Areas*, 2011, ISBN 978-3-942036-05-4
- 202 Franke, Jörg: *Einfluss der Überwachung auf die Versagenswahrscheinlichkeit von Staustufen*, 2011, ISBN 978-3-942036-06-1
- 203 Bakimchandra, Oinam: *Integrated Fuzzy-GIS approach for assessing regional soil erosion risks*, 2011, ISBN 978-3-942036-07-8
- 204 Alam, Muhammad Mahboob: *Statistical Downscaling of Extremes of Precipitation in Mesoscale Catchments from Different RCMs and Their Effects on Local Hydrology*, 2011, ISBN 978-3-942036-08-5
- 205 Hrsg.: Koschitzky, Hans-Peter; Braun, Jürgen: *VEGAS-Kolloquium 2011 Flache Geothermie - Perspektiven und Risiken*, Tagungsband zur Veranstaltung am 06. Oktober 2011 an der Universität Stuttgart, Campus Stuttgart-Vaihingen, 2011, ISBN 978-3-933761-09-2
- 206 Haslauer, Claus: *Analysis of Real-World Spatial Dependence of Subsurface Hydraulic Properties Using Copulas with a Focus on Solute Transport Behaviour*, 2011, ISBN 978-3-942036-10-8
- 207 Dung, Nguyen Viet: *Multi-objective automatic calibration of hydrodynamic models – development of the concept and an application in the Mekong Delta*, 2011, ISBN 978-3-942036-11-5
- 208 Hung, Nguyen Nghia: *Sediment dynamics in the floodplain of the Mekong Delta, Vietnam*, 2011, ISBN 978-3-942036-12-2
- 209 Kuhlmann, Anna: *Influence of soil structure and root water uptake on flow in the unsaturated zone*, 2012, ISBN 978-3-942036-13-9

- 210 Tuhtan, Jeffrey Andrew: *Including the Second Law Inequality in Aquatic Ecodynamics: A Modeling Approach for Alpine Rivers Impacted by Hydropeaking*, 2012, ISBN 978-3-942036-14-6
- 211 Tolossa, Habtamu: *Sediment Transport Computation Using a Data-Driven Adaptive Neuro-Fuzzy Modelling Approach*, 2012, ISBN 978-3-942036-15-3
- 212 Tatomir, Alexandru-Bodgan: *From Discrete to Continuum Concepts of Flow in Fractured Porous Media*, 2012, ISBN 978-3-942036-16-0
- 213 Erbertseder, Karin: *A Multi-Scale Model for Describing Cancer-Therapeutic Transport in the Human Lung*, 2012, ISBN 978-3-942036-17-7
- 214 Noack, Markus: *Modelling Approach for Interstitial Sediment Dynamics and Reproduction of Gravel Spawning Fish*, 2012, ISBN 978-3-942036-18-4
- 215 De Boer, Cjstmir Volkert: *Transport of Nano Sized Zero Valent Iron Colloids during Injection into the Subsurface*, 2012, ISBN 978-3-942036-19-1
- 216 Pfaff, Thomas: *Processing and Analysis of Weather Radar Data for Use in Hydrology*, 2013, ISBN 978-3-942036-20-7
- 217 Lebreuz, Hans-Henning: *Addressing the Input Uncertainty for Hydrological Modeling by a New Geostatistical Method*, 2013, ISBN 978-3-942036-21-4
- 218 Darcis, Melanie Yvonne: *Coupling Models of Different Complexity for the Simulation of CO₂ Storage in Deep Saline Aquifers*, 2013, ISBN 978-3-942036-22-1
- 219 Beck, Ferdinand: *Generation of Spatially Correlated Synthetic Rainfall Time Series in High Temporal Resolution - A Data Driven Approach*, 2013, ISBN 978-3-942036-23-8
- 220 Guthke, Philipp: *Non-multi-Gaussian spatial structures: Process-driven natural genesis, manifestation, modeling approaches, and influences on dependent processes*, 2013, ISBN 978-3-942036-24-5
- 221 Walter, Lena: *Uncertainty studies and risk assessment for CO₂ storage in geological formations*, 2013, ISBN 978-3-942036-25-2
- 222 Wolff, Markus: *Multi-scale modeling of two-phase flow in porous media including capillary pressure effects*, 2013, ISBN 978-3-942036-26-9

Die Mitteilungshefte ab der Nr. 134 (Jg. 2005) stehen als pdf-Datei über die Homepage des Instituts: www.iws.uni-stuttgart.de zur Verfügung.